

Computational modeling of hemodynamics for surgical planning and device development

T.M.J. (Diederik) van Bakel

Lay-out and printing by Optima Grafische Communicatie

ISBN: 978-94-6361-239-5

Computational modeling of hemodynamics for surgical planning and device development

Computerondersteund modelleren van hemodynamica voor chirurgische planning
en hulpmiddel ontwikkeling
(met een samenvatting in het Nederlands)

Proefschrift

ter verkrijging van de graad van doctor aan de Universiteit Utrecht op gezag van
de rector magnificus, prof. dr. H.R.B.M. Kummeling, ingevolge het besluit van het
college voor promoties in het openbaar te verdedigen op donderdag 11 april 2019
des middags te 2.30 uur

door

Theodorus Marinus Johannes van Bakel

geboren op 17 november 1989 te Dordrecht

Promotor: Prof. dr. F.L. Moll

Copromotoren: Dr. J.A. van Herwaarden
Dr. S. Trimarchi

Financial support by the Stichting Prof. Michaël - van Vlotenfonds for part of the research projects of this thesis is gratefully acknowledged.

Financial support by the Dutch Heart Foundation and Chirurgisch Fonds UMC Utrecht for the publication of this thesis is gratefully acknowledged.

Contents

Part I: Introduction

Chapter 1	Introduction and outline of thesis	9
Chapter 2	Patient-specific modeling of hemodynamics: supporting surgical planning in a Fontan circulation correction <i>Journal of Cardiovascular Translational Research. 2018;11:145-155</i>	13

Part II: Impact of stiffness mismatch on aortic hemodynamics

Chapter 3	Cardiac remodeling following thoracic endovascular aortic repair for descending aortic aneurysms <i>European Journal of Cardio-Thoracic Surgery. Doi: 10.1093/ejcts/ezy399</i>	33
Chapter 4	Ascending aortic rupture after zone 2 endovascular repair: a multiparametric computational analysis <i>European Journal of Cardio-Thoracic Surgery. Doi: 10.1093/ejcts/ezy458.</i>	49

Part III: Endovascular branch vessel preservation techniques

Chapter 5	Status of branched endovascular aortic arch repair <i>Annals of Cardiothoracic Surgery. 2018;7:406-413</i>	65
Chapter 6	A computational analysis of different endograft designs for zone 0 aortic arch repair <i>European Journal of Cardio-Thoracic Surgery. Editor's Choice – 2018;54:389-396</i>	77
Chapter 7	Patient-specific computational fluid dynamics analysis of renal artery hemodynamics following complex endovascular aortic repair <i>In preparation</i>	93

Part IV: Morphological studies for aortic repair

- Chapter 8 The Modified Arch Landing Areas Nomenclature (MALAN) improves prediction of stent graft displacement forces: proof of concept by computational fluid dynamics modeling
European Journal of Vascular and Endovascular Surgery. 2018;55:584-592 107
- Chapter 9 Blood flow after endovascular repair in the arch: a computational analysis
Aorta. In press 123
- Chapter 10 Computational analysis of renal artery flow characteristics by modeling aortoplasty and aortic bypass interventions for abdominal aortic coarctation
Journal of Vascular Surgery. In press 137

Part V: Endovascular repair of aortic dissection

- Chapter 11 Challenges of thoracic endovascular aortic repair for type B aortic dissection
Journal of Endovascular Therapy. 2018;25:578-580 157
- Chapter 12 Dynamic mesenteric malperfusion in aortic dissection
Journal of Endovascular Therapy. 2019;26:88-89 163

Part VI: Summary and discussion

Chapter 13	Summary and general discussion	167
Chapter 14	Samenvatting en discussie in het Nederlands	177
Chapter 15	Review Committee	189
	Acknowledgements	191
	List of publications	194
	Curriculum vitae	197

Chapter 1

Introduction and outline of thesis

The mechanical coupling of blood flow and vascular tissue is an essential part of the cardiovascular system. Various mechanisms have been identified that enable cardiovascular remodeling in response to hemodynamic stressors acting on global and local levels.¹ Furthermore, hemodynamic disturbances have been recognized as triggering factors in the pathogenesis of cardiovascular diseases.^{2,3} To study these mechanisms, and analyze how pathologic flow patterns can be prevented or treated, highly detailed data on local and regional hemodynamics are necessary.

Computational fluid dynamics (CFD) is a modeling technique that is used in various engineering fields, such as aerospace, automotive and biomedical engineering, to study fluid flows in complex geometries. More recently, CFD techniques have been used in cardiovascular research to study blood flow.⁴ In this thesis, patient-specific CFD models are used to aid understanding of the pathophysiology of cardiovascular disease and guide surgical planning and device optimization.

Chapter 2 is an introduction to computational modeling of hemodynamics. First, an overview of the CFD modeling methods is given. Then, a case of computationally supported surgical planning is presented. Lastly, the challenges for clinical applications of CFD modeling are discussed.

In the second part of this thesis, CFD techniques are used to calculate the impact of thoracic endovascular aortic repair (TEVAR) on aortic hemodynamics. Current endografts for TEVAR are much stiffer than the native aorta. The consequences of this stiffness mismatch on the left ventricle and unstented segments of the aorta are poorly understood. **Chapter 3** is a study where the impact of TEVAR on the left ventricle is quantified using morphologic measurements and stroke work calculations before and after TEVAR. **Chapter 4** presents a patient who expired from ascending aortic rupture following zone 2 TEVAR. The pathophysiology of this rupture was studied using a multiparametric computational analysis, focusing on the stiffness mismatch between endograft and native aorta.

The third part of this thesis presents studies on complex endovascular aortic repair and device optimization. Multiple manufacturers are developing endografts that facilitate minimally invasive repair of aortic pathologies in the vicinity of critical branch vessels. Different branched endograft designs have been introduced, with varying number, size and orientation of the branches that redirect flow to the target arteries. **Chapter 5** presents an overview of the literature on currently investigated branched endografts for deployment in the aortic arch. In **Chapter 6**, the postoperative hemodynamic performance of different endograft designs for zone 0 endovascular arch repair is tested. In **Chapter 7**, similar computational techniques are used to test the hemodynamic performance of branched, fenestrated and parallel stent-grafting solutions for endovascular aortic repair with renal artery vascularization.

In part four, morphological studies of the aorta are reported that aim to aid surgical planning. **Chapter 8** presents a computational study quantifying hemodynamic displacement forces in the proximal landing zones for TEVAR according to the MALAN classification. **Chapter 9** investigates the pathophysiology of endograft migration and type Ib endoleak following zone 2 TEVAR by calculating hemodynamic displacement forces on endografts after deployment. **Chapter 10** presents a computational analysis of renal artery flow characteristics in a pediatric patient with therapy resistant hypertension caused by a suprarenal abdominal aortic coarctation. In this patient, the hemodynamic performance of different patch aortoplasty and thoracoabdominal bypass repairs was tested.

Finally, part five comprises of two chapters that comment on the challenges of endovascular repair for aortic dissection. **Chapter 11** discusses the challenges of TEVAR for type B aortic dissection. **Chapter 12** discusses endovascular treatment of mesenteric malperfusion in complicated type B aortic dissection.

References

- 1 Humphrey JD, Dufresne ER, Schwartz MA. Mechanotransduction and extracellular matrix homeostasis. *Nat Rev Mol Cell Biol* 2014;15(12):802–12. Doi: 10.1038/nrm3896.
- 2 Caro CG, Fitz-Gerald JM, Schroter RC. Arterial wall shear and distribution of early atheroma in man. *Nature* 1969;223(5211):1159–60.
- 3 Humphrey JD, Schwartz MA, Tellides G, et al. Role of mechanotransduction in vascular biology: focus on thoracic aortic aneurysms and dissections. *Circ Res* 2015;116(8):1448–61. Doi: 10.1161/CIRCRESAHA.114.304936.
- 4 Taylor CA, Figueroa CA. Patient-specific modeling of cardiovascular mechanics. *Annu Rev Biomed Eng* 2009;11:109–34. Doi: 10.1146/annurev.bioeng.10.061807.160521.

Chapter 2

Patient-specific modeling of hemodynamics: supporting surgical planning in a Fontan circulation correction

Theodorus M.J. van Bakel¹, MD

Kevin D. Lau¹, PhD

Jennifer Hirsch-Romano³, MD

Santi Trimarchi⁴, MD, PhD

Adam L. Dorfman³, MD

C. Alberto Figueroa^{1,2}, PhD

1. Department of Surgery, University of Michigan, Ann Arbor, Michigan, USA.

2. Department of Biomedical Engineering, University of Michigan, Ann Arbor, Michigan, USA.

3. University of Michigan C.S. Mott Children's Hospital Congenital Heart Center, Ann Arbor, Michigan, USA.

4. Thoracic Aortic Research Center, Policlinico San Donato IRCCS, San Donato Milanese, Italy.

Journal of Cardiovascular Translational Research. 2018;11:145-155

Abstract

Computational fluid dynamics (CFD) is a modeling technique that enables calculation of the behavior of fluid flows in complex geometries. In cardiovascular medicine, CFD methods are being used to calculate patient-specific hemodynamics for a variety of applications, such as disease research, noninvasive diagnostics, medical device evaluation and surgical planning. This paper provides a concise overview of the methods to perform patient-specific computational analyses using clinical data, followed by a case study where CFD-supported surgical planning is presented in a patient with Fontan circulation complicated by unilateral pulmonary arteriovenous malformations. In closing, the challenges for implementation and adoption of CFD modeling in clinical practice are discussed.

Introduction

Hemodynamic disturbances are recognized as a triggering factor in the pathogenesis of cardiovascular disease.¹ Computational fluid dynamics (CFD) is a well-established computational technique that has been developed to study fluid flows in a variety of applications such as aerospace, automotive and biomedical engineering. Over the past decades, numerous CFD methods have been developed to study blood flow in cardiovascular health and disease. Taylor and Figueroa wrote a comprehensive review on the methods to perform patient-specific simulations of cardiovascular mechanics.² To calculate hemodynamics on a patient-specific basis, CFD models can be constructed through incorporation of medical imaging and physiologic data and the use of adequate inflow and outflow boundary condition methods. These models provide high-resolution data on *in vivo* hemodynamics that can be used to study pathogenesis of cardiovascular diseases,³ perform non-invasive diagnostics,⁴ assist in medical device evaluation,^{5,6} and support clinical decision making through prediction of changes in blood flow following different therapeutic interventions.^{7,8}

In addition to the methodological advances noted above, faster parallel computers and user-friendly commercial software packages make patient-specific simulation of hemodynamics more accessible to clinical research settings. However, the relative user-friendliness of these tools makes it such that unqualified users can produce un-physiologic computational predictions. It is thus imperative for the user to understand key aspects of computational modeling such as mesh refinement and solution validation against clinical data.

The aim of this paper is to report on the practical aspects of using patient-specific modeling in clinical applications. First, we present a concise overview of the methods we use to construct image-based hemodynamic models in the context of clinical decision making, specifically surgical planning. Then, we present and discuss a specific case of CFD-supported surgical planning of a Fontan correction in a patient suffering from unilateral pulmonary arteriovenous malformations (PAVMs). We conclude by discussing adoption challenges for patient-specific modeling in the clinical practice, and potential strategies for overcoming those challenges.

Methods for Patient-Specific Modeling of Hemodynamics

A patient-specific modeling workflow necessitates the following elements: (1) A CFD code to solve the Navier-Stokes equations, characterizing the motion of an incompressible fluid (blood) in a domain (rigid or deformable). There are numerous commercial and academic solutions, which rely either on the Finite Element or the

Finite Volume methods. It is outside the scope of this work to discuss these methods in detail; (2) a three-dimensional (3D) geometric model of the vascular anatomy of interest; and (3) a set of inflow and outflow boundary conditions that represent the physiologic flow and pressure conditions of the subject. The geometric model and the inflow/outflow boundary conditions must be extracted from the available imaging and hemodynamic data (e.g. flow and pressure).

Geometric Model Construction and Mesh Generation

Vascular geometric models can be constructed from 3D imaging modalities such as computed tomography (CT) and magnetic resonance angiography (MRA) using a variety of segmentation methods. For cardiovascular applications, the segmentation procedure seeks to delineate the boundaries of the vessels of interest in a certain region. Segmentation methods range from automatic to manual, and the outcome is either a discrete triangulated surface mesh (e.g. STereoLithography) or smooth analytical description of the vessel boundaries (e.g., computer-aided design (CAD)).

Numerous software packages offer automatic or semi-automatic methods such as threshold and region-growing algorithms that eventually produce a discrete surface triangulation. Notable examples are the open source Vascular Modeling Toolkit (www.vmtk.org)⁹ and the commercial Materialise Mimics (Materialise NV, Leuven, Belgium).¹⁰ These methods work well on high quality image data and usually render a 3D model suitable for computational analysis within minutes. However, the resolution of the vascular model is limited by the discrete surface triangulation, and additional smoothing operations are needed in order to accommodate mesh refinement procedures.

When the image data is noisy, the segmentation process often requires significant input from the user. The custom package CRIMSON (www.cirmson.software)¹¹ offers semi-automatic segmentation tools whereby manually constructed centerlines and two-dimensional (2D) segmentations of the vessel lumen are used to create a CAD model of the vessels of interest via lofting operations. Analytical models offer the advantage of being easy to manipulate (e.g. adding or removing blood vessels, a critical attribute for vascular surgical planning) and because they offer a smooth surface that can easily accommodate an arbitrary number of mesh refinement operations.¹² This workflow is more time-consuming and user-dependent. The time needed to produce an analytical vascular model suitable for mesh generation depends on the size and complexity of the model. Typically, an expert user would need 60 minutes to create an analytical vascular model of a healthy thoracic aorta, including the supra-aortic and coronary arteries suitable for mesh generation. Creating a more complex model of e.g. an aortic dissection would typically take 120 minutes, while creating a less complicated model, e.g. an abdominal aortic aneurysm, would approximately take 30 minutes.

Whichever workflow is chosen (analytical or surface triangulation models), a volumetric computational mesh must be created for the computational analysis. The mesh must be such that it captures not only the complex boundaries of the vascular region, but also the complexities of the blood flow field. Field-mesh mesh-adaption techniques are thus critical to ensure good quality grids that can produce mesh-independent computational results.¹³

Physiologic Data and Boundary Conditions

Patient-specific hemodynamic modeling requires information on physiologic data such as cardiac output, blood pressure and flow splits between different vessels. Conceptually, boundary conditions on flow and/or pressure must be prescribed in all inlets and outlets of the computational model. However, in real-life clinical settings it is nearly impossible to acquire flow and pressure data for all vessels of interest, under the same hemodynamic conditions. Therefore, numerical methods that allow the user to prescribe meaningful boundary conditions in the absence of direct measurements are critical. Multi-scale methods have been derived to couple CFD solvers for the Navier-Stokes equations with reduced-order, lumped-parameter models of the circulation.¹⁴ These models use electric-circuit analogues such as resistors, capacitors, and diodes to mimic properties such as vascular resistance, compliance, and the behavior of valves. Therefore, the reduced-order models, via the specification of meaningful values for their parameters, allow the user to include the impact of the vasculature not contained within the image data and specify boundary conditions in the absence of direct clinical measurements. The most-widely used lumped-parameter model is the 3-element Windkessel. The parameters of these models can be obtained using either data on flow and pressure, or morphometric considerations (larger vessels carry larger flows, etc.). Another strength of lumped-parameter models is that they represent a convenient choice for boundary condition specification in situations in which clinical data is not directly available, such as in virtual surgical planning. Here, one can use the same pre-operatively determined lumped parameter models to represent the behavior of a distal vascular bed in the post-operative scenario (instead of a direct measurement such as a pressure or flow waveform).

Deciding which hemodynamic measurements to use for CFD modeling purposes depends primarily on the availability of the data. It is necessary to understand the acquisition methods and their limitations, as inconsistencies between data (e.g., lack of mass conservation) and measurement errors affect the simulation results.¹⁵

Phase contrast Magnetic Resonance Imaging (PC-MRI) provides noninvasive data on 3D velocity maps in large blood vessels.¹⁶ Local blood flow can then be calculated by integrating the velocity maps over the cross-sectional area of the vessel. PC-MRI

velocity measurements must be acquired at each location of interest. Together with the angiography MRA sequence, the total duration of an MRI examination may range from 30 minutes to an hour. Consequently, changes in the physiology within the subject may occur over the examination.¹⁷ These changes need to be identified to avoid inconsistencies in the measured data.

Duplex Doppler ultrasonography can also be used to noninvasively acquire blood flow measurements. Compared to PC-MRI techniques, Duplex Doppler ultrasonography is cheaper, faster and more widely available in clinical practice. However, Ultrasonic techniques produce operator-dependent results, are affected by tissue signal attenuation and thus cannot reliably be used to measure flow in deep vessels.¹⁸

Recent developments on dynamic imaging have enabled noninvasive assessment of wall motion, producing useful information to characterize tissue strain.^{19,20}

Pressure data can be obtained invasively from catheterization procedures and noninvasively from applanation tonometry or cuff measurements. Catheter measurements are the gold standard, however they are invasive and induce hemodynamic changes through introduction of a catheter in the vessel lumen.²¹ Applanation tonometry, on the other hand, can only be used for superficial vessels and is prone to measurement errors and highly operator dependent, impacting the accuracy of the results.¹⁵ Cuff measurements do not capture the pressure waveform over time but only the systolic and diastolic extremes at one location.

Invasive cardiac catheterization, the gold standard method to assess cardiac output, can be used to obtain simultaneous measurements of blood flow and pressure.^{22,23} The method provides direct measurements of blood pressure, and blood oxygenation, which can then be used to assess cardiac output via the Fick principle. Therefore, no information on time-resolved flow waveforms is obtained, and there is a small risk of peri-interventional complications.

Treatment of the vessel walls

Vessel walls are often modelled as rigid structures. This approach is computationally efficient and it produces good approximations for the velocity and pressure fields. Alternatively, the deformability of the vessels can be taken into account using fluid structure interaction (FSI) simulation techniques.²⁴ Here, mechanical properties such as material stiffness and vessel thickness are assigned to the vessel wall, and the elasto-dynamic equations describing wall motion are solved simultaneously with the Navier-Stokes equations. Cardiovascular FSI simulations therefore describe blood velocity and pressure, as well as wall motion and provide a more realistic description of cardiovascular physiology, enabling calculation of quantities such as pulse wave velocity (PWV), elastic energy storage and distensibility under different hemodynamic and/or vascular stiffness conditions.³ FSI simulations also provide

more accurate descriptions of flow quantities that are affected by the compliance of the vessel wall, such as wall shear stress. Cardiovascular FSI simulations are therefore more complex and entail significantly higher computational costs compared to those of rigid wall simulations. In practice, this means that FSI simulations take significantly more time to run, limiting their applicability in clinical practice. Furthermore, FSI simulations require time-resolved data on wall motion and wall thickness. This information is often not available in routine clinical practice. Therefore, the choice between rigid or FSI hemodynamic analysis must be made depending on the specific quantities of interest and the availability of clinical data.²⁵

Computational analysis

Once geometric model, computational mesh, inflow and outflow boundary conditions are set, the Navier-Stokes equations are numerically solved over multiple cardiac cycles. The cardiac cycle is split in small time increments (typically in the range of 1e-3 to 1e-4 seconds) to accurately calculate blood velocity and pressure. Consequently, cardiovascular CFD simulations typically entail solving millions of equations for tens of thousands of time steps. Compared to clinical measurements, CFD simulation results have much higher spatial and temporal resolution. These analyses must therefore be run on high performance computing (HPC) systems. This is particularly important to produce solutions in clinically-relevant timeframes. The time that is required to calculate the solution of a CFD simulation depends on the complexity of the model and the hardware that is being used. Typically, computations of a healthy thoracic aorta (mesh size ± 1.5 million elements), with rigid walls, take 48 hours for 5 cardiac cycles on a HPC system with 80 cores. The same hardware would need approximately 240 hours to compute solutions for a healthy thoracic aorta with deformable walls (FSI).

Computational results can be post-processed to calculate variables such as flow distribution, wall shear stress, displacement forces on medical devices,²⁶ and metrics of hemodynamic disturbances such as turbulent kinetic energy²⁷ and platelet activation potential.⁷

Surgical Planning Supported by Computational Modeling

The current paradigm in cardiovascular surgical planning relies on anatomic assessments, results from clinical studies and the experience of the clinician performing the intervention. Different surgeons, when faced with the same problem, would often choose different surgical corrections. Furthermore, an assessment of how the hemodynamics would differ for different surgical alternatives is never made. Con-

ceptually, this is a ‘trial-and-error’ or ‘build-and-test’ paradigm, which only relies on previous experiences to make choices about the current problem. In numerous engineering fields, the ‘build-and-test’ paradigm has long been replaced by a ‘virtual testing’ paradigm, whereby computational simulations are used to optimize the design of cars, airplanes, structures, etc. before any physical model is built.

Patient-specific computational modeling of hemodynamics therefore offers great promise to change the current paradigm in cardiovascular surgical planning. Computational modeling, if properly executed, could inform the surgeon on specific hemodynamic differences between surgical alternatives and thus enable to theoretically identify an optimal solution based on function rather than on anatomical considerations. The optimality condition will be defined by the goals of the surgery (e.g. maximizing flow to a territory, minimizing energy losses due to turbulence, etc.). It is critically important though that the simulation workflow is set up in such a way that the computations reflect the actual anatomic and physiologic state of the patient, and that the results of the predictions can be verified after the procedure is performed.

Therefore, the workflow to perform patient-specific computational simulations to support surgical planning should consist of a two-step approach. Step 1 creates a clinically validated baseline (pre-operative) solution matching anatomical and hemodynamic data. In Step 2, the validated pre-operative solution is adapted to reflect different surgical options, with the goal of identifying the hemodynamically superior alternative. A schematic representation of this approach is presented in Figure 1. In the following, we present and discuss a case of computational-supported surgical planning of a Fontan correction in a patient suffering from unilateral PAVMs.

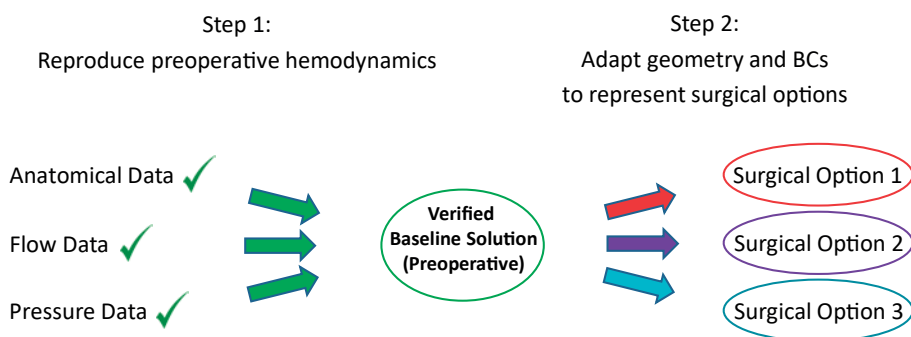


Figure 1. Two-step workflow for image-based surgical planning: In step 1, a 3D anatomical model is constructed from the image data and boundary conditions are tuned to reproduce pre-operative hemodynamics. This step produces a calibrated virtual representation of the hemodynamics of the patient. In step 2, the anatomical model and/or boundary conditions are adapted to reflect different surgical options. BCs = boundary conditions.

Single Ventricle Circulation and Pulmonary Arteriovenous Malformations

A healthy cardiac configuration consists of a biventricular system supplying the pulmonary and systemic circulation. Desaturated blood from the systemic circulation enters the heart through the right atrium and gets pumped into the pulmonary circulation by the right ventricle. Blood is oxygenated in the alveoli of the lungs and returns to the left side of the heart via the pulmonary veins. From there, the oxygenated blood is pumped to the aorta to supply the systemic circulation of oxygenated blood.

Children born with an anatomic or physiologic single ventricle do not have separate systemic and pulmonary circulations in series as described above. In this configuration, oxygenated blood from the pulmonary veins is mixed with desaturated blood from the systemic veins and is ejected together into the systemic circulation. Complications resulting from this physiology are related to ventricular volume overload and hypoxia in the systemic circulation, among other problems.

To improve oxygen saturation in the systemic circulation and reduce ventricular volume overload, a Fontan circulation is surgically created in multiple stages.²⁸ A good overview of this surgical solution is given by Gewillig.²⁹ Briefly, in this circulation, the systemic venous return bypasses the heart and is directly connected to the pulmonary arteries through a cavopulmonary anastomosis (CVPA). The single ventricle is connected to the aorta and functions as the systemic pump. Multiple surgical options are available to complete the Fontan circulation and computational studies have been performed to calculate the impact of postoperative geometry on energy loss and exercise intolerance.^{6,8} One important complication following CVPA is the formation of PAVMs.^{30,31} PAVMs are abnormal shunts between the pulmonary arteries and veins proximal to the alveoli, resulting in reduced oxygenation of blood from the affected lung returning to the heart and elevated cardiac output due to the reduction of flow resistance induced by the arteriovenous shunts. Development and progression of PAVMs are attributed to the absence of hepatic venous flow (HVF), containing angiogenesis inhibitors, in the affected lung(s).^{30,31} Revision of the Fontan circulation, aiming to direct sufficient HVF to the affected lung has shown to reverse progression of PAVMs.³²⁻³⁴ Multiple surgical options are available to reroute HVF to the lungs, however it can be difficult to discern from traditional clinical data how the HVF is distributed over both lungs and which surgical option would result in the best hemodynamic outcome. Patient-specific computational simulations can be performed to gain detailed information on regional flow and pressure waveforms and HVF distributions to each lung. Furthermore, the impact of different surgical options on HVF distribution can be quantified to select the procedure that renders the optimal results.³⁵

Case Description

An 18-year-old female presented with shortness of breath and exercise intolerance at our institution. Medical history included heterotaxy syndrome with polysplenia, interrupted inferior vena cava (IVC), dextrocardia, unbalanced atrioventricular septal defect, and double outlet right ventricle with pulmonary stenosis. Surgical history included a Kawashima operation³⁶ at 16 months of age and insertion of an extracardiac Fontan conduit (FN) at 32 months of age. Because of the interrupted IVC, most of the systemic venous return was transported through the azygos vein (AZV). The Kawashima operation involved creation of an anastomosis between the superior vena cava, AZV and main pulmonary artery. The base of the main pulmonary artery was ligated from the right ventricle. The FN connected the hepatic vein (HV) to the proximal left pulmonary artery to redirect HVF to the lungs, completing the Fontan circulation.²⁹

Clinical Data

Oxygen saturation at rest was 82%. CT imaging of the thorax revealed severe unilateral PAVMs in the right pulmonary artery (RPA). Flow measurements were acquired from PC-MRI at different locations in the Fontan circulation. Figure 2 presents the thoracic vascular anatomy and the measured flow data. Local pressure measurements were obtained through cardiac catheterization, as was cardiac output using the Fick principle.²²

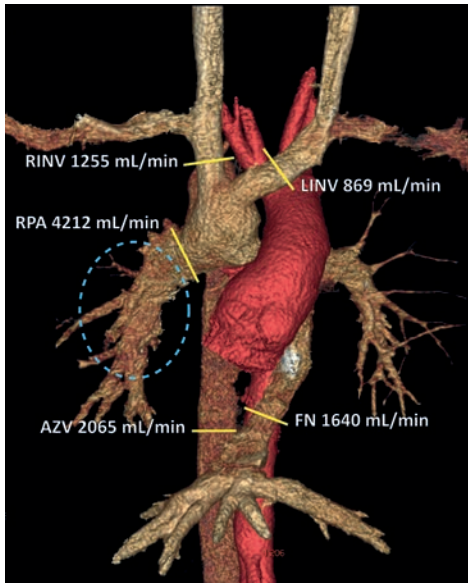


Figure 2. CT data of the thoracic vasculature and Fontan circulation. Flow data, acquired via PC-MRI, is indicated with numerical values and yellow lines at the following locations: AZV, FN, LINV, RINV and RPA. LPA flow could not be acquired due to artefacts induced by two embolization coils. The difference in morphology between LPA and RPA vasculatures is apparent, as a result of the pulmonary arteriovenous malformations in the RPA (circled in blue). AZV = azygos vein, CT = computed tomography, FN = Fontan conduit, LINV = left innominate vein, LPA = left pulmonary artery, PC-MRI = phase contrast magnetic resonance imaging, RINV = right innominate vein, RPA = right pulmonary artery.

Patient-Specific Computational Simulations

Patient-specific computational simulations were performed to gain detailed information on local distribution of HVF in the pulmonary circulation. A pre-operative 3D anatomical model was constructed from the CT imaging data using the built-in analytical segmentation tool in the validated software package CRIMSON.¹¹ The workflow for this procedure is presented in Figure 3. Once the geometric model was created, boundary conditions were tuned to match the clinically measured flow and pressure data from PC-MRI and cardiac catheterization, respectively. Specifically, PC-MRI derived flow waveforms were mapped to the FN conduit, AZV, and right and left innominate veins (RINV and LINV) using a time-varying parabolic velocity

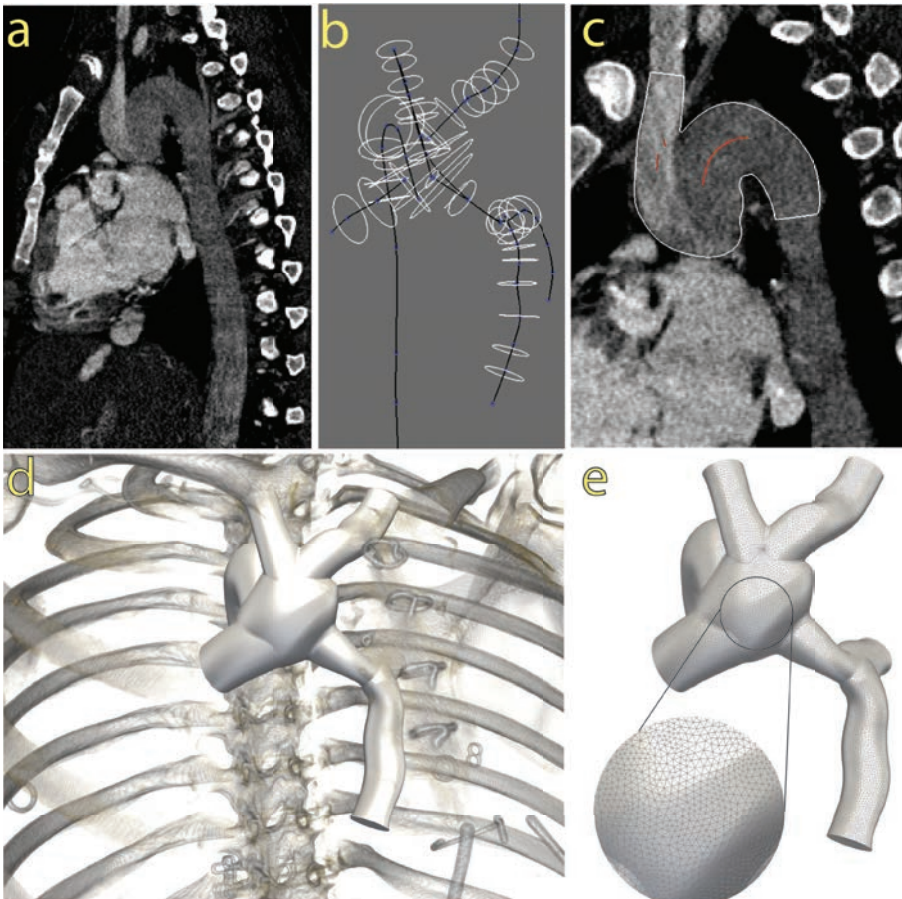


Figure 3. Workflow for geometric modeling using CT data in the CRIMSON software package. (a) Image data. (b) Vessel centerlines and 2D contours of the vessels of interest. (c) Lofting operations were performed and a good match between the contours of the geometric model and the image data was confirmed. (d) Completed 3D geometric CAD model. (e) The CAD model was discretized into a finite element mesh consisting of 1,768,104 linear tetrahedral elements. CAD = computed-aided design.

profile. The choice for parabolic velocity profiles at the inflow sections is valid for developed venous flows.³⁷ Three-element Windkessel models were tuned and mapped to the outlets of RPA and left pulmonary artery (LPA). An overview of the specifications of the boundary conditions at the inflow and outflow sections is presented in Table 1. As previously mentioned, lumped parameter models are a convenient choice for outflow boundary conditions in virtual surgical planning, because they represent the behavior of the distal vascular bed (rather than a fixed flow or pressure waveform). Since we needed the simulation results within a clinically reasonable timeframe, we adopted a rigid wall assumption. We argue that alterations in the HVF distribution are mainly caused by the 3D vascular anatomy in the different surgical scenarios, rather than the vessel wall compliance. Furthermore, all scenarios are equally affected by this assumption, so this would not affect the comparison.

The patient's heart rate at time of the cardiac catheterization differed from during MRI examination. To overcome inconsistencies in the duration of the cardiac cycle, the time scale of the pressure recordings was normalized to match the time scale of the flow measurements.

Table 1. Parameter Values of Boundary Conditions Applied at the Inflow and Outflow Sections of the geometric model

Inflow section	Mean flow rate [mL/s]	Proportion [%]	
AZV	34.90	35.53	
FN	27.09	27.59	
LINV	14.99	15.26	
RINV	21.23	21.62	
Total	98.21	100.00	
Outflow section	Proximal Resistor [Pa·s/mm ³]	Capacitor [mm ³ /Pa]	Distal Resistor [Pa·s/mm ³]
LPA	2.64E-05	1.86E+02	2.19E-02
RPA	5.19E-05	4.38E+01	4.66E-02

Flow waveforms derived from phase-contrast MRI were mapped to the inflow sections, mean flow rates and proportions of total flow are reported. On the outflow sections, three-element Windkessel models were attached and tuned to match flow and pressure measurements of the RPA and LPA. AZV = azygos vein, FN = Fontan conduit, LINV = left innominate vein, LPA = left pulmonary artery, MRI = magnetic resonance imaging, RINV = right innominate vein, RPA = right pulmonary artery.

Results

Baseline Simulation Results

The baseline solution successfully reproduced the patient's hemodynamics see, Figure 4. Iterative refinements on the values of the LPA and RPA Windkessel models

were made until the difference in mean and pulse values relative to the data was less than 5%. A ‘particle tracking’ postprocessing analysis was used to assess the distribution of HVF between both lungs.³⁸ A one mL bolus representing a control volume of HVF was injected in the FN and the RPA:LPA split of the particles defining the bolus was analyzed. All particles flowed into the LPA, leaving the RPA deprived from any HVF. This result is consistent with the presence of PAVMs in the right lung. Completion of this validated baseline solution achieves Step 1 in Figure 1.

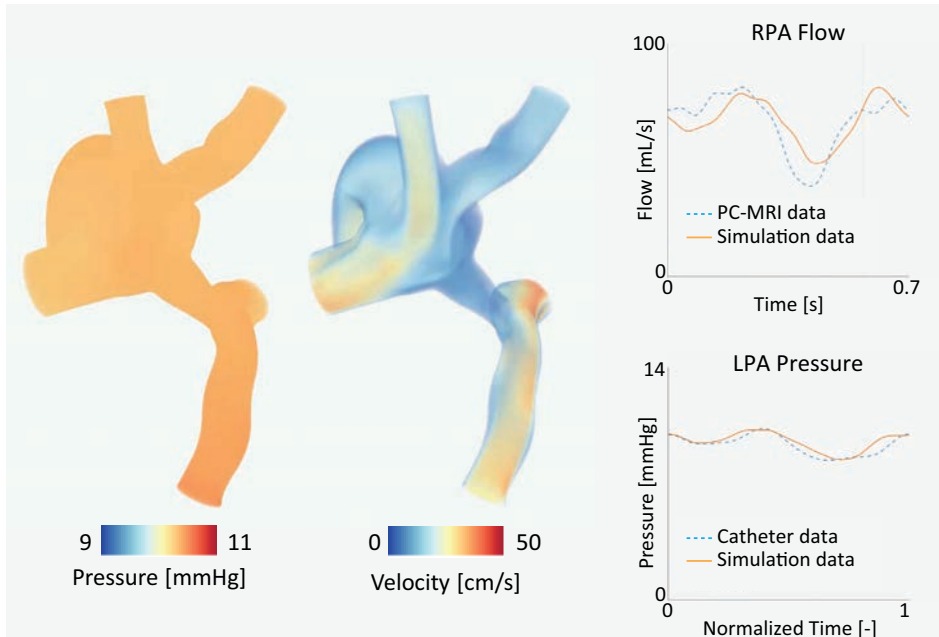


Figure 4. Step 1 of the surgical planning workflow: Left: Snapshot of pressure and velocity fields of the verified baseline solution. Here, boundary condition parameters were iteratively refined until a good match between computed and measured flow and pressure waveforms was achieved (right). LPA = left pulmonary artery, PC-MRI = phase contrast magnetic resonance imaging, RPA = right pulmonary artery.

Surgical Planning

Surgical revision of the FN was proposed to achieve a more balanced distribution of HVF between both lungs. Two options were considered, based on clinical feasibility. In option 1, Hepatic-to-Azygos, the FN is removed and an anastomosis is made from the HV to the AZV. In option 2, Fontan-to-Innominate, the FN is detached from the LPA and extended to the LINV. Figure 5 depicts the two proposed surgical options. Computations were performed to predict hemodynamics in both surgical options, leaving inflow and outflow conditions unchanged relative to the baseline solution, except for the inflow alterations resulting from the different surgical manipulations

(Step 2 Figure 1). The RPA:LPA HVF distribution was calculated for each option using the bolus tracking techniques. Furthermore, to assess the sensitivity of HVF distribution to the time of bolus injection, the bolus tracking analysis was performed at 55 different time-points in the cardiac cycle.

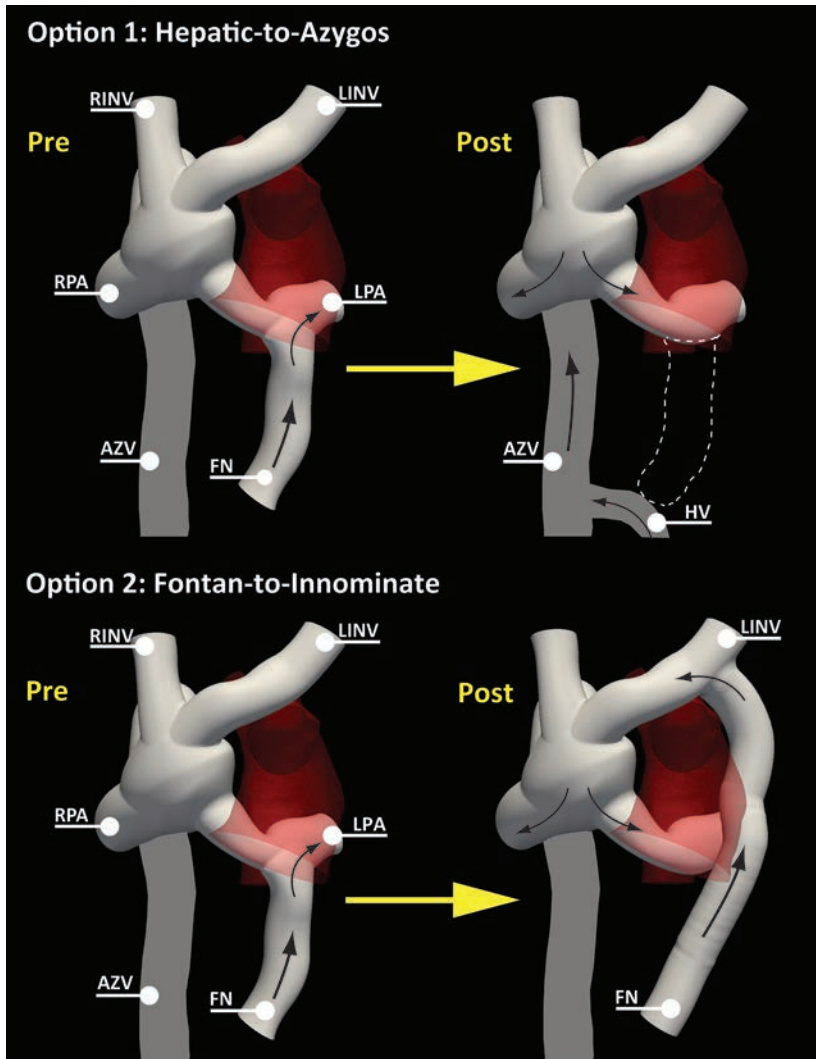


Figure 5. Step 2 of the surgical planning workflow: Two surgical options were considered as potential repair solutions. Option 1 (Hepatic-to-Azygos) consists of the removal of the FN from the LPA and the anastomosis of the HV directly to the distal part of the AZV. Option 2 (Fontan-to-Innominate): consists of detaching the FN from the LPA and extending it to the LINV. The black arrows indicate the direction of the hepatic venous flow in each option. AZV = azygos vein, FN = Fontan conduit, HV = hepatic vein, LINV = innominate vein, LPA = left pulmonary artery, RPA = right pulmonary artery, RINV = right innominate vein.

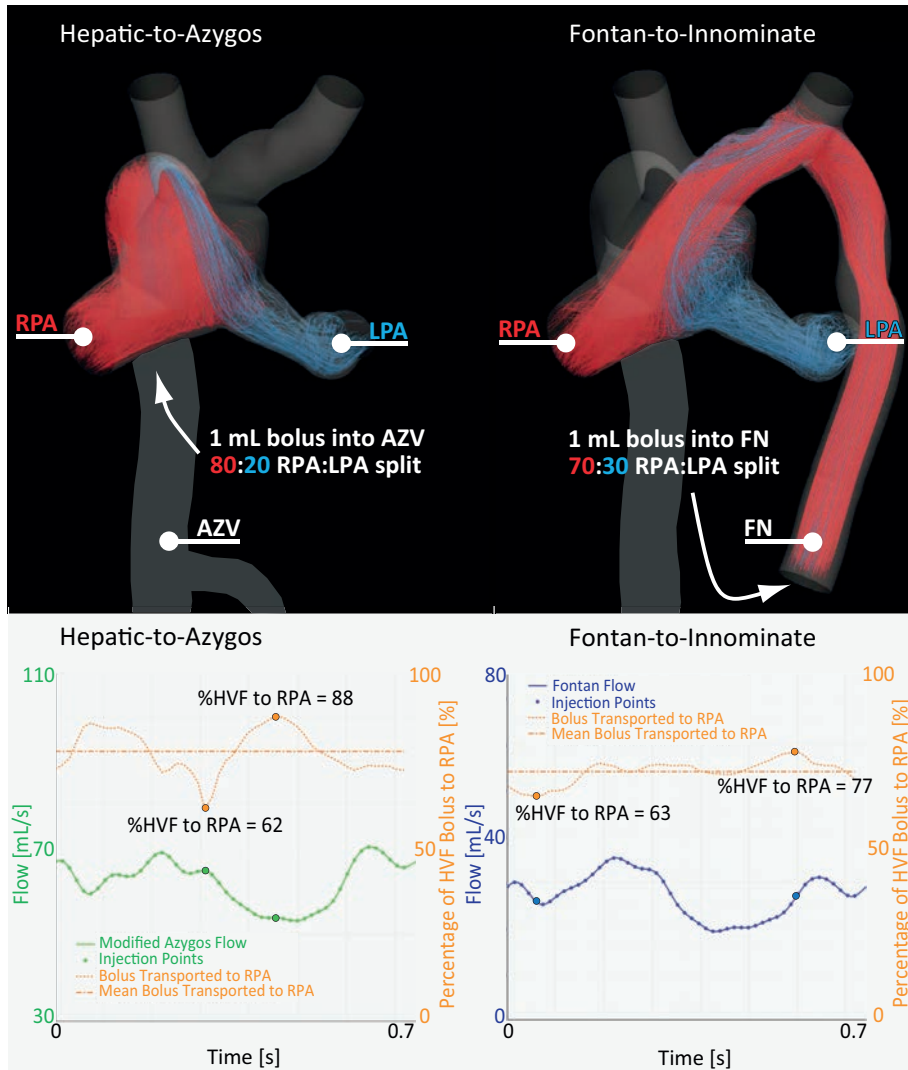


Figure 6. HVF distribution for the two surgical options. Top panel: path lines of HVF distribution between RPA (red lines) and LPA (blue lines) for the Hepatic-to-Azygos and Fontan-to-Innominate options. The RPA:LPA HVF distribution is 80:20 and 70:30 in the Hepatic-to-Azygos and Fontan-to-Innominate options, respectively. Bottom panel: Analysis of % of HVF transported to the RPA for 55 different bolus injection points. The injection points corresponding with maximum and minimum %HVF transported to the RPA are highlighted for each surgical scenario. The Hepatic-to-Azygos option shows a large variability in the %HVF transported to the RPA (maximum and minimum values of 88% and 62%, respectively). In contrast, the Fontan-to-Innominate option shows a much smaller variability for the different bolus injection times (maximum and minimum values of 63% and 77%, respectively). These findings suggest that the Fontan-to-Innominate option is hemodynamically superior. AZV = azygos vein, FN = Fontan conduit, HVF = hepatic venous flow, LPA = left pulmonary artery, RPA = right pulmonary artery, T = time.

Simulation Results of the Surgical Options

Computational results for both surgical options are summarized in Figure 6. The Hepatic-to-Azygos option resulted in a mean RPA:LPA HVF distribution of 80:20, and a wide variability through the cardiac cycle in %HVF reaching the RPA (max. 88%, min: 62%). Conversely, the Fontan-to-Innominate option resulted in a mean RPA:LPA HVF distribution of 70:30, and a much smaller variability in %HVF reaching the RPA (max. 77%, min. 63%). Due to the more balanced RPA:LPA HVF ratio and smaller variability over the cycle, the Fontan-to-Innominate option was selected after discussing it within the multi-disciplinary research and surgical team.

Clinical Outcomes

The Fontan-to-Innominate surgical procedure was successfully performed. Figure 7 presents pre-operative and post-operative angiograms. The pre-operative angiogram shows a clear bias of HVF towards the left lung, in agreement with the particle tracking analysis of the Baseline solution. Conversely, the post-operative angiogram showed a much more balanced distribution of HVF between the left and right lungs, consistent with our simulation results. At most recent clinical follow-up, 11 months post-operative, overall symptoms had improved. The patient denied shortness of breath and exercise intolerance. Furthermore, oxygen saturation at rest had increased from 82% to 96%, suggesting that increased levels of HVF reverted the progression of PAVMs.

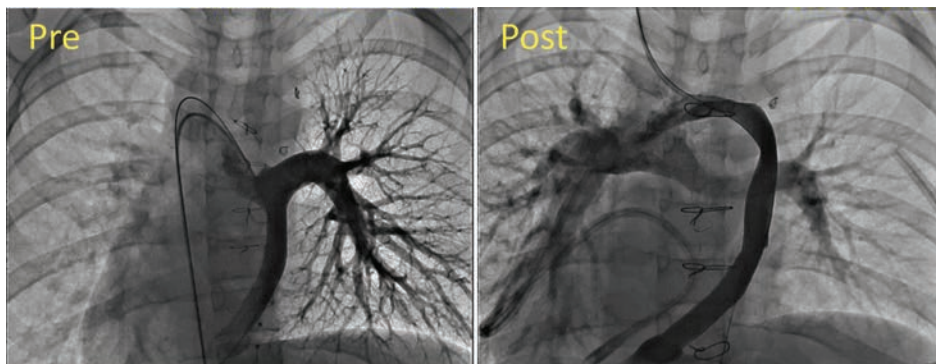


Figure 7. Angiographic imaging was used to visualize the transport of HVF to the lungs. Left: pre-operative angiogram shows that contrast injected in the FN is being transported exclusively to the LPA. The right lung is completely deprived from HVF. Right: post-operative angiogram reveals that contrast injected in the FN now reaches both lungs, with arguably larger presence of contrast in the right lung. These findings agree well with our computational results. FN = Fontan conduit, HVF = hepatic venous flow.

Present and Future Challenges

Computational modeling techniques have the potential to aid cardiovascular disease research and clinical decision making.³⁹ Nonetheless, there are multiple obstacles in the way of routine clinical application.

Computations are time-consuming, typically requiring multiple days to run, despite advances in HPC processing speeds. Near real-time solutions are therefore not feasible and thus computations can only aid clinical decision making in elective cases.

The time-intensive and somewhat operator-dependent nature of model construction, parameterization and validation also affects the clinical applicability of the workflow. Inconsistencies in clinical data can also potentially lead to inaccurate results.¹⁵ Automated workflows relying on data-driven simulations, machine and deep learning tools will help mitigate some of these issues. Ideally, surgical planning supported by computational modeling should involve clinicians and bioengineers working together in multidisciplinary teams. Clinicians should oversee informing the patient, acquiring necessary clinical data and proposing surgically feasible options. Engineers should then perform the analyses following the two-step workflow in Figure 1 and extract clinically meaningful conclusions. Results should then be discussed in a multidisciplinary conference and subsequently presented to the patient.

Current modeling paradigms only predict acute hemodynamic responses immediately after the surgery. Short-term hemodynamic adaptations (intrinsic or extrinsic) are usually left out of the simulation pipeline. Progress has been recently made in developing computational methods to predict short-term hemodynamic extrinsic (e.g. baroreflex effects⁴⁰) or intrinsic adaptations (e.g. metabolic and adrenergic responses in the coronary bed⁴¹). A bigger challenge is to predict the long-term response of the surgical solution due to tissue growth-and-remodeling. Although theoretical foundations for stress-mediated vascular growth and remodeling are currently being explored,⁴² these are far from ready to be applied in clinical decision making.

In the future, guidelines should be created to support best practices resulting in reproducible computational approaches for specific surgical procedures. The outcomes of the computer-guided surgical planning could then be added to the diagnostic workup. Additionally, training courses in computational modeling geared towards surgical planning can be held to train participants in producing reliable simulation workflows.

Conclusions

The potential applications for computational modeling in the cardiovascular field are numerous. Patient-specific simulations enable prediction of hemodynamic outcomes in different interventional procedures, allowing development of individually tailored treatment plans in complex vascular pathologies. In order for these analyses to be routinely used in clinical practice, the accuracy of the simulation results needs to be assessed. Multidisciplinary collaboration between biomedical engineers and clinicians is key to provide accurate computational simulations that benefit research and treatment of cardiovascular disease.

References

- 1 Cecchi E, Giglioli C, Valente S, et al. Role of hemodynamic shear stress in cardiovascular disease. *Atherosclerosis* 2011;214(2):249–56. Doi: 10.1016/j.atherosclerosis.2010.09.008.
- 2 Taylor CA, Figueroa CA. Patient-specific modeling of cardiovascular mechanics. *Annu Rev Biomed Eng* 2009;11:109–34. Doi: 10.1146/annurev.bioeng.10.061807.160521.
- 3 Cuomo F, Roccabianca S, Dillon-Murphy D, et al. Effects of age-associated regional changes in aortic stiffness on human hemodynamics revealed by computational modeling. *PLoS One* 2017;12(3). Doi: 10.1371/journal.pone.0173177.
- 4 Taylor CA, Fonte TA, Min JK. Computational Fluid Dynamics Applied to Cardiac Computed Tomography for Noninvasive Quantification of Fractional Flow Reserve. *J Am Coll Cardiol* 2013;61(22):2233–41. Doi: 10.1016/j.jacc.2012.11.083.
- 5 Figueroa CA, Yeh V, Taylor CA, et al. In vivo displacement force (DF) is higher in patients who experience aortic endograft migration: A 3D computational analysis. *J Vasc Surg* 2010;51(6):93S.
- 6 Trusty PM, Wei Z, Tree M, et al. Local Hemodynamic Differences Between Commercially Available Y-Grafts and Traditional Fontan Baffles Under Simulated Exercise Conditions: Implications for Exercise Tolerance. *Cardiovasc Eng Technol* 2017;8(3):390–9. Doi: 10.1007/s13239-017-0310-5.
- 7 Nauta FJ, Lau KD, Arthurs CJ, et al. Computational Fluid Dynamics and Aortic Thrombus Formation Following Thoracic Endovascular Aortic Repair. *Ann Thorac Surg* 2017. Doi: 10.1016/j.athoracsur.2016.09.067.
- 8 Tang E, Wei Z, Whitehead KK, et al. Effect of Fontan geometry on exercise haemodynamics and its potential implications. *Heart* 2017;103(22):1806–12. Doi: 10.1136/heartjnl-2016-310855.
- 9 Antiga L, Steinman DA. The Vascular Modeling Toolkit. <http://www.vmtk.org>. www.vmtk.org.
- 10 Materialise Mimics. <http://biomedical.materialise.com/mimics>.
- 11 CRIMSON. The software for Cardiovascular Modelling and Simulation. www.crimson.software.
- 12 Vieira MS, Hussain T, Figueroa CA. Patient-Specific Image-Based Computational Modeling in Congenital Heart Disease: A Clinician Perspective. *J Cardiol Ther* 2015;2(6):436–48.

- 13 Sahni O, Müller J, Jansen KE, et al. Efficient anisotropic adaptive discretization of the cardiovascular system. *Comput Methods Appl Mech Eng* 2006;195(41–43):5634–55. Doi: 10.1016/j.cma.2005.10.018.
- 14 Vignon-Clementel IE, Figueroa CA, Jansen KE, et al. Outflow boundary conditions for 3D simulations of non-periodic blood flow and pressure fields in deformable arteries. *Comput Methods Biomech Biomed Engin* 2010;13(5):625–40. Doi: 10.1080/10255840903413565.
- 15 Alastruey J, Xiao N, Fok H, et al. On the impact of modelling assumptions in multi-scale, subject-specific models of aortic haemodynamics. *J R Soc Interface* 2016;13(119). Doi: 10.1098/rsif.2016.0073.
- 16 Pelc NJ, Sommer FG, Li KC, et al. Quantitative magnetic resonance flow imaging. *Magn Reson Q* 1994;10(3):125–47.
- 17 Bushberg JT, Seibert JA, Leidholdt EM, et al. *The Essential Physics of Medical Imaging*. Third Edit. Philadelphia, PA: Lippincott Williams & Wilkins; 2012.
- 18 Hoskins P, Martin K, Thrush A. *Diagnostic Ultrasound: Physics and Equipment*. 2nd Editio. Cambridge: Cambridge University Press; 2010.
- 19 Gatehouse PD, Keegan J, Crowe LA, et al. Applications of phase-contrast flow and velocity imaging in cardiovascular MRI. *Eur Radiol* 2005;15(10):2172–84. Doi: 10.1007/s00330-005-2829-3.
- 20 de Beaufort HWL, Nauta FJH, Conti M, et al. Extensibility and Distensibility of the Thoracic Aorta in Patients with Aneurysm. *Eur J Vasc Endovasc Surg* 2017;53(2):199–205. Doi: 10.1016/j.ejvs.2016.11.018.
- 21 Cuomo F, Ferruzzi J, Humphrey JD, et al. An Experimental–Computational Study of Catheter Induced Alterations in Pulse Wave Velocity in Anesthetized Mice. *Ann Biomed Eng* 2015;43(7):1555–70. Doi: 10.1007/s10439-015-1272-0.
- 22 Fagard R, Conway J. Measurement of cardiac output: Fick principle using catheterization. *Eur Heart J* 1990;11(suppl I):1–5. Doi: 10.1093/eurheartj/11.suppl_1.1.
- 23 Pugsley J, Lerner AB. Cardiac Output Monitoring: Is There a Gold Standard and How Do the Newer Technologies Compare? *Semin Cardiothorac Vasc Anesth* 2010;14(4):274–82. Doi: 10.1177/1089253210386386.
- 24 Figueroa CA, Vignon-Clementel IE, Jansen KE, et al. A coupled momentum method for modeling blood flow in three-dimensional deformable arteries. *Comput Methods Appl Mech Eng* 2006;195(41–43):5685–706. Doi: 10.1016/j.cma.2005.11.011.
- 25 Brown AG, Shi Y, Marzo A, et al. Accuracy vs. computational time: translating aortic simulations to the clinic. *J Biomech* 2012;45(3):516–23. Doi: 10.1016/j.jbiomech.2011.11.041.
- 26 Prasad A, To LK, Gorrepati ML, et al. Computational analysis of stresses acting on inter-modular junctions in thoracic aortic endografts. *J Endovasc Ther* 2011;18(4):559–68. Doi: 10.1583/11-3472.1.
- 27 Les AS, Shadden SC, Figueroa CA, et al. Quantification of hemodynamics in abdominal aortic aneurysms during rest and exercise using magnetic resonance imaging and computational fluid dynamics. *Ann Biomed Eng* 2010;38(4):1288–313. Doi: 10.1007/s10439-010-9949-x.
- 28 Fontan F, Baudet E. Surgical repair of tricuspid atresia. *Thorax* 1971;26(3):240–8.
- 29 Gewillig M. The Fontan circulation. *Heart* 2005;91(6):839–46. Doi: 10.1136/hrt.2004.051789.
- 30 Duncan BW, Desai S. Pulmonary arteriovenous malformations after cavopulmonary anastomosis. *Ann Thorac Surg* 2003;76(5):1759–66.

- 31 Srivastava D, Preminger T, Lock JE, et al. Hepatic venous blood and the development of pulmonary arteriovenous malformations in congenital heart disease. *Circulation* 1995;92(5):1217–22.
- 32 Pike NA, Vricella LA, Feinstein JA, et al. Regression of severe pulmonary arteriovenous malformations after Fontan revision and “hepatic factor” rerouting. *Ann Thorac Surg* 2004;78(2):697–9. Doi: 10.1016/j.athoracsur.2004.02.003.
- 33 McElhinney DB, Marx GR, Marshall AC, et al. Cavopulmonary pathway modification in patients with heterotaxy and newly diagnosed or persistent pulmonary arteriovenous malformations after a modified Fontan operation. *J Thorac Cardiovasc Surg* 2011;141(6):1362–70. e1. Doi: 10.1016/j.jtcvs.2010.08.088.
- 34 Shah MJ, Rychik J, Fogel MA, et al. Pulmonary AV malformations after superior cavopulmonary connection: resolution after inclusion of hepatic veins in the pulmonary circulation. *Ann Thorac Surg* 1997;63(4):960–3.
- 35 de Zélicourt DA, Haggerty CM, Sundareswaran KS, et al. Individualized computer-based surgical planning to address pulmonary arteriovenous malformations in patients with a single ventricle with an interrupted inferior vena cava and azygous continuation. *J Thorac Cardiovasc Surg* 2011;141(5):1170–7. Doi: 10.1016/j.jtcvs.2010.11.032.
- 36 Kawashima Y, Kitamura S, Matsuda H, et al. Total cavopulmonary shunt operation in complex cardiac anomalies. A new operation. *J Thorac Cardiovasc Surg* 1984;87(1):74–81.
- 37 Helps EPW, McDonald DA. Observations on laminar flow in veins. *J Physiol* 1954;124(3):631–9. Doi: 10.1113/jphysiol.1954.sp005135.
- 38 Shadden SC, Hendabadi S. Potential fluid mechanic pathways of platelet activation. *Biomech Model Mechanobiol* 2013;12(3):467–74. Doi: 10.1007/s10237-012-0417-4.
- 39 Biglino G, Capelli C, Bruse J, et al. Computational modelling for congenital heart disease: how far are we from clinical translation? *Heart* 2016;0:1–6. Doi: 10.1136/heartjnl-2016-310423.
- 40 Lau KD, Figueroa CA. Simulation of short-term pressure regulation during the tilt test in a coupled 3D-0D closed-loop model of the circulation. *Biomech Model Mechanobiol* 2015;14(4):915–29. Doi: 10.1007/s10237-014-0645-x.
- 41 Arthurs CJ, Lau KD, Asrress KN, et al. A mathematical model of coronary blood flow control: simulation of patient-specific three-dimensional hemodynamics during exercise. *Am J Physiol - Hear Circ Physiol* 2016;310(9):H1242–58. Doi: 10.1152/ajpheart.00517.2015.
- 42 Figueroa CA, Baek S, Taylor CA, et al. A Computational Framework for Fluid-Solid-Growth Modeling in Cardiovascular Simulations. *Comput Methods Appl Mech Eng* 2009;198(45–46):3583–602. Doi: 10.1016/j.cma.2008.09.013.

Chapter 3

Cardiac remodeling following endovascular aortic repair of descending aortic aneurysms

Theodorus M.J. van Bakel^{1,5,7}, MD

Christopher J. Arthurs⁶, DPhil

Foeke J.H. Nauta^{1,5,7}, MD, PhD

Kim A. Eagle³, MD

Joost A. van Herwaarden⁵, MD, PhD

Frans L. Moll⁵, MD, PhD

Santi Trimarchi^{7,8}, MD, PhD

Himanshu J. Patel⁴, MD

C. Alberto Figueroa^{1,2}, PhD

1. Department of Surgery, University of Michigan, Ann Arbor, Michigan, USA.
2. Department of Biomedical Engineering, University of Michigan, Ann Arbor, Michigan, USA.
3. Department of Cardiology, University of Michigan, Ann Arbor, Michigan, USA.
4. Department of Cardiac Surgery, University of Michigan, Ann Arbor, Michigan, USA.
5. Department of Vascular Surgery, University Medical Center Utrecht, Utrecht, The Netherlands.
6. Division of Imaging Sciences and Biomedical Engineering, King's College London, UK.
7. Thoracic Aortic Research Center, Policlinico San Donato IRCCS, San Donato Milanese, Italy.
8. Department of Biomedical Sciences for Health, University of Milan, Milan, Italy.

European Journal of Cardio-Thoracic Surgery. Doi: 10.1093/ejcts/ezy399

Abstract

Objective

Current endografts for thoracic endovascular aortic repair (TEVAR) are much stiffer than the aorta and have been shown to induce acute stiffening. In this study, we aimed to estimate the impact of TEVAR on left ventricular (LV) stroke work and mass using a non-invasive image-based workflow.

Methods

The University of Michigan database was searched for patients treated with TEVAR for descending aortic pathologies (2013 to 2016). Patients with available pre-TEVAR and post-TEVAR computed tomography angiography (CTA) and echocardiography data were selected. LV stroke work was estimated via patient-specific fluid structure interaction (FSI) analyses. LV remodelling was quantified through morphological measurements using echocardiography and electrocardiographic-gated CTA data.

Results

Eight subjects were included, mean age was 68 (73,25) years old, six were female. All patients were prescribed antihypertensive drugs following TEVAR. FSI simulations computed a 26% increase in LV stroke work post-TEVAR (0.94 (0.89,0.34) J to 1.18 (1.11,0.65) J, $P=.012$). Morphological measurements revealed an increase in LV mass index post-TEVAR of +26% in echocardiography (72 (73,17) g/m^2 to 91 (87,26) g/m^2 , $P=.017$) and +15% in CTA (52 (46,29) g/m^2 to 60 (57,22) g/m^2 , $P=.043$). The post- to pre-TEVAR LV mass index ratio was positively correlated with the post- to pre-TEVAR ratios of stroke work and mean blood pressure ($\rho=.690$, $P=.058$ and $\rho=.786$, $P=.021$, respectively).

Conclusions

TEVAR was associated with increased LV stroke work and mass during follow-up. Medical device manufacturers should develop more compliant devices to reduce the stiffness mismatch with the aorta. Additionally, intensive anti-hypertensive management is needed to control blood pressure post-TEVAR.

Introduction

Thoracic endovascular aortic repair (TEVAR) is the treatment of choice for descending thoracic aortic aneurysms.¹ Due to its superior early and mid-term outcomes over open surgery, the use of TEVAR is increasing rapidly.² The treatment range for TEVAR is extending with endografts deployed more proximally into the aortic arch and in younger patients.³⁻⁵ Current endografts are made of materials much stiffer than the native thoracic aorta.^{6,7} These materials enhance durability and reduce the risk of Type IV endoleaks, but they stiffen the aorta. Aortic compliance serves a critical function to reduce the impedance and workload of cardiac ejection.⁸ The healthy aorta stiffens with age, this process is accelerated by smoking, high cholesterol, hypertension and genetic predisposition. Aortic stiffening is known to play a significant role in cardiovascular disease development and progression.^{8,9} Several pre-clinical studies have reported on acute stiffening of the aorta following TEVAR, resulting in acute elevated pulse pressure, hypertension, reduced coronary perfusion, and eventually heart failure.^{10,11} These findings have been confirmed by computational studies using simplified blood flow models.¹² More recently, a clinical study revealed left ventricular (LV) remodelling in a mixed population of thoracic and abdominal aneurysm patients treated with endovascular repair using ultrasonography data to assess changes in aortic pulse wave velocity and myocardial mass.¹³

The present study aimed to elucidate the impact of TEVAR-induced acute aortic stiffening on LV stroke work (SW) and mass using patient-specific fluid structure interaction (FSI) analyses and image-based measurements of cardiac remodelling from echocardiography and computed tomography angiography (CTA) data.

Materials and Methods

The University of Michigan Adult Cardiac Surgery database was retrospectively queried for patients treated with TEVAR for descending aortic aneurysms between 2013 and 2016. The following inclusion criteria were used: available pre-TEVAR and post-TEVAR echocardiography and CTA data. Exclusion criteria were: aortic dissection, prior surgical or endovascular aortic repair, prior open-heart surgery, atrial fibrillation and echocardiographic ejection fraction of <50%. Approval was obtained from the Institutional Review Board (HUM00112350), the need for informed consent was waived. Information on demographics, medical and surgical history, and clinical outcomes was retrieved.

Patient-Specific Computational Modelling of Hemodynamics

FSI techniques were used to simulate aortic hemodynamics, including interactions between blood, aorta, and endograft using validated computational tools.¹⁴ Patient-specific simulations were performed pre-TEVAR and post-TEVAR. Each simulation required the following: (1) a three-dimensional model of the aorta and its side-branches; (2) stiffness properties of the vessel walls and endografts; and (3) boundary conditions describing inflow and outflow waveforms.

Computational models of thoracic aorta, coronary arteries, and the supra-aortic arteries were created from CTA data using the cardiovascular modelling software CRIMSON.¹⁵ The workflow for this procedure is illustrated in Figure 1. Figure 2 presents the pre-TEVAR and post-TEVAR geometrical models.

Wall thickness and stiffness were assigned to the different vessels using literature data, values and references are reported in the Table 1. Figure 3 shows stiffness maps of the pre-TEVAR and post-TEVAR aorta for Patient 4. Aortic wall thickness and stiffness were specified along the center lumen line in all models. Pre-TEVAR, the thickness and stiffness at the level of the descending aortic aneurysm were set to 4.0 mm and 2.56 MPa, respectively, rendering a structural stiffness (i.e., the product of thickness and stiffness) of 10.2 MPa-mm. Post-TEVAR, thickness and stiffness at the level of the endograft were set to 2.8 mm and 55.2 MPa, respectively, rendering a structural stiffness of 154.6 MPa-mm. This is more than fifteen times stiffer than the region of the aneurysm in the pre-TEVAR models.

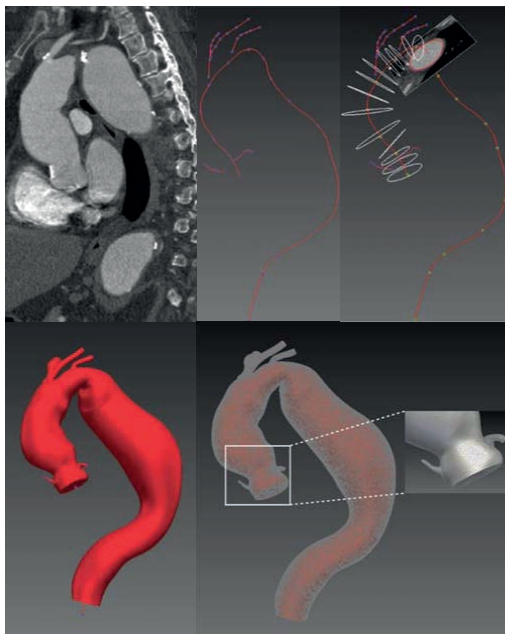


Figure 1. Patient-specific models of the thoracic aorta and its side-branches were constructed from CTA data. First, center lumen lines were selected in each artery. Then, two-dimensional segmentations were made along the center lumen line, delineating the vessel walls. The individually segmented arteries were combined through an automated lofting and blending process, completing the three-dimensional geometry. This geometry was then discretized into a highly-refined finite element mesh.

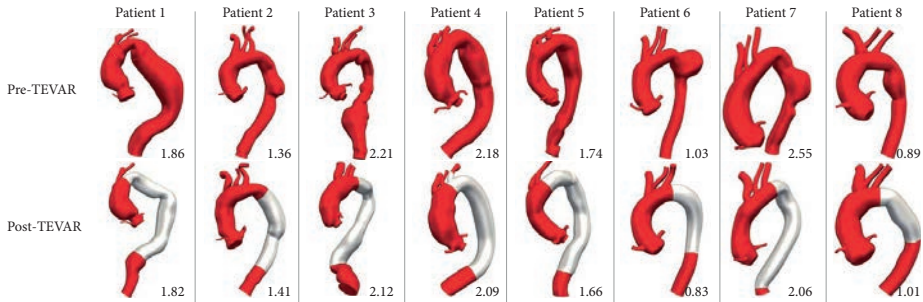


Figure 2. Pre- and post-TEVAR geometric models for all patients. Finite element mesh sizes are reported in millions of elements.

Boundary Condition Specification and Parameterization

Since invasive pressure measurements of the LV were not available, we developed a workflow to estimate the LV end-diastolic pressure-volume (PV) relationship using image-based computational modelling. A two-step approach was adopted to assign inflow and outflow boundary conditions. First, a preliminary FSI simulation was performed using aortic inflow duplex-Doppler echocardiography data to calculate the pressure-volume (PV) relationship in the aortic root. Then, these simulation results were used to calibrate a lumped-parameter heart model¹⁶ that enabled quantification of LV SW. In the following, the methods of performing the preliminary simulation and constructing the heart model will be reviewed.

The pre-TEVAR and post-TEVAR cardiac outputs and inflow waveforms were derived from transthoracic duplex-Doppler echocardiography measurements at the LV outflow tract and imposed at the aortic root of the corresponding computational model. We did not have direct measurements of the flow and pressure waveforms at the side branches of the aorta. Therefore, we used three-element Windkessel models to represent the resistance and compliance of the distal vascular bed for each branch.¹⁷ The parameters of the Windkessel models were iteratively tuned to match reported literature data on flow splits¹⁸ and patient-specific brachial cuff blood pressure measurements that were taken at rest during the preoperative and follow-up office visit. Of note, the blood pressure measurements were taken routinely by the same staff, ensuring similar conditions between the consecutive measurements. The following flow splits were assigned as percentages of cardiac output: brachiocephalic trunk 18%; left common carotid artery 8%; left subclavian artery (LSA) 8%; left coronary artery (LCA) 4%; right coronary artery (RCA) 2% and descending aorta 60%. If the LSA was over-stented during TEVAR, the left common carotid artery would be assigned 16% of the cardiac output.

Table 1. Numerical values of vessel wall parameters for FSI analysis

	Young's Modulus [MPa]	Thickness [mm]
Aortic root	1.68	2.6
Ascending aorta	1.68	2.6
Right coronary artery	3.20	0.9
Left coronary artery	3.20	0.9
Brachiocephalic trunk	2.00	1.2
Left common carotid artery	2.00	1.2
Left subclavian artery	2.00	1.2
Distal aorta	1.84	2.8
Ascending aortic aneurysm	2.00	2.6
Descending aortic aneurysm	2.56	4.0
Endograft	55.2	2.8

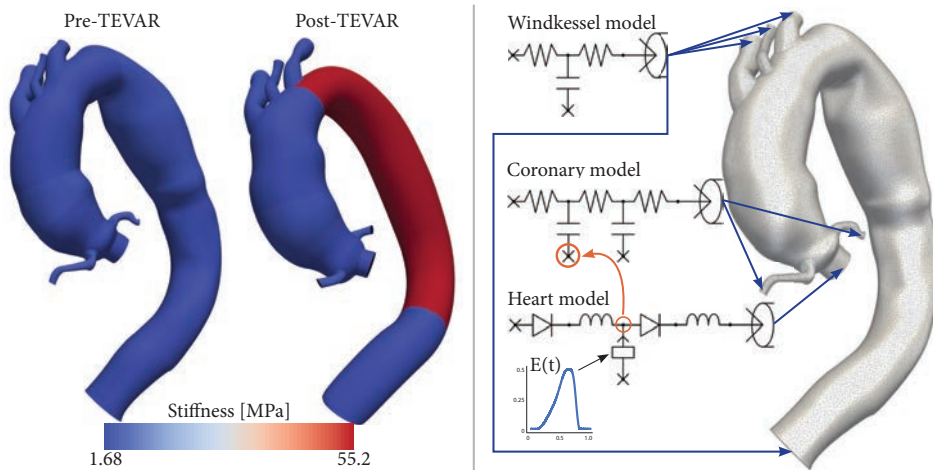


Figure 3. Left: Distribution of aortic and endograft stiffness. Right: Reduced order models were attached to the in- and outflow sections of the 3D computational model. The parameters of the Windkessel, heart and coronary models were tuned to match patient-specific flow and pressure data. The patient-specific left-ventricular elastance function ($E(t)$) describes the pressure generation in the heart model. In the coronary circulation, extravascular myocardial compression is modelled by broadcasting left ventricular pressure to each coronary¹⁶ (orange arrow).

Heart Model

A lumped-parameter heart model including diodes and inductors to represent the mitral and aortic valves, a pressure source representing left atrial pressure and a volume-tracking pressure chamber representing the left ventricle was then calibrated and coupled to the inflow face of all aortic models (Figure 3). The compliance and contractility of the pressure chamber are defined by a time-varying elastance function ($E(t)$).¹⁶ Patient-specific pre-TEVAR and post-TEVAR elastance functions were

computed from the PV relationship at the aortic root in the preliminary simulations. While the aortic valve is open, the aortic root pressure provides an approximation of the LV pressure. The diastolic part of the elastance function was completed by assuming an exponential decay following aortic valve closure to 5% of the peak elastance,¹⁹ followed by an exponential systolic rise until aortic valve opening.^{19,20} Pre-TEVAR LV end-diastolic volume (EDV) was estimated for each patient using age, gender and body surface area (BSA) data.²¹ Since there is no significant change in BSA Post-TEVAR, LV EDV was estimated from the echocardiography data using the modified Simpson's rule²² as follows:

$$\text{Post - TEVAR EDV} = \text{estimated Pre - TEVAR EDV} \Big|_{\text{BSA}} \left(\frac{\text{Post - TEVAR EDV}}{\text{Pre - TEVAR EDV}} \right) \Big|_{\text{Modified Simpson's rule}}$$

Estimated LV EDVs were compared with electrocardiographic (ECG) gated CTA data whenever available. If the discrepancy between estimated and ECG-gated CTA ratios of post-and pre-TEVAR EDV was larger than 5%, the ECG-gated CTA data were used.

Coronary Models

We used lumped-parameter models to represent the vascular beds of LCA and RCA (Figure 3). The heart model enabled tracking of LV pressure throughout the cardiac cycle. The LV pressure was broadcasted to a lumped parameter model of the LCA, to reproduce diastolically-dominant coronary flow waveforms.¹⁶ Since the right ventricle operates at a lower pressure than the left ventricle, the LV pressure broadcasted to the RCA coronary model was scaled down to 33%. These lumped-parameter models enable to capture essential features of coronary flow waveforms and therefore their impact on ascending thoracic aortic hemodynamics.

Computations

Blood was modelled as an incompressible Newtonian fluid with a density of 1060 kg/m³ and a dynamic viscosity of 4.0 mPa. Computations were performed using the CRIMSON flow solver on 80 cores at the University of Michigan High Performance Computing Cluster ConFlux. Typical computational time was 80 hours per cardiac cycle. After the FSI simulations reached cycle-to-cycle periodicity, and successfully reproduced patient-specific pressure and flow data within 5% margins, pre-TEVAR and post-TEVAR LV PV-loops were generated from the heart models and SW was calculated.

Cardiac Remodelling

Changes in LV mass were measured from pre-TEVAR and post-TEVAR echocardiography and ECG-gated CTA image data. Echocardiography examinations were performed by an independent operator. LV mass [g] was calculated from end-diastolic LV dimensions as follows²²:

$$\text{LV mass} = 0.8 \cdot \{1.04 [\text{LVID} + \text{PWT} + \text{SWT}]^3 - \text{LVID}^3\} + 0.6$$

where LVID = LV internal diameter [mm], PWT = posterior wall thickness [mm] and SWT = septal wall thickness [mm].

In patients who had undergone ECG-gated CTA examinations, volumetric measurements of the LV myocardium were taken in the diastolic phase of the cardiac cycle, at 75% of the R-R interval using the automatic image processing tools in Vitrea (Vital Images Inc., Minnetonka, MN) (Figure 4). LV mass was calculated from the product of the LV myocardial volume and the density of myocardial tissue (1.04 g/cm³).²³



Figure 4. Left ventricular mass measurements from ECG-gated CTA data pre-TEVAR (left) and post-TEVAR (right) in Patient 4.

Statistical Analysis

Analysis of the data was performed using SPSS Statistics version 24 (IBM, Armonk, NY). Continuous data are presented as mean (median, interquartile range). Comparisons between pre-TEVAR and post-TEVAR data were made using the Wilcoxon signed rank test. Correlations were made using Spearman's rank correlation coefficient. No correction for multiple testing was performed. All the statistical tests were two-sided and P-values of 0.05 or less were considered statistically significant.

Results

Study Sample

In total 195 patients were treated with TEVAR at the University of Michigan between 2013 and 2016. Eight patients met the inclusion and exclusion criteria, six were female. Mean age was 68 (73,25) years old. The average time between the pre-TEVAR

and follow-up CTA scan was 458 (374,562) days. A comparison of pre-TEVAR and post-TEVAR patient data is reported in Table 2.

Table 2. Patient data pre-TEVAR and post-TEVAR

	Pre-TEVAR	Post-TEVAR	P-value
<i>Physical Examination (n=8)</i>			
Heart rate [beats/min]	71 (70,12)	67 (68,16)	
Systolic blood pressure [mmHg]	123 (123,23)	146 (149,29)	
Diastolic blood pressure [mmHg]	69 (71,19)	79 (77,15)	
Mean blood pressure [mmHg]	86 (85,15)	100 (99,22)	<u>.036</u>
Pulse pressure [mmHg]	54 (52,25)	67 (57,36)	
BMI [kg/m ²]	28.2 (28.6,12.1)	28.1 (26.1,11.2)	
BSA [m ²]	1.93 (1.91,0.44)	1.89 (1.90,0.36)	
<i>Echocardiography (n=8)</i>			
Cardiac output [L/min]	4.8 (4.5,1.6)	4.9(5.1,2.2)	
Stroke volume [mL]	69 (62,31)	73 (67,25)	
LV end diastolic volume [mL]	90 (91,21)	100 (102,14)	
LV fractional shortening [%]	43 (43,17)	34 (34,16)	
LV internal diameter systole [cm]	2.44 (2.37,1.30)	2.90 (3.27,1.10)	
LV internal diameter diastole [cm]	4.22 (4.23,0.88)	4.43 (4.34,1.37)	
Interventricular septum thickness [cm]	0.99 (0.93,0.20)	1.18 (1.18,0.47)	
<i>LV mass index</i>			
Echocardiography [g/m ²] (n=8)	72 (73,17)	91 (87,26)	<u>.017</u>
ECG-gated CTA [g/m ²] (n=5)	52 (46,29)	60 (57,22)	<u>.043</u>
<i>Antihypertensive drugs (n=8)</i>			
B-blocker [n (%)]	4 (50.0)	7 (87.5)	
ACE-inhibitor [n (%)]	0 (0)	2 (25.0)	
Ca-channel blocker [n (%)]	3 (37.5)	2 (25.0)	
Angiotensin II receptor blocker [n (%)]	2 (25.0)	2 (25.0)	

Continuous data are presented as mean (median, interquartile range). ACE = angiotensin converting enzyme; BMI = body mass index; BSA = body surface area; ECG = electrocardiography; LV = left ventricular.

Computational Outcomes

Pre-TEVAR and post-TEVAR simulation results successfully reproduced patient-specific data on pressure, stroke volume, and end-diastolic volume within 5% margins for all patients. Figure 5 demonstrates an example of pre-TEVAR and post-TEVAR waveforms in all aortic branches for Patient 4. LV SW increased in all patients post-TEVAR, the mean SW increment was 26% (0.94 (0.89,0.34) J to 1.18 (1.11,0.65) J, P=.012). Figure 6 presents a comparison of pre-TEVAR and post-TEVAR PV-loops for all patients. There was no correlation between SW increment and endograft size.

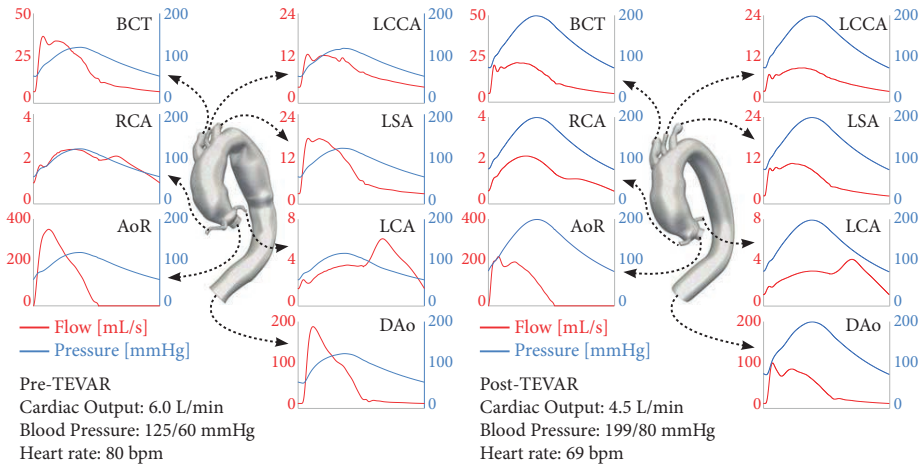


Figure 5. Flow and pressure waveforms for Patient 4. AoR = aortic root, BCT = brachiocephalic trunk, DAo = descending aorta, LCA = left coronary artery, LCCA = left common carotid artery, LSA = left subclavian artery, LVOT = left ventricular outflow tract.

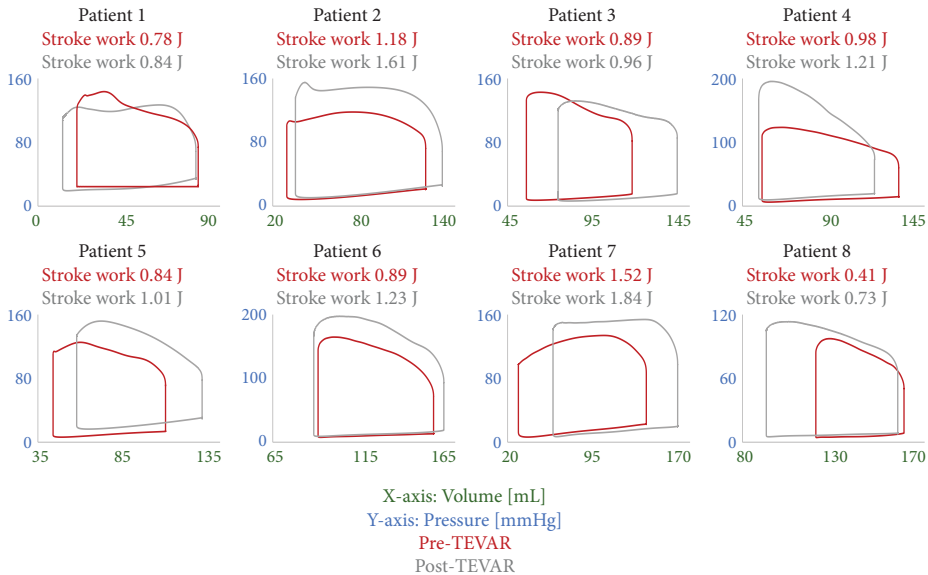


Figure 6. Comparison of pre- and post-TEVAR LV PV-loops. Stroke work increased in all cases.

Cardiac Remodelling

Morphologic measurements from echocardiography revealed a 26% increase in LV mass index (72 (73,17) g/m² to 91 (87,26) g/m², P=.017) following TEVAR. There was a positive correlation between the ratio of post- to pre-TEVAR LV mass index and the ratios of post- to pre-TEVAR LV SW and mean blood pressure ($\rho=.690$, P=.058 and

$\rho=.786$, $P=.021$, respectively), Figure 7. Volumetric measurements from ECG-gated CTA also revealed an increase in LV mass index following TEVAR, albeit smaller than that obtained with echocardiography (+15%, 52 (46,29) g/m^2 to 60 (57,22) g/m^2 , $P=.043$). There was no correlation between post- to pre-TEVAR LV mass index ratio and total endograft surface area for either the echocardiography or the CTA data.

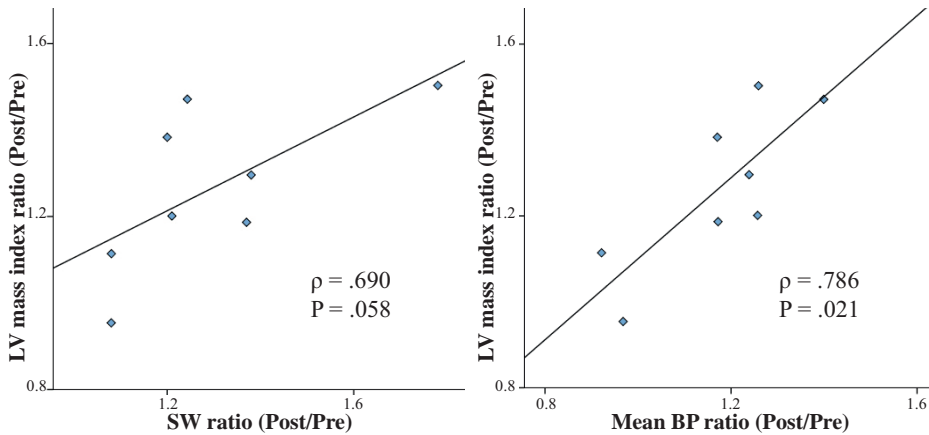


Figure 7. Positive correlation between post- to pre-TEVAR LV mass index ratio measured from echocardiography and both stroke work (SW) and mean blood pressure (BP) ratio.

Discussion

The goal of the present study was to elucidate the effects of TEVAR-induced acute aortic stiffening on LV SW and remodelling. We present a workflow for non-invasive quantification of LV SW through patient-specific FSI analyses. Using this workflow, we unveiled a significant increase in LV SW post-TEVAR. The post- to pre-TEVAR ratios of LV SW and LV mass index showed a positive correlation. Additionally, despite anti-hypertensive therapy, mean blood pressure increased post-TEVAR. The post- to pre-TEVAR ratios of mean blood pressure and LV mass index also showed a positive correlation.

Myocardial and aortic stiffening are well-known determinants of all-cause mortality and cardiovascular events.^{8,24,25} Multiple clinical studies have reported increased pulse wave velocity and pulse pressure following endograft deployment.^{13,26,27} In pre-clinical studies, similar effects were observed with additional findings of increased LV myocardial oxygen consumption and LV mass.^{28,29}

In this study, we confirmed the deleterious late consequences of increased in-vivo impedance and stiffness mismatch after TEVAR on LV remodelling, using a computational modelling workflow that enabled us to quantify LV SW from non-invasive

imaging and pressure data. Our findings suggest that medical device manufacturers should develop more compliant endografts for TEVAR to reduce the stiffness mismatch between aorta and device. Additionally, intensive antihypertensive therapy is needed to control blood pressure post-TEVAR.

In some of our patients, we found that TEVAR resulted in a less tortuous configuration of the aortic lumen. We hypothesize that this could contribute to an overall reduction in LV SW despite the increase in aortic stiffness. This interplay between aortic tortuosity and stiffness will be a topic of future research, as it may have implications for patients presenting with pathologies compromising the lumen, such as aortic dissection.

Limitations

As we did not have invasive measurements of aortic and LV pressure available, we had to estimate the parameters for the heart model from echocardiography and CTA image data. This lack of data is most apparent in the end diastolic pressure-volume relationships depicted in Figure 6, which were generated by similar assumptions regarding the exponential decay of the systolic part of the elastance function. Therefore, even though there is evidence of ventricular remodelling, the diastolic pressure-volume relationships do not reflect a stiffer behaviour. However, we submit that even with this imperfect definition of the diastolic part of the PV loops, our results reflect a clear trend in SW increase following TEVAR. Future studies are needed to calibrate this workflow using invasive pressure measurements in pre-clinical models or Doppler-derived atrio-ventricular pressure gradients.

The number of patients included in this study is relatively small, as the majority of patients that were treated at our institution were excluded. We acknowledge that this potentially induced selection bias. Furthermore, we performed a retrospective non-invasive analysis, it was not possible to obtain patient-specific tissue properties for our computational models. Therefore, we had to rely on literature data. Furthermore, we assigned the same flow splits to the outflow branches of all patients pre-TEVAR and post-TEVAR. By doing so, we assumed that TEVAR does not affect regional blood flow distributions. To overcome the above mentioned limitations, our group is currently recruiting patients for a prospective study where additional flow, myocardial perfusion and myocardial strain measurements are acquired using MRI techniques.³⁰

Lastly, running FSI analyses is computationally expensive. Typically, two weeks of simulation time in a super-computer were needed for each patient-specific FSI analysis. This limits their clinical applicability for now, but optimizations of computational methods or access to larger computer hardware will make it possible to perform these simulations in clinically feasible time-frames in the future.

Conclusion

TEVAR increased LV SW and induced LV growth during follow-up. Medical device manufacturers should consider the impact of the stiffness mismatch between graft material and native aorta when developing new endografts for TEVAR, particularly considering the emerging role of endovascular repair in more proximal aortic segments and younger patient populations. Additionally, intensive antihypertensive therapy should prevent mean blood pressure to increase post-TEVAR.

References

- 1 Hiratzka LF, Bakris GL, Beckman JA, et al. 2010 ACCF/AHA/AATS/ACR/ASA/SCA/SCAI/SIR/STS/SVM guidelines for the diagnosis and management of patients with Thoracic Aortic Disease: a report of the American College of Cardiology Foundation/American Heart Association Task Force on Practice Guidelines, A. *Circulation* 2010;121(13):e266-369. Doi: 10.1161/CIR.0b013e3181d4739e.
- 2 von Allmen RS, Anjum A, Powell JT. Incidence of descending aortic pathology and evaluation of the impact of thoracic endovascular aortic repair: a population-based study in England and Wales from 1999 to 2010. *Eur J Vasc Endovasc Surg Off J Eur Soc Vasc Surg* 2013;45(2):154–9. Doi: 10.1016/j.ejvs.2012.12.007.
- 3 Geisbüsch P, Kotelis D, Hyhlik-Dürr A, et al. Endografting in the Aortic Arch - Does the Proximal Landing Zone Influence Outcome? *Eur J Vasc Endovasc Surg* 2010;39(6):693–9. Doi: 10.1016/j.ejvs.2010.03.018.
- 4 van Bakel TM, Arthurs CJ, van Herwaarden JA, et al. A computational analysis of different endograft designs for Zone 0 aortic arch repair†. *Eur J Cardio-Thoracic Surg* 2018;54(2):389–96. Doi: 10.1093/ejcts/ezy068.
- 5 van Bakel TM, de Beaufort HW, Trimarchi S, et al. Status of branched endovascular aortic arch repair. *Ann Cardiothorac Surg* 2018;7(3):406–13. Doi: 10.21037/acs.2018.03.13.
- 6 Kleinstreuer C, Li Z, Basciano CA, et al. Computational mechanics of Nitinol stent grafts. *J Biomech* 2008;41(11):2370–8. Doi: 10.1016/j.jbiomech.2008.05.032.
- 7 Roccabianca S, Figueroa CA, Tellides G, et al. Quantification of regional differences in aortic stiffness in the aging human. *J Mech Behav Biomed Mater* 2014;29:618–34. Doi: 10.1016/j.jmbbm.2013.01.026.
- 8 Redheuil A, Wu CO, Kachenoura N, et al. Proximal aortic distensibility is an independent predictor of all-cause mortality and incident CV events: the MESA study. *J Am Coll Cardiol* 2014;64(24):2619–29. Doi: 10.1016/j.jacc.2014.09.060.
- 9 Humphrey JD, Harrison DG, Figueroa CA, et al. Central Artery stiffness in hypertension and aging a problem with cause and consequence. *Circ Res* 2016;379–81. Doi: 10.1161/CIRCRESAHA.115.307722.
- 10 Dobson G, Flewitt J, Tyberg J V., et al. Endografting of the descending thoracic aorta increases ascending aortic input impedance and attenuates pressure transmission in dogs. *Eur J Vasc Endovasc Surg Off J Eur Soc Vasc Surg* 2006;32(2):129–35. Doi: 10.1016/j.ejvs.2006.01.020.

- 11 Zacharoulis AA, Arapi SM, Lazaros GA, et al. Changes in coronary flow reserve following stent implantation in the swine descending thoracic aorta. *J Endovasc Ther* 2007;14(4):544–50. Doi: 10.1583/1545-1550(2007)14[544:CICFRF]2.0.CO;2.
- 12 Vardoulis O, Coppens E, Martin B, et al. Impact of aortic grafts on arterial pressure: A computational fluid dynamics study. *Eur J Vasc Endovasc Surg* 2011;42(5):704–10. Doi: 10.1016/j.ejvs.2011.08.006.
- 13 Takeda Y, Sakata Y, Ohtani T, et al. Endovascular aortic repair increases vascular stiffness and alters cardiac structure and function. *Circ J* 2014;78(2):322–8.
- 14 Figueroa CA, Vignon-Clementel IE, Jansen KE, et al. A coupled momentum method for modeling blood flow in three-dimensional deformable arteries. *Comput Methods Appl Mech Eng* 2006;195(41–43):5685–706. Doi: 10.1016/j.cma.2005.11.011.
- 15 CRIMSON. The software for Cardiovascular Modelling and Simulation. www.crimson.software.
- 16 Arthurs CJ, Lau KD, Asress KN, et al. A mathematical model of coronary blood flow control: simulation of patient-specific three-dimensional hemodynamics during exercise. *Am J Physiol - Hear Circ Physiol* 2016;310(9):H1242–58. Doi: 10.1152/ajpheart.00517.2015.
- 17 Vignon-Clementel IE, Figueroa CA, Jansen KE, et al. Outflow boundary conditions for 3D simulations of non-periodic blood flow and pressure fields in deformable arteries. *Comput Methods Biomech Biomed Engin* 2010;13(5):625–40. Doi: 10.1080/10255840903413565.
- 18 Lantz BMT, Foerster JM, Link DP, et al. Regional distribution of cardiac output: Normal values in man determined by video dilution technique. *Am J Roentgenol* 1981;137(5):903–7. Doi: 10.2214/ajr.137.5.903.
- 19 Senzaki H, Chen C-H, Kass DA. Single-Beat Estimation of End-Systolic Pressure-Volume Relation in Humans: A New Method With the Potential for Noninvasive Application. *Circulation* 1996;94(10):2497–506. Doi: 10.1161/01.cir.94.10.2497.
- 20 Scalia GM, Greenberg NL, McCarthy PM, et al. Noninvasive assessment of the ventricular relaxation time constant (τ) in humans by Doppler echocardiography. *Circulation* 1997;95(1):151–5. Doi: 10.1161/01.CIR.95.1.151.
- 21 Maceira AM, Prasad SK, Khan M, et al. Normalized left ventricular systolic and diastolic function by steady state free precession cardiovascular magnetic resonance. *J Cardiovasc Magn Reson* 2006;8(3):417–26. Doi: 10.1080/10976640600572889.
- 22 Lang RM, Bierig M, Devereux RB, et al. Recommendations for chamber quantification: A report from the American Society of Echocardiography’s guidelines and standards committee and the Chamber Quantification Writing Group, developed in conjunction with the European Association of Echocardiograph. *J Am Soc Echocardiogr* 2005;1440–63. Doi: 10.1016/j.echo.2005.10.005.
- 23 van Deel E, Ridwan Y, van Vliet JN, et al. In Vivo Quantitative Assessment of Myocardial Structure, Function, Perfusion and Viability Using Cardiac Micro-computed Tomography. *J Vis Exp* 2016;(108):53603. Doi: 10.3791/53603.
- 24 Kingwell BA, Waddell TK, Medley TL, et al. Large artery stiffness predicts ischemic threshold in patients with coronary artery disease. *J Am Coll Cardiol* 2002;40(4):773–9.
- 25 Watanabe H, Ohtsuka S, Kakahana M, et al. Coronary circulation in dogs with an experimental decrease in aortic compliance. *J Am Coll Cardiol* 1993;21(6):1497–506.
- 26 de Beaufort HWL, Coda M, Conti M, et al. Changes in aortic pulse wave velocity of four thoracic aortic stent grafts in an ex vivo porcine model. *PLoS One* 2017;12(10):e0186080. Doi: 10.1371/journal.pone.0186080.

- 27 Tzilalis VD, Kamvysis D, Panagou P, et al. Increased pulse wave velocity and arterial hypertension in young patients with thoracic aortic endografts. *Ann Vasc Surg* 2012;26(4):462–7. Doi: 10.1016/j.avsg.2011.06.021.
- 28 Morita S, Asou T, Kuboyama I, et al. Inelastic vascular prosthesis for proximal aorta increases pulsatile arterial load and causes left ventricular hypertrophy in dogs. *J Thorac Cardiovasc Surg* 2002;124(4):768–74.
- 29 Kelly RP, Tunin R, Kass DA. Effect of reduced aortic compliance on cardiac efficiency and contractile function of in situ canine left ventricle. *Circ Res* 1992;71(3):490–502.
- 30 Nauta FJH, Kamman A V, Ibrahim E-SH, et al. Assessment of Cardiovascular Remodeling following Endovascular aortic repair through imaging and computation: The CORE prospective observational cohort study protocol. *BMJ Open* 2016;6(11). Doi: 10.1136/bmjopen-2016-012270.

Chapter 4

Ascending aortic rupture after zone 2 endovascular repair: a multiparametric computational analysis

Theodorus M.J. van Bakel^{1,5,6}, MD

Nicholas S. Burris², MD

Himanshu J. Patel³, MD

C. Alberto Figueroa^{1,4}, PhD

1. Department of Surgery, University of Michigan, Ann Arbor, Michigan, USA.
2. Department of Radiology, University of Michigan, Ann Arbor, Michigan, USA.
3. Department of Cardiac Surgery, University of Michigan, Ann Arbor, Michigan, USA.
4. Department of Biomedical Engineering, University of Michigan, Ann Arbor, Michigan, USA.
5. Thoracic Aortic Research Center, Policlinico San Donato IRCCS, San Donato Milanese, Italy.
6. Department of Vascular Surgery, University Medical Center Utrecht, Utrecht, The Netherlands.

After: European Journal of Cardio-Thoracic Surgery. Doi: 10.1093/ejcts/ezy458.

Abstract

Objectives

In this work, we study the pathophysiology of ascending aortic rupture following branched zone 2 thoracic endovascular aortic repair (TEVAR) using a multi-parametric image-based computational analysis consisting of fluid structure interaction (FSI) simulations and vascular deformation mapping (VDM) techniques.

Methods

A 74-year-old female with a stable ascending aortic aneurysm and a growing proximal descending aneurysm was treated with branched TEVAR in Zone 2. The procedure was complicated by infolding and bird-beak of a proximal extender. Three months following TEVAR, the patient suddenly expired from ascending aortic rupture. Patient-specific models of pre-TEVAR, post-TEVAR and virtual uncomplicated endograft deployment (VUED) anatomy were constructed from computed tomography angiography (CTA) data. FSI simulations were used to calculate the TEVAR-induced alterations in ascending aortic pressure. Additionally, VDM was used to assess aortic strain changes following TEVAR.

Results

FSI simulations calculated a 35% increase in ascending aortic pulse pressure post-TEVAR. VUED increased ascending aortic pulse pressure by 31%. VDM revealed increased strain in the unstented aortic segments. Aortic wall distensibility increased by 173% in the rupture region.

Conclusions

TEVAR increased pulse pressure in the ascending aorta by 35% due to the markedly elevated stiffness of the endograft relative to the native aorta. This under-recognized phenomenon should be considered when planning TEVAR, especially in cases with a concomitant ascending aneurysm, as the resulting increases in proximal aortic wall stresses can lead to complications. To overcome this issue, more compliant endografts should be developed.

Introduction

Branched endografts extend the application of thoracic endovascular aortic repair (TEVAR) in the proximal aorta, obviating the need for extra-anatomical bypass surgery when performing TEVAR in zone 2 and providing a minimally invasive alternative for treatment of proximal descending aortic pathologies in patients who are deemed unfit for open arch repair. Early results are promising,¹ yet significant complications have been reported that warrant further investigation. One such severe complication is aortic rupture.

Current endografts for TEVAR are made of materials much stiffer than the native aorta.² As a result, aortic compliance is reduced, and mean and pulse pressure is elevated, leading to increased stress in the unstented aortic segments. This is evidenced by the increased pulsatile strains measured proximal and distal to the endograft.³ Increased wall stresses are particularly problematic in the diseased ascending aorta, where elastic fragmentation has occurred⁴ and increased distensibility has shown to be related to aortic complications.⁵

In this study, we examine the pathophysiology of a specific case of aortic rupture in a patient enrolled in the feasibility trial of the Gore Thoracic Branch Endoprosthesis (TBE) at our institution, three months following zone 2 TEVAR.^[2] To analyze how hemodynamic loads changed post-TEVAR, three different patient-specific fluid structure interaction (FSI) simulations were performed. Additionally, image-based Vascular Deformation Mapping (VDM) was used to analyze changes in the pressure-strain relationships before and after TEVAR.

Methods

This retrospective study was approved by the University of Michigan Institutional Review Board (HUM00112350), with waiver of informed consent.

Patient history

A 74-year-old female presented with an asymptomatic mid-ascending (49 mm) and proximal descending aortic aneurysm (63 mm). Medical history included hypertension, hypercholesterolemia, hypothyroidism and 25 pack-years of cigarette smoking. She had a maternal family history of aortic aneurysms. Annual imaging follow-up with computed tomography angiography (CTA) examinations showed rapid enlargement of the descending aortic diameter to 73 mm and modest increase in the ascending aorta to 53 mm in 2 years (Figure 1). We elected to treat the larger aneurysm first with zone 2 branched TEVAR, anticipating a second stage repair of the ascending aorta two months thereafter.

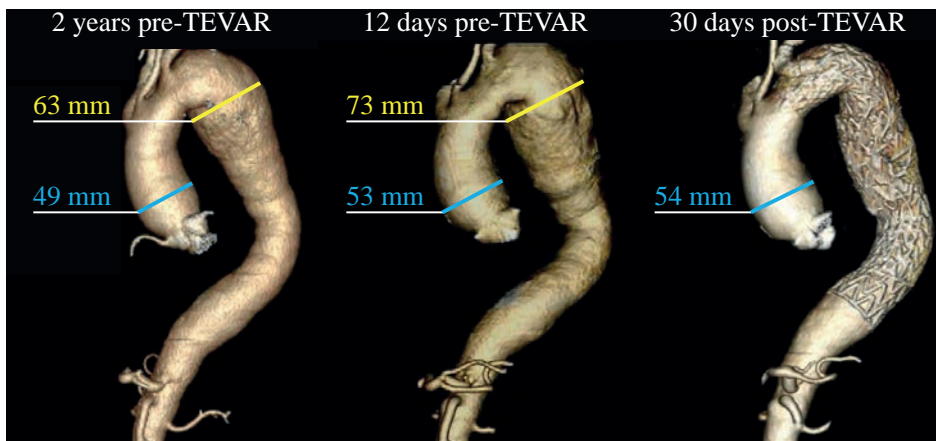


Figure 1. Aortic geometry 2 years prior to TEVAR (left), 12 days before TEVAR (middle) and 30 days after TEVAR (right). The outer diameters of the aortic wall at the level of the ascending aneurysm and proximal descending aneurysm are reported in yellow and blue, respectively. CTA = computed tomography angiography; TEVAR = thoracic endovascular aortic repair.

Procedure

The diameters of the proximal and distal landing zone for the descending aneurysm were 34 mm and 42 mm, respectively. The diameters and lengths of the proximal Gore TBE and distal Conformable Gore TAG endoprostheses were 37x100-mm and 45x150-mm, respectively, resulting in 9% proximal and 7% distal endograft oversizing. Controlled hypotension (with a systolic pressure of 80 mmHg) was used to reduce the risk of malpositioning. Deployment of the branched proximal component, using the Gore TBE delivery system, was technically challenging. The procedure was complicated by 5 mm distal dislocation resulting in type Ia endoleak. To overcome these issues, two extension devices were deployed proximal to the endograft. After balloon dilation of these extension devices, infolding in the greater curvature and bird-beaking in the lesser curvature of the arch was observed (Figure 2). As angiography showed brisk filling of the LSA and no pressure gradient was detected in the aortic arch, no additional procedures were performed. The patient recovered well and was discharged 10 days after the procedure.

Blood Pressure during Follow-up

Blood pressure measurements and antihypertensive medication during follow-up are reported in Table 1. At discharge, the patient had a similar blood pressure compared to preoperative, with a 19% higher pulse pressure, while using a four-times higher dosage of Metoprolol (100 mg daily) and two additional antihypertensive drugs.

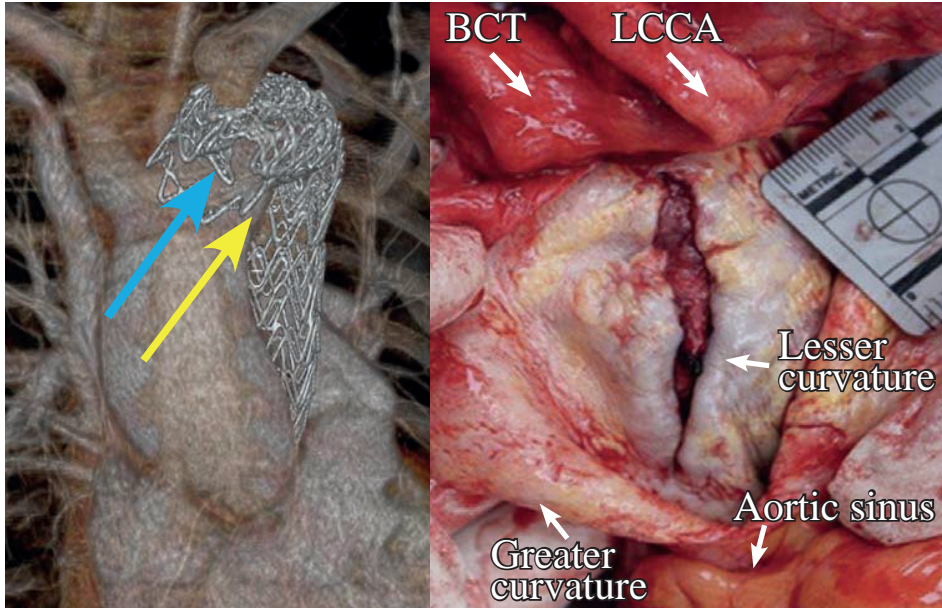


Figure 2. Left: post-TEVAR infolding (blue arrow) and bird-beak (yellow arrow). Right: Image of the luminal side of the ascending aorta that was taken during autopsy, after opening the aortic wall along the greater curvature. A 4.0 cm longitudinal tear was identified in the lesser curvature of the aortic wall, 2.5 cm distal to the aortic valve. There was no associated dissection and the tear did not extend to the proximal landing zone of the endograft.

Table 1. Antihypertensive Therapy and Blood Pressure

	Preoperative	Post-TEVAR day 7	Post-TEVAR day 10 (discharge)	Post-TEVAR day 30	Post-TEVAR day 31
Antihypertensive Medication [mg/day]	Metoprolol 25	Metoprolol 50 Furosemide 20	Metoprolol 100 Furosemide 20 Lisinopril 5	Metoprolol 100 Lisinopril 5	Metoprolol 50 Lisinopril 5
Systolic BP [mmHg]	100	146	106	81	126
Diastolic BP [mmHg]	53	66	50	55	58
Pulse pressure [mmHg]	47	80	56	26	68
Heart rate [bpm]	53	74	64	58	65

Antihypertensive therapy and blood pressures are reported during follow-up. Furosemide was prescribed for five days following discharge. At 30-day follow-up, blood pressure was low and the patient reported unstable gait and falling. Consequently, Metoprolol dosage was halved. The next day, blood pressure had increased markedly.

At the 30-day post-TEVAR visit, computed tomography angiography (CTA) demonstrated stable position of the endograft without evidence of endoleak. Ascending aortic aneurysm diameter had increased by 1 mm (Figure 1). The patient exhibited low blood pressure and reported several falls since discharge due to unsteady gait. Consequently, beta-blocker dosage was halved. During a subsequent visit in the next day, a marked blood pressure increase was noted. At this time (31 days post-TEVAR), pulse pressure was 32% higher than preoperative, despite the use of additional anti-hypertensive medication.

Three months post- TEVAR, the patient died suddenly in her sleep. Autopsy determined the cause of death to be hemopericardium due to a full thickness 4.0 cm longitudinal tear in the lesser curvature of the ascending aorta, 2.5 cm distal to the aortic valve, with no associated dissection (Figure 2).

Clinical data used for Computational Analysis

Pre-TEVAR and 30-day post-TEVAR ECG-gated CTA imaging data were acquired with a 64-slice scanner after intravenous injection of 120 mL iopamidol intravenous contrast (Isoview 370, Bracco Diagnostics, Milan, Italy). CTA data was retrospectively reconstructed at 10 phases throughout the cardiac cycle (0-90% R-R interval). Preoperative duplex Doppler ultrasonography examinations of the heart and carotid arteries were available, including measurements of surface area and flow velocity, enabling calculation cardiac output and flow volumes in the carotid arteries.

Patient-Specific Computational Analysis

FSI techniques were used to study aortic hemodynamics, including interactions between blood, aorta, and endograft using validated computational methods.⁶ Specifically, computational models were built from CTA image data and clinically measured flow and pressure data, with the overall objective of examining alterations in hemodynamics directly attributable to the presence of the device.⁷⁻⁹ First, a pre-TEVAR patient-specific model was created and validated by matching patient-specific clinical measurements of cardiac output, blood pressure and cervical blood flow. Subsequently, two additional models were constructed to represent post-TEVAR conditions. Each computational model required definition of: (1) a three-dimensional geometry of aorta and supra-aortic branches; (2) stiffness and thickness of vessels and endografts; and (3) a set of inflow and outflow boundary conditions that describe patient-specific flow and pressure conditions.

Geometric Models

All computational models were created using the validated cardiovascular modeling and simulation software CRIMSON¹⁰ and included the thoracic aorta, coronary and supra-aortic arteries.

The pre-TEVAR geometric model was made from preoperative CTA image data. A post-TEVAR geometric model was made from the 30-day post-TEVAR CTA image data and included the proximal infolding and bird-beak. A second post-TEVAR model was generated representing virtual uncomplicated endograft deployment (VUED) of the branched endograft (i.e. without infolding and bird-beak). The bird-beak and infolding resulted in an area reduction in the aortic arch of 38% relative to the VUED model.

Locally varying wall thickness and stiffness were assigned along the vessel walls using literature data.¹¹ Figure 3 presents the regional stiffness distribution of aortic wall and endografts in the pre-TEVAR, post-TEVAR and VUED models.

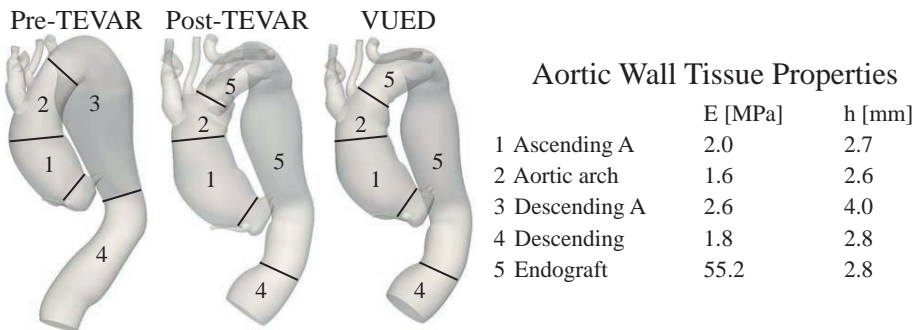


Figure 3. Distribution of aortic wall stiffness (E) and thickness (h) for the pre-TEVAR (left), post-TEVAR (middle), and VUED (right) model. The stiffness and thickness of the endograft were set to 2.8 mm and 55.2 MPa, rendering a fifteen-times larger structural stiffness than the descending aneurysm in the pre-TEVAR model: $154.6 \text{ MPa}\cdot\text{mm}$ vs $10.4 \text{ MPa}\cdot\text{mm}$ for the endograft and the aorta, respectively. A = aneurysm; TEVAR = thoracic endovascular aortic repair; VUED = virtual uncomplicated endograft deployment.

Boundary Conditions

Patient-specific cardiac output was measured from echocardiography and imposed at the aortic root of the computational models. Three-element Windkessel models were used to represent the resistance and compliance of the distal vascular beds of the outflow branches.¹² The parameters of the Windkessel models were tuned to match patient-specific pre-TEVAR flow measurements in the carotid arteries and brachial blood pressure. Flow measurements were not available for the subclavian and coronary arteries, therefore, previously reported flow distributions were assigned to these branches.^{13,14} After parameterization of the boundary conditions, lumped-parameter heart and coronary models were assigned to the aortic inlet and coronary

outlets to enable ventricular- and coronary-vascular interactions.¹⁵ The post-TEVAR and VUED models were run using the same inflow and outflow boundary conditions as the computationally validated pre-TEVAR model.

Computations

Blood was modeled as an incompressible Newtonian fluid with a density of 1060 kg/m³ and a dynamic viscosity of 4.0 mPa. Computations were performed using the CRIMSON flow solver on 80 cores at the University of Michigan High Performance Computing Cluster ConFlux. Typical computational time was 80 hours per cardiac cycle.

Vascular Deformation Mapping

Vascular deformation mapping (VDM) is a medical image processing technique that enables quantification of vascular deformation occurring between two image datasets.¹⁶ These datasets can be either systolic and diastolic configurations obtained from a gated scan, or follow-up scans over time. In this work, VDM was used to examine strain in the aortic wall over the cardiac cycle using the pre-TEVAR and 30-day post-TEVAR ECG-gated CTA data. For each CTA dataset, VDM measured strain through the following steps: (1) segmentation of the aorta in peak systole and end-diastole; (2) non-rigid registration of the two aortic segmentations; and (3) quantification of wall strain between the two phases, defining a scalar metric of strain for every point of the aorta known as Jacobian (J). Values of J larger than 1 represent expansion, while values smaller than 1 represent compression. To consider the large differences in blood pressure between the pre-TEVAR and 30-day post-TEVAR CTA examinations (Table 1), we defined a normalized index of distensibility (NID)¹⁷ for each time point as follows:

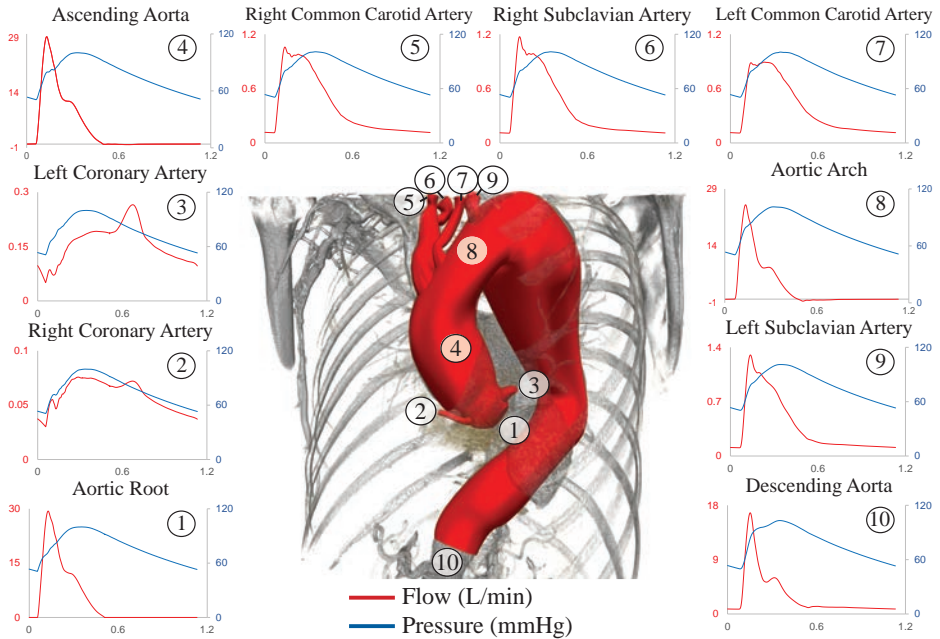
$$\text{Normalized Index of Distensibility (NID)} = (J - 1) / (\text{Pulse Pressure})$$

Therefore, positive values of NID imply expansion, while negative values imply contraction.

Results

Computational Fluid Dynamics

Pre-TEVAR simulation results successfully matched the preoperative clinical data on flow and pressure within 5% (Figure 4), producing a validated preoperative solution. Subsequently, computations of the post-TEVAR and VUED models were performed assuming the same parameters for the heart, coronary, and three-element Windkessel models. Differences in cardiac output and flow distributions between the three



Blood Flow and Pressure: Patient Data vs. Simulation Results

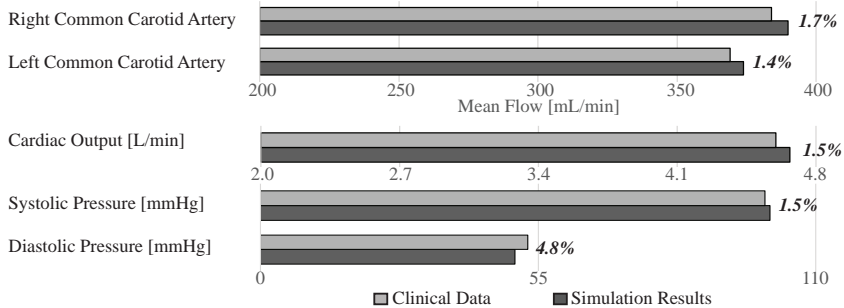


Figure 4. Top: pressure (blue) and flow (red) waveforms at the inlet (1) and all outlets of the preoperative model. The measurement locations are numbered. Bottom: comparison between clinically measured and computed blood flows and pressures in the preoperative model. All flows and pressures were matched within 5%.

simulations were minimal (Table 2). Nonetheless, pulse pressure increased from 49 mmHg pre-TEVAR to 66 mmHg post-TEVAR (+35%). Figure 5 compares ascending aortic pressure waveforms for all simulations. Removal of proximal infolding and bird-beak in VUED decreased ascending aortic pulse pressure by only 2 mmHg. This finding is consistent with the intraoperative pressure measurements, which did not reveal a pressure gradient in the aortic arch due to the infolding and bird-beaking.

Table 2. Simulated Mean Flow Values (mL/min)

	Pre-TEVAR	Post-TEVAR	VUED
Aortic Root	4,670	4,575	4,609
Right Coronary Artery	59	57	56
Left Coronary Artery	156	149	151
Right Common Carotid Artery	390	381	383
Right Subclavian Artery	380	370	372
Left Common Carotid Artery	374	366	367
Left Subclavian Artery	380	371	374
Descending Aorta	2,943	2,887	2,907

TEVAR = thoracic endovascular aortic repair; VUED = virtual uncomplicated endograft deployment.

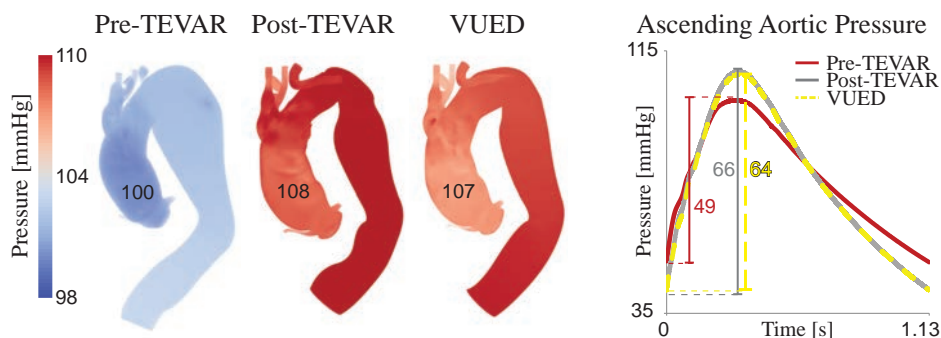


Figure 5. Left: Color-coded pressure mapping in peak systole ($t=0.42$ s). Peak systolic pressure in the ascending aorta is reported. Right: Ascending aortic pressure waveforms for all models. Pulse pressure increased with 35% post-TEVAR and 31% in VUED compared to pre-TEVAR. Notably, removal of proximal infolding and bird-beak in VUED resulted in minimal changes in ascending aortic pressure compared to post-TEVAR.

Vascular Deformation Mapping

Figure 6 depicts NID maps for the pre-TEVAR and 30 days post-TEVAR image data. Notably, NID increased in the unstented segments of the aorta post-TEVAR, revealing a 173% increase in NID in the rupture region in the lesser curvature (from 3.3 pre-TEVAR to 9.0 post-TEVAR). These findings confirm that the unstented segments of the aortic wall experience increased strain post-TEVAR.

Comment

The pathophysiology of ascending aortic rupture following branched zone 2 TEVAR was studied using a multiparametric image-based computational analysis. The goal of this analysis was to understand how the introduction of a stiff endograft in the descending aorta changed the biomechanical environment in the ascending aorta.

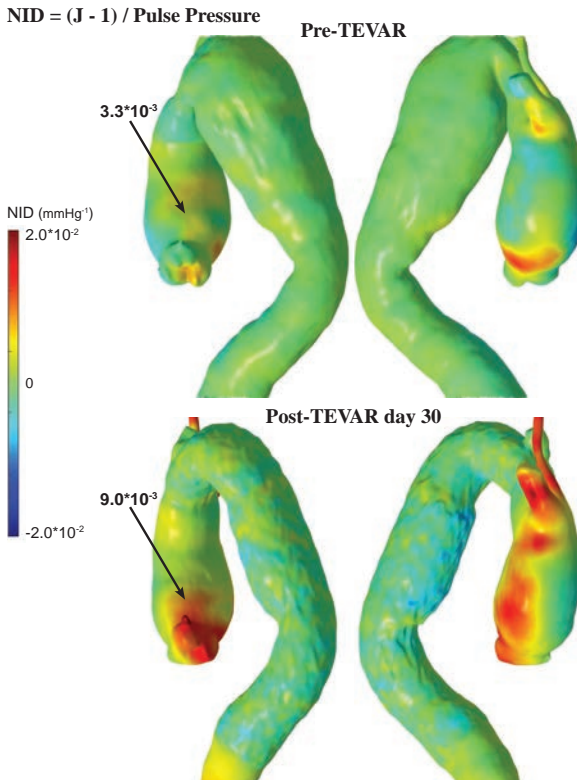


Figure 6. Pre-TEVAR (top) and 30 days post-TEVAR (bottom) NID maps are presented. Notably, NID increased in the unstented segments of the aorta and supra-aortic arteries post-TEVAR. In the rupture region, NID increased with 173%. CTA = computed tomography angiography; NID = Normalized Index of Distensibility; TEVAR = thoracic endovascular aortic repair.

Aortic compliance plays a key role in reducing the impedance of cardiac ejection.¹⁸ The proximal thoracic aorta is more compliant than the distal thoracic and abdominal aorta¹¹ and accounts for half of the total arterial compliance.¹⁹ Consequently, the impact of the stiffness mismatch between endograft and native aorta is larger when performing endovascular repair in the proximal descending thoracic aorta compared to the distal descending and abdominal aorta.²⁰ Even in older subjects with relatively stiff aortas, such as the one in this study, the endograft is 15 times stiffer than the native aorta, see Figure 3.

Diminished aortic compliance post-TEVAR leads to higher systolic and pulse pressures, which increase stresses in the aortic wall and may ultimately trigger fatigue-induced wall rupture.^{4,5} In this case, clinical blood pressure measurements indeed revealed increases in both systolic and pulse pressure post-TEVAR, despite the use of additional antihypertensive therapy.

FSI simulations allow us to exclude the role of medications and only examine the impact of the endograft. Under the assumption of fixed cardiac performance parameters in our heart model (e.g., contractility and heart rate), computations revealed a 35% increase in ascending aortic pulse pressure post-TEVAR. It is interesting to note

that TEVAR did not affect cardiac output, as previous studies showed that aortic stiffening may lead to reduced cardiac output in porcine models in the absence of increased contractility.¹⁴ This can be explained by the baseline stiffness of the aortic wall. The aortic wall of a 74-year-old patient is much stiffer than that of a mini-pig.²¹ Therefore, the additional stiffness due to TEVAR has a smaller impact in ventricular function in older, stiffer aortas.

At the 30-day post-TEVAR CTA examination, maximum ascending aortic aneurysm diameter had increased 1 mm compared to pre-TEVAR. This increase could be deemed negligible, yet, the patient had low blood pressure that day (81/55 mmHg). The ascending aortic diameter would likely have been larger had the patient undergone CTA examination the next day, as her blood pressure increased markedly (to 126/58 mmHg) when beta-blocker dosage was halved. Table 1 shows a large variability in blood pressure in this patient post-operatively, as direct result of antihypertensive therapy changes. This underlines the critical need for adequate antihypertensive management following TEVAR.

VDM was used to compute NID, a normalized metric of distensibility in the ascending aorta before and after TEVAR. Increased NID was found in the unstented segments of the aorta post-TEVAR. Interestingly, the greater curvature of the ascending aorta experienced the largest NID increase, while rupture occurred in the lesser curvature. Martin et al.²² studied ascending aortic aneurysm inflation and rupture using mechanical tissue testing and finite element models. They found that stress distributions are highly dependent on local tissue properties and geometry, and that peak wall stresses were typically located in the lesser curvature at the level of maximum diameter. These findings agree with typical ascending aortic rupture sites in type A aortic dissection.

VDM is a novel technique not routinely used in clinical practice. Currently, two-dimensional diameter measurements along the aortic centerline are the gold standard for measuring aortic morphology over time. Thus, cyclic aortic deformation resulting from blood pressure loading are generally neglected. Our findings highlight the importance of including blood pressure in the assessment of vascular deformation via a distensibility metric, rather than just assessing diameters in isolation.

Besides the stiffness mismatch resulting in increased blood pulse pressure, TEVAR in this patient was complicated by distal migration and type I endoleak. The proximal extenders implanted to treat the type I endoleak caused proximal infolding and bird-beaking (Figure 2). This complicated deployment was attributed to a type III aortic arch anatomy, which is more tortuous²³ and experiences higher cranial displacement forces compared to type I or type II arches.²⁴ Therefore, special attention should be given to landing zone length and location when performing proximal TEVAR in type III arches. Notably, virtual removal of infolding and bird-beak reduced ascending

aortic pulse pressure by only 2 mmHg. This finding confirms that the increased pulse pressure in this patient was not due to suboptimal endograft deployment, but due to the stiffness of the device itself. Another potential etiology (albeit not confirmed during autopsy or imaging studies) that could have contributed to aortic rupture in this patient is guidewire or device induced ascending aortic injury during deployment.

Limitations

Data on the arterial wall stiffness was not available for this patient. Therefore, we had to rely on literature data for regional stiffness properties. All postoperative scenarios were run with the same boundary conditions as the preoperative model, meaning that left ventricular contractility and compliance and resistance of the distal vascular beds were kept constant. In doing so, the calculated changes in aortic pulse pressure post-TEVAR assumed that there are no changes in anti-hypertensive therapy and no cardiovascular remodelling takes place. The validity of these assumptions has yet to be determined. Our group is currently enrolling patients in a prospective clinical trial investigating TEVAR-induced cardiovascular remodelling.²⁵ Results of this trial may further support the need for new endograft designs that reduce adverse cardiovascular remodelling following TEVAR.

Conclusion

TEVAR reduces arterial compliance and increases pulse pressure in the ascending aorta following TEVAR. This under-recognized phenomenon should be considered in preoperative planning, especially in patients with a concomitant ascending aortic aneurysm, as the resulting increased wall stresses can lead to complications in the unstented segments of the aorta. To overcome this issue, more compliant endografts should be developed that reduce the stiffness mismatch with the native aorta. For now, patients presenting with a proximal descending and concomitant ascending aortic aneurysm should be counselled to undergo ascending aortic repair with a frozen elephant trunk procedure and early completion TEVAR.

References

- 1 van Bakel TM, de Beaufort HW, Trimarchi S, et al. Status of branched endovascular aortic arch repair. *Ann Cardiothorac Surg* 2018;7(3). Doi: 10.3978/16472.
- 2 de Beaufort HWL, Coda M, Conti M, et al. Changes in aortic pulse wave velocity of four thoracic aortic stent grafts in an ex vivo porcine model. *PLoS One* 2017;12(10):e0186080. Doi: 10.1371/journal.pone.0186080.

- 3 Nauta FJ, van Bogerijen GH, Trentin C, et al. Impact of Thoracic Endovascular Aortic Repair on Pulsatile Circumferential and Longitudinal Strain in Patients With Aneurysm. *J Endovasc Ther* 2017;24(2):281–9. Doi: 10.1177/1526602816687086.
- 4 Klima T, Spjut HJ, Coelho A, et al. The morphology of ascending aortic aneurysms. *Hum Pathol* 1983;14(9):810–7. Doi: 10.1016/S0046-8177(83)80303-7.
- 5 Humphrey JD, Schwartz MA, Tellides G, et al. Role of mechanotransduction in vascular biology: Focus on thoracic aortic aneurysms and dissections. *Circ Res* 2015;1448–61. Doi: 10.1161/CIRCRESAHA.114.304936.
- 6 Figueroa CA, Vignon-Clementel IE, Jansen KE, et al. A coupled momentum method for modeling blood flow in three-dimensional deformable arteries. *Comput Methods Appl Mech Eng* 2006;195(41–43):5685–706. Doi: 10.1016/j.cma.2005.11.011.
- 7 van Bakel TMJ, Lau KD, Hirsch-Romano J, et al. Patient-Specific Modeling of Hemodynamics: Supporting Surgical Planning in a Fontan Circulation Correction. *J Cardiovasc Transl Res* 2018;11(2):145–55. Doi: 10.1007/s12265-017-9781-x.
- 8 Nauta FJH, Lau KD, Arthurs CJ, et al. Computational Fluid Dynamics and Aortic Thrombus Formation Following Thoracic Endovascular Aortic Repair. *Ann Thorac Surg* 2017;103(6):1914–21. Doi: 10.1016/j.athoracsur.2016.09.067.
- 9 Arthurs CJ, Agarwal P, John A V., et al. Reproducing Patient-Specific Hemodynamics in the Blalock–Taussig Circulation Using a Flexible Multi-Domain Simulation Framework: Applications for Optimal Shunt Design. *Front Pediatr* 2017;5:78. Doi: 10.3389/fped.2017.00078.
- 10 CRIMSON. The software for Cardiovascular Modelling and Simulation. www.crimson.software.
- 11 Roccabianca S, Figueroa CA, Tellides G, et al. Quantification of regional differences in aortic stiffness in the aging human. *J Mech Behav Biomed Mater* 2014;29:618–34. Doi: 10.1016/j.jmbbm.2013.01.026.
- 12 Vignon-Clementel IE, Figueroa CA, Jansen KE, et al. Outflow boundary conditions for 3D simulations of non-periodic blood flow and pressure fields in deformable arteries. *Comput Methods Biomech Biomed Engin* 2010;13(5):625–40. Doi: 10.1080/10255840903413565.
- 13 Lantz BMT, Foerster JM, Link DP, et al. Regional distribution of cardiac output: Normal values in man determined by video dilution technique. *Am J Roentgenol* 1981;137(5):903–7. Doi: 10.2214/ajr.137.5.903.
- 14 Coogan JS, Humphrey JD, Figueroa CA. Computational simulations of hemodynamic changes within thoracic, coronary, and cerebral arteries following early wall remodeling in response to distal aortic coarctation. *Biomech Model Mechanobiol* 2013;12(1):79–93. Doi: 10.1007/s10237-012-0383-x.
- 15 Arthurs CJ, Lau KD, Asrress KN, et al. A mathematical model of coronary blood flow control: simulation of patient-specific three-dimensional hemodynamics during exercise. *Am J Physiol - Hear Circ Physiol* 2016;310(9):H1242–58. Doi: 10.1152/ajpheart.00517.2015.
- 16 Burris NS, Hoff BA, Kazerooni EA, et al. Vascular Deformation Mapping (VDM) of Thoracic Aortic Enlargement in Aneurysmal Disease and Dissection. *Tomography* 2017;3(3):163–73. Doi: 10.18383/j.tom.2017.00015.
- 17 de Beaufort HW, Nauta FJ, Conti M, et al. Extensibility and Distensibility of the Thoracic Aorta in Patients with Aneurysm. *Eur J Vasc Endovasc Surg* 2016. Doi: 10.1016/j.ejvs.2016.11.018.
- 18 Belz GG. Elastic properties and Windkessel function of the human aorta. *Cardiovasc Drugs Ther* 1995;9(1):73–83.

- 19 Ioannou CV, Stergiopoulos N, Katsamouris AN, et al. Hemodynamics induced after acute reduction of proximal thoracic aorta compliance. *Eur J Vasc Endovasc Surg* 2003;26(2):195–204. Doi: 10.1053/EJVS.2002.1917.
- 20 Vardoulis O, Coppens E, Martin B, et al. Impact of Aortic Grafts on Arterial Pressure: A Computational Fluid Dynamics Study. *Eur J Vasc Endovasc Surg* 2011;42(5):704–10. Doi: 10.1016/j.ejvs.2011.08.006.
- 21 De Beaufort HWL, Ferrara A, Conti M, et al. Comparative Analysis of Porcine and Human Thoracic Aortic Stiffness 2017. Doi: 10.1016/j.ejvs.2017.12.014.
- 22 Martin C, Sun W, Elefteriades J. Patient-specific finite element analysis of ascending aorta aneurysms. *Am J Physiol - Hear Circ Physiol* 2015;308(10):H1306–16. Doi: 10.1152/ajpheart.00908.2014.
- 23 Marrocco-Trischitta MM, de Beaufort HW, Secchi F, et al. A geometric reappraisal of proximal landing zones for thoracic endovascular aortic repair according to aortic arch types. *J Vasc Surg* 2017. Doi: 10.1016/j.jvs.2016.10.113.
- 24 Marrocco-Trischitta MM, van Bakel TM, Romarowski RM, et al. The Modified Arch Landing Areas Nomenclature (MALAN) Improves Prediction of Stent Graft Displacement Forces: Proof of Concept by Computational Fluid Dynamics Modelling. *Eur J Vasc Endovasc Surg* 2018;55(4):584–92. Doi: 10.1016/j.ejvs.2017.12.019.
- 25 Nauta FJH, Kamman A V, Ibrahim E-SH, et al. Assessment of Cardiovascular Remodeling following Endovascular aortic repair through imaging and computation: The CORE prospective observational cohort study protocol. *BMJ Open* 2016;6(11). Doi: 10.1136/bmjopen-2016-012270.

Chapter 5

Status of branched endovascular aortic arch repair

Theodorus M.J. van Bakel^{1,2,3*}, MD

Hector W.L. de Beaufort^{1,2*}, MD, PhD

Santi Trimarchi^{2,4}, MD, PhD

Massimiliano M. Marrocco-Trischitta², MD

Jean Bismuth⁵, MD

Frans L. Moll¹, MD, PhD

Himanshu J. Patel⁶, MD

Joost A. van Herwaarden¹, MD, PhD

1. Department of Vascular Surgery, University Medical Center Utrecht, Utrecht, The Netherlands.
2. Thoracic Aortic Research Center, Policlinico San Donato IRCCS, San Donato Milanese, Italy.
3. Department of Surgery, University of Michigan, Ann Arbor, Michigan, USA.
4. Department of Biomedical Sciences for Health, University of Milan, Milan, Italy
5. Houston Methodist DeBakey Heart & Vascular Center, Houston, Texas, USA
6. Department of Cardiac Surgery, University of Michigan, Ann Arbor, Michigan, USA.

* contributed equally

Annals of Cardiothoracic Surgery. 2018;7:406-413

Abstract

Multiple medical device manufacturers are developing branched endografts for thoracic endovascular aortic repair (TEVAR), to provide a minimally invasive alternative for the treatment of aortic arch pathologies in patients who are deemed unfit for open or hybrid arch repair. Different branched endografts have been introduced, with varying number, size and orientation of the branches that redirect flow to the supra-aortic arteries. We present an overview of the currently investigated devices and review their outcomes. The results of branched TEVAR are promising, yet stroke remains the predominant periprocedural concern. For now, these procedures should be limited to select expert centers where the design and deployment procedure of branched endografts can be further developed to reduce stroke risks.

Introduction

Open surgical repair is the gold standard for the treatment of aortic arch pathologies.¹ Due to the invasive nature of the procedure, which involves sternotomy or thoracotomy, hypothermic circulatory arrest and cardiopulmonary bypass, many patients are deemed unfit for surgery.² Hybrid aortic arch repairs, such as the “frozen elephant trunk” technique, reduce cardiac ischemia times, but are still invasive procedures associated with postoperative stroke rates up to 13% and 30-day mortality rates up to 12%.³ Thoracic endovascular aortic repair (TEVAR) could be a minimally invasive alternative for patients who are deemed unfit for open or hybrid surgical repair. Yet, the origin of the supra-aortic arteries and aortic arch angulation pose anatomical challenges for the deployment of endografts.^{4,5} As a result, the outcomes of TEVAR in combination with extensive supra-aortic interventions or chimney techniques show substantial rates of postoperative stroke, Type I endoleak and retrograde Type A dissection.⁶ Multiple medical device manufacturers are now developing branched endografts for aortic arch deployment, extending the application of TEVAR to the proximal aorta. In the following, we review the literature on the technical characteristics and outcomes of branched TEVAR in the aortic arch and discuss the challenges and future perspectives of endovascular arch repair.

Current techniques of branched TEVAR

The PubMed database was searched for studies on branched endovascular repair of aortic arch pathologies (zone 0 – 2). Original reports were included if the operative techniques and postoperative outcomes were reported. If multiple reports described (partly) the same patient cohort, the most recent report was selected. A total of 14 studies were included, describing endovascular treatment of 302 patients with branched endografts.^{7–20} Overall proportions were calculated with a meta-analysis of proportions in R version 3.4.3, using the R package ‘meta’.²¹

Branched endograft designs

Technical characteristics of the endografts that were described in the included studies are reported in Table 1. Figure 1 presents the single branch endografts, Figure 2 presents the double branched endografts. W.L. Gore (Flagstaff, AZ, USA) and Medtronic Vascular (Santa Rosa, CA, USA) have developed single branch endografts that are connected to the target vessel using a bridging stent.^{7,20} The main difference between the designs of these devices is that the W.L. Gore device has an internal branch with a retrograde orientation and the Medtronic device has volcano-shaped

Table 1. Technical characteristics of investigational branched endografts

First author	Manufacturer*	Stent material	Graft material	Landing zone	No. of branches	Inner branch	Separate branch component	Total no. components	Aortic graft diam. [mm]	Branch graft diam. [mm]	Sheath main device [F]	Sheath branch device [F]
Inoue 1999, Tazaki 2017	PTMC	Nickel titanium	Dacron	0–2	1–3	No	No	1	18–46	8–20	20–24	5–7
Piffaretti 2013	Bolton	Nitinol	Polyester	0	1	1 antegrade	Yes	2	46	20	26	NA
Haulon 2014, Spear 2016	Cook	Nitinol	Polyester	0	2	2 antegrade	Yes	3	38–46	N/A	22–24	14–16
Lim 2015	S&G	Nitinol	Polyester	0	2	No	Yes	3	44	18, 10	21, 18	N/A
Lu 2015	MicroPort	Nitinol	Polyester	0	1	No	No	1	28–40	7.5–14	22	4–8
Roselli 2015	Medtronic	Nitinol	Polyester	2	1	No	Yes	2	30–46	10–14	24–25	15
Zhang 2016, Huang 2017	MicroPort	Nitinol	Polyester	2	1	No	No	1	30–34	10–16	18–24	8
Patel 2017	W.L. Gore	Nitinol	PTFE	2	1	1 retrograde	Yes	2	21–53	N/A	N/A	N/A
Spear 2017	Cook	Nitinol	Polyester	0	3	2 antegrade, 1 retrograde	Yes	4	N/A	N/A	22–24	N/A
D'Onofrio 2017	Endospan	Nitinol	PTFE	0	1	No	No	2	36–43	14–20	20	N/A
Czerny 2018	Bolton	Nitinol	Polyester	0	2	2 antegrade	Yes	3	N/A	N/A	25	14

PTFE = polytetrafluoroethylene. *Device manufacturers: Bolton Medical, (Sunrise, FL, USA); Cook Medical (Bloomington, IN, USA); Endospan (Herzlia, Israel); Medtronic Vascular (Santa Rosa, CA, USA); MicroPort Medical Co, Ltd (Shanghai, China); PTMC institute (Kyoto, Japan); S&G Biotech Inc (Seongnam, Korea); W.L. Gore (Flagstaff, AZ, USA)

opening without an internal branch. Endospa (Herzlia, Israel) and MicroPort Medical Co, Ltd (Shanghai, China) developed single branched endografts with a unibody design that can be combined with one or more fenestrations to accommodate perfusion of additional supra-aortic arteries.^{10,13} Bolton Medical, (Sunrise, FL, USA) and Cook Medical (Bloomington, IN, USA) developed double branched endografts for zone 0 deployment that feature anterior facing internal branches that are connected to the brachiocephalic trunk (BCT) and left common carotid artery (LCCA) with bridging stents.^{8,12,18} Both endograft systems are individually made to fit the patient's anatomy, the main differences between the endograft designs are the position and size of the two internal branches. In the Bolton design, the internal branches are positioned side-by-side, while in the Cook endograft the internal branch to the LCCA is smaller and positioned diagonally behind the internal branch to the BCT. Another important difference is that the Bolton system includes the bridging stents, while the Cook system is not delivered with bridging stents. This means that with the Cook system additional bridging stents need to be used, outside their instructions for use. The Inoue Stent Graft has a unibody design without internal branches. This endograft has been developed at the PTMC institute (Kyoto, Japan) and is individually constructed from a woven Dacron polyester fabric. The branches are sewn upon the main body at the location of the target vessels.¹⁶

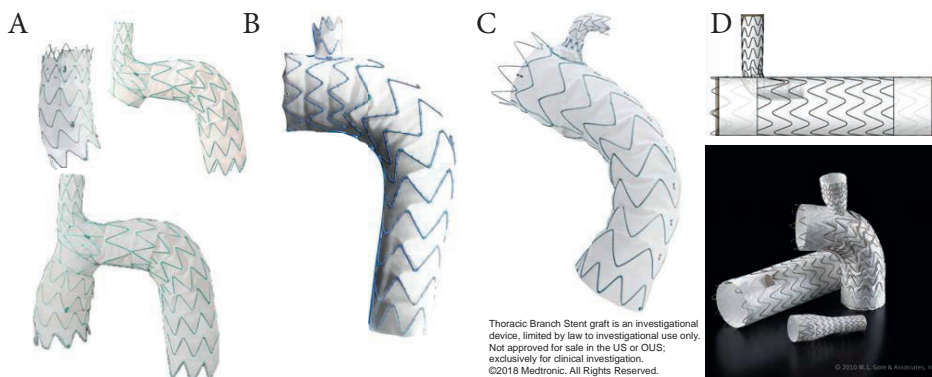


Figure 1. Single-branched endografts. (A) Nexus™ Stent Graft System for zone 0 from Endospa (Herzlia, Israel), this endograft is customizable with an additional fenestration for the left common carotid artery. Image provided courtesy of Endospa; (B) Castor™ branched endograft from MicroPort Medical Co., Ltd. (Shanghai, China), customizable with two additional fenestrations. Image provided courtesy of MicroPort Medical; (C) thoracic branch stent graft from Medtronic Vascular (Santa Rosa, CA, USA). Image provided courtesy of Medtronic Vascular; (D) GORE® TAG® thoracic endoprosthesis with retrograde internal branch from W.L. Gore (Flagstaff, AZ, USA). Image provided courtesy of W.L. Gore & Associates, Inc.

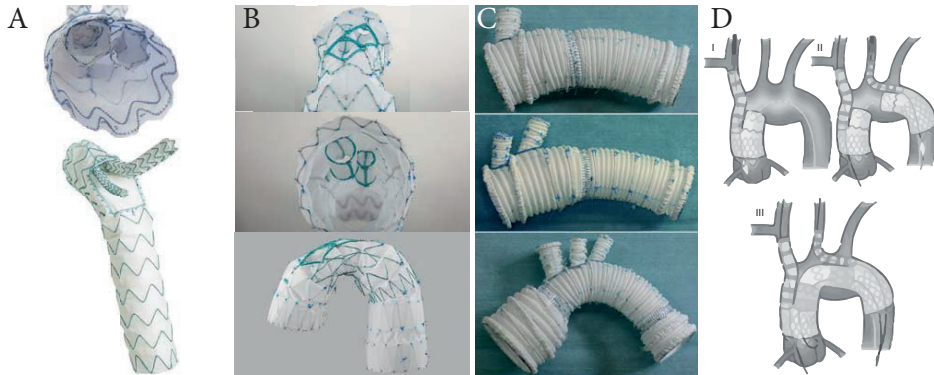


Figure 2. Multi-branched endografts. (A) Zone 0 endograft from Bolton Medical, permission for use was granted by Bolton Medical, Sunrise, Florida; (B) zone 0 endograft from Cook Medical, permission for use was granted by Cook Medical, Bloomington, Indiana; (C) three versions of the Inoue Stent Graft from the PTMC institute (Kyoto, Japan), image from Tazaki et al.¹⁶; (D) three component solution for zone 0 deployment from S&G Biotech, Inc. (Seongnam, Korea), image from Lim et al.¹¹

Deployment procedures

The deployment procedure for branched endografts is similar to the procedure for regular TEVAR, yet additional guidewires are inserted for deployment of the branch components. Through-and-through access is optional, depending on the patient's anatomy and physician's preference.²⁰ Inoue et al. reported the first total endovascular aortic arch repair in 1999,⁹ the triple branched Inoue Stent Graft was inserted transfemorally with one large caliber sheath (24 F). The branch sections of the endograft were pulled into the target vessels by traction wires that were inserted via the bilateral brachial arteries and LCCA using small caliber sheaths (5 – 7 F). The deployment procedure of modular branched endografts is similar, however, additional components need to be introduced via the supra-aortic arteries to connect the branches in the main body to the target vessels. The brachial, axillary and carotid arteries can be used as access vessels to advance guidewires and bridging components into the aorta, depending on local vascular anatomy and preference of the physician.

Outcomes of branched TEVAR

Table 2 presents the outcomes of the included studies. The overall technical success rate was high and the endografts provided good patency during follow-up (94% and 96%, respectively). The overall rate of retrograde Type A dissection was 3.3% and overall mortality was 6.1%, which is low considering the fact that the vast majority of patients had multiple comorbidities and were deemed unfit for open surgical repair.

Table 2. Outcomes of branched TEVAR

First author	No. of patients	Intended no. of branch vessels	Proximal landing zone 0/1/2	Technical success	Early mortality	Disabling stroke	Minor stroke	Permanent paraplegia	Retrograde type A dissection	Follow-up in months (average)	Patency	Type I endoleak	Endovascular reintervention	Open reintervention
Inoue 1999	15	17	1/0/14	60%	0%	6.7%	0%	0%	0%	13	100%	26.7%	6.7%	0%
Haulon 2014	38	76	38/0/0	84.2%	13.2%	2.6%	10.5%	2.6%	0%	12	93.9%	3.0%	6.1%	3.0%
Lu 2015	51	90*	33/0/18	100%	2.0%	0%	0%	N/A	N/A	44	100%	0%	0%	0%
Roselli 2015	9	9	0/0/9	100%	0%	0%	33.3%	0%	0%	6	100%	0%	0%	0%
Zhang 2016	9	9	0/0/9	100%	0%	0%	N/A	N/A	N/A	6	N/A	N/A	N/A	N/A
Spear 2016	27	54	27/0/0	100%	0%	11.1%	3.7%	0%	N/A	12	N/A	N/A	7.4%	0%
Huang 2017	21	21	0/0/21	100%	0%	0%	0%	N/A	N/A	N/A	100%	0%	N/A	N/A
Tazaki 2017	89	121	7/18/64	100%	4.5%	15.7%	N/A	1.1%	2.2%	44	N/A	10.1%	8.2%	3.4%
Patel 2017	22	22	0/0/22	100%	0%	0%	0%	0%	0%	8	100%	0%	0%	0%
Spear 2017	3	9	3/0/0	100%	0%	0%	0%	0%	0%	6	100%	0%	0%	0%
Czerny 2018	15	30	15/0/0	100%	6.7%	6.7%	13.3%	0%	0%	9	100%	0%	6.7%	0%
Case reports	3	5	3/0/0	100%	0%	0%	0%	0%	0%	4	100%	0%	0%	0%
Overall	302	463	127/18/157	94%	6.1%	9.6%	8.6%	3.1%	3.3%	27	96%	7.5%	6.6%	3.3%
				[86 - 98]	[3.7 - 9.8]	[6.2 - 14.7]	[4.3 - 16.4]	[1.3 - 6.9]	[1.4 - 7.4]		[91 - 98]	[3.8 - 14.4]	[4.0 - 10.6]	[1.7 - 6.6]

* 53 branched and 37 fenestration. Overall percentages were calculated with a meta-analysis of proportions, 95%-confidence intervals are reported within brackets.

The results from Haulon et al.⁸ highlighted a steep learning curve even for the highly skilled endovascular specialist, with an early mortality rate of 30% in the first 10 cases. An improvement followed in the next 28 cases, with a mortality rate of 7.1%. Postoperative stroke is the Achilles' heel of endovascular arch repair, with an overall combined incidence of 14%. Multi-branched endograft deployments were associated with high stroke rates. Tazaki et al. reported stroke rates of 33% with the double branched and 40% for the triple branched Inoue Stent Graft.¹⁶ Spear et al. reported a 14.8% stroke rate with the double branched endograft from Cook¹⁸ and Czerny et al. reported a combined stroke rate of 20% with the Bolton double branched endograft.¹² Guidewire manipulation in the arch and supra-aortic arteries, which are frequently burdened by atherosclerosis,^{7,8} is most likely the cause of embolic stroke in these cases.^{12,18}

Challenges of branched TEVAR

A recent CT-based anatomical feasibility study estimated that about 70% of patients with arch aneurysms after surgical replacement of the ascending aorta are feasible for endovascular treatment with one of the currently investigated double branched devices.²² This is particularly interesting as redo sternotomies add significant risks for postoperative complications.²³ Still, the majority of multi-branched endografts for aortic arch deployment are individually made, which takes several weeks and limits the application of total endovascular arch repair to elective cases. The case report from D'Onofrio et al. presented a successful off-the-shelf solution for total endovascular arch repair, using the single branched modular Nexus system from Endospan (Herzlia, Israel).¹³ Before deployment of this single branched endograft, the patient underwent an extra-anatomic reconstruction of the supra-aortic arteries with a right common carotid to LSA bypass and reimplantation of the LCCA on the graft. A recent computational study from our group analyzed the postoperative hemodynamic outcomes of different endograft designs for zone 0 repair.²⁴ We found that a single branched design resulted in reduced perfusion of the supra-aortic arteries with elevated blood shear rates compared to double branched alternatives. The case report from Lim et al. presented a double branched off-the-shelf solution for zone 0 endovascular arch repair, using bifurcated endografts in the BCT and LCCA that were connected with a bridging component in the aortic arch.¹¹ An important limitation of this technique is the need to introduce large caliber devices via the carotid arteries

These devices may damage the arterial wall of the carotid arteries, increasing postoperative stroke risks. Additionally, the hemodynamic displacement forces in the arch need to be taken into account,⁵ as they pose a challenge for proximal sealing and integrity of modular endografts during follow-up.²⁵

Our perspective

Branched TEVAR is a promising extension of the armamentarium of endovascular specialists. However, this technically challenging procedure requires optimal equipment and endovascular experience and is associated with a steep learning curve. Pre-operative planning is vital for a successful branched TEVAR procedure and should include imaging with echocardiographic-gated computed tomography angiography (CTA) to reduce artefacts generated by prior surgery material and cardiac motion.²⁶ The images are then processed using software-assisted centerline reconstructions to acquire accurate measurements of the luminal diameter, arch angulation and proximal and distal landing zones lengths. These measurements should be discussed within the endovascular team, including the endograft manufacturer, to determine the feasibility of branched TEVAR and select the optimal endograft. Complex endovascular procedures, such as branched TEVAR, should be performed in hybrid operating rooms that combine an optimal open surgical environment with advanced imaging capabilities to facilitate endovascular navigation and increase accuracy of endograft deployment. Moreover, the use of CTA image fusion with live fluoroscopy has shown to reduce radiation exposure and contrast injection during complex repairs.²⁷ Further development of endograft design and deployment procedure is needed to reduce stroke rates following branched TEVAR. Routine use of transcranial Doppler ultrasonography can help to identify the procedural aspects most associated with cerebral embolization.²⁸ Perera et al. recently reported that robotic catheter placement resulted in significantly less cerebral embolization during TEVAR compared with manual techniques.²⁹ Additional carbon dioxide flushing of the endograft prior to insertion could reduce the risk of air embolism during deployment.³⁰ The use of cerebral protection devices, which have proven to be effective at reducing embolization in transcatheter aortic valve replacement,³¹ could also be effective for branched arch TEVAR. Additionally, patient-specific computational fluid dynamics analysis can help to predict the hemodynamic outcomes of different treatment scenarios and aid endograft selection.^{24,32}

Conclusion

Multiple medical device manufacturers are developing branched endografts for aortic arch deployment, providing a minimally invasive solution for patients who are deemed unfit for open or hybrid arch repair. The results of branched TEVAR are promising, yet stroke remains the predominant periprocedural concern of total endovascular arch repair. For now, these procedures should be limited to select expert

centers where the design and deployment procedure of branched endografts can be further developed to reduce stroke risks.

References

- 1 Hiratzka LF, Bakris GL, Beckman JA, et al. 2010 ACCF/AHA/AATS/ACR/ASA/SCA/SCAI/SIR/STS/SVM guidelines for the diagnosis and management of patients with Thoracic Aortic Disease: a report of the American College of Cardiology Foundation/American Heart Association Task Force on Practice Guidelines, A. *Circulation* 2010;121(13):e266-369. Doi: 10.1161/CIR.0b013e3181d4739e.
- 2 Lioupis C, Abraham CZ. Results and challenges for the endovascular repair of aortic arch aneurysms. *Perspect Vasc Surg Endovasc Ther* 2011;23(3):202–13. Doi: 10.1177/1531003511413608.
- 3 Shrestha M, Beckmann E, Krueger H, et al. The elephant trunk is freezing: The Hannover experience. *J Thorac Cardiovasc Surg* 2015;149(5):1286–93. Doi: 10.1016/j.jtcvs.2015.01.044.
- 4 Marrocco-Trischitta MM, de Beaufort HW, Secchi F, et al. A geometric reappraisal of proximal landing zones for thoracic endovascular aortic repair according to aortic arch types. *J Vasc Surg* 2017. Doi: 10.1016/j.jvs.2016.10.113.
- 5 Marrocco-Trischitta MM, van Bakel TM, Romarowski RM, et al. The Modified Arch Landing Areas Nomenclature (MALAN) Improves Prediction of Stent Graft Displacement Forces: Proof of Concept by Computational Fluid Dynamics Modelling. *Eur J Vasc Endovasc Surg* 2018;55(4):584–92. Doi: 10.1016/j.ejvs.2017.12.019.
- 6 Andradi TB, Grossmann M, Zenker D, et al. Supra-aortic interventions for endovascular exclusion of the entire aortic arch. *J Vasc Surg* 2017;66(1):281–297.e2. Doi: 10.1016/j.jvs.2017.04.024.
- 7 Roselli EE, Arko FR, Thompson MM. Results of the Valiant Mona LSA early feasibility study for descending thoracic aneurysms. *J Vasc Surg* 2015;62(6):1465–1471.e3. Doi: 10.1016/j.jvs.2015.07.078.
- 8 Haulon S, Greenberg RK, Spear R, et al. Global experience with an inner branched arch endograft. *J Thorac Cardiovasc Surg* 2014;148(4):1709–16. Doi: 10.1016/j.jtcvs.2014.02.072.
- 9 Inoue K, Hosokawa H, Iwase T, et al. Aortic Arch Reconstruction by Transluminally Placed Endovascular Branched Stent Graft. *Circulation* 1999;100(Supplement 2):II-316-II-321. Doi: 10.1161/01.CIR.100.suppl_2.II-316.
- 10 Lu Q, Feng J, Zhou J, et al. Endovascular repair by customized branched stent-graft: A promising treatment for chronic aortic dissection involving the arch branches. *J Thorac Cardiovasc Surg* 2015;150(6):1631–1638.e5. Doi: 10.1016/j.jtcvs.2015.08.032.
- 11 Lim JW, Choi CW, Her K, et al. Totally endovascular aortic arch repair by branched stent graft placement. *J Vasc Surg Cases* 2015;1(4):279–82. Doi: 10.1016/j.jvsc.2015.10.003.
- 12 Czerny M, Rylski B, Morlock J, et al. Orthotopic branched endovascular aortic arch repair in patients who cannot undergo classical surgery. *Eur J Cardio-Thoracic Surg* 2018. Doi: 10.1093/ejcts/ezx493.
- 13 D’Onofrio A, Antonello M, Lachat M, et al. Endovascular treatment of aortic arch aneurysm with a single-branched double-stage stent graft. *J Thorac Cardiovasc Surg* 2017;154(5):e75–7. Doi: 10.1016/j.jtcvs.2017.06.030.
- 14 Piffaretti G, Rivolta N, Fontana F, et al. Aortic arch aneurysm repair with a new branched device. *J Vasc Surg* 2013;57(6):1664–7. Doi: 10.1016/j.jvs.2012.10.080.

- 15 Zhang T, Jiang W, Lu H, et al. Thoracic Endovascular Aortic Repair Combined with Assistant Techniques and Devices for the Treatment of Acute Complicated Stanford Type B Aortic Dissections Involving Aortic Arch. *Ann Vasc Surg* 2016;32:88–97. Doi: 10.1016/j.avsg.2015.10.030.
- 16 Tazaki J, Inoue K, Higami H, et al. Thoracic endovascular aortic repair with branched Inoue Stent Graft for arch aortic aneurysms. *J Vasc Surg* 2017;66(5):1340–1348.e5. Doi: 10.1016/j.jvs.2017.03.432.
- 17 Huang H, Jiao Y, Zhang Y, et al. Implantation of Unibody Single-Branched Stent Graft for Patients with Type B Aortic Dissections Involving the Left Subclavian Artery: 1-Year Follow-Up Outcomes. *Cardiovasc Intervent Radiol* 2017;40(11):1678–86. Doi: 10.1007/s00270-017-1748-4.
- 18 Spear R, Haulon S, Ohki T, et al. Editor's Choice - Subsequent Results for Arch Aneurysm Repair with Inner Branched Endografts. *European Journal of Vascular and Endovascular Surgery*, vol. 51. 2016. pp. 380–5.
- 19 Spear R, Clough RE, Fabre D, et al. Total Endovascular Treatment of Aortic Arch Disease Using an Arch Endograft with 3 Inner Branches. *J Endovasc Ther* 2017;24(4):534–8. Doi: 10.1177/1526602817714569.
- 20 Patel HJ, Dake MD, Bavaria JE, et al. Branched Endovascular Therapy of the Distal Aortic Arch: Preliminary Results of the Feasibility Multicenter Trial of the Gore Thoracic Branch Endoprosthesis. *Annals of Thoracic Surgery*, vol. 102. 2016. pp. 1190–8.
- 21 Schwarzer G, Carpenter JR, Rücker G. *Meta-Analysis with R*. 1st ed. Heidelberg: Springer; 2015.
- 22 Milne CPE, Amako M, Spear R, et al. Inner-Branched Endografts for the Treatment of Aortic Arch Aneurysms After Open Ascending Aortic Replacement for Type A Dissection. *Ann Thorac Surg* 2016;102(6):2028–35. Doi: 10.1016/j.athoracsur.2016.05.012.
- 23 Rylski B, Desai ND, Bavaria JE, et al. Type A aortic dissection after previous cardiac surgery: Results of an integrated surgical approach. *Ann Thorac Surg* 2014;97(5):1582–9. Doi: 10.1016/j.athoracsur.2013.12.064.
- 24 van Bakel TM, Arthurs CJ, van Herwaarden JA, et al. A computational analysis of different endograft designs for Zone 0 aortic arch repair†. *Eur J Cardio-Thorac Surg* 2018;54(2):389–96. Doi: 10.1093/ejcts/ezy068.
- 25 Prasad A, To LK, Gorrepati ML, et al. Computational analysis of stresses acting on inter-modular junctions in thoracic aortic endografts. *J Endovasc Ther* 2011;18(4):559–68. Doi: 10.1583/11-3472.1.
- 26 Valente T, Rossi G, Lassandro F, et al. MDCT evaluation of acute aortic syndrome (AAS). *Br J Radiol* 2016:20150825. Doi: 10.1259/bjr.20150825.
- 27 Hertault A, Maurel B, Sobocinski J, et al. Impact of hybrid rooms with image fusion on radiation exposure during endovascular aortic repair. *Eur J Vasc Endovasc Surg* 2014:382–90. Doi: 10.1016/j.ejvs.2014.05.026.
- 28 Bismuth J, Garami Z, Anaya-Ayala JE, et al. Transcranial Doppler findings during thoracic endovascular aortic repair. *J Vasc Surg* 2011;54(2):364–9. Doi: 10.1016/j.jvs.2010.12.063.
- 29 Perera AH, Riga C V., Monzon L, et al. Robotic Arch Catheter Placement Reduces Cerebral Embolization During Thoracic Endovascular Aortic Repair (TEVAR). *Eur J Vasc Endovasc Surg* 2017;53(3):362–9. Doi: 10.1016/j.ejvs.2016.10.017.
- 30 Rohlfs F, Tsilimparis N, Saleptsis V, et al. Air Embolism During TEVAR: Carbon Dioxide Flushing Decreases the Amount of Gas Released from Thoracic Stent-Grafts During Deployment. *J Endovasc Ther* 2017;24(1):84–8. Doi: 10.1177/1526602816675621.

- 31 Giustino G, Sorrentino S, Mehran R, et al. Cerebral Embolic Protection During TAVR: A Clinical Event Meta-Analysis. *J Am Coll Cardiol* 2017;465–6. Doi: 10.1016/j.jacc.2016.12.002.
- 32 van Bakel TMJ, Lau KD, Hirsch-Romano J, et al. Patient-Specific Modeling of Hemodynamics: Supporting Surgical Planning in a Fontan Circulation Correction. *J Cardiovasc Transl Res* 2018;11(2):145–55. Doi: 10.1007/s12265-017-9781-x.

Chapter 6

A computational analysis of different endograft designs for zone 0 aortic arch repair

Theodorus M.J. van Bakel^{1,5,6}, MD

Christopher J. Arthurs⁷, DPhil

Joost A. van Herwaarden⁶, MD, PhD

Frans L. Moll⁶, MD, PhD

Kim A. Eagle³, MD

Himanshu J. Patel⁴, MD

Santi Trimarchi⁵, MD, PhD

C. Alberto Figueroa^{1,2}, PhD

1. Department of Surgery, University of Michigan, Ann Arbor, Michigan, USA.
2. Department of Biomedical Engineering, University of Michigan, Ann Arbor, Michigan, USA.
3. Department of Cardiology, University of Michigan, Ann Arbor, Michigan, USA.
4. Department of Cardiac Surgery, University of Michigan, Ann Arbor, Michigan, USA.
5. Thoracic Aortic Research Center, Policlinico San Donato IRCCS, San Donato Milanese, Italy.
6. Department of Vascular Surgery, University Medical Center Utrecht, Utrecht, The Netherlands.
7. Division of Imaging Sciences and Biomedical Engineering, King's College London, London, UK.

European Journal of Cardio-Thoracic Surgery. Editor's Choice – 2018;54:389-396

Abstract

Objectives

Aortic arch repair remains a major surgical challenge. Multiple manufacturers are developing branched endografts for Zone 0 endovascular repair, extending the armamentarium for minimally invasive treatment of aortic arch pathologies. We hypothesize that the design of the Zone 0 endograft has a significant impact on the postoperative hemodynamic performance, particularly in the cervical arteries. The goal of our study was to compare the postoperative hemodynamic performance of different Zone 0 endograft designs.

Methods

Patient-specific, clinically validated, Computational Fluid Dynamics (CFD) simulations were performed of a 71-year old female with a 6.5-cm saccular aortic arch aneurysm. Additionally, four endovascular repair scenarios using different endograft designs were created. Hemodynamic performance was evaluated by calculation of postoperative changes in blood flow and platelet activation potential (PLAP) in the cervical arteries.

Results

Preoperative cervical blood flow and mean PLAP were 1,080 mL/min and 151.75, respectively. Cervical blood flow decreased and PLAP increased following endovascular repair in all scenarios. Endografts with two antegrade inner branches performed better compared to single branch endografts. Scenario 3 performed worst with a decrease in total cervical blood flow of 4.8%, a decrease in left hemisphere flow of 6.7%, and an increase in PLAP of 74.3%.

Conclusions

Endograft design has a significant impact on hemodynamic performance following Zone 0 endovascular repair, potentially affecting cerebral blood flow during follow-up. Our results demonstrate the use of computational modelling for virtual testing of therapeutic interventions and underline the need to monitor the long-term outcomes in this cohort of patients.

Introduction

Open surgical repair of aortic arch pathologies remains a major challenge in aortic surgery that requires sternotomy or thoracotomy and cardiopulmonary bypass.¹ Many patients are not considered fit for this invasive procedure due to preexisting comorbidities.²

To address this issue, multiple device manufacturers are developing Zone 0 endografts for total endovascular repair of the aortic arch, eliminating the need for open surgical repair.³ This approach involves deployment of an endograft in the ascending aorta with either one or two branches that redirect flow to the brachiocephalic trunk (BCT) alone or to the BCT and left common carotid artery (LCCA), in combination with one or two extra-anatomical bypasses.⁴ Different Zone 0 endograft designs have been introduced, with varying number, size and orientation of the branches that redirect flow to the supra-aortic arteries.³

Early results of Zone 0 endovascular aortic arch repair are promising and encourage the use of these devices, especially in patients with aortic pathologies that would be considered unreparable otherwise.^{4,5} Stroke remains a significant complication following endovascular repair of the aortic arch,^{4,6,7} with reported incidences up to 11%.⁴ Guidewire manipulation and covering of the supra-aortic arteries are procedural factors known to increase stroke risk.^{5,7} Yet, little is known about the impact of branched endograft design on the risk for cerebrovascular complications. We hypothesize that the design of the Zone 0 endograft has a significant impact on the postoperative hemodynamic performance, particularly in the cervical arteries.

The goal of the present study was to assess and compare the postoperative hemodynamic performance of different Zone 0 endograft designs. Advanced computational fluid dynamics (CFD) tools have been used to support clinical decision making through calculation of the hemodynamic outcomes of different therapeutic interventions using a 'virtual testing' paradigm.⁸⁻¹⁰ The virtual testing paradigm, that has been used in various engineering fields to replace the 'build-and-test' paradigm, uses computational simulations to optimize a proposed design before any physical model is built. We applied these methods in a patient with a saccular aortic arch aneurysm to calculate cervical blood flow and blood shear rates in four virtual postoperative scenarios featuring different Zone 0 endograft designs.

Methods

Approval for this study was obtained from the institutional review board (University of Michigan protocol number HUM00112350), the need for patient consent was waived.

Patient History

A 71-year-old female presented with a 6.5-cm isolated saccular aortic arch aneurysm. Her medical history included hypertension, obstructive sleep apnea, dilated non-ischemic cardiomyopathy and paroxysmal atrial fibrillation for which a dual-chamber implantable cardioverter defibrillator had been implanted.

Clinical Data

Computed tomography angiography (CTA) was performed using a 64-slice scanner after intravenous injection of 150 mL Iopamidol 76% contrast agent. Ultrasonography examinations of the heart and the cervical arteries were acquired, including measurements of surface area and flow velocity with duplex Doppler ultrasonography, enabling calculation of flow volumes in the cervical arteries. A cardiac catheterization procedure was performed using 80 mL Iopamidol 76% contrast agent, providing information on aortic pressure and cardiac output via the Fick principle.¹¹

Patient-Specific Computational Modeling

Computational modeling techniques were used to calculate patient-specific hemodynamics based on the physical laws of fluid flows. CFD is a well-established technique that enables calculation of the motion of an incompressible fluid by solving the Navier-Stokes equations. CFD methods have been used profusely in applications such as aerospace and automotive engineering. Over the past decades, CFD methods have also been applied to study hemodynamics in cardiovascular health and disease.¹² Here, a computational model of hemodynamics requires the definition of: (1) a three-dimensional geometric model of the vessels of interest, and (2) a set of inflow and outflow boundary conditions that represent the flow and pressure conditions of the subject.

For this study, we first produced a validated baseline (preoperative) solution, matching patient-specific clinical measurements on cardiac output, aortic pressure and cervical blood flow¹⁰. Then, the geometry of the preoperative model was modified to construct four postoperative scenarios featuring different Zone 0 endograft designs, representing the currently available branched endograft options for total endovascular repair of the aortic arch³. All scenarios were run with the same inflow and outflow boundary conditions. Using this two-step approach, we can quantify

hemodynamic alterations induced by the different endograft designs based on the physical laws of fluid dynamics.

The preoperative patient-specific geometric model was built from the CTA image data using the validated custom software package CRIMSON.¹³ The preoperative model and the four endovascular repair scenarios are presented in Figure 1. A summary of the specifications of the endograft designs is listed in Table 1. All Zone 0 endovascular repair models included an extra-anatomical bypass from the left common carotid artery LCCA to the left subclavian artery (LSA) (8-mm diameter).

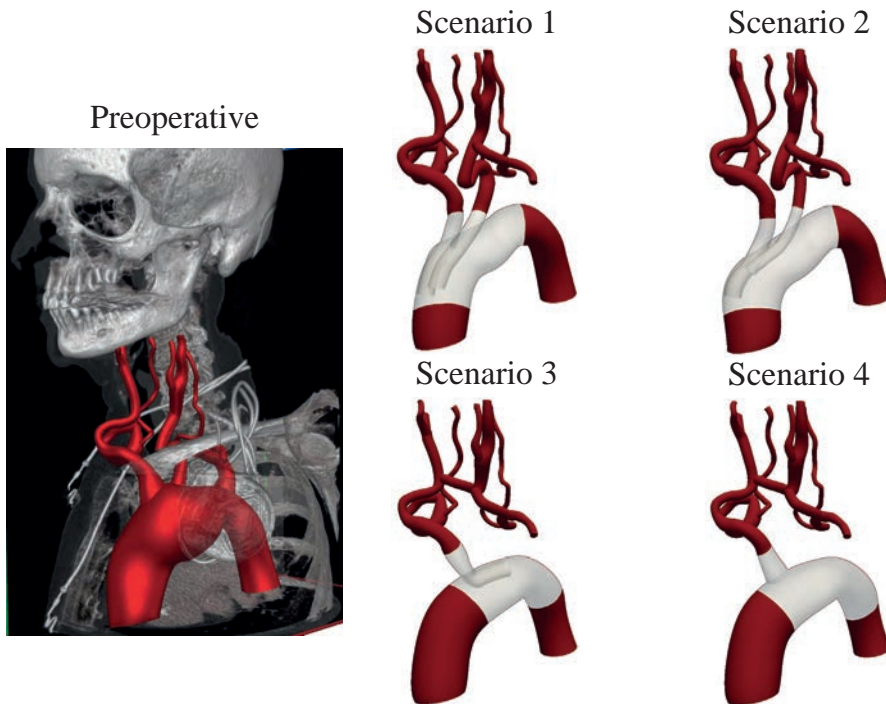


Figure 1. Geometric models of the preoperative situation and four endovascular repair scenarios.

Table 1. Specifications of Endograft Designs

Scenario	Number of Branches	Branch Orientation	Dimensions Inner Branch to BCT (mm)	Dimensions Inner Branch to LCCA (mm)
1	2	Antegrade	12x44	12x40
2	2	Antegrade	12x21	8x21
3	1	Retrograde	12x25	N/A
4	1	Cranial	N/A	N/A

Dimensions of the inner branches are given in diameter \times length. BCT = brachiocephalic trunk; LCCA = left common carotid artery.

Scenario 1 used an endograft with two antegrade inner branches of equal diameter positioned side-by-side, carrying blood flow to the BCT and LCCA. Scenario 2 also featured an endograft with two antegrade inner branches, however the inner branch to the LCCA had a smaller diameter and was positioned oblique behind the inner branch to the BCT. Scenario 3 used an endograft with a single retrograde inner branch carrying flow to the BCT, combined with an extra-anatomical bypass from the right common carotid artery (RCCA) to the LCCA (8-mm diameter). Lastly, scenario 4 used an endograft with a single volcano-shaped branch redirecting flow to the BCT, combined with an extra-anatomical bypass from the RCCA to the LCCA (8-mm diameter).

To solve the blood flow equations, a computational mesh is required. The mesh breaks down the anatomical model into many small elements. The resolution of the mesh must be such that it captures the complex velocity patterns near and around the branches of the device and the vessel walls. Therefore, automatic mesh refinement procedures¹⁴ were used to capture such hemodynamics. Figure 2 presents a cut-through view of the mesh with the total number of elements noted for each model. The models with inner branches (scenarios 1, 2 and 3) required significantly more elements to produce similar accuracy as the preoperative and scenario 4 models.

Blood was modeled as a Newtonian fluid with a density of $1,060 \text{ kg/m}^3$ and a dynamic viscosity of $0.004 \text{ Pa}\cdot\text{s}$. The vessel walls were modeled as rigid. A volumetric flow waveform was imposed at the inflow face of the ascending aorta using echocardiography data, adjusted to match the cardiac output measured during cardiac catheterization via the Fick principle.¹¹ As outflow boundary conditions, three-element Windkessel models were specified representing the behavior of the distal vascular bed at each outlet.¹⁵ A three-element Windkessel model consists of three parameters: a proximal resistor, capacitor, and distal resistor. The numerical values of these parameters were tuned to match the clinical measurements from duplex Doppler ultrasonography and cardiac catheterization. The choice for this type of boundary condition was motivated by the fact that in virtual surgical planning no direct measurements of postoperative flow and pressure are typically available. Furthermore, due to the lack of patient-specific flow measurements at the left and right subclavian arteries, we assigned previously reported flow rates measuring 6% of the cardiac output to each subclavian artery.¹⁶

Computations were performed using the CRIMSON incompressible Navier-Stokes flow solver on 80 cores at the University of Michigan High Performance Computing (HPC) cluster ConFlux. Typical computational time was 24 hours per cardiac cycle, varying depending on the number of elements in the mesh.

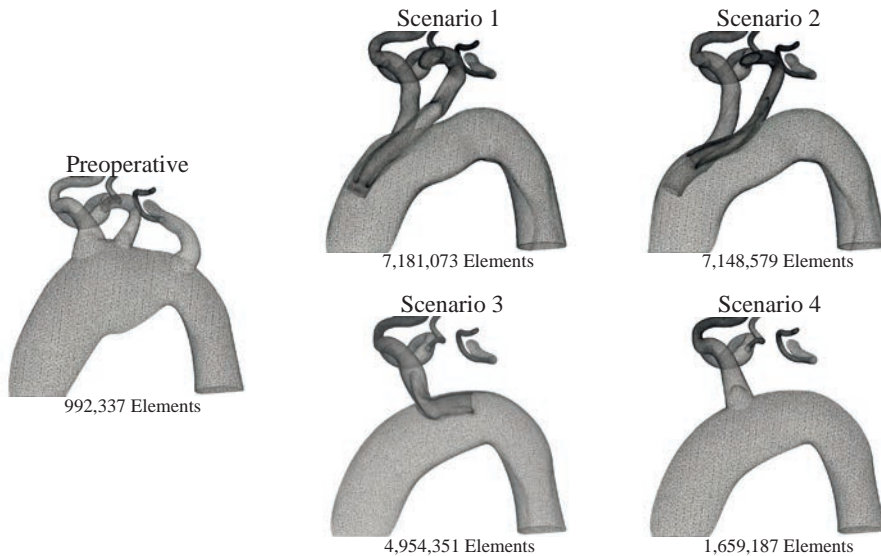


Figure 2. Computational mesh refinement near the supra-aortic arteries in the preoperative anatomy (left) and in the four endovascular repair scenarios (right). Mesh refinement is needed to capture complex hemodynamics around the inner branches. Therefore, the postoperative cases have computational meshes with more elements, leading to higher computational costs.

Particle Tracking and Platelet Activation Potential

In addition to quantifying flow and pressure waveforms in the cervical arteries for the different scenarios, we were interested in assessing the risk of thrombus formation relative to the preoperative configuration. It is well known that high blood shear rates lead to platelet activation and can trigger thrombus formation.^{17,18} Therefore, we used a CFD tool called ‘particle tracking’ which enables tracing the path of thousands of blood particles as they move through the aorta and endograft. We can then calculate a metric known as “platelet activation potential” (PLAP),^{19,20} which has been recently linked to thrombus formation in thoracic and abdominal aortic flows.^{8,20} The PLAP metric is a dimensionless scalar quantifying accumulated blood shear rate. Using PLAP, the impact of endograft-induced shear distortion can be compared between the different virtual endovascular repair scenarios. In this work, 110,000 particles were injected at the ascending aorta and collected in virtual spheres at the outflows of the supra-aortic arteries (Figure 3).

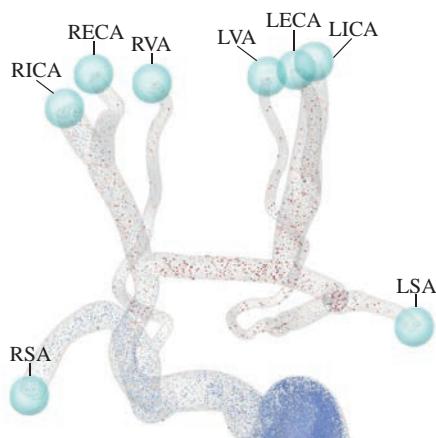


Figure 3. Representation of the virtual spheres used to capture particles leaving the domain through each vessel, enabling calculation of average PLAP values for each of the supra-aortic arteries. LECA = left external carotid artery; LICA = left internal carotid artery; LSA = left subclavian artery; LVA = left vertebral artery; PLAP = platelet activation potential; RECA = right external carotid artery; RICA = right internal carotid artery; RSA = right subclavian artery; RVA = right vertebral artery.

Results

Flow and Pressure Waveforms in the Preoperative Model

The preoperative simulation successfully reproduced the clinical data of the patient. Figure 4 presents the computed preoperative flow and pressure waveforms and a comparison between clinical data and computation results at selected locations. All computed flow and pressure values lie within 5% of the clinical data.

Impact of Endograft Design on Cervical Blood Flow

Table 2 presents the computed mean flow for the preoperative and four endovascular repair scenarios. Blood flow to the right hemisphere (RHS) was calculated as the sum of the flows through the right internal carotid artery, right external carotid artery and right vertebral artery. Similarly, blood flow to the left hemisphere (LHS) was calculated as the sum of the flows through left internal carotid artery, left external carotid artery and left vertebral artery. Total cervical blood flow (CBF) was calculated as the sum of LHS and RHS flows.

Total CBF was reduced in all endovascular repair scenarios, double branch scenarios performed better compared to single branch alternatives (CBF changes of -1.4% and -2.0% for scenarios 1 and 2 versus -4.8% and -3.6% in scenarios 3 and 4, respectively). Blood flow to the LHS decreased more compared to RHS flow in all repair scenarios. Again, scenarios with a double branch endograft performed better compared to the single branch alternatives (LHS flow changes of -2.3% and -3.4% in scenarios 1 and 2 versus -6.7% and -5.6% in scenarios 3 and 4, respectively).

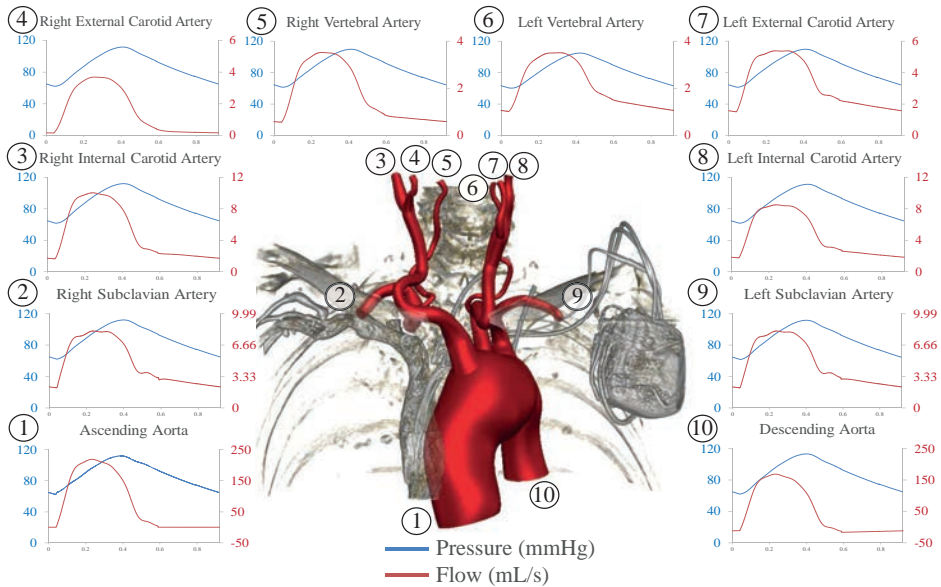


Figure 4. Top: Pressure (blue lines) and flow (red lines) waveforms at the inlet (ascending aorta) and all outlets of the preoperative model. The location of each measurement is denoted by a number. Bottom: Comparison between measured and computed blood flows and pressures in the preoperative model, with percentage differences between the two shown.

Impact of Endograft Design on Blood Shear Rate

PLAP metrics were computed following injection and tracking of particles during ten cardiac cycles. Average PLAP was calculated at the outflows of the cervical arteries. Significant differences in PLAP were revealed between the different endovascular repair scenarios. Table 3 summarizes the calculated mean PLAP values for all scenarios. Figure 5 presents a qualitative comparison of PLAP maps, showing color-coded advected particles 2.4 seconds after virtual injection.

Table 2. Simulated Mean Flow Values (mL/min)

	Preoperative	Scenario 1	Scenario 2	Scenario 3	Scenario 4
Ascending Aorta	4,665	4,665	4,665	4,665	4,665
Right Subclavian Artery	283	280	280	282	286
Right External Carotid Artery	90	90	90	87	88
Right Internal Carotid Artery	296	294	295	287	290
Right Vertebral Artery	104	103	104	104	105
Left Vertebral Artery	126	120	119	117	118
Left Internal Carotid Artery	272	269	266	255	258
Left External Carotid Artery	192	188	186	179	181
Left Subclavian Artery	284	273	270	264	267
Descending Aorta	3,019	3,053	3,059	3,093	3,072
Mean Flow to RHS	490	488 (-0.4%)	488 (-0.3%)	477 (-2.5%)	483 (-1.3%)
Mean Flow to LHS	591	577 (-2.3%)	570 (-3.4%)	551 (-6.7%)	558 (-5.6%)
Total Mean CBF	1,080	1,065 (-1.4%)	1,059 (-2.0%)	1,029 (-4.8%)	1,041 (-3.6%)

CBF = cervical blood flow; LHS = left hemisphere; RHS = right hemisphere

Mean PLAP was increased in all endovascular repair scenarios compared to the preoperative situation. Scenario 1 performed best with a mean PLAP increase of 14.7% in the cervical arteries. Scenario 3 performed worst with a mean PLAP increase of 74.3%. The endograft used in Scenario 3 has a single retrograde inner branch which necessitates all blood that flows to the supra-aortic arteries to make a U-turn in the aortic arch and pass through the single outlet, increasing blood shear rates.

Table 3. Calculated Mean PLAP Values at the Outflow Branches

	Preoperative	Scenario 1	Scenario 2	Scenario 3	Scenario 4
Right Subclavian Artery	106.42	109.67	120.08	164.08	125.43
Right External Carotid Artery	129.66	132.22	129.05	200.53	181.34
Right Internal Carotid Artery	119.53	105.49	110.57	188.82	162.98
Right Vertebral Artery	173.87	182.98	192.51	238.05	201.29
Left Vertebral Artery	218.15	340.34	388.18	427.16	361.87
Left Internal Carotid Artery	127.89	135.04	170.37	261.69	214.74
Left External Carotid Artery	141.37	147.89	183.29	270.89	230.30
Left Subclavian Artery	108.31	153.45	202.50	263.17	219.48
Descending Aorta	78.80	60.13	70.06	67.86	61.15
Mean PLAP cervical arteries	151.75	173.99 (+14.7%)	195.66 (+28.9%)	264.52 (+74.3%)	225.42 (+48.6%)

PLAP = platelet activation potential

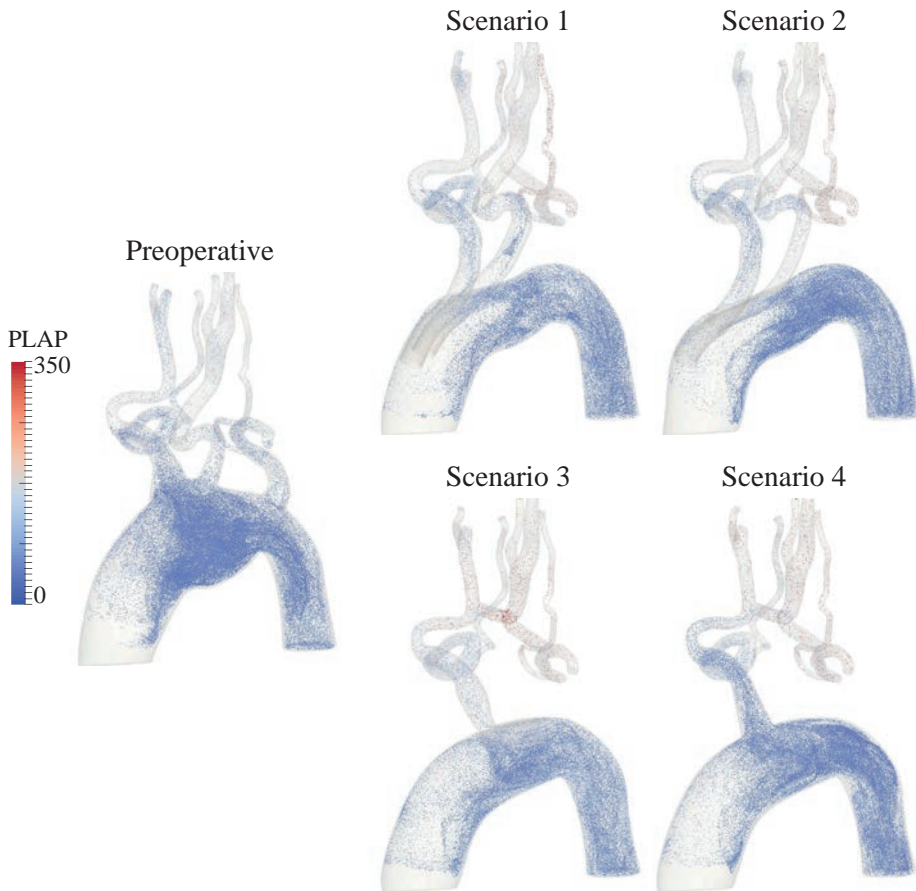


Figure 5. The image visualizes the position and platelet activation potential (PLAP) values, representing the amount of accumulated blood shear rate, of particles 2.4 seconds after virtual injection at the ascending aorta for all scenarios. All postoperative scenarios show elevated values of shear rate in the supra-aortic arteries compared to the preoperative situation. Furthermore, Scenarios 3 and 4 present higher values of blood shear rate in the cervical arteries compared to Scenarios 1 and 2.

Discussion

Multiple manufacturers are developing branched endografts for Zone 0 deployment, enabling total endovascular repair of the aortic arch. These devices extend the armamentarium for treatment of aortic arch pathologies, providing a solution for patients unfit for open surgical repair. The present study aimed to compare the postoperative hemodynamic performance of different endograft designs for Zone 0 endovascular aortic repair using advanced computational modeling analyses. This approach enables studying detailed hemodynamic indices without the need of performing invasive interventions in diseased patients. Furthermore, it facilitates

virtual testing of different treatment scenarios in the same patient in a controlled setting. Hemodynamic performance was quantified for the different endograft designs by calculating changes in total cervical blood flow and average blood shear rate in the cervical arteries.

The use of double branch endografts, with two antegrade inner branches, resulted in smaller reductions in cervical blood flow compared to single branched alternatives (-1.4% and -2.0% versus -4.8% and -3.6%, respectively). When differential changes in blood flow to the RHS and LHS were calculated, blood flow to the LHS experienced the largest reduction in all endovascular repair scenarios (up to -6.7% in Scenario 3). This finding underlines the need for assessment of the Circle of Willis before performing total endovascular aortic arch repair, as normal anatomy with a complete circle is present in only 28% of the population.²¹ Most frequent anatomical variations include hypoplasia of the posterior communicators (22%) and absence or hypoplasia of either the A1 segment of the anterior cerebral artery (25%) or the posterior communicator (15%).^{22,23} This is valuable information when planning Zone 0 endovascular repair, as patients with incomplete circles cannot compensate a reduction in blood flow to the LHS through redistribution.²¹ Reductions in cerebral blood flow could hypothetically be compensated through cerebral autoregulation, nonetheless this would be the same for all endograft designs. Besides, the target population for these endografts is diseased patients, where reserve capacity for cerebral autoregulation will likely be impaired.^{24,25}

The alterations in blood shear rate were calculated using the so-called PLAP index, which has been related to thrombus formation in aortic flows previously.^{8,20} Both single branch endografts resulted in larger increments in blood shear rates in the cervical arteries compared to the double branch devices (74.3% and 48.6% increase versus 14.7% and 28.9% increase, respectively). The increases in blood shear rate are inherent and mostly unavoidable consequences of the altered morphology of the aorta and supra-aortic arteries following Zone 0 repair.

Reduced perfusion, in combination with increased blood shear rates may have negative long-term consequences, particularly in the cerebral microcirculation. Evidence from epidemiological, clinical and experimental studies indicates that cerebral hypoperfusion and microcirculatory dysfunction plays a critical role in the pathogenesis of many types of vascular cognitive impairment and dementia, including Alzheimer's disease.²⁵⁻²⁷

We hypothesized that Zone 0 endograft design has a significant impact on the postoperative hemodynamic performance, particularly in the cervical arteries. Our results confirm this hypothesis. In the present study, double branch endografts offered better postoperative hemodynamic performance compared to single branch alternatives. We believe that the closer an endograft design is to preserving preop-

erative aortic morphology, the smaller the postoperative hemodynamic disturbances will be.

The advantages of a double branch design highlighted above focus on postoperative hemodynamic performance and may be offset during device deployment. Single branch devices could be easier to deploy, requiring less catheter manipulation in the aortic arch, which is considered to be the main risk factor for perioperative embolic stroke.⁶ On the other hand, single branch devices require an additional extra-anatomical bypass, potentially increasing perioperative risks.⁴

Limitations

The patient that is presented in this study was not treated with any of the studied endografts, making it impossible to relate our computational predictions to in vivo follow-up data. Furthermore, performing the same ‘virtual testing’ analysis in patients with different anatomical features could potentially lead to different postoperative results. However, as the differences in aortic arch anatomy between patients are relatively small compared to the differences between the endograft designs and resulting postoperative morphology, we can say from our experience that the likelihood of obtaining drastically different results among patients is small.

When considering the value of “population-based” analyses, it is important to realize the fundamental differences between these and “patient-specific” analyses. In “population-based” studies, few aspects of the system are known or controlled, and therefore many subjects are needed to extract conclusions. In computational modeling, a “patient-specific” paradigm produces highly detailed results for one specific patient that can be used to identify optimal devices or interventions for that specific patient.¹⁰ The value of this paper is to offer a controlled, “apples-to-apples” comparison between different device designs for the same patient, and as such we are confident that our results are sound, given the extensive validation work done in our code.

All postoperative scenarios were run with equal boundary conditions relative to the preoperative model, meaning that the cardiac output and outflow boundary conditions (i.e., Windkessel parameters) did not change after endovascular intervention and between the different scenarios. These assumptions enable fair comparison of hemodynamics between the endovascular repair scenarios, but their validity has not been determined yet. The endograft alters the postoperative left ventricular afterload due to the much higher stiffness relative to the native aorta, potentially affecting cardiac performance.²⁸ Additionally, the reduced number of postoperative supra-aortic outflow tracts may also contribute to an increase in left ventricular afterload relative to the preoperative conditions. Furthermore, it has been reported previously that devices or catheters inserted in the aorta lead to increases in left ventricular afterload

and ultimately to changes in cardiac performance.²⁹ Besides, following endovascular repair, patients are often prescribed antihypertensive medications, which affect the vascular resistance and may alter cardiac output chronically.

The computations in this work have been carried out assuming a rigid behavior for the arterial wall. Simulating the interactions between blood flow and vessel wall motion is possible,³⁰ but it would increase computational cost significantly without altering the observed differences in hemodynamics between the different endograft designs. Of note, all computed flow and pressure values lied within 5% of the clinical data in the preoperative simulation.

Conclusions

Double branch Zone 0 endograft designs offer superior postoperative hemodynamic performance compared to single branch alternatives for total endovascular aortic arch repair, minimizing reductions in cervical blood flow and alterations in blood shear rate that could potentially lead to cerebral ischemic events. Reductions in cervical blood flow might be particularly problematic in patients with an incomplete Circle of Willis, where reductions in blood flow to the LHS cannot be compensated through redistribution.

CFD provides a powerful tool to enhance our understanding of hemodynamics in complex aortic anatomies and optimize the design and planning of advanced endovascular procedures.

References

- 1 Patel HJ, Deeb MG. Ascending and arch aorta pathology, natural history, and treatment. *Circulation* 2008;188–95. Doi: 10.1161/CIRCULATIONAHA.107.690933.
- 2 Lioupis C, Abraham CZ. Results and challenges for the endovascular repair of aortic arch aneurysms. *Perspect Vasc Surg Endovasc Ther* 2011;23(3):202–13. Doi: 10.1177/1531003511413608.
- 3 Anthony Lee W. Status of Branched Grafts for Thoracic Aortic Arch Endovascular Repair. *Semin Vasc Surg* 2016:84–9. Doi: 10.1053/j.semvascsurg.2016.06.006.
- 4 Andradi TB, Grossmann M, Zenker D, et al. Supra-aortic interventions for endovascular exclusion of the entire aortic arch. *J Vasc Surg* 2017;66(1):281–297.e2. Doi: 10.1016/j.jvs.2017.04.024.
- 5 Spear R, Haulon S, Ohki T, et al. Editor's Choice - Subsequent Results for Arch Aneurysm Repair with Inner Branched Endografts. *European Journal of Vascular and Endovascular Surgery*, vol. 51. 2016. pp. 380–5.
- 6 Ullery BW, McCarvey M, Cheung AT, et al. Vascular distribution of stroke and its relationship to perioperative mortality and neurologic outcome after thoracic endovascular aortic repair. *J Vasc Surg* 2012;56(6):1510–7. Doi: 10.1016/j.jvs.2012.05.086.

- 7 Melissano G, Tshomba Y, Bertoglio L, et al. Analysis of stroke after TEVAR involving the aortic arch. *Eur J Vasc Endovasc Surg* 2012;43(3):269–75. Doi: 10.1016/j.ejvs.2011.12.009.
- 8 Nauta FJ, Lau KD, Arthurs CJ, et al. Computational Fluid Dynamics and Aortic Thrombus Formation Following Thoracic Endovascular Aortic Repair. *Ann Thorac Surg* 2017. Doi: 10.1016/j.athoracsur.2016.09.067.
- 9 Arthurs CJ, Agarwal P, John A V., et al. Reproducing Patient-Specific Hemodynamics in the Blalock–Taussig Circulation Using a Flexible Multi-Domain Simulation Framework: Applications for Optimal Shunt Design. *Front Pediatr* 2017;5:78. Doi: 10.3389/fped.2017.00078.
- 10 van Bakel TMJ, Lau KD, Hirsch-Romano J, et al. Patient-Specific Modeling of Hemodynamics: Supporting Surgical Planning in a Fontan Circulation Correction. *J Cardiovasc Transl Res* 2018;11(2):145–55. Doi: 10.1007/s12265-017-9781-x.
- 11 Fagard R, Conway J. Measurement of cardiac output: Fick principle using catheterization. *Eur Heart J* 1990;11(suppl I):1–5. Doi: 10.1093/eurheartj/11.suppl_1.1.
- 12 Taylor CA, Figueroa CA. Patient-specific modeling of cardiovascular mechanics. *Annu Rev Biomed Eng* 2009;11:109–34. Doi: 10.1146/annurev.bioeng.10.061807.160521.
- 13 CRIMSON. The software for Cardiovascular Modelling and Simulation. www.crimson.software.
- 14 Sahni O, Müller J, Jansen KE, et al. Efficient anisotropic adaptive discretization of the cardiovascular system. *Comput Methods Appl Mech Eng* 2006;195(41–43):5634–55. Doi: 10.1016/j.cma.2005.10.018.
- 15 Westerhof N, Lankhaar JW, Westerhof BE. The arterial windkessel. *Med Biol Eng Comput* 2009;131–41. Doi: 10.1007/s11517-008-0359-2.
- 16 Lantz BMT, Foerster JM, Link DP, et al. Regional distribution of cardiac output: Normal values in man determined by video dilution technique. *Am J Roentgenol* 1981;137(5):903–7. Doi: 10.2214/ajr.137.5.903.
- 17 Nobili M, Sheriff J, Morbiducci U, et al. Platelet Activation Due to Hemodynamic Shear Stresses: Damage Accumulation Model and Comparison to In Vitro Measurements. *ASAIO J* 2008;54(1):64–72. Doi: 10.1097/MAT.0b013e31815d6898.
- 18 Shankaran H, Alexandridis P, Neelamegham S. Aspects of hydrodynamic shear regulating shear-induced platelet activation and self-association of von Willebrand factor in suspension. *Blood* 2003;101(7):2637–45. Doi: 10.1182/blood-2002-05-1550.
- 19 Shadden SC, Hendabadi S. Potential fluid mechanic pathways of platelet activation. *Biomech Model Mechanobiol* 2013;12(3):467–74. Doi: 10.1007/s10237-012-0417-4.
- 20 Di Achille P, Tellides G, Figueroa CA, et al. A haemodynamic predictor of intraluminal thrombus formation in abdominal aortic aneurysms. *Proc R Soc A Math Phys Eng Sci* 2014;470(2172):20140163–20140163. Doi: 10.1098/rspa.2014.0163.
- 21 Karatas A, Coban G, Cinar C, et al. Assessment of the Circle of Willis with Cranial Tomography Angiography. *Med Sci Monit* 2015;21:2647–52. Doi: 10.12659/MSM.894322.
- 22 Riggs H, Rupp C. Variation in Form of Circle of Willis. The Relation of the Variations to Collateral Circulation: Anatomic Analysis. *Arch Neurol* 1962;8:24–30. Doi: 10.1001/archneur.1963.00460010024002.
- 23 Fabian TC. Blunt cerebrovascular injuries: Anatomic and pathologic heterogeneity create management enigmas. *J Am Coll Surg* 2013;216(5):873–85. Doi: 10.1016/j.jamcollsurg.2012.12.053.
- 24 Roy B, Woo MA, Wang DJJ, et al. Reduced regional cerebral blood flow in patients with heart failure. *Eur J Heart Fail* 2017. Doi: 10.1002/ehf.874.

- 25 Toth P, Tarantini S, Csiszar A, et al. Functional vascular contributions to cognitive impairment and dementia: mechanisms and consequences of cerebral autoregulatory dysfunction, endothelial impairment, and neurovascular uncoupling in aging. *Am J Physiol Heart Circ Physiol* 2017;312(1):H1–20. Doi: 10.1152/ajpheart.00581.2016.
- 26 Kim HA, Miller AA, Drummond GR, et al. Vascular cognitive impairment and Alzheimer's disease: role of cerebral hypoperfusion and oxidative stress. *Naunyn Schmiedebergs Arch Pharmacol* 2012;385(10):953–9. Doi: 10.1007/s00210-012-0790-7.
- 27 Duncombe J, Kitamura A, Hase Y, et al. Chronic cerebral hypoperfusion: a key mechanism leading to vascular cognitive impairment and dementia. Closing the translational gap between rodent models and human vascular cognitive impairment and dementia. *Clin Sci (Lond)* 2017;131(19):2451–68. Doi: 10.1042/CS20160727.
- 28 Nauta FJH, Kamman A V, Ibrahim E-SH, et al. Assessment of Cardiovascular Remodeling following Endovascular aortic repair through imaging and computation: The CORE prospective observational cohort study protocol. *BMJ Open* 2016;6(11). Doi: 10.1136/bmjopen-2016-012270.
- 29 Cuomo F, Ferruzzi J, Humphrey JD, et al. An Experimental–Computational Study of Catheter Induced Alterations in Pulse Wave Velocity in Anesthetized Mice. *Ann Biomed Eng* 2015;43(7):1555–70. Doi: 10.1007/s10439-015-1272-0.
- 30 Figueroa CA, Vignon-Clementel IE, Jansen KE, et al. A coupled momentum method for modeling blood flow in three-dimensional deformable arteries. *Comput Methods Appl Mech Eng* 2006;195(41–43):5685–706. Doi: 10.1016/j.cma.2005.11.011.

Chapter 7

Patient-Specific Analysis of Renal Artery Flows After Complex Endovascular Aortic Repair

Sabrina Ben Ahmed¹, MD, PhD

Theodorus M.J. van Bakel^{2,3}, MD

Christopher J. Arthurs⁴, DPhil

C. Alberto Figueroa^{1,5}, PhD

1. CHU Clermont-Ferrand, Department of Vascular Surgery, F63003 Clermont-Ferrand, France
2. Department of Surgery, University of Michigan, Ann Arbor, Michigan, USA.
3. Department of Vascular Surgery, University Medical Center Utrecht, Utrecht, The Netherlands.
4. Division of Imaging Sciences and Biomedical Engineering, King's College London, London, UK.
5. Department of Biomedical Engineering, University of Michigan, Ann Arbor, Michigan, USA.

In preparation

Abstract

Objectives

To assess and compare the postoperative haemodynamic performance of branched, fenestrated and parallel stent-grafting solutions for endovascular aortic repair (EVAR) of juxtarenal abdominal aortic aneurysms (AAAs) with renal vascularization.

Methods

We used computational fluid dynamics techniques to calculate detailed haemodynamic indices in three patients that were treated with EVAR for juxtarenal AAAs. For each patient, three models were constructed: (1) preoperative; (2) postoperative; and (3) a virtual EVAR solution. These models included one branched or fenestrated EVAR solution and one parallel stent-grafting solution. Haemodynamic performance was quantified by calculating total blood flow, wall shear stress (WSS) and platelet activation potential (PLAP) in the renal arteries.

Results

Renal blood flow remained constant following all EVAR solutions. The average WSS in the renal arteries was within the homeostatic range for all models. Renal PLAP increased in all patients post-EVAR. Parallel stent-grafting resulted in larger PLAP increments in the renal arteries than branched and fenestrated solutions. This was attributed to the larger extend of intraluminal protrusion of the renal artery stent-grafts into the aorta.

Conclusions

Complex EVAR resulted in aortorenal flow disturbances that potentially contribute to renal stent-graft complications during follow-up. Parallel stent-grafting of the renal arteries resulted in highest PLAP increments, potentially explaining the increased rate of postoperative renal dysfunction associated with parallel stent-grafting compared to branched or fenestrated alternatives.

Introduction

Juxtarenal abdominal aortic aneurysms (AAAs) are deemed unsuitable for conventional endovascular aortic repair (EVAR), because the ostia of the renal arteries are located in the landing zone of the endograft. In the past decades, multiple techniques have been developed that target vascularization of branching vessels, expanding the application of EVAR. Currently, the following complex EVAR solutions are available to vascularize the renal arteries: fenestrated endografts (F-EVAR); branched endografts (B-EVAR); parallel chimney stent-grafts (Ch-EVAR); and parallel periscope stent-grafts (P-EVAR). In F-EVAR, the main endograft has custom fenestrations located at the ostia of the target arteries. Through these fenestrations, stent-grafts are deployed that connect the main endograft to the target arteries. In B-EVAR, the endograft has custom branches that cannulate the target arteries during deployment. Subsequently, stent-grafts are deployed through these branches securing the connection of the main endograft to the target arteries. Ch-EVAR and P-EVAR are off-the-shelf solutions where stent-grafts are deployed parallel to a 'standard' endograft. In Ch-EVAR, these stent-grafts extend from the proximal end of the main endograft. In P-EVAR, these stent-grafts extend from the distal end of the main endograft. P-EVAR is predominantly performed for endovascular repair of thoracoabdominal aneurysms.¹

Although F-EVAR, B-EVAR and parallel stent-graft procedures are all effective modalities to repair AAAs, there are concerns about postoperative kidney function. Indeed, up to 25% of patients has postoperative renal failure,²⁻⁵ and up to 5% requires permanent dialysis.²⁻⁵ Renal artery stenosis and occlusion are the main reasons for postoperative renal failure. Interestingly, these adverse events seem to occur more frequently in patients treated with Ch-EVAR compared to F-EVAR.² We hypothesize that the configuration of the aortorenal connection affects the haemodynamic performance of the different EVAR solutions.

Aortic and renal artery anatomy is unique in every patient. Therefore, it is impossible to make an apples-to-apples comparison of the impact of different EVAR solutions on aortorenal hemodynamics in vivo. Virtual testing, using computational fluid dynamics (CFD) analyses, can fill this void. This technique has been used in various engineering fields, such as aerospace and automotive, to test different designs without the need to manufacture prototypes. Recently, CFD techniques have been used to support clinical decision making through calculation of the haemodynamic performance of different therapeutic interventions using patient-specific image-based modelling.⁶⁻⁸ In the present study, we use CFD techniques to assess and compare the postoperative haemodynamic performance of three different EVAR solutions for renal vascularization in three different patients.

Methods

Approval for this non-interventional retrospective study was obtained from the institutional review board of the University Hospitals of Clermont-Ferrand and Saint-Etienne. As data were treated anonymously, the need for patient consent was waived. The study complied with the principles of the Declaration of Helsinki.

Patient Population

Three patients who were treated for aortic aneurysms using EVAR with renal artery vascularization were selected. Patient 1 is an 84-year-old male with a juxtarenal aneurysm who was treated with F-EVAR. Patient 2 was a 65-year-old male with a juxtarenal aneurysm who was treated with Ch-EVAR. Patient 3 was a 70-year-old man treated with a thoraco-abdominal aneurysm that was treated with B-EVAR.

Patient-Specific Computational Modelling

Computational models were constructed from patient-specific computed tomography angiography (CTA) image data and clinical flow and pressure measurements using the validated cardiovascular modelling and simulation software CRIMSON.⁹ First, geometric models were created by segmenting the fluid domain of interest from the CTA image data. Three models were created for each patient: (1) preoperative; (2) postoperative; and (3) a virtual EVAR solution (VES). The VES model was constructed from the postoperative CTA image data by introducing an EVAR solution different from the one that was used during the actual operation. In total, each patient had one preoperative model, one B-EVAR or F-EVAR model, and one P-EVAR or Ch-EVAR model. All models are presented in Figure 1.

After segmentation, each geometric model was discretized into a computational mesh consisting of millions of tetrahedral elements. The resolution of the mesh was iteratively adapted to capture the complex velocity patterns near and around the stent-grafts and the vessel walls.¹⁰ A mesh independence analysis was performed for each model. Numerical results were deemed mesh-independent when the difference in regional pressures was < 1% between two successive meshes. The mesh size ranged between 6×10^6 and 8×10^6 elements in all models.

Boundary Conditions

Patient-specific volumetric flow waveforms were extracted from duplex Doppler ultrasonography and assigned to the aortic inlet of each model with a Womersley velocity profile.^{11,12} The flow fraction that feeds the supra-aortic and mesenteric arteries was subtracted from the cardiac output. At the outlets, 3-element Windkessel models were assigned that mimic the resistance and capacitance of the distal vasculature of

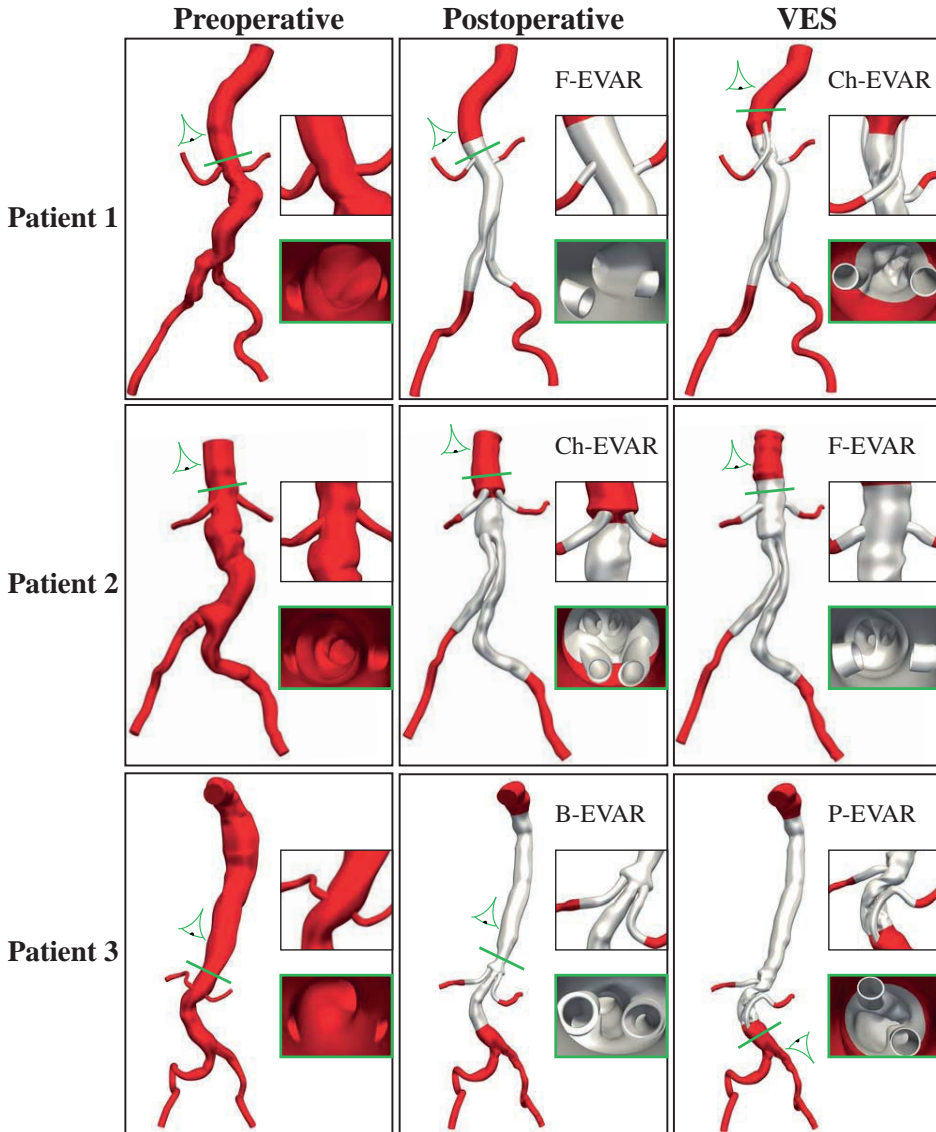


Figure 1. For each patient, three geometric models were constructed: preoperative (left); postoperative (middle); and VES (right). All models are presented with a close-up of the renal artery insertion and intra-aortic view of the renal artery ostia. The luminal area of the arterial walls is shown in red, the surface of the endograft and renal stent-grafts in grey. The green line and eye depict the plane and point of view for the intra-aortic view (delineated in green). B-EVAR = branched endovascular aortic repair; Ch-EVAR = chimney endovascular aortic repair; F-EVAR = fenestrated endovascular aortic repair; P-EVAR = periscope endovascular aortic repair; VES = virtual EVAR solution.

the iliac and renal arteries. To match physiologic resting conditions,^{13,14} 20% of the cardiac output was assigned to the renal arteries. The same boundary conditions

were applied in the three simulations (preoperative, postoperative and VES) for each patient. Simulations were run until cycle-to-cycle periodic solutions were reached, the results from the last cycle are reported.

Computations were performed using the CRIMSON incompressible Navier-Stokes flow solver. The vessel walls were modelled as rigid. Blood was treated as a Newtonian fluid with a dynamic viscosity of 4 mPa.s and a density of 1060 kg/m³.

Data Collection

For each model, systolic pressure (SP), diastolic pressure (DP), pulse pressure (PP), mean pressure (MP) and mean flow (Q_m) were measured at inlet, renal and iliac outlets. Peak velocity was measured at 4 locations in the renal arteries (at the beginning of the stent graft, in the middle of the stent graft, at the end of the stent graft and at 1cm after the stent graft in the native renal artery). Additionally, time-averaged wall shear stress (TAWSS) in the renal arteries was calculated for all models.

Particle Tracking and Platelet Activation Potential

One of our goals was to assess flow disturbances that could lead to thrombus formation in the renal arteries. It is well known that high blood shear rates lead to platelet activation and can trigger thrombus formation.^{15,16} Therefore, we used a CFD tool called 'particle tracking' which allows evaluation of the blood shear rate that a particle experiences along its path within a fluid.¹⁷ From this information, we can calculate a metric known as "platelet activation potential" (PLAP),^{17,18} that has been linked to thrombus formation in thoracic and abdominal aortic flows.^{6,17} For the particle tracking analysis, a bolus with 1 million particles was injected into the aortic inlet. The advected particles were collected after at the outlets of the renal and iliac arteries 10 cardiac cycles, where the average PLAP was calculated from the history of blood shear rates experienced by the collected particles. Using PLAP, the impact of endograft-induced shear distortion was compared between the different EVAR solutions for renal artery vascularization.

Results

Flows and Pressures

The mean flows at the inlet and outlets of all models are reported in Table 1. Minimal differences were calculated in the mean flow rates of the preoperative, postoperative and VES models. Local pressures were recorded at the inlet and outlets in all models, the pressure waveforms are presented in Figure 2.

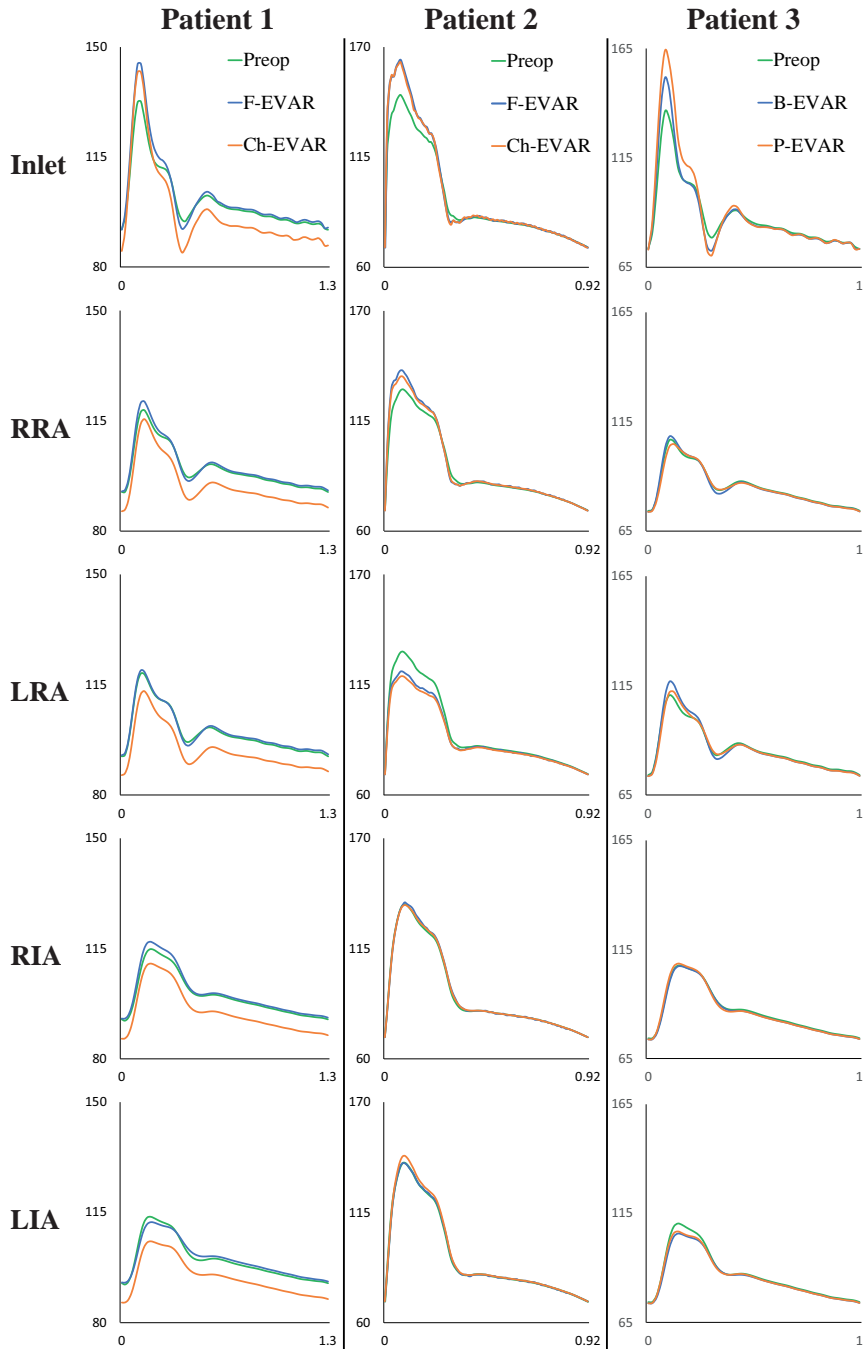


Figure 2. Pressure waveforms (mmHg) from the inlet and outlets of all models. B-EVAR = branched endovascular aortic repair; Ch-EVAR = chimney endovascular aortic repair; F-EVAR = fenestrated endovascular aortic repair; LIA = left iliac artery; LRA = left renal artery; P-EVAR = periscope endovascular aortic repair; preop = preoperative; RIA = right iliac artery; RRA = right renal artery.

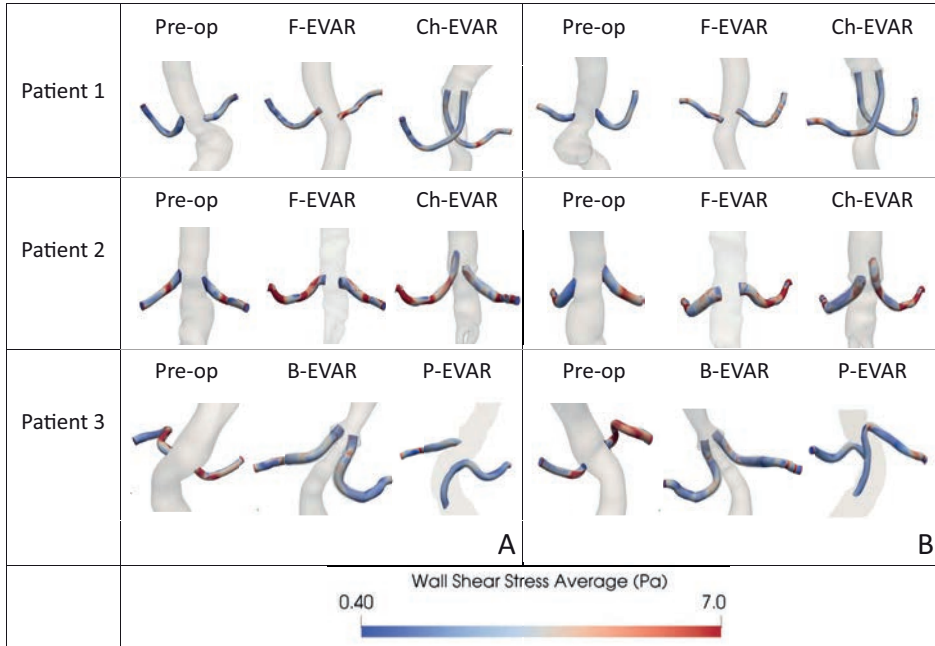


Figure 3. Color-coded TAWSS maps of the renal arteries in all models. For each model, the anterior view is presented on the left (A) and the posterior view is presented on the right (B). TAWSS = time averaged wall shear stress

Table 1. Flows and pressures

	Patient 1			Patient 2			Patient 3		
	Preop	F-EVAR	Ch-EVAR	Preop	Ch-EVAR	F-EVAR	Preop	B-EVAR	P-EVAR
Inlet	2.00	2.00	2.00	2.91	2.91	2.91	2.23	2.23	2.23
Right Renal Artery	0.36	0.36	0.35	0.56	0.57	0.57	0.51	0.51	0.51
Left Renal Artery	0.37	0.36	0.35	0.59	0.57	0.57	0.42	0.43	0.42
Right Iliac Artery	0.63	0.64	0.65	0.80	0.80	0.80	0.69	0.69	0.69
Left Iliac Artery	0.64	0.65	0.65	0.96	0.97	0.97	0.61	0.6	0.61

Mean flow (L/min) at the inlet and outlets for all models. B-EVAR = branched endovascular aortic repair; Ch-EVAR = chimney endovascular aortic repair; F-EVAR = fenestrated endovascular aortic repair; P-EVAR = periscope endovascular aortic repair; Preop = preoperative

Impact of endograft design on TAWSS

The homeostatic range for TAWSS in arteries is approximately 1.0 – 7.0 Pa.¹⁹ Regions exposed to low TAWSS are known to favour cell adhesion and thrombus formation.^{19,20} The mean TAWSS values in the renal arteries are reported in Table 2. In summary, all TAWSS values were within the homeostatic range. Higher TAWSS values were found in the parallel grafting anatomies (Ch-EVAR and P-EVAR) compared to the branched and fenestrated anatomies. Figure 3 presents the TAWSS maps in all

models. Interestingly, focal regions with disturbed TAWSS ($1.0 > \text{TAWSS} > 7.0 \text{ Pa}$) were found in all models.

Table 2. Renal TAWSS in all models

	Patient 1			Patient 2			Patient 3		
	Preop	F-EVAR	Ch-EVAR	Preop	Ch-EVAR	F-EVAR	Preop	B-EVAR	P-EVAR
Entire RRA	2.2	2.5	2.9	3.7	4.5	4.1	4.5	2.5	4.6
Entire LRA	2.7	2.9	3.7	5.0	5.8	5.3	4.1	2.1	5.7
Stented RRA	NA	2.3	2.9	NA	2.9	3.0	NA	2.2	2.9
Stented LRA	NA	2.8	4.9	NA	4.6	3.9	NA	2.2	4.6
Unstented RRA	NA	2.8	2.9	NA	6.1	4.6	NA	3.0	6.1
Unstented LRA	NA	3.2	3.1	NA	7.1	6.6	NA	1.9	7.1

TAWSS values (Pa) in the left and right renal arteries are reported for all models. Separate values were calculated for the stented segments and non-stented segments. All TAWSS values were within the homeostatic range of 1.0 – 7.0 Pa. In all patients, the renal TAWSS were lowest preoperative and highest in the parallel stent-grafting simulations (Ch-EVAR and P-EVAR). B-EVAR = branched endovascular aortic repair; Ch-EVAR = chimney endovascular aortic repair; F-EVAR = fenestrated endovascular aortic repair; LRA = left renal artery; NA = not applicable; P-EVAR = periscope endovascular aortic repair; Preop = preoperative; RRA = right renal artery; TAWSS = Time-averaged wall shear stress.

Impact of endograft design on blood shear rate

Average PLAP values were calculated at the outflows of the renal and iliac arteries. Table 3 presents the mean PLAP values in all models. After EVAR, PLAP increased in the renal arteries in all patients. Ch-EVAR and P-EVAR resulted in higher renal

Table 3. Average blood shear rates at the outlets of in all models

	Patient 1			Patient 2			Patient 3		
	Preop	F-EVAR	Ch-EVAR	Preop	Ch-EVAR	F-EVAR	Preop	B-EVAR	P-EVAR
RRA	72.9	89.5 (+23%)	98.9 (+36%)	53.5	78.8 (+47%)	64.7 (+21%)	115.4	112.9 (-2%)	219.7 (+90%)
LRA	88.3	91.6 (+4%)	101.8 (+15%)	39.9	84.0 (+111%)	68.5 (+72%)	55.1	90.0 (+63%)	196.8 (+257%)
RIA	251.6	222.4 (-12%)	253.3 (+1%)	160.4	168.7 (+5%)	166.15 (+4%)	200.1	240.7 (+20%)	267.9 (+34%)
LIA	221.3	201.6 (-9%)	237.5 (+7%)	165.4	166.15 (+3%)	191.4 (+16%)	196.7	223.7 (+14%)	258.7 (+31%)

Mean PLAP values at the outlets of all models are reported. In the post-EVAR models, the change in PLAP relative to the preoperative value is given within brackets. PLAP increased in all patients post-EVAR. Parallel stent-grafting (Ch-EVAR and P-EVAR) resulted in larger PLAP increments in the renal arteries compared to B-EVAR and F-EVAR. B-EVAR = branched endovascular aortic repair; Ch-EVAR = chimney endovascular aortic repair; F-EVAR = fenestrated endovascular aortic repair; LIA = left iliac artery; LRA = left renal artery; P-EVAR = periscope endovascular aortic repair; PLAP = platelet activation potential; RIA = right iliac artery; RRA = right renal artery

PLAP values than B-EVAR and F-EVAR. The P-EVAR simulation in patient 3 resulted in the highest renal PLAP increment compared to preoperative (+257%). Following

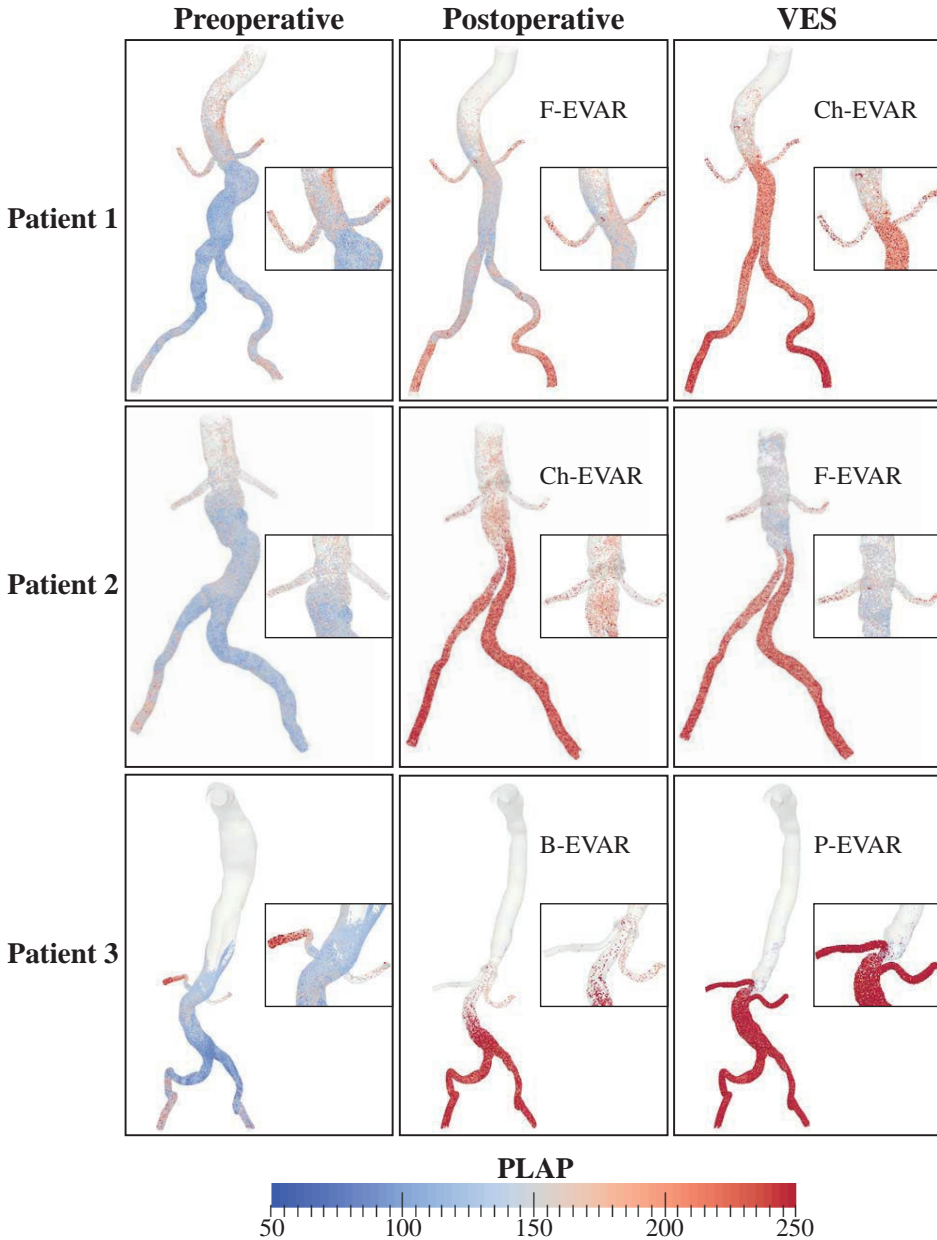


Figure 4. PLAP maps with a close-up near the renal arteries are presented for each model, 4.6 s after virtual injection. The particles in the image are color-coded for their PLAP values, representing the amount of accumulated blood shear rate. Parallel stent-grafting (Ch-EVAR and P-EVAR) resulted in higher PLAP values compared to the F-EVAR and B-EVAR. PLAP = platelet activation potential.

P-EVAR, blood makes a U-turn in the abdominal aorta to enter the parallel renal stent-grafts, resulting in disturbed flows with high blood shear rates. B-EVAR in patient 3 resulted in a markedly smaller postoperative PLAP increment (+63%). A qualitative comparison of the PLAP maps in all models is presented in Figure 4.

Discussion

Complex EVAR is increasingly being used to treat AAAs unsuitable for conventional EVAR. For juxtarenal AAAs, physicians have the option to vascularize the renal arteries endovascularly using F-EVAR, B-EVAR or parallel stent-grafting solutions. Currently, endografts for F-EVAR and B-EVAR are custom made and require six to eight weeks to be manufactured, limiting their applicability to elective cases. Parallel stent-grafting techniques (Ch-EVAR and P-EVAR) enable renal artery vascularization using readily available devices, enabling endovascular repair of emergent cases.

Complex EVAR procedures offer a minimally invasive alternative for open surgical repair of juxtarenal AAAs, however, postoperative renal dysfunction often occurs. Deterioration of renal function after complex EVAR has been attributed to the endovascular procedure itself, which is associated with increased use of nephrotoxic contrast agents, guidewire manipulation in the renal arteries, and risk of renal artery stent-graft kinking.⁵ During follow-up, renal dysfunction can be caused by different processes that compromise patency of the renal arteries, such as arterial inflammation, neointimal hyperplasia and thrombus formation. It is well known that disturbed blood flow and abnormal wall shear stresses contribute to the occurrence of intimal hyperplasia²¹ and thrombus formation.^{15,16} These postoperative renal complications seem to occur more frequently following Ch-EVAR than F-EVAR.² It is unclear if this discrepancy could be attributed to differences in postoperative aortorenal configuration following Ch-EVAR and F-EVAR.

The objective of the present study was to assess and compare the postoperative haemodynamic performance of different EVAR solutions for juxtarenal AAAs with renal vascularization. We used advanced computational modelling techniques to calculate detailed haemodynamic indices without the need of performing invasive interventions in three patients. Furthermore, this approach facilitated virtual testing of multiple EVAR solutions in each patient in a highly controlled setting.

Haemodynamic performance was quantified for the different EVAR solutions by calculating total blood flow, TAWSS and average blood shear rate in the renal arteries. Renal blood flow remained constant following all EVAR solutions. The average TAWSS in the renal arteries was within the homeostatic range for all models, however, focal areas of elevated and reduced TAWSS were found in each model. Renal

PLAP increased in all patients post-EVAR. This was attributed to aortorenal flow disturbances that are caused by stent-graft protrusion into the aortic lumen. Parallel stent-grafting of the renal arteries (Ch-EVAR and P-EVAR) resulted in larger PLAP increments in the renal arteries than B-EVAR and F-EVAR. This is most likely caused by the larger extent of the intra-aortic segment of the parallel stent-graft.

Our results reveal that there are significant differences between the postoperative hemodynamic performance of different EVAR solutions for renal vascularization. We hypothesize that locally disturbed TAWSS in combination with increased blood shear rates could cause intimal hyperplasia and thrombosis. This would explain the increased occurrence of renal dysfunction following parallel stent-grafting compared to F-EVAR.

Patient-specific CFD modelling enables detailed, highly controllable, non-invasive testing of different complex EVAR solutions that can aid surgical planning and device development. Further research is needed to correlate the results from CFD analyses with postoperative clinical outcomes in a larger patient population.

Limitations

The analysis was performed with a total of nine models from three patients. As the differences in abdominal aortic anatomy between patients were relatively small compared to the geometric differences between the different EVAR solutions for renal vascularization, the outcomes in terms of hemodynamic performance were very similar between patients. Performing the same analysis in a larger patient cohort would increase generalizability of our results.

The VES models were built based on the post-EVAR anatomy and surgical experience of the authors. The configuration of the VES models would potentially have been different if they were constructed by different surgeons.

The computational analyses in this study were conducted with the assumption that the walls of the geometric models were rigid. Simulating hemodynamics with a deformable wall is possible, however, this dramatically increases computational costs.²² As the endograft material is relatively stiff, and does not change between the different EVAR solutions, we do not expect that this assumption alters our findings.

The patients presented in this study did not have renal dysfunction following the EVAR procedure. Therefore, it was not possible to relate our computational results to renal complications. Future prospective cohort studies should be conducted to analyse the correlation between calculated hemodynamic performance and postoperative renal function.

Conclusion

Complex EVAR resulted in aortorenal flow changes that could potentially contribute to renal dysfunction during follow-up. Parallel stent-grafting of the renal arteries resulted in highest blood shear rates, potentially explaining the increased rate of postoperative renal dysfunction compared to branched and fenestrated alternatives. The present study underlines the value of patient-specific computational modelling to aid surgical planning and device development for complex EVAR. Prospective studies with more patients are needed to verify our computational results with clinical outcomes.

References

- 1 Wilson A, Zhou S, Bachoo P, et al. Systematic review of chimney and periscope grafts for endovascular aneurysm repair. *BJS* 2013;100(12):1557–64. Doi: 10.1002/bjs.9274.
- 2 Li Y, Hu Z, Bai C, et al. Fenestrated and Chimney Technique for Juxtarenal Aortic Aneurysm: A Systematic Review and Pooled Data Analysis. *Sci Rep* 2016;6:20497. Doi: 10.1038/srep20497.
- 3 Martin-Gonzalez T, Pinçon C, Hertault A, et al. Renal outcomes analysis after endovascular and open aortic aneurysm repair. *J Vasc Surg* 2015;62(3):569–77. Doi: 10.1016/j.jvs.2015.03.075.
- 4 Reilly LM, Rapp JH, Grenon SM, et al. Efficacy and durability of endovascular thoracoabdominal aortic aneurysm repair using the caudally directed cuff technique. *J Vasc Surg* 2012;56(1):53–64. Doi: 10.1016/j.jvs.2012.01.006.
- 5 Tran K, Fajardo A, Ullery BW, et al. Renal function changes after fenestrated endovascular aneurysm repair. *J Vasc Surg* 2016;64(2):273–80. Doi: 10.1016/j.jvs.2016.01.041.
- 6 Nauta FJ, Lau KD, Arthurs CJ, et al. Computational Fluid Dynamics and Aortic Thrombus Formation Following Thoracic Endovascular Aortic Repair. *Ann Thorac Surg* 2017. Doi: 10.1016/j.athoracsur.2016.09.067.
- 7 van Bakel TM, de Beaufort HW, Trimarchi S, et al. Status of branched endovascular aortic arch repair. *Ann Cardiothorac Surg* 2018;7(3):406–13. Doi: 10.21037/acs.2018.03.13.
- 8 van Bakel TM, Arthurs CJ, van Herwaarden JA, et al. A computational analysis of different endograft designs for Zone 0 aortic arch repair. *Eur J Cardio-Thorac Surg* 2018;54(2):389–96. Doi: 10.1093/ejcts/ezy068.
- 9 Cardiovascular Integrated Modelling and Simulation (CRIMSON). Available from: <http://www.crimson.software/> n.d.
- 10 Sahni O, Müller J, Jansen KE, et al. Efficient anisotropic adaptive discretization of the cardiovascular system. *Comput Methods Appl Mech Eng* 2006;195(41–43):5634–55. Doi: 10.1016/j.cma.2005.10.018.
- 11 Odenstedt H, Åneman A, Oi Y, et al. Descending aortic blood flow and cardiac output: A clinical and experimental study of continuous oesophageal echo-Doppler flowmetry: Monitoring of descending aortic blood flow. *Acta Anaesthesiol Scand* 2001;45(2):180–7. Doi: 10.1034/j.1399-6576.2001.450208.x.

- 12 Osinnski JN, Ku DN, Mukundan S, et al. Determination of wall shear stress in the aorta with the use of MR phase velocity mapping. *J Magn Reson Imaging* 1995;5(6):640–7. Doi: 10.1002/jmri.1880050605.
- 13 Moore J, Ku DN. Pulsatile Velocity Measurements in a Model of the Human Abdominal Aorta Under Resting Conditions. *J Biomech Eng* 1994;116(3):337–46. Doi: 10.1115/1.2895740.
- 14 Williams LR, Leggett RW. Reference values for resting blood flow to organs of man. *Clin Phys Physiol Meas* 1989;10(3):187–217. Doi: 10.1088/0143-0815/10/3/001.
- 15 Nobili M, Sheriff J, Morbiducci U, et al. Platelet Activation Due to Hemodynamic Shear Stresses: Damage Accumulation Model and Comparison to In Vitro Measurements. *ASAIO J* 2008;54(1):64–72. Doi: 10.1097/MAT.0b013e31815d6898.
- 16 Shankaran H, Alexandridis P, Neelamegham S. Aspects of hydrodynamic shear regulating shear-induced platelet activation and self-association of von Willebrand factor in suspension. *Blood* 2003;101(7):2637–45. Doi: 10.1182/blood-2002-05-1550.
- 17 Di Achille P, Tellides G, Figueroa CA, et al. A haemodynamic predictor of intraluminal thrombus formation in abdominal aortic aneurysms. *Proc R Soc A Math Phys Eng Sci* 2014;470(2172):20140163–20140163. Doi: 10.1098/rspa.2014.0163.
- 18 Shadden SC, Hendabadi S. Potential fluid mechanic pathways of platelet activation. *Biomech Model Mechanobiol* 2013;12(3):467–74. Doi: 10.1007/s10237-012-0417-4.
- 19 Chiu J-J, Chien S. Effects of disturbed flow on vascular endothelium: pathophysiological basis and clinical perspectives. *Physiol Rev* 2011;91(1):327–87. Doi: 10.1152/physrev.00047.2009.
- 20 Jackson M, Wood NB, Zhao S, et al. Low wall shear stress predicts subsequent development of wall hypertrophy in lower limb bypass grafts. *Artery Res* 2009;3(1):32–8. Doi: 10.1016/j.artres.2009.01.001.
- 21 Humphrey JD, Schwartz MA, Tellides G, et al. Role of mechanotransduction in vascular biology: Focus on thoracic aortic aneurysms and dissections. *Circ Res* 2015;1448–61. Doi: 10.1161/CIRCRESAHA.114.304936.
- 22 Figueroa CA, Vignon-Clementel IE, Jansen KE, et al. A coupled momentum method for modeling blood flow in three-dimensional deformable arteries. *Comput Methods Appl Mech Eng* 2006;195(41–43):5685–706. Doi: 10.1016/j.cma.2005.11.011.

Chapter 8

The Modified Arch Landing Areas Nomenclature (MALAN) improves prediction of stent graft displacement forces: proof of concept by computational fluid dynamics modeling

Massimiliano M. Marrocco-Trischitta^{1,2}, MD

Theodorus M.J. van Bakel², MD

Rodrigo M. Romarowski³, PhD

Hector W.L. de Beaufort², MD, PhD

Michele Conti⁴, PhD

Joost A. van Herwaarden⁵, MD, PhD

Frans L. Moll⁵, MD, PhD

Ferdinando Auricchio⁴, PhD

Santi Trimarchi^{1,2,6}, MD, PhD

1. Division of Vascular Surgery II, Policlinico San Donato IRCCS, San Donato Milanese, Italy

2. Thoracic Aortic Research Center, Policlinico San Donato IRCCS, San Donato Milanese, Italy.

3. 3D and Computer Simulation Laboratory, Policlinico San Donato IRCCS, San Donato Milanese, Italy

4. Department of Civil Engineering and Architecture, University of Pavia, Pavia, Italy

5. Department of Vascular Surgery, University Medical Center Utrecht, Utrecht, The Netherlands.

6. Department of Biomedical Sciences for Health, University of Milan, Milan, Italy

European Journal of Vascular and Endovascular Surgery. 2018;55:584-592

Abstract

Objective

To assess whether the Modified Arch Landing Areas Nomenclature (MALAN), which merges Ishimaru's map with the Aortic Arch Classification, predicts displacement forces magnitude and orientation in proximal landing zones for TEVAR.

Methods

Computational fluid dynamic (CFD) modelling was employed to prove our hypothesis. Healthy aortas CT angiography scans were selected based on aortic arch geometry to reflect Type of arch I to III equally (each n=5). CFDs were used to compute pulsatile displacement forces along the Ishimaru's landing zones in each aorta including their three dimensional orientation along upward component and sideways component. Values were normalized to the corresponding aortic wall area to calculate equivalent surface traction (EST).

Results

In Type I and Type II arches, EST did not change across proximal landing zones ($P=.297$ and $P=.054$ respectively), whereas within Type III, EST increased towards more distal landing zones ($P=.019$). Comparison of EST between adjacent zones, however, showed that EST was greater in 3/II than in 2/II ($P=.016$), and in 3/III than in 2/III ($P=.016$). Notably, these differences were related the upward component, that was four times greater in 3/II compared to 2/II ($P<.001$), and five times greater in 3/III compared to 2/III ($P<.001$).

Conclusion

CFD modeling suggests that MALAN improves discrimination of expected displacement forces in proximal landing zones for TEVAR, which might influence clinical outcomes. The clinical relevance of our finding, however, remains to be validated in a dedicated postoperative outcome analysis of patients treated with TEVAR of the arch.

Introduction

Thoracic endovascular aortic repair (TEVAR) is currently the first line treatment for aortic disease affecting the descending thoracic aorta, because in selected patients¹ it provides low procedural morbidity and mortality, and satisfactory midterm results. Endovascular procedures involving the aortic arch, however, are associated with higher rates of postoperative clinical failure,² and remain complex and challenging due the angulation and tortuosity of the arch and its peculiar biomechanical environment.³

Preoperative planning for TEVAR of the arch is based on Ishimaru's classification⁴ that, however, disregards landing zones angulation and tortuosity, that represent critical anatomical features associated with higher rates of endograft failure.⁵⁻⁷

In addition, Ishimaru's aortic map does not take into account the pulsatile forces acting on the aortic wall, that are transmitted as displacement forces on the terminal fixation sites of the endograft after its deployment, potentially leading to an insufficient proximal seal and/or an endograft migration.^{3,8} These forces can be calculated by computational fluid dynamics (CFD), a well-established engineering tool extensively employed in cardiovascular medicine, which by solving differential equations can simulate blood flow, and allows computing aortic hemodynamic parameters.³

In a previous article,⁹ we proposed a Modified Arch Landing Areas Nomenclature (MALAN) (Figure 1) that merges Ishimaru's map with the Aortic Arch Classification, originally described for predicting difficult carotid stenting,¹⁰ in which each landing area is identified indicating both proximal landing zone and Type of arch (e.g. 0/I). Our study showed that arch Types are associated with a consistent geometric pattern of Ishimaru's zones that allows identifying specific proximal landing areas with suboptimal angulation and tortuosity for stent-graft deployment.⁹

In the present study, we aimed to analyze displacement forces magnitude and orientation in the aortic arch according to the MALAN classification by means of CFD modeling, in order to potentially identify also a consistent fluid dynamic pattern, and identify specific areas with a hostile hemodynamic environment.

Methods

Patient population

This study reviewed anonymized thoracic CT angiography (CTA) scans from patients undergoing diagnostic evaluation for various indications at our institution in 2015 and was approved by the local Ethic Committee. The need for patient informed consent was waived because of the retrospective nature of the analysis and the use of

anonymized data. For the purpose of the present analysis, we specifically reviewed 15 thoracic CTA scans, 5 per Type of Arch, randomly chosen among the 60 selected for the previous study from our group that defined the MALAN classification.⁹ Only thin-cut (1.0 mm or 1.5 mm) CTs of patients with a healthy aortic arch with visible origins of the supra-aortic branches were considered. Inclusion and exclusion criteria were previously described in detail.⁹ Of note, as we conceived the study as a proof of concept of the original description of the aortic arch classification,¹⁰ which is based on healthy (i.e. non-aneurysmatic aortas), we chose a diameter of the thoracic aorta >40 mm as an exclusion criterion.⁹ Proximal landing zones were defined as previously described in detail.⁹


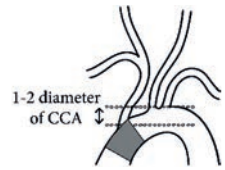
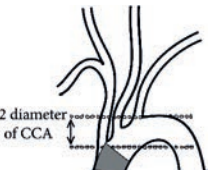

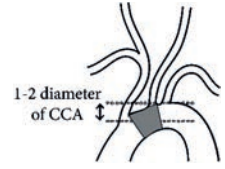
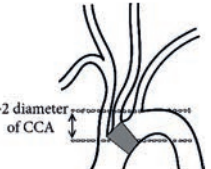
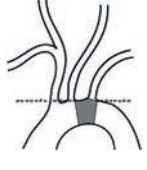
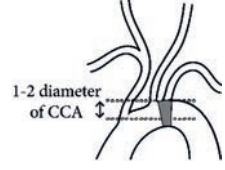
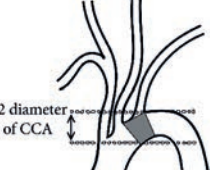
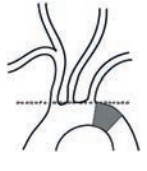
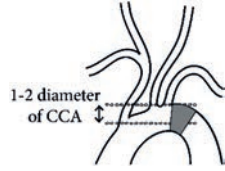
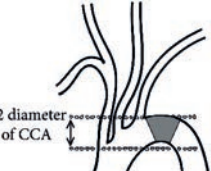
	<i>Type I</i>	<i>Type II</i>	<i>Type III</i>
<i>Zone 0</i>			
MALAN	0/I	0/II	0/III
<i>Zone 1</i>			
MALAN	1/I	1/II	1/III
<i>Zone 2</i>			
MALAN	2/I	2/II	2/III
<i>Zone 3</i>			
MALAN	3/I	3/II	3/III

Figure 1. Modified Arch Landing Areas Nomenclature (MALAN), that comprises proximal landing zones according to the Ishimaru' Aortic Arch Map and Types of Arch according to the Aortic Arch Classification.

Computational modeling

Patients aortic arch hemodynamics were calculated by means of CFD, a computational modeling method that has been developed to study the behavior of fluid flows by solving the Navier-Stokes equations, characterizing the motion of an incompressible fluid (i.e. blood), in a specified domain (i.e. aorta). Each CFD analysis requires definition of a three-dimensional (3D) model of the vascular anatomy of interest, and of the boundary conditions describing the flow conditions near the boundaries of the model.

Geometric Model Construction

In our study, the vascular anatomy of interest was extracted from the CTA scans using the software Mimics v18.0 (Materialise NV, Leuven, Belgium). The aortic tract between the aortic valve annulus and the diaphragm was considered, including the proximal tract of brachiocephalic trunk, left common carotid artery, and left subclavian artery. The final 3D model was exported in stereolithographic format (.stl), and artificially extended by inserting cylindrical regions, called flow extensions, at the boundary sections¹¹ using the open source library Vascular Modeling ToolKit (VMTK) v1.3.¹² This approach aimed to reduce the impact of modeling choices and uncertainties in the boundary conditions on the numerical results.¹³ Such fictitious domain extensions were then removed during the post-processing analysis.

The 3D aortic model was then discretized by VMTK v1.3 to generate a computational mesh suitable for CFD analysis. An average cut-off of 1.8 million of tetrahedral elements was considered for the simulations. This cut-off was based on a mesh convergence analysis that showed that further mesh refining would have produced a difference of less than 1% in the computed displacement forces.

Boundary Conditions

Given the retrospective nature of the study, no patient-specific hemodynamic data were available for the considered cohort of patients, and therefore the same inflow and outflow boundary conditions were applied in all cases. On the inflow section of the ascending aorta, a flow waveform representing a cardiac output of 4.88 L/min was used as input. This flow waveform was derived from phase-contrast magnetic resonance imaging data of a previous cohort of patients from our hospital and represents a typical ascending aortic flow waveform and cardiac output for adult patients. On the outflow sections, 3-element Windkessel circuits were attached to mimic the compliance and resistance of distal vasculature in a reliable way.^{3,14} A schematic representation of the inflow and outflow boundary conditions is presented in Figure 2. The use of such values led to physiologic pressure values in the simulation; the average of systolic/diastolic pressure among the 15 cases investigated in the present

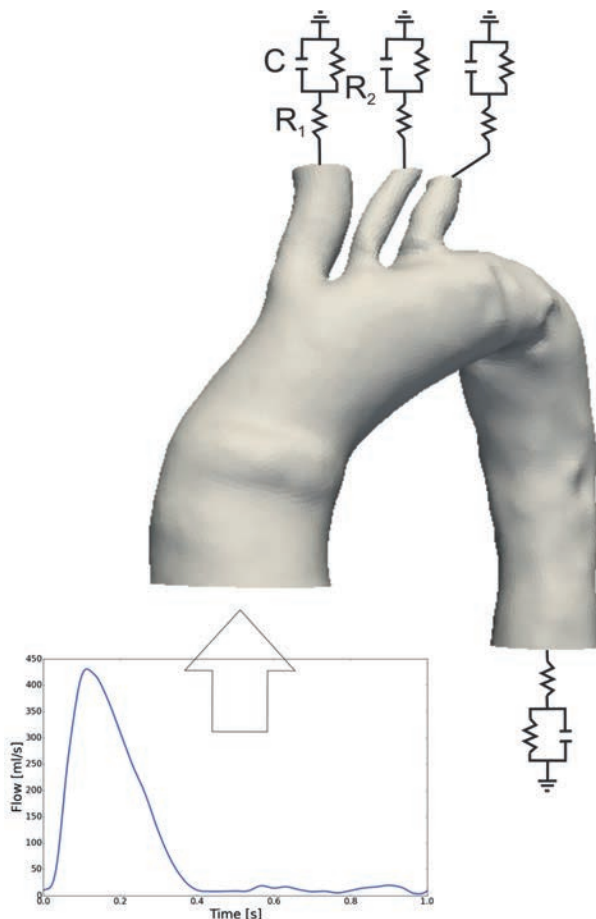


Figure 2. Schematic representation of a 3D aortic arch model with the inflow waveform and 0D Windkessel circuits representing the compliance and resistance and of the distal vascular beds.

study was 117/71 mmHg. A null velocity was prescribed to the luminal surface of the model, meaning that the arterial walls were assumed to be rigid.

Computational Analysis

Numerical simulations were carried out by solving the incompressible unsteady Navier-Stokes equations in the region of interest, under the hypothesis of Newton rheology (i.e. assuming a constant viscosity), as commonly performed in the case of large and medium-sized vessels.¹⁵

All the CFD analyses were performed by the open-source parallel finite element solver based on C++ library LifeV (www.lifev.org), tailored to blood flow applications.¹⁶

The simulated cardiac cycle lasted 1 second and was solved with a constant time step size of 0.001 s. The computational analysis was run for six heartbeats, to ensure the convergence of velocity and pressure fields.¹⁴

Post processing

The CFD simulation consisted of blood velocity, pressure, and wall shear stress (WSS), calculated on each element of the computational mesh over the cardiac cycle (Figure 3).¹⁷ The results of the simulations were post-processed using Python script and Paraview software v4.4 (Kitware Inc., France) to isolate the aortic wall in each landing area for all models. The displacement forces were then calculated by integrating the wall pressure and the WSS at systolic peak along the aortic wall in each MALAN area (Equation 1). As previously reported, the contribution of the pressure to the total displacement forces was several orders of magnitude larger than the WSS contribution,³ and therefore the impact of blood viscosity resulted to be negligible.¹⁸

Equation 1.

$$\overline{DF} = \int p \bar{n} da + \int \bar{\tau} dA$$

Where \overline{DF} is the displacement force in Newtons (N), $\int p \bar{n} da$ is the force exerted by the blood pressure along a given segment of the aortic wall in N and $\int \bar{\tau} dA$ is the WSS along the same segment in N.

The magnitude and the direction of the displacement forces for each landing zone (0-3) were calculated in all patients. As the surface areas of the proximal landing zones are different across the arch, a normalized displacement forces value, equivalent surface traction (EST), was proposed to account for the impact of the geometrical differences only. The EST was calculated dividing the displacement forces magnitude by the surface area of the corresponding proximal landing zone (Equation 2).

Equation 2.

$$EST = |DF| / A$$

Where EST is equivalent surface traction in N/m^2 , DF is displacement force in N and A is the surface area in m^2 .

Furthermore, the individual components of each displacement force vector were compared among the landing areas to evaluate the change in orientation (upward vs. sideways) in the different Types of arch.

Of note, both engineers and clinicians were involved in the CFD analysis.

Statistical analysis

Data were analyzed using SPSS Statistics version 24 (SPSS Inc., Chicago, Illinois). Normality of the distribution of the data was tested using the Shapiro-Wilk test, after which comparisons between landing zones and Types of arch were made using the

one-way analysis of variance for normally distributed data. Post hoc comparisons were made with the Least Significant Difference test. Continuous data are reported as the mean value with 95% confidence interval within parenthesis. Statistical significance was assumed at $P < .05$.

Results

The 15 selected patients (73% male) were 77 ± 9 years old. The three groups defined by the Type of arch were comparable in age ($P = .595$) and gender. The surface areas of the proximal landing zones were not different between the Types of Arch ($P = .672$), thus enabling a comparison of the displacement forces magnitude between the Types of Arch.

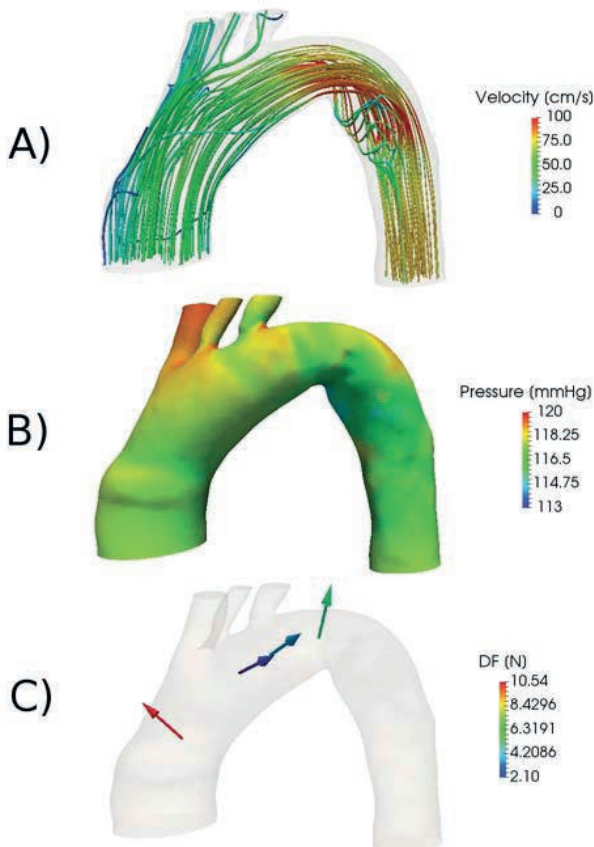


Figure 3. Illustrative representation of the simulation results at peak systole. The case of a Type 3 arch is presented. A) Velocity streamlines; B) Pressure; C) Displacement force vectors in each proximal landing zone.

Displacement forces magnitude and orientation

Comparison between Types of arch (Table 1), showed that displacement forces magnitude was significantly different in Zone 3 ($P=.007$), with 3/II and 3/III having significantly greater values than 3/I ($P=.004$ and $P=.008$ respectively). Comparison within Types of arch (Table 1), showed that displacement forces magnitude was significantly different across landing zones in all the Types of arch, with Zone 0 having the highest magnitude regardless the Type of arch ($P<.001$). Furthermore, displacement forces magnitude in 3/III was almost two-fold greater than in 2/III ($P=.033$), as also in 3/II compared to 2/II ($P=.032$).

Analysis of the displacement forces orientation (Figure 4, Tables 2 and 3), showed that the greater changes in displacement forces magnitude in 3/II and 3/III were related to the upward component, that was four times greater in 3/II compared to 2/II ($P=.001$), and five times greater in 3/III compared to 2/III ($P<.001$). On the contrary, in Type I arch the upward component did not differ through proximal landing zones 1-3. Finally, the sideways component did not change between proximal landing zones 1-3 in any Type of arch.

Table 1. Displacement force in MALAN areas with comparisons across landing zone and Type of Arch.

	Type I	Type II	Type III	P
Zone 0	0/I 13.2 (8.7 – 17.7) N	0/II 14.1 (9.9 – 18.2) N	0/III 9.5 (6.4 – 12.6) N	.090
Zone 1	1/I 1.7 (1.0 – 2.3) N	1/II 2.4 (1.6 – 3.1) N	1/III 2.3 (1.3 – 3.2) N	.211
Zone 2	2/I 3.4 (1.4 – 5.3) N	2/II 3.3 (2.2 – 4.3) N	2/III 3.1 (1.1 – 5.0) N	.937
Zone 3	3/I 2.6 (1.6 – 3.7) N	3/II 6.1 (4.2 – 8.0) N	3/III 5.8 (3.2 – 8.3) N	.007
P	<.001	<.001	<.001	

Results are reported as mean with 95% Confidence Interval between parentheses. 3/I vs. 3/II $P=.010$; 3/I vs. 3/III $P=.019$.

Equivalent surface traction

Consistently with displacement forces values, comparison between Types of arch (Table 4), showed that equivalent surface traction was significantly different in Zone 3 ($P=.009$), with that in 3/II and in 3/III being two-fold greater than in 3/I ($P=.008$ and $P=.006$). Comparisons within Types of arch (Table 4) showed no change in equivalent surface traction across proximal landing zones within Type I arch ($P=.297$), and Type II arch ($P=.054$), whereas equivalent surface traction increased towards more distal proximal landing zones within Type III ($P=.019$). Between adjacent landing areas,

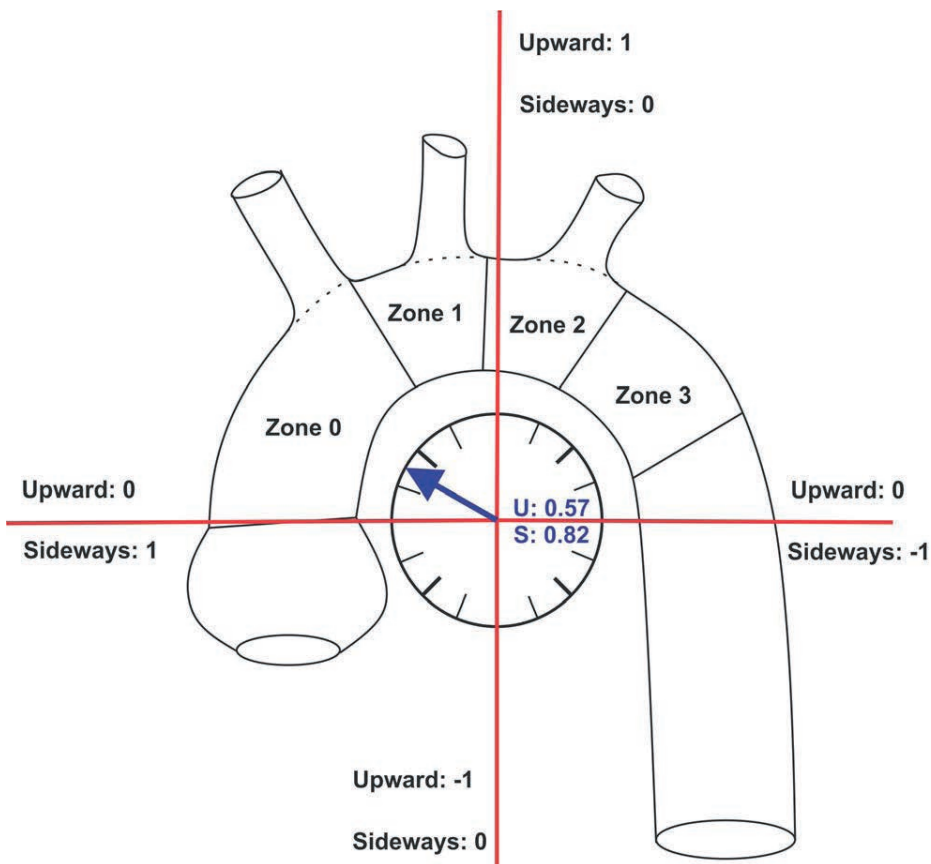


Figure 4. Schematic representation of Displacement Forces orientation.

equivalent surface traction was greater in 3/III than in 2/III ($P=.016$), and in 3/II than in 2/II ($P=.016$).

Discussion

The present work, which was conceived as a proof of concept study, showed that the MALAN classification is associated with consistent hemodynamic features that, in addition to the geometric pattern previously reported,⁹ further improve its predictive value to identify hostile proximal landing zones for TEVAR of the arch. We found that normalized DF (i.e. EST) do not vary along Ishimaru's zones in Type I arch, whereas they change in Type II and III, and specifically in the distal part of the arch. Our data remain to be validated by CFD analysis in pathological aortas, and the clinical relevance of our finding needs to be proven in a dedicated postoperative outcome

Table 2. Upwards (U) and sideways (S) direction in MALAN areas with comparisons across landing zone and Type of Arch.

	Type I	Type II	Type III	P
	0/I	0/II	0/III	
Zone 0	U: 0.57 (0.47 – 0.67) S: 0.82 (0.74 – 0.89)	U: 0.61 (0.43 – 0.80) S: 0.77 (0.61 – 0.93)	U: 0.53 (0.34 – 0.71) S: 0.83 (0.71 – 0.96)	U: .607 S: .609
	1/I	1/II	1/III	
Zone 1	U: 0.15 (-0.27 – 0.56) S: 0.94 (0.83 – 1.04)	U: 0.17 (-0.09 – 0.43) S: 0.97 (0.92 – 1.02)	U: 0.27 (-0.03 – 0.57) S: 0.94 (0.84 – 1.03)	U: .744 S: .759
	2/I	2/II	2/III	
Zone 2	U: -0.12 (-0.33 – 0.01) S: 0.98 (0.94 – 1.02)	U: -0.29 (-0.70 – 0.13) S: 0.90 (0.78 – 1.03)	U: 0.35 (0.03 – 0.67) S: 0.90 (0.76 – 1.05)	U: .007 S: .344
	3/I	3/II	3/III	
Zone 3	U: 0.52 (0.02 – 1.01) S: 0.71 (0.28 – 1.14)	U: 0.63 (0.12 – 1.13) S: 0.64 (0.27 – 1.00)	U: 0.87 (0.75 – 0.99) S: 0.44 (0.17 – 0.72)	U: .267 S: .349
P	U: .004 S: .123	U: <.001 S: .034	U: <.001 S: <.001	

Results are reported as mean with 95% Confidence Interval between parentheses. U: 3/III vs. 2/III P=.004; 3/II vs. 2/II P=.001

Table 3. Upward force in MALAN areas with comparisons across landing zone and type of arch.

	Type I	Type II	Type III	P
	0/I	0/II	0/III	
Zone 0	7.5 (5.1 – 9.9) N	8.3 (6.4 – 10.1) N	4.9 (2.8 – 6.9) N	.020
	1/I	1/II	1/III	
Zone 1	0.3 (-0.6 – 1.2) N	0.4 (-0.2 – 1.0) N	0.5 (0.0 – 1.0) N	.826
	2/I	2/II	2/III	
Zone 2	-0.4 (-1.1 – 0.3) N	-1.1 (-2.6 – 0.5) N	1.0 (0.1 – 2.0) N	.010
	3/I	3/II	3/III	
Zone 3	1.3 (0.0 – 2.7) N	4.3 (0.79 – 7.8) N	5.0 (3.1 – 6.8) N	.027
P	<.001	<.001	<.001	

3/III vs. 2/III P<.001; 3/II vs. 2/II P=.001

Table 4. Equivalent surface traction in MALAN areas with comparisons across landing zone and Type of Arch.

	Type I	Type II	Type III	P
	0/I	0/II	0/III	
Zone 0	2265 (179 – 2739) N/m ²	2393 (2096 – 2691) N/m ²	1807 (1286 – 2328) N/m ²	.054
	1/I	1/II	1/III	
Zone 1	2389 (1514 – 3264) N/m ²	3134 (1792 – 4475) N/m ²	2765 (1624 – 3906) N/m ²	.460
	2/I	2/II	2/III	
Zone 2	2195 (1632 – 2757) N/m ²	1953 (1141 – 2766) N/m ²	2138 (1006 – 3271) N/m ²	.851
	3/I	3/II	3/III	
Zone 3	1725 (929 – 2521) N/m ²	3357 (2092 – 4622) N/m ²	3442 (2557 – 4327) N/m ²	.009
P	.297	.054	.019	

Results are reported as mean with 95% Confidence Interval between parentheses.

analysis of patients treated with TEVAR of the arch. Both these studies are currently in progress and, based on the findings reported herein, are focused on Zone 2 and 3 of Type II and III arch. The results of these works are expected to provide relevant information to simplify the MALAN classification by reducing the landing areas of interest, and potentially improve the applicability and acceptance of this new nomenclature.

TEVAR planning is currently based only on the analysis of aortic morphology and size by means of static imaging protocols.^{19,20} The aorta, conversely, is an elastic and dynamic conduit that expands significantly at relevant levels per heartbeat^{21,22} and exerts displacement forces that have a relevant impact on endograft performance.³ Hence, the introduction of dynamic measurements into clinical practice by CFD modeling is expected to improve TEVAR planning and stent-graft design.²³

The magnitude of the aortic arch displacement forces, which is expressed by definition in Newtons, depends on the blood pressure and the WSS. The pivotal study of Figueroa et al.³ belied the commonly held view that the main component of the displacement forces is the shearing force of the flow and that, as a consequence, their main orientation is in the downstream direction of the flow. In fact, the primary contributor to the displacement forces magnitude is the blood pressure, and their orientation depends on the geometry of the arch and is mainly in the upward direction.³

In the present study, we described for the first time how the displacement forces of the arch are distributed in the different proximal landing areas for TEVAR, defined according to the MALAN classification.⁹ Our data showed that Zone 0, regardless the Type of arch (i.e. 0/I-III), presents the higher displacement forces magnitude compared to the other arch zones, and that the displacement forces vector in Zone 0 is oriented orthogonally to the aortic blood flow and to the vessel longitudinal axis in that area. Despite these unfavorable hemodynamic conditions, however, TEVAR in Zone 0 is less likely to be complicated by endoleak,²⁴ or stent-graft migration, because it provides a longer neck length compared to the other zones,²⁴ and a moderate angulation and a negligible tortuosity, regardless the Type of arch.⁹ Also, computation of equivalent surface traction in each landing area showed that the higher displacement forces magnitude in Zone 0 is due to its consistently greater surface area, a factor that positively correlates with displacement forces magnitude.

Displacement forces with a greater magnitude and a vector orthogonal to the aortic flow and longitudinal axis were also found in 3/II and in 3/III, compared to the proximal adjacent areas (i.e., 2/II and 2/III respectively). These findings were even more evident when a comparison was made based on equivalent surface traction. Interestingly also, we found that the greater equivalent surface traction was related to changes in the upward component of the vector, while the sideways component remained unchanged.

In contrast to 0/I-III landing areas, 3/II and 3/III are associated with suboptimal angulation and tortuosity,⁹ which require a longer proximal neck length²⁵ often

unavailable due to the anatomical restraint of the origin of left subclavian. As a consequence, the resulting biomechanical environment of 3/II and 3/III appears unfavorable for endograft deployment, and therefore a more proximal aortic landing zone should be probably chosen. In this respect, the use of scalloped devices appears as a viable option to overcome the issue of short and/or angulated proximal necks in Zone 3 by means of a stand-alone TEVAR, i.e. without additional extra-anatomical surgical bypass or left subclavian endovascular branching.²⁶

In addition to the relevance for TEVAR planning, our findings regarding displacement forces magnitude and orientation in Zone 0, and in Zone 3 of Type II and Type III arch, may have implications also in the development of proximal entry tears in spontaneous Type A and Type B aortic dissections. Further studies currently in progress will disclose whether an anatomical risk factor may be identified based on the hemodynamic mapping reported herein, consistently with previous reports.^{27,28} Our data may also provide useful insights for the technical development of specific stent-grafts for endovascular repair of the ascending aorta.²⁹

Indeed, we recognize some limitations of our study. First, healthy aortas (i.e. non-aneurysmatic) were employed, consistently with the original definition of Types of Arch.¹⁰ Second, due to the lack of information on patient-specific hemodynamic environment, the same flow boundary conditions were employed in all cases. However, these limitations did not hinder the comparison between the hemodynamic patterns of the different landing zones, being related to their consistent geometric features. Finally, the limitations inherent to the computational methods, namely the assumptions of a Newtonian fluid and of a rigid arterial wall, should be also considered.³ Nevertheless, given the small impact of WSS, the relevance of blood viscosity is considered negligible,¹⁸ and the use of CFD with a rigid wall is a reasonable approach in a clinical context with limited resources,³⁰ because the DF mainly depends on pressure distributions that can be accurately calculated with a rigid wall assumption.^{3,30}

In conclusion, we believe that our findings support further studies to introduce fluid dynamics parameters among the criteria employed for TEVAR planning.

References

- 1 Marrocco-Trischitta MM, Melissano G, Kahlberg A, et al. Chronic kidney disease classification stratifies mortality risk after elective stent graft repair of the thoracic aorta. *J Vasc Surg* 2009;49(2):296–301. Doi: 10.1016/J.JVS.2008.09.041.
- 2 Böckler D, Brunkwall J, Taylor PR, et al. Thoracic Endovascular Aortic Repair of Aortic Arch Pathologies with the Conformable Thoracic Aortic Graft: Early and 2 year Results from a European Multicentre Registry. *Eur J Vasc Endovasc Surg* 2016;51(6):791–800. Doi: 10.1016/J.EJVS.2016.02.006.

- 3 Figueroa CA, Taylor CA, Chiou AJ, et al. Magnitude and direction of pulsatile displacement forces acting on thoracic aortic endografts. *J Endovasc Ther* 2009;16(3):350–8. Doi: 10.1583/09-2738.1.
- 4 Ishimaru S. Endografting of the aortic arch. *J Endovasc Ther* 2004;11 Suppl 2:II62–71. Doi: 10.1583/04-1407.1.
- 5 Grabenwoger M, Alfonso F, Bachet J, et al. Thoracic Endovascular Aortic Repair (TEVAR) for the treatment of aortic diseases: a position statement from the European Association for Cardio-Thoracic Surgery (EACTS) and the European Society of Cardiology (ESC), in collaboration with the European Assoc. *Eur J Cardio-Thoracic Surg* 2012;42(1):17–24. Doi: 10.1093/ejcts/ezs107.
- 6 Chen C-K, Liang I-P, Chang H-T, et al. Impact on outcomes by measuring tortuosity with reporting standards for thoracic endovascular aortic repair. *J Vasc Surg* 2014;60(4):937–44. Doi: 10.1016/J.JVS.2014.04.008.
- 7 Ueda T, Takaoka H, Raman B, et al. Impact of Quantitatively Determined Native Thoracic Aortic Tortuosity on Endoleak Development After Thoracic Endovascular Aortic Repair. *Am J Roentgenol* 2011;197(6):W1140–6. Doi: 10.2214/AJR.11.6819.
- 8 Molony DS, Kavanagh EG, Madhavan P, et al. A Computational Study of the Magnitude and Direction of Migration Forces in Patient-specific Abdominal Aortic Aneurysm Stent-Grafts. *Eur J Vasc Endovasc Surg* 2010;40(3):332–9. Doi: 10.1016/J.EJVS.2010.06.001.
- 9 Marrocco-Trischitta MM, de Beaufort HW, Secchi F, et al. A geometric reappraisal of proximal landing zones for thoracic endovascular aortic repair according to aortic arch types. *J Vasc Surg* 2017. Doi: 10.1016/j.jvs.2016.10.113.
- 10 Madhwal S, Rajagopal V, Bhatt DL, et al. Predictors of difficult carotid stenting as determined by aortic arch angiography. *J Invasive Cardiol* 2008;20(5):200–4.
- 11 Morbiducci U, Ponzini R, Rizzo G, et al. In Vivo Quantification of Helical Blood Flow in Human Aorta by Time-Resolved Three-Dimensional Cine Phase Contrast Magnetic Resonance Imaging. *Ann Biomed Eng* 2009;37(3):516–31. Doi: 10.1007/s10439-008-9609-6.
- 12 Antiga L, Piccinelli M, Botti L, et al. An image-based modeling framework for patient-specific computational hemodynamics. *Med Biol Eng Comput* 2008;46(11):1097–112. Doi: 10.1007/s11517-008-0420-1.
- 13 Gallo D, De Santis G, Negri F, et al. On the use of in vivo measured flow rates as boundary conditions for image-based hemodynamic models of the human aorta: Implications for indicators of abnormal flow. *Ann Biomed Eng* 2012;40(3):729–41. Doi: 10.1007/s10439-011-0431-1.
- 14 Les AS, Shadden SC, Figueroa CA, et al. Quantification of hemodynamics in abdominal aortic aneurysms during rest and exercise using magnetic resonance imaging and computational fluid dynamics. *Ann Biomed Eng* 2010;38(4):1288–313. Doi: 10.1007/s10439-010-9949-x.
- 15 Formaggia L, Quarteroni A, Veneziani A. *Cardiovascular Mathematics*. vol. 3. 2009.
- 16 Passerini T, Quaini A, Villa U, et al. Validation of an open source framework for the simulation of blood flow in rigid and deformable vessels. *Int j Numer Method Biomed Eng* 2013;29(11):1192–213. Doi: 10.1002/cnm.2568.
- 17 Taylor CA, Hughes TJ, Zarins CK. Finite element modeling of three-dimensional pulsatile flow in the abdominal aorta: relevance to atherosclerosis. *Ann Biomed Eng* 1998;26(6):975–87.
- 18 Fung GSK, Lam SK, Cheng SWK, et al. On stent-graft models in thoracic aortic endovascular repair: A computational investigation of the hemodynamic factors. *Comput Biol Med* 2008;38(4):484–9.

- 19 Erbel R, Aboyans V, Boileau C, et al. 2014 ESC Guidelines on the diagnosis and treatment of aortic diseases: Document covering acute and chronic aortic diseases of the thoracic and abdominal aorta of the adult. The Task Force for the Diagnosis and Treatment of Aortic Diseases of the European . *Eur Heart J* 2014;35(41):2873–926. Doi: 10.1093/eurheartj/ehu281.
- 20 Writing Committee, Rimbau V, Böckler D, et al. Editor's Choice – Management of Descending Thoracic Aorta Diseases. *Eur J Vasc Endovasc Surg* 2017;53(1):4–52. Doi: 10.1016/j.ejvs.2016.06.005.
- 21 van Bogerijen GH, Tolenaar JL, Conti M, et al. Contemporary Role of Computational Analysis in Endovascular Treatment for Thoracic Aortic Disease. *Aorta (Stamford)* 2013;1(3):171–81. Doi: 10.12945/j.aorta.2013.13-003.
- 22 de Beaufort HWL, Nauta FJH, Conti M, et al. Extensibility and Distensibility of the Thoracic Aorta in Patients with Aneurysm. *Eur J Vasc Endovasc Surg* 2017;53(2):199–205. Doi: 10.1016/j.ejvs.2016.11.018.
- 23 van Bogerijen GHW, van Herwaarden JA, Conti M, et al. Importance of dynamic aortic evaluation in planning TEVAR. *Ann Cardiothorac Surg* 2014;3(3):300–6. Doi: 10.3978/j.issn.2225-319X.2014.04.05.
- 24 Melissano G, Civilini E, Bertoglio L, et al. Results of Endografting of the Aortic Arch in Different Landing Zones. *Eur J Vasc Endovasc Surg* 2007;33(5):561–6. Doi: 10.1016/J.EJVS.2006.11.019.
- 25 Altnji HE, Bou-Said B, Walter-Le Berre H. Morphological and stent design risk factors to prevent migration phenomena for a thoracic aneurysm: a numerical analysis. *Med Eng Phys* 2015;37(1):23–33. Doi: 10.1016/j.medengphy.2014.09.017.
- 26 Ben Abdallah I, El Batti S, Sapoval M, et al. Proximal Scallop in Thoracic Endovascular Aortic Aneurysm Repair to Overcome Neck Issues in the Arch. *Eur J Vasc Endovasc Surg* 2016;51(3):343–9. Doi: 10.1016/J.EJVS.2015.09.012.
- 27 Poullis MP, Warwick R, Oo A, et al. Ascending aortic curvature as an independent risk factor for type A dissection, and ascending aortic aneurysm formation: a mathematical model. *Eur J Cardio-Thorac Surg* 2008;33(6):995–1001. Doi: 10.1016/j.ejcts.2008.02.029.
- 28 Weiss G, Wolner I, Folkmann S, et al. The location of the primary entry tear in acute type B aortic dissection affects early outcome. *Eur J Cardio-Thorac Surg* 2012;42(3):571–6. Doi: 10.1093/ejcts/ezs056.
- 29 Roselli EE, Idrees J, Greenberg RK, et al. Endovascular stent grafting for ascending aorta repair in high-risk patients. *J Thorac Cardiovasc Surg* 2015;149(1):144–54. Doi: 10.1016/j.jtcvs.2014.07.109.
- 30 Brown AG, Shi Y, Marzo A, et al. Accuracy vs. computational time: translating aortic simulations to the clinic. *J Biomech* 2012;45(3):516–23. Doi: 10.1016/j.jbiomech.2011.11.041.

Chapter 9

Blood flow after endovascular repair in the arch: a computational analysis

Theodorus M.J. van Bakel^{1,2}, MD

Rodrigo M. Romarowski^{1,3}, PhD

Simone Morganti³, PhD

Joost A. van Herwaarden², MD, PhD

Frans L. Moll², MD, PhD

Hector W.L. de Beaufort^{1,2}, MD

Massimiliano M. Marrocco-Trischitta¹, MD, PhD

Francesco Secchi⁴, MD

Michele Conti³, PhD

Ferdinando Auricchio³, PhD

Santi Trimarchi^{1,5}, MD, PhD

1. Thoracic Aortic Research Center, IRCCS Policlinico San Donato, San Donato Milanese, Italy.
2. Department of Vascular Surgery, University Medical Center Utrecht, Utrecht, The Netherlands.
3. Department of Civil Engineering and Architecture, University of Pavia, Pavia, Italy
4. Department of Radiology, IRCCS Policlinico San Donato, San Donato Milanese, Italy.
5. Department of Biomedical Sciences for Health, University of Milan, Milan, Italy

Aorta. In press.

Abstract

Objective

The benefits of thoracic endovascular aortic repair (TEVAR) have encouraged endograft deployment more proximally in the aortic arch. The present study quantifies the hemodynamic impact of TEVAR in proximal landing zone 2 on the thoracic aorta and the proximal supra-aortic branches.

Methods

Patients treated with TEVAR in proximal landing zone 2 having available preoperative and 30-day postoperative computer tomography angiography (CTA) and phase-contrast magnetic resonance imaging (PC-MRI) data were retrospectively selected. Blood flow was studied using patient-specific computational fluid dynamics (CFD) simulations.

Results

Four patients were included. Following TEVAR in proximal landing zone 2, the mean flow in the left common carotid artery (LCCA) increased almost threefold, from 0.21 (0.12 – 0.41) L/min to 0.61 (0.24 – 1.08) L/min (+294%). The surface area of the LCCA had not yet increased commensurately and therefore maximum flow velocity in the LCCA increased from 44.9 (27.0 – 89.3) cm/s to 72.6 (40.8 – 135.0) cm/s (+62%). One of the patients presented with Type Ib endoleak at 1-year follow-up. The displacement force acting on the surface of the endograft in this patient measured 32.1 N and was directed dorsocranial, perpendicular to the distal sealing zone.

Conclusion

TEVAR in proximal landing zone 2 alters blood flow in the supra-aortic branches, resulting in increased flow with high flow velocities in the LCCA. High displacement forces were calculated and related to endograft migration and Type I endoleak during 1-year follow-up.

Introduction

Thoracic endovascular aortic repair (TEVAR) has decreased perioperative mortality and morbidity in treatment of diseases of the descending thoracic aorta.^{1,2} The benefits of endovascular treatment compared to open aortic repair have encouraged most vascular surgeons to deploy endografts also more proximally, in the aortic arch. Despite the less invasive character of TEVAR compared to open repair, stroke remains an important complication with significant morbidity and mortality.³

Early on in the adoption of TEVAR as first line treatment, a classification for preoperative planning of TEVAR in the aortic arch was proposed, identifying four proximal landing zones in the ascending aorta and aortic arch: zone 0 to zone 3.⁴ Endograft deployment in zone 0, zone 1 and zone 2 determines the coverage of one or more proximal supra-aortic branches, which is generally managed by creating an extra-anatomical bypass, redirecting blood flow.

TEVAR in zone 2 is frequently accompanied by a left carotid-to-subclavian bypass and is performed in a third or more of patients undergoing TEVAR.⁵ The benefits of embolization or revascularization of the LSA are still subject of debate.^{6,7}

The hemodynamic effects of TEVAR in zone 2 are not well understood. Zone 2 deployment is generally considered safe,⁷ however, there is an increased risk of stroke⁸ and Type I endoleak⁹ compared to deployment in the descending thoracic aorta distal to the left subclavian artery (LSA). Calculation of the hemodynamic effects of endograft deployment in zone 2 may provide additional information to help understand the pathophysiology of these complications. In this setting, computational fluid dynamics (CFD) simulations can be performed to calculate hemodynamic indices in patient-specific models of the aorta. The aim of the present study was to use this powerful tool to quantify the impact of TEVAR in zone 2 on blood flow in the aorta and the supra-aortic branches.

Methods

Patient selection

The database of IRCCS Policlinico San Donato was retrospectively queried for patients who underwent zone 2 TEVAR for thoracic aortic diseases between 2013 and 2016. Patients who had available preoperative and 30-day postoperative computer tomography angiography (CTA) and phase contrast magnetic resonance imaging (PC-MRI) data were included. Clinical data at 30-day and one-year follow-up were noted. This study was approved by the local Ethical Committee, which waived the

need for patients' informed consent due to the retrospective nature of the analysis and the use of anonymized data.

Medical imaging

The standard CTA protocol for aortic imaging at our institution includes a 64-multislice computed tomography (CT) scan (SOMATOM Definition AS, Siemens, Germany) after administration of a contrast agent (Iomeron 370, Bracco, Italy). Image reconstructions were done with 1 mm slice thickness. CTA imaging data were used for measurement of the surface areas of the proximal supra-aortic branches and constructing the models for CFD simulations.

The protocol for PC-MRI imaging in patients with aortic pathologies at our institution uses a 1.5 Tesla magnetic resonance imaging (MRI) scanner (MAGNETOM Aera, Siemens, Germany). Flow measurements were taken at the level of the ascending aorta, BCT, LCCA, LSA and descending aorta and used to set the inflow and outflow boundary conditions for the CFD simulations.

CFD simulations

Three-dimensional models of the thoracic aorta were constructed from CTA imaging data using the Vascular Modeling Toolkit levelset segmentation (VMTK software suite version 1.3). The models included the ascending aorta, aortic arch, the proximal part of the supra-aortic branches, and the descending thoracic aorta. Once the models were segmented, a computational mesh was created to follow the fluid domain. The surface was smoothed with a Taubin algorithm in order to avoid shrinking.

CFD simulations were performed to retrieve blood flow velocity, pressure, and wall shear stress fields using previously described techniques.¹⁰ Boundary conditions were imposed in a patient-specific manner. In particular, flow profiles as extracted from each patient's preoperative and postoperative PC-MRI were imposed at the ascending aorta. On the outflow sections, classical 3-element Windkessel circuits were applied to mimic the compliance and resistance of the distal vascular bed.^{11,12} The parameter values of the Windkessel circuits were calibrated to match patient-specific blood pressures (from brachial cuff pressure measurements) and flow measurements from PC-MRI. Convergence of velocity and pressure data is a requirement to obtain meaningful CFD simulation results.¹² Therefore, CFD simulations of six cardiac cycles were performed and results from the last cardiac cycle were used. Post-processing was done using open source software Paraview version 4.1.0.

Outcome measures

CFD simulations were performed using preoperative and 30-day postoperative imaging data. Mean flow was calculated in the ascending aorta, brachiocephalic trunk

(BCT), left common carotid artery (LCCA), LSA and descending aorta. Blood flow through the ascending aorta, proximal supra-aortic branches and descending aorta, was calculated before and after intervention.

Flow velocity measurements were taken just distal to the origin of the proximal supra-aortic branches on the center lumen line.

Hemodynamic displacement forces acting on the surface of the endograft were calculated from postoperative CFD simulation results (Equation 1).^{13,14}

Equation 1.

$$DF = \int p dA + \int \tau dA$$

Where displacement force (DF) in Newton is calculated by the sum of the pressure (p) and wall shear stress (τ) on the surface area of the endograft (A) in systolic peak.

Statistical analysis

Data were analyzed using SPSS Statistics version 24 (IBM, Armonk, NY). Continuous data are reported as mean values with the range given between brackets. Differences between the preoperative and postoperative results are reported in percentages.

Results

Patient characteristics

Four patients were selected (Table 1). All patients were treated with TEVAR in Zone 2 using Medtronic Valiant endografts (Medtronic Vascular, Santa Rosa, California) and were submitted to a left carotid-to-subclavian bypass within the same procedure.

At the 30-day postoperative visit clinical follow-up was uneventful for all patients. At one-year follow-up, Patient 4 presented with a Type Ib endoleak. Patients 1, 2, and 3 were free of complications.

Table 1. Patient characteristics

Patient	Age	Gender	Disease	Endograft dimensions
1	48	M	TAA	28-24-150
2	65	M	PAU	42-42-100
3	74	M	TAA	Combined 44-44-200/46-46-200/46-46-150
4	81	M	TAA	Combined 42-42-200/46-46-200/46-46-150

Endograft dimensions are given in mm: proximal diameter - distal diameter - length

TAA = Thoracic aortic aneurysm; PAU = penetrating aortic ulcer

Mean flows

Figure 1 presents the mean flows before TEVAR and after 30-days follow-up; data are given in Table 2. Before TEVAR, the mean flow in the ascending aorta was 5.18 (3.69 – 6.31) L/min. Mean flow in the BCT was 0.62 (0.54 – 0.75) L/min, in the LCCA 0.21 (0.12 – 0.41) L/min, in the LSA 0.25 (0.17 – 0.33) L/min, and in the descending aorta 4.10 (2.25 – 5.26) L/min.

Following TEVAR, the mean flow in the LCCA increased almost threefold (+294%), while blood flow in the ascending aorta and descending aorta decreased (-11% and -20%, respectively).

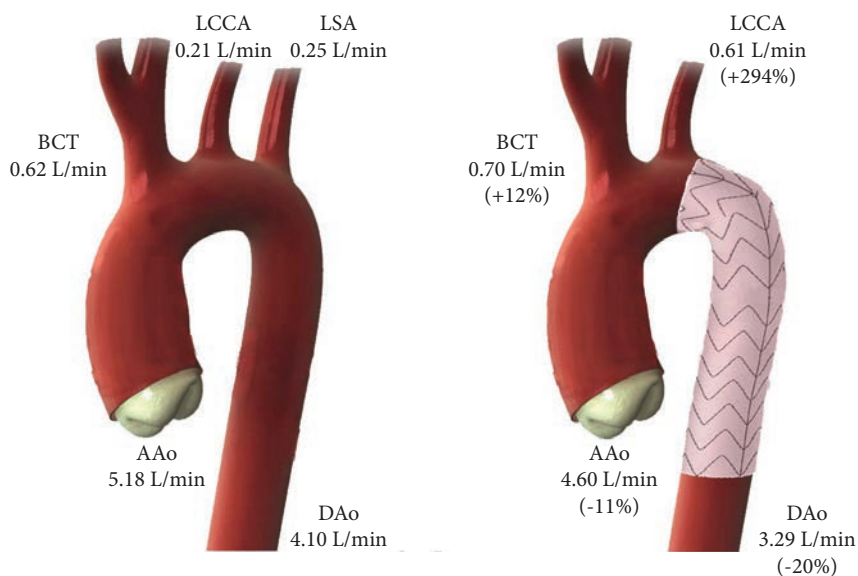


Figure 1. Mean flows in the ascending aorta, proximal supra-aortic branches and descending aorta before preoperative (left) and at 30-days follow-up (right). The difference given within brackets. AAo = ascending aorta; BCT = brachiocephalic trunk; DAo = descending aorta; LCCA = left common carotid artery; LSA = left subclavian artery.

Surface areas of proximal supra-aortic branches

The surface areas of the proximal supra-aortic branches were measured on preoperative and 30-days postoperative CT-images. Data are given in Table 3. Before TEVAR, the surface area of the BCT was 3.16 (0.95 – 6.09) cm², the surface area of the LCCA was 0.94 (0.39 – 1.44) cm² and the surface area of the LSA was 1.61 (0.75 – 2.9) cm². At 30-days follow-up, the surface area of the BCT had not changed (+1%). The surface area of the LCCA had increased by 9%.

Table 2. Blood flow before and after zone 2 TEVAR

Patient	Before TEVAR				After TEVAR				
	AAo	BCT	LCCA	LSA	DAo	AAo	BCT	LCCA	DAo
1	6.31	0.54	0.19	0.33	5.26	6.64	1.21	1.08	4.35
2	5.98	0.67	0.12	0.17	5.01	4.61	0.57	0.24	3.81
3	4.74	0.54	0.12	0.24	3.85	4.53	0.72	0.76	3.05
4	3.69	0.75	0.41	0.28	2.26	2.62	0.30	0.37	1.95
Mean	5.18	0.62	0.21	0.25	4.10	4.60	0.70	0.61	3.29

Blood flow measurements are presented in L/min. AAO = ascending aorta; BCT = brachiocephalic trunk; DAo = descending aorta LCCA = left common carotid artery; LSA = left subclavian artery

Table 3. Surface area of the proximal supra-aortic branches before and after zone 2 TEVAR

Patient	Before TEVAR			After TEVAR	
	BCT	LCCA	LSA	BCT	LCCA
1	0.95	0.39	0.75	1.05	0.57
2	2.22	0.67	0.82	2.10	0.76
3	3.40	1.27	1.95	3.53	1.30
4	6.09	1.44	2.90	6.06	1.46
Mean	3.16	0.94	1.61	3.19	1.02

Surface areas were measured just distal to the origin from the aortic arch and are given in cm². BCT = brachiocephalic trunk; LCCA = left common carotid artery; LSA = left subclavian artery

Flow velocities

Data of maximum flow velocity in the proximal supra-aortic branches are given in Table 4. Before TEVAR, maximum flow velocity in the BCT was 47.9 (14.1 – 104.4) cm/s, in the LCCA 44.9 (27.0 – 89.3) cm/s, and in the LSA 47.6 (13.3 – 105.3) cm/s. Following TEVAR, maximum flow velocity in the LCCA increased by +62%. Figure 2 presents a mapping of the peak systolic flow profiles in the proximal supra-aortic branches of Patient 3 before and after TEVAR.

Table 4. Maximum flow velocity in the proximal supra-aortic branches

Patient	Before TEVAR			After TEVAR	
	BCT	LCCA	LSA	BCT	LCCA
1	104.4	89.3	105.3	106.7	134.9
2	36.6	27.0	25.8	33.7	40.8
3	35.9	33.8	45.9	28.3	71.4
4	14.1	29.3	13.3	8.9	43.2
Mean	47.8	44.9	47.6	44.5	72.6

Maximum flow velocity before TEVAR in Zone 2 and after 30-days follow-up was measured just distal to the origin from the aortic arch and given in cm/s. BCT = brachiocephalic trunk; LCCA = left common carotid artery; LSA = left subclavian artery

Table 5. Blood pressures measurements (mmHg)

Patient	Before TEVAR			After TEVAR		
	Systolic	Diastolic	Mean	Systolic	Diastolic	Mean
1	131	58	82	127	66	87
2	110	49	80	108	56	80
3	117	61	89	114	65	88
4	94	62	77	106	55	77
Mean	113	58	82	114	61	83

Blood pressures measurements were taken from CFD simulation results at the ascending aorta.

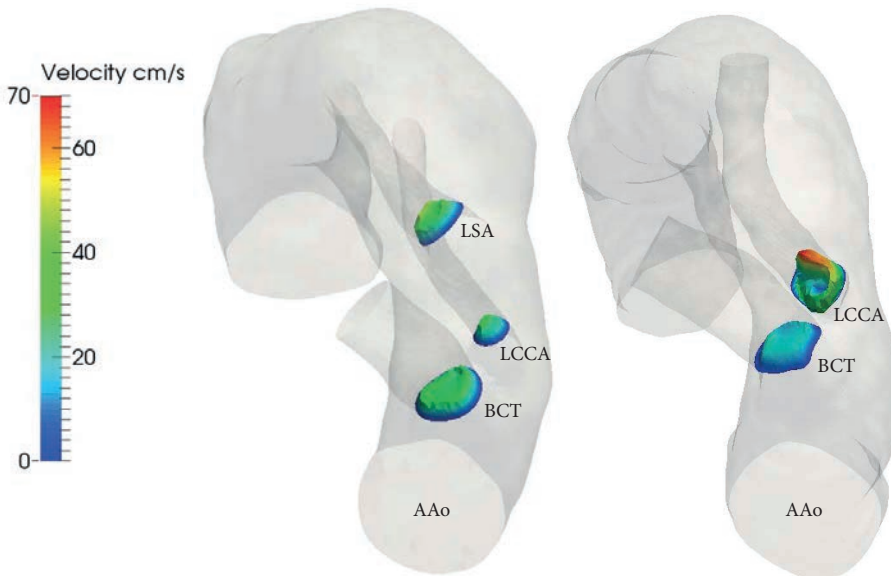


Figure 2. Peak systolic velocity is mapped just distal to the origin of the proximal supra-aortic branches preoperative (left) and at 30-days follow-up (right). AAo = ascending aorta; BCT = brachiocephalic trunk; LCCA = left common carotid artery; LSA = left subclavian artery.

Displacement forces

The magnitude of the displacement force acting on the endografts ranged from 12.2 to 32.1 N. The displacement force vector was directed dorsocranial in all patients (Figure 3).

Patient 4 presented with Type Ib endoleak at 1-year follow-up. The center of the distal end of the endograft had migrated 17.1 mm dorsocranial in the direction of the displacement force (Figure 4). Although the total surface area of the endograft in Patient 3 was not as large as in Patient 4, the magnitude of the displacement force was similar. This is caused by the higher blood pressure in Patient 3 compared to Patient 4 (Table 5).

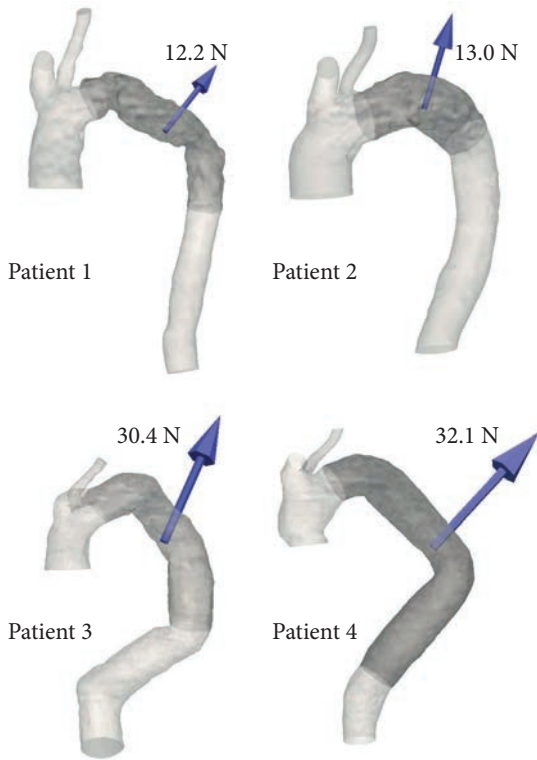


Figure 3. The displacement force vectors that are acting on the surface of the endograft in peak systole are presented in each patient. The contours of the endografts are outlined in dark grey, the magnitude of the displacement force is given in Newton.

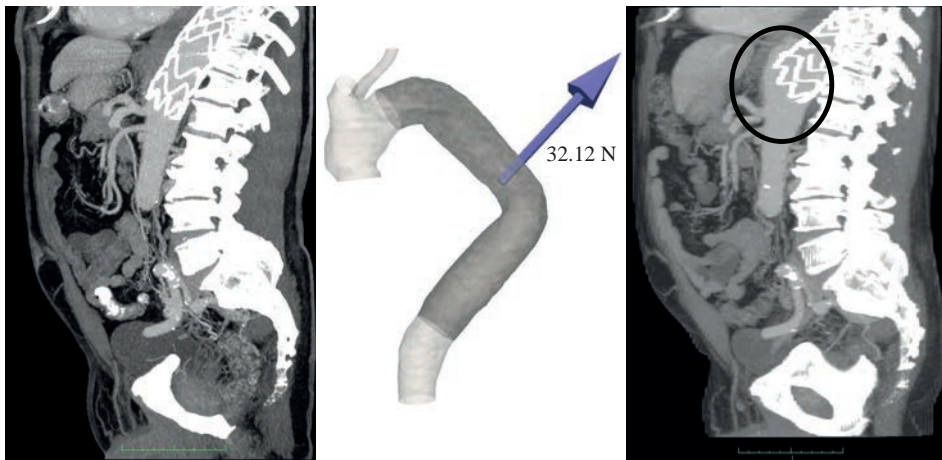


Figure 4. Sagittal views of the postoperative endograft and displacement force. Left: 30-day postoperative CTA examination. Middle: postoperative CFD model with displacement force vector. Right: 1-year follow-up CTA is shown, where proximal migration of the endograft and resulting Type Ib endoleak was found (black with circle).

Discussion

In this study we used patient-specific CFD simulations to quantify some of the hemodynamic effects of TEVAR in zone 2 on blood flow in the aorta and the supra-aortic branches. Our results show that blood flow predominantly changed in the proximal LCCA, where flow increased almost threefold. The vessel size of the LCCA had not changed commensurately at 30-days follow-up and consequently flow velocity had increased.

Little is known about the effects of TEVAR in zone 2 on blood flow in the carotid arteries. Our results show that blocking the LSA and redirecting blood flow to the left arm via the LCCA and left carotid-to-subclavian bypass increases flow velocities in the proximal LCCA. This is likely to induce arterial remodeling in the proximal LCCA during follow-up.¹⁵ The correlation between flow alterations and intimal thickening and stenosis has been investigated extensively.¹⁶ Moreover, increased flow velocities induce elevated endothelial shear stresses, which are not only a triggering factor for arterial remodeling, but also atherosclerotic plaque formation and inflammatory processes.^{17,18} Besides inducing arterial remodeling, the outflow tract of the left carotid-to-subclavian bypass can be a relatively low resistance path compared to the distal LCCA, especially if a stenosis is present distal to the bypass, resulting in subclavian steal from the LCCA. Further research is warranted to study these scenarios and the impact of different treatment options, such as the use of a branched endograft versus left carotid-to-subclavian bypass, on blood flow in the carotid and vertebral arteries following zone 2 TEVAR.

Previous studies showed the relationship between displacement forces and endograft migration in the abdominal aorta.¹⁹ Compared to the abdominal aorta, the displacement force is significantly larger and directed cranial in the thoracic aorta.^{14,20} Endograft size is a key determinant of the magnitude of the displacement force.²¹ Our results confirm these findings. The patient in whom we had calculated the highest displacement force, measuring 31.1 N, presented with Type Ib endoleak after 1-year follow-up. The displacement force calculated in this patient lies within the range of pull-out forces described by Rahmani et al.²² Interestingly, we calculated a similar displacement force in Patient 3, measuring 30.4 N, however no migration or endoleak was found in this case. We hypothesize that the direction of the displacement force being perpendicular to the distal sealing zone might have attributed to the endograft being pulled out of its original position.

Further investigation of the hemodynamic displacement force and the complex of compensatory radial and frictional forces, securing stability of the endograft in the sealing zones, is needed. In the future these mechanisms could potentially be taken

into account in preoperative planning for TEVAR, thus reducing the risk of Type I endoleak.

Limitations

A limitation of the CFD simulations performed for this study is the rigid wall assumption. More accurate simulations would include fluid structure interaction, for which computational costs are significantly higher.²³

We simulated only flow through arteries for which we had patient-specific flow measurements; therefore, we did not include the coronary and distal carotid arteries in our models.

Our CFD simulation results showed increased flow velocities in the LCCA. Future prospective studies that focus on the impact of TEVAR in zone 2 on cerebral blood flow should also include flow measurements more distal in the internal and external carotid arteries and in the vertebral arteries.

The small number of patients included in the present study limits the impact of the results. Although clear trends were found, studies consisting of a larger study population are needed to confirm our findings.

Conclusion

TEVAR in proximal landing zone 2 alters blood flow in the supra-aortic branches, resulting in increased flow with high flow velocities in the LCCA. Our results warrant further investigation of cerebral blood flow following TEVAR in the aortic arch. The use of large endografts in the thoracic aorta results in high displacement forces, increasing the risk of endograft migration and Type I endoleak during follow-up.

References

- 1 Goodney PP, Travis L, Lucas FL, et al. Survival after open versus endovascular thoracic aortic aneurysm repair in an observational study of the Medicare population. *Circulation* 2011;124(24):2661–9. Doi: 10.1161/CIRCULATIONAHA.111.033944.
- 2 Gopaldas RR, Huh J, Dao TK, et al. Superior nationwide outcomes of endovascular versus open repair for isolated descending thoracic aortic aneurysm in 11,669 patients. *J Thorac Cardiovasc Surg* 2010;140(5):1001–10. Doi: 10.1016/j.jtcvs.2010.08.007.
- 3 Gutsche JT, Cheung AT, McGarvey ML, et al. Risk factors for perioperative stroke after thoracic endovascular aortic repair. *Ann Thorac Surg* 2007;84(4):1195–200; discussion 1200. Doi: 10.1016/j.athoracsur.2007.04.128.
- 4 Ishimaru S. Endografting of the aortic arch. *J Endovasc Ther* 2004;11 Suppl 2:II62-71. Doi: 10.1583/04-1407.1.

- 5 Patterson B, Holt P, Nienaber C, et al. Aortic pathology determines midterm outcome after endovascular repair of the thoracic aorta: report from the Medtronic Thoracic Endovascular Registry (MOTHER) database. *Circulation* 2013;127(1):24–32. Doi: 10.1161/CIRCULATIONAHA.112.110056.
- 6 Sobocinski J, Patterson BO, Karthikesalingam A, et al. The Effect of Left Subclavian Artery Coverage in Thoracic Endovascular Aortic Repair. *Ann Thorac Surg* 2016;101(2):810–7. Doi: 10.1016/j.athoracsur.2015.08.069.
- 7 Contrella BN, Sabri SS, Tracci MC, et al. Outcomes of Coverage of the Left Subclavian Artery during Endovascular Repair of the Thoracic Aorta. *J Vasc Interv Radiol* 2015;26(11):1609–14. Doi: 10.1016/j.jvir.2015.07.022.
- 8 Ullery BW, McGarvey M, Cheung AT, et al. Vascular distribution of stroke and its relationship to perioperative mortality and neurologic outcome after thoracic endovascular aortic repair. *J Vasc Surg* 2012;56(6):1510–7. Doi: 10.1016/j.jvs.2012.05.086.
- 9 Kanaoka Y, Ohki T, Maeda K, et al. Analysis of Risk Factors for Early Type I Endoleaks After Thoracic Endovascular Aneurysm Repair. *J Endovasc Ther* 2016. Doi: 10.1177/1526602816673326.
- 10 Van Bogerijen GHW, Auricchio F, Conti M, et al. Aortic hemodynamics after thoracic endovascular aortic repair, with particular attention to the bird-beak configuration. *J Endovasc Ther* 2014;21(6):791–802.
- 11 Alimohammadi M, Agu O, Balabani S, et al. Development of a patient-specific simulation tool to analyse aortic dissections: assessment of mixed patient-specific flow and pressure boundary conditions. *Med Eng Phys* 2014;36(3):275–84. Doi: 10.1016/j.medengphy.2013.11.003.
- 12 Vignon-Clementel IE, Figueroa CA, Jansen KE, et al. Outflow boundary conditions for 3D simulations of non-periodic blood flow and pressure fields in deformable arteries. *Comput Methods Biomech Biomed Engin* 2010;13(5):625–40. Doi: 10.1080/10255840903413565.
- 13 Morris L, Delassus P, Walsh M, et al. A mathematical model to predict the in vivo pulsatile drag forces acting on bifurcated stent grafts used in endovascular treatment of abdominal aortic aneurysms (AAA). *J Biomech* 2004;37(7):1087–95. Doi: 10.1016/j.jbiomech.2003.11.014.
- 14 Figueroa CA, Taylor CA, Chiou AJ, et al. Magnitude and direction of pulsatile displacement forces acting on thoracic aortic endografts. *J Endovasc Ther* 2009;16(3):350–8. Doi: 10.1583/09-2738.1.
- 15 Nichols W, O'Rourke M, Vlachopoulos C. The nature of flow of a liquid. In: Nichols, W., O'Rourke, M., Vlachopoulos, C.. *McDonald's blood flow in arteries: theoretical, experimental and clinical principles*. 6th ed. New York: CRC Press; 2011.
- 16 Grant EG, Benson CB, Moneta GL, et al. Carotid artery stenosis: gray-scale and Doppler US diagnosis—Society of Radiologists in Ultrasound Consensus Conference. *Radiology* 2003;229(2):340–6. Doi: 10.1148/radiol.2292030516.
- 17 Cecchi E, Giglioli C, Valente S, et al. Role of hemodynamic shear stress in cardiovascular disease. *Atherosclerosis* 2011;214(2):249–56. Doi: 10.1016/j.atherosclerosis.2010.09.008.
- 18 Morbiducci U, Kok AM, Kwak BR, et al. Atherosclerosis at arterial bifurcations: evidence for the role of haemodynamics and geometry. *Thromb Haemost* 2016;115(3):484–92. Doi: 10.1160/TH15-07-0597.
- 19 Figueroa CA, Yeh V, Taylor CA, et al. In vivo displacement force (DF) is higher in patients who experience aortic endograft migration: A 3D computational analysis. *J Vasc Surg* 2010;51(6):93S.

- 20 Krsmanovic D, Koncar I, Petrovic D, et al. Computer modelling of maximal displacement forces in endoluminal thoracic aortic stent graft. *Comput Methods Biomech Biomed Engin* 2014;17(9):1012–20. Doi: 10.1080/10255842.2012.735661.
- 21 Prasad A, To LK, Gorrepati ML, et al. Computational analysis of stresses acting on inter-modular junctions in thoracic aortic endografts. *J Endovasc Ther* 2011;18(4):559–68. Doi: 10.1583/11-3472.1.
- 22 Rahmani S, Grewal IS, Nabovati A, et al. Increasing angulation decreases measured aortic stent graft pullout forces. *J Vasc Surg* 2016;63(2):493–9.
- 23 Brown AG, Shi Y, Marzo A, et al. Accuracy vs. computational time: translating aortic simulations to the clinic. *J Biomech* 2012;45(3):516–23. Doi: 10.1016/j.jbiomech.2011.11.041.

Chapter 10

Computational analysis of renal artery flow characteristics by modeling aortoplasty and aortic bypass interventions for abdominal aortic coarctation

Christopher Tossas-Betancourt^{1*}, BSc

Theodorus M.J. van Bakel^{2*}, MD

Christopher J. Arthurs³, DPhil

Dawn M. Coleman², MD

John Eliason², MD

C. Alberto Figueroa^{1,2}, PhD

James C. Stanley², MD

1. Department of Biomedical Engineering, University of Michigan, Ann Arbor, Michigan, USA.

2. Department of Surgery, University of Michigan, Ann Arbor, Michigan, USA.

3. Division of Imaging Sciences and Biomedical Engineering, King's College London, London, UK.

*contributed equally

Journal of Vascular Surgery. In press

Abstract

Objectives

Suprarenal abdominal aortic coarctation (SAAC) alters flow and pressure patterns to the kidneys and is often associated with severe angiotensin-mediated hypertension, refractory to drug therapy. SAAC is most often treated by a thoracoabdominal bypass (TAB) or patch aortoplasty (PA). It is currently unclear what effect these interventions have on renal flow and pressure waveforms. This study, using retrospective data from a SAAC patient subject to a TAB, undertook computational modeling to analyze aortorenal blood flow preoperatively as well as postoperatively following a variety of TAB and PA interventions.

Methods

Patient-specific anatomical models were constructed from preoperative computed tomographic angiograms of a 9-year old child with an isolated SAAC. Fluid-structure interaction (FSI) simulations of hemodynamics were performed to analyze preoperative renal flow and pressure waveforms. A parametric study was then performed to examine the hemodynamic impact of different bypass diameters and patch oversizing.

Results

Preoperative FSI results documented diastolic-dominated renal perfusion with considerable high frequency disturbances in blood flow and pressure. The postoperative TAB right and left kidney volumes increased by 58% and 79%, respectively, reflecting the increased renal artery blood flows calculated by the FSI analysis. Postoperative increases in systolic flow accompanied decreases in high frequency disturbances, aortic pressure and collateral flow following all surgical interventions. In general, lesser degrees of high frequency disturbances followed PA interventions. High frequency disturbances were eliminated with the 0% PA, in contrast to the 30% and 50% PA oversizing and TAB interventions in which these flow disturbances remained.

Conclusions

Both TAB and PA dramatically improved renal artery flow and pressure waveforms, although disturbed renal waveforms remained in many of the surgical scenarios. Importantly, only the 0% PA oversizing scenario eliminated all high frequency disturbances, resulting in near normal aortorenal blood flow. The study also establishes the relevance of patient-specific computational modeling when planning interventions for the midaortic syndrome.

Introduction

Suprarenal abdominal aortic coarctations (SAAC) are often associated with renal arterial stenoses and severe renin-mediated arterial hypertension.¹ In these circumstances, the increased blood pressure and development of collateral vessels circumventing the aortic and renal artery narrowings tend to increase mean renal blood flow toward normal. However, this response is inadequate and the abnormal release of renin persists. Whether the principal cause of the abnormal renin release is due to decreased renal artery pressure or abnormal renal artery flow waveforms is an unsettled issue.

The abnormal renin release and angiotensin generation coupled with secondary increases in aldosterone production make this form of hypertension refractory to most drug therapies. Lowering the systemic arterial pressure with drugs without treating the aortic and renal artery narrowings only results in further diminutions of intrarenal blood flow and continued excesses in renin production. Because of these medical failures, restoration of normal renal blood flow by open operative or endovascular interventions have evolved as the favored means of managing this disease.

The University of Michigan's history of treating occlusive lesions of the renal arteries and abdominal aorta in pediatric patients has extended for more than 4 decades.¹⁻⁶ Postoperative blood pressure control in this experience has been optimal when treating patients with isolated renal artery stenoses, in contrast to less salutary outcomes when the renal artery procedures have been accompanied by a thoracoabdominal bypass (TAB) or patch aortoplasty (PA) for a coexisting abdominal aortic coarctation. Even after successful anatomic aortic and renal artery reconstructions, postoperative hypertension has been noted to persist.^{1,7,8}

It is hypothesized that the aortic reconstructive procedures may not normalize renal artery blood flow. A TAB from above a SAAC to below the renal arteries may cause turbulent and abnormal renal artery perfusion as retrograde aortic flow encounters antegrade flow in the region of the renal vasculature. In addition, performance of a PA, given the commonplace practice of oversizing the patch in younger patients to accommodate for later growth, may also result in abnormal renal blood flow and contribute to the persistence of the hypertensive state.

Methods

Aortorenal blood flow was retrospectively studied using patient-specific fluid-structure interaction (FSI) simulations in a child that was treated for a SAAC. Subsequently, the impact of the most commonly undertaken surgical repairs (TAB and PA)

on aortorenal blood flow was analyzed. The study was approved by the University of Michigan Board of Review (HUM00112350 and HUM00006223).

Patient history

A 9-year-old girl was referred to the authors' institution with a diagnosis of middle aortic syndrome and renin mediated hypertension. Her initial elevated blood pressures in the 130-150/90-95 mmHg range were only modestly improved to the 140/80 mmHg range following treatment with a beta-blocker and calcium channel blocker. In addition, she initially complained of lower extremity weakness and fatigue that was progressive with activity. Duplex Doppler ultrasonography estimated a pressure gradient of 58 mmHg across the SAAC. She was considered an appropriate candidate for surgical repair of the abdominal aortic coarctation.

Imaging data

Preoperative anatomy and hemodynamic data were obtained using duplex Doppler ultrasonography, computed tomography angiography (CTA) and phase contrast magnetic resonance imaging (PC-MRI). CTA imaging revealed a SAAC of 15 mm in length, with a 2.5 mm anterior-posterior diameter, and no renal artery involvement (Figure 1). The celiac artery (CA) and superior mesenteric artery (SMA) arose from the coarctation itself, and both exhibited ostial narrowings. Extensive collaterals circumvented the coarcted aorta, with an intact inferior mesenteric artery (IMA) being the dominant source of blood flow to the intestines. The internal mammary arteries were enlarged and communicated with the epigastric arteries that had multiple collaterals to the lower extremities and abdominal visceral organs. MRI examinations performed at 10-day and 1-year after the TAB provided postoperative data for analysis.

Thoracoabdominal bypass

The basis for choosing a TAB over a PA was that the 2.5 mm diameter of the coarctation and the involvement of the CA and SMA would have made an aortoplasty inordinately challenging and risky. In this case a midline abdominal incision was made from the xiphoid to the pubis, followed by medial visceral rotation of the left colon, to provide exposure of the entire abdominal aorta.

The supra celiac aorta was occluded with a Satinsky clamp, following which a 14 mm polytetrafluoroethylene (PTFE) bypass graft was anastomosed to a lateral aortotomy. The proximal aorta was occluded for 17 minutes during which time blood flow to the lower extremities and abdominal viscera, although reduced, was maintained through the preexisting large retroperitoneal and abdominal wall collaterals. The graft was then clamped just beyond its aortic origin and antegrade aortic blood

flow was restored following removal of the supraceliac aortic clamp. The graft was passed behind the left kidney and then anastomosed in an end-to-side manner to a lateral aortotomy just above the IMA (Figure 1). During the distal anastomosis, the infrarenal aorta was occluded for a time similar to that of the proximal anastomosis.

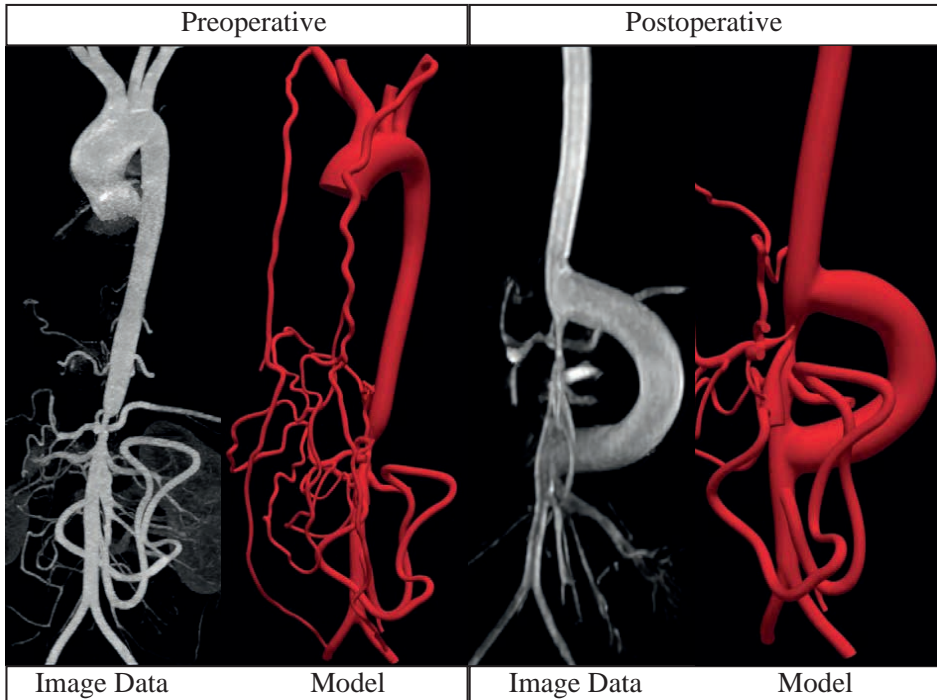


Figure 1. Preoperative (left) and postoperative (right) image data and corresponding computational models.

Kidney Size

Analyzing the preoperative and 10-day follow-up imaging data, an increase in kidney length was observed. Following this finding, preoperative and 10-day postoperative kidney volumes were measured using semi-automatic segmentation tools in Mimics version 21.0 (Materialise NV, Leuven, Belgium).

Computational modeling

Patient-specific FSI simulations were performed to assess preoperative blood flow and compare the hemodynamic performance of TAB versus PA using a “virtual testing” paradigm (Figure 2).⁹ First, a preoperative model was created and calibrated to match the anatomical and hemodynamic clinical data (Figure 3). Then, the calibrated preoperative model was adapted to reflect six surgical interventions (Figure 4), including three different TABs with 12 mm, 14 mm and 16 mm diameters, respec-

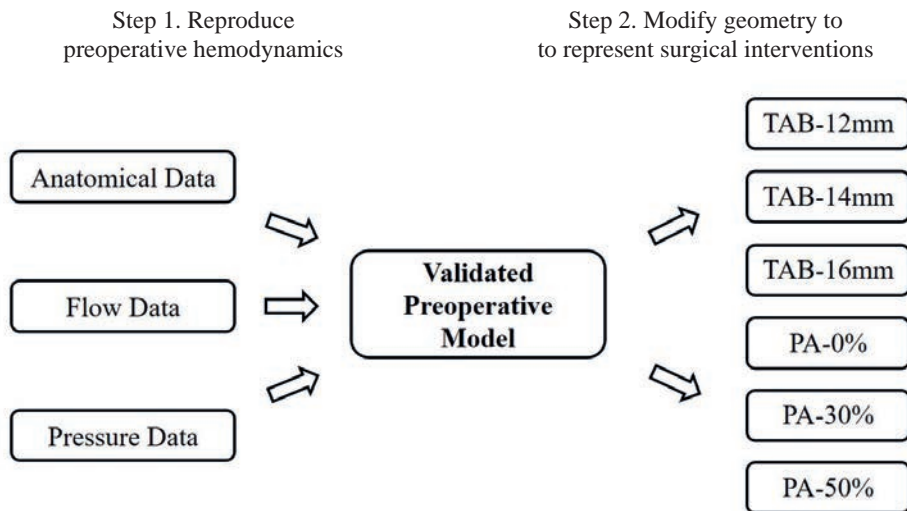


Figure 2. The patient-specific computational modeling paradigm is composed of two steps. First, a validated preoperative model is generated that matches clinical data on anatomy, flow and pressure. Then, the geometry of the validated preoperative model is modified to reflect the different surgical options. This approach enables a rigorous comparison between aortorenal hemodynamics following each virtual surgical option.

tively (TAB-12mm, TAB-14mm and TAB-16mm); and three different PAs producing increases in aortic diameters of 0%, 30% and 50% (PA-0%, PA-30% and PA-50%) relative to the native aorta. Additionally, a control case was constructed by adjusting the preoperative model to produce a healthy anatomy without coarctation and collateral vessels.

The preoperative and six surgical repair models were constructed from the CTA image data using the cardiovascular modeling and simulation software CRIMSON.¹⁰ Besides the vascular anatomy, each FSI model requires specification of arterial wall material properties (thickness and stiffness) as well as outflow boundary conditions at each branch. These boundary conditions represent the compliance and resistance of the distal vasculature not included in the anatomical model. The wall properties and outflow boundary conditions were calibrated to match the simulation results with the clinically acquired flow and pressure data and achieve reasonable regional flow distributions¹¹ (Figure 3). In the control case, the boundary conditions were tuned to match the preoperative flow splits and a blood pressure appropriate for this patient's size and age (96/65 mmHg).¹² In the postoperative models, cardiac output and outflow boundary conditions were kept the same as preoperative; with the exception of the supra-aortic arteries, where the outflow boundary conditions were adjusted to reproduce physiologic cerebral flow rates.¹¹

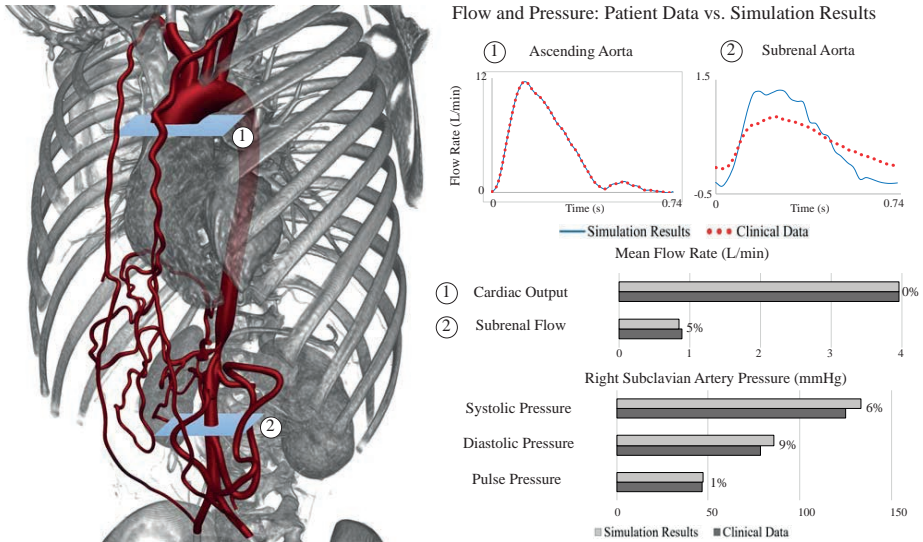


Figure 3. Left: Preoperative anatomy containing the PC-MRI planes (1 and 2) at which the flow measurements were acquired. Right: Comparison between the clinically measured flow and pressure data, and the simulation results in the validated preoperative model. The clinically measured flow data (red dotted line) and simulated flow results (blue line) correspond to the indicated PC-MRI planes (1 and 2). The bar graphs in the bottom right corner compare mean values of clinical data (dark grey) and simulation results (light grey). All mean preoperative clinical flow data is matched within a 5% error margin; and the pressure clinical data within a 10% error margin.

Computations

Blood was modeled as an incompressible Newtonian fluid with a density of 1,060 kg/m³ and a dynamic viscosity of 4.0 Pa·s. Computations were performed using the CRIMSON Navier-Stokes flow solver on 160 cores at the University of Michigan high-performance computing cluster ConFlux. Simulations were run until cycle-to-cycle periodicity was achieved in the pressure fields, this typically took three to five cycles. Computation time per cardiac cycle was approximately 48 hours.

Results

Postoperative course

Complete resolution of the patient's lower extremity discomfort was evident in the early postoperative period. Her serum creatinine which ranged from 0.48 to 0.57 mg/dL preoperatively, decreased to 0.28 to 0.3 mg/dL postoperatively. However, she remained mildly hypertensive during her postoperative hospitalization, and at 1-year follow-up she remained on a low dose calcium channel blocker with resting blood pressures in the 110-115/65-70 mmHg range.

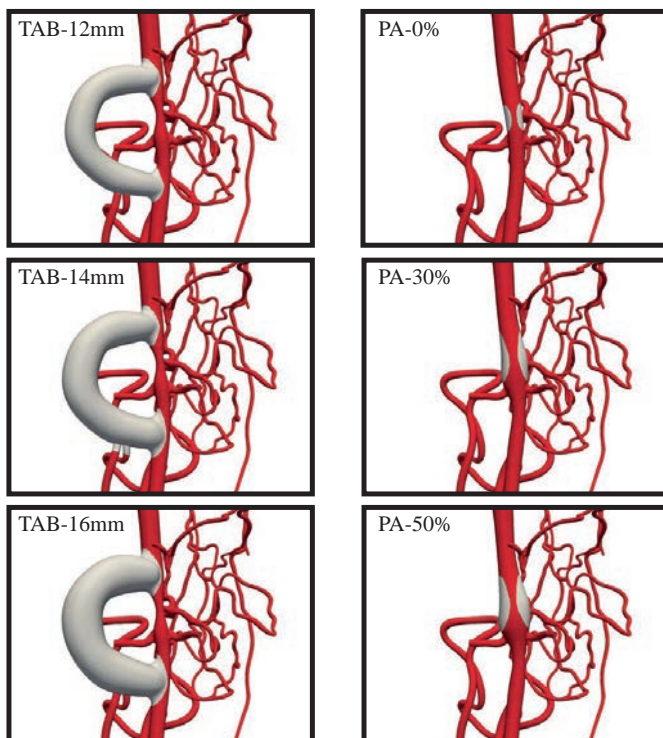


Figure 4. Close-up posterior views of the abdominal coarctation region and the renal arteries of all TAB (left) and PA (right) options. Graft material of the bypass and patch is presented in grey. TAB = thoracoabdominal bypass; PA = patch aortoplasty.

Preoperative Simulation

The baseline preoperative model successfully reproduced the patient's hemodynamic data, as documented in a comparison between clinical data and simulation results at different locations in the circulation (Figure 3). The computed flows were all within 5% of the clinically measured data, and computed pressures were within 10%.

The FSI simulation results revealed a pressure gradient of 55 mmHg across the coarctation at peak-systole (Figure 5), which matched the pressure gradient derived from duplex Doppler ultrasonography (58 mmHg). Additionally, disturbed flow patterns were present distal to the coarctation which propagated into the renal arteries. Assessment of the renal artery flow and pressure waveforms revealed diastolic dominated renal flows with high frequency oscillations (Figure 5 and Video 1). Renal artery pressure was markedly lower than ascending aortic pressure.

In the control case, systolic dominated renal flows without high-frequency disturbances were found. The results for the control anatomy are presented in the Appendix and Video 1. A direct comparison of the pressure and flow waveforms between preoperative and control cases is reported in Figure 6.

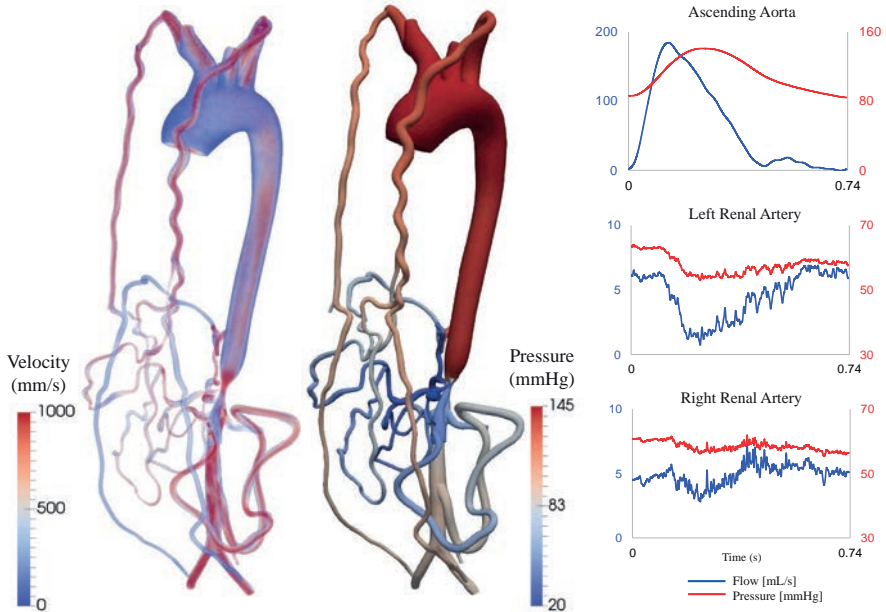


Figure 5. Left: 3D maps of preoperative hemodynamics in peak systole. Note the high velocities and large pressure gradient through the coarctation. Right: flow (blue) and pressure (red) waveforms in the ascending aorta, left renal artery, and right renal artery. The renal artery waveforms reveal diastolic dominated flows with high frequency disturbances and low pressures compared to aortic pressure.

Postoperative Simulations

The computed mean flows at the outlets of the preoperative model and all six surgical repair models (Table 1) were revealing. All six interventions successfully reduced pressures at the ascending aorta (Figure 7) and increased renal artery flow rates (Table 1). Furthermore, all surgical repairs resulted in systolic dominated flow waveforms (Figure 8), with a reduction of the high frequency flow and pressure disturbances in the renal arteries (Figures 8 and 9). Although most postoperative simulations retained some degree of the high frequency oscillations, the PA-0% eliminated the high frequency oscillations completely.

The flow waveforms from the TAB-14mm simulation were compared with the PC-MRI data at 1-year follow-up (Figure 10). The patient's cardiac output decreased during follow-up (-13%, from 3.9 to 3.2 L/min). The shape of the waveform changed as a result of a reduction in ventricular afterload following surgery. The computed (TAB-14mm) and 1-year follow-up PC-MRI data on flow through the bypass documented an excellent match: the percentages of cardiac output through the bypass were 38% and 39% for the computations and the PC-MRI data, respectively.

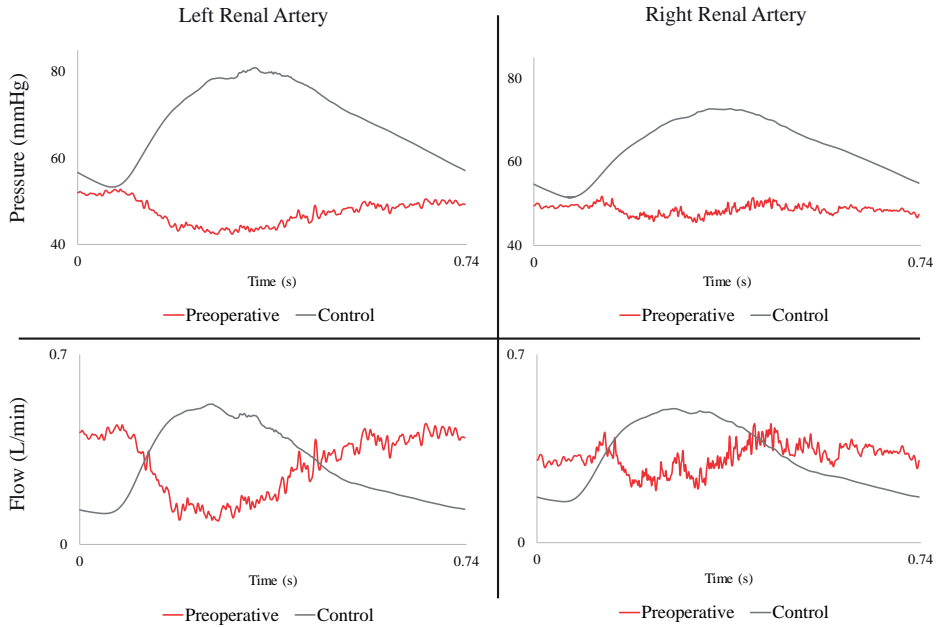


Figure 6. Comparison of the renal artery waveforms between the preoperative and control case shows that removal of the pathologic anatomy results in higher renal pressures, elimination of the high-frequency disturbances and systolic dominated waveforms.

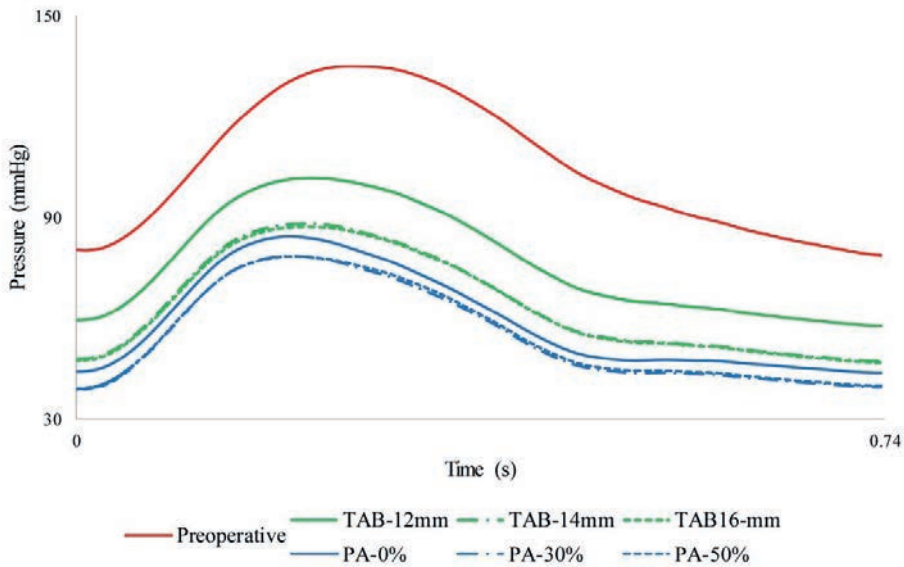


Figure 7. Ascending aortic pressure waveforms in all models. All postoperative models exhibited an important pressure reduction compared to the preoperative state. PA procedures resulted in a greater decrease of aortic pressure compared to TAB procedures. PA = patch aortoplasty; TAB = thoracoabdominal bypass.

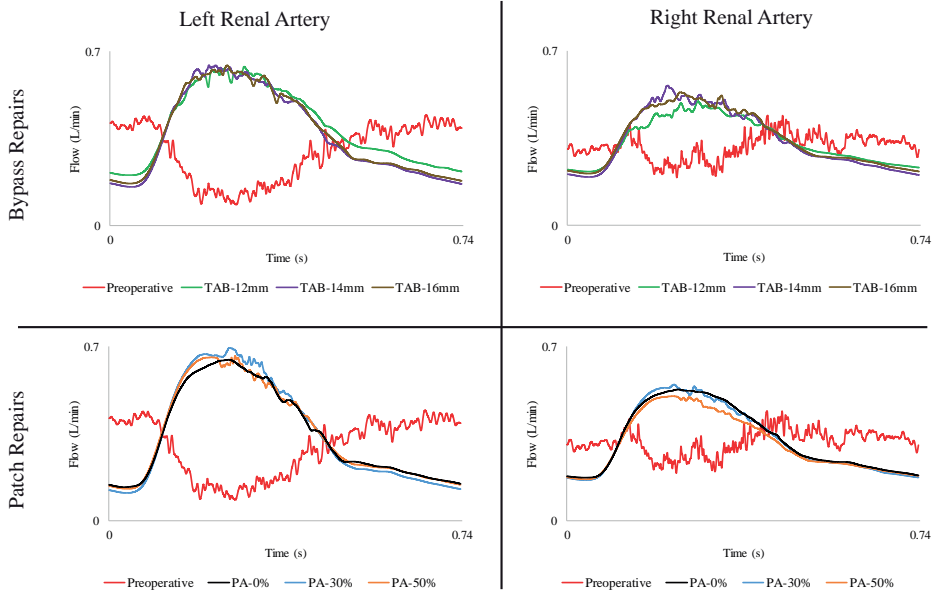


Figure 8. Renal flow waveforms in all models. Both TAB and PA resulted in restoration of systolic-dominated renal flows, reduction of high frequency disturbances and increased flow. Some degree of high-frequency disturbances persisted in all postoperative scenarios, with the exception of PA-0%, which revealed near normal renal flow waveforms.

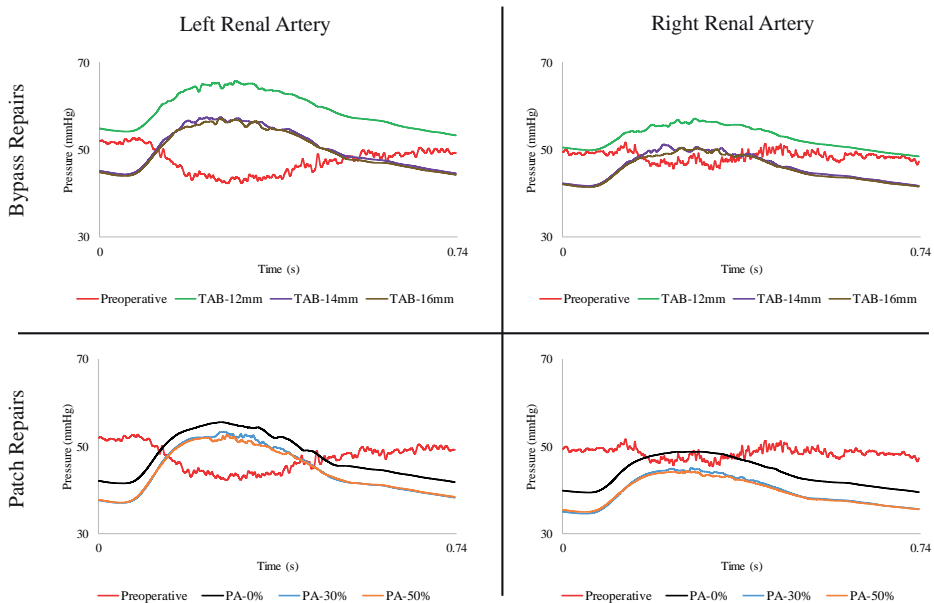


Figure 9. Renal pressure waveforms in all models. Most surgical repairs resulted in a reduction in renal artery pressures, associated with the large reductions in aortic pressures in all postoperative models (Figure 7).

Table 1. Simulated mean flow rates (mL/min)

Vessel	Preoperative	TAB-12mm	TAB-14mm	TAB-16mm	PA-0%	PA-30%	PA-50%
LCCA	275	351	319	308	321	344	356
LSA	269	330	305	295	305	328	336
RCCA	276	351	320	309	321	344	357
RSA	274	325	306	296	305	328	331
SMA	573	566	528	534	551	557	580
LGA	292	207	265	273	262	233	212
SA	300	175	249	257	267	227	219
HA1	98	50	94	101	94	80	60
HA2	159	84	128	124	127	108	101
LRA	291	394	370	374	353	360	360
RRA	313	337	345	350	331	331	317
IMA	91	84	78	79	75	74	76
LIA	278	255	230	233	226	227	230
RIA	282	262	236	239	232	231	235
Renal Flow	605	732 (+21%)	715 (+18%)	724 (+20%)	684 (+13%)	691 (+14%)	677 (+12%)
Mesenteric Flow	1421	1082 (-24%)	1263 (-11%)	1289 (-9%)	1301 (-8%)	1206 (-15%)	1173 (-17%)
Cerebral Flow	551	702 (+27%)	639 (+16%)	617 (+12%)	642 (+17%)	688 (+25%)	713 (+29%)

Mean flow to the kidneys is calculated by the sum of the left and right renal arteries. Mean flow to mesenteric region includes all flow through the left gastric artery, splenic artery, hepatic artery 1, and hepatic artery 2. Mean cerebral flow includes flow in the left and right common carotid arteries. Percentages are reported relative to the preoperative model.

HA1 = Hepatic Artery 1; HA2 = Hepatic Artery 2; IMA = Inferior Mesenteric Artery; LCCA = Left Common Carotid Artery; LGA = Left Gastric Artery; LIA = Left Iliac Artery; LRA = Left Renal Artery; LSA = Left Subclavian Artery; PA = patch aortoplasty; RCCA = Right Common Carotid Artery; RIA = Right Iliac Artery; RRA = Right Renal Artery; RSA = Right Subclavian Artery; SA = Splenic Artery; SMA = Superior Mesenteric Artery; TAB = thoracoabdominal bypass.

Kidney Size

Considerable changes in the kidney length were noted at 10-day follow-up. To accurately quantify the change in kidney size, volumetric measurements of both kidneys were obtained (Figure 11). Right and left kidney volumes increased from 50.3 to 79.6 cm³ (+58%) and 51.5 to 92.0 cm³ (+79%), respectively. The observed increments in kidney volume reflected the calculated increases in right and left renal flow from the TAB-14mm FSI analysis (+9% and +26%, respectively).

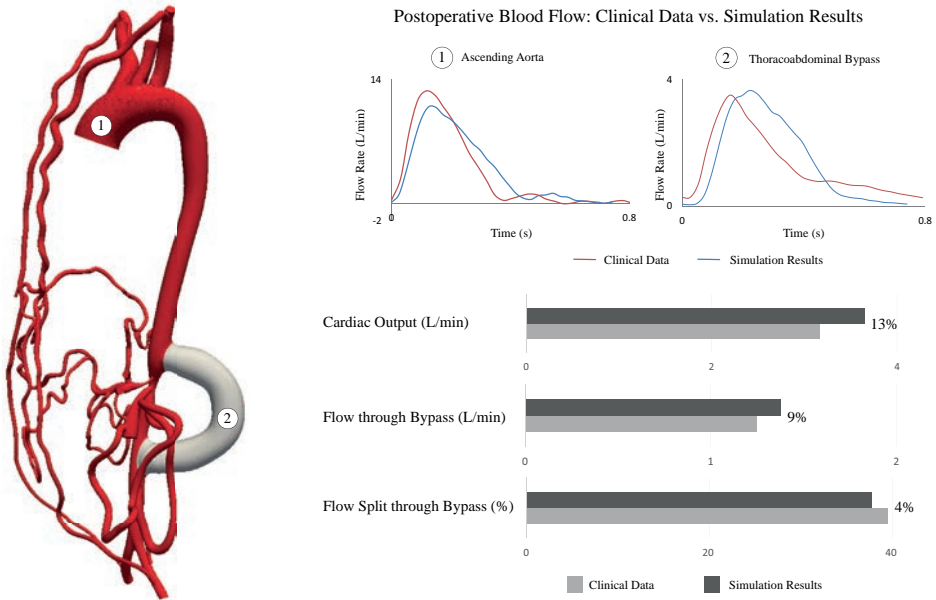


Figure 10. Comparison of the flow waveforms from the TAB-14mm simulation results and PC-MRI imaging data at 1-year follow-up. Cardiac output decreased during follow-up (from 3.9 to 3.2 L/min). The shape of the waveform changed as a result of a reduction in ventricular afterload following surgery. The computed (TAB-14mm) and 1-year follow-up PC-MRI data on flow through the bypass documented an excellent match: the percentages of cardiac output through the bypass were 38% and 39% for the computations and the PC-MRI data, respectively.

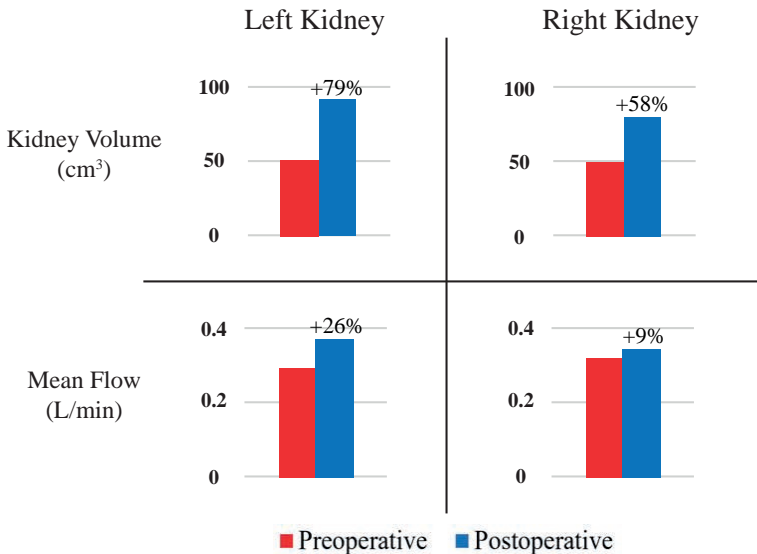


Figure 11. Preoperative (red) and postoperative (TAB-14mm, blue) clinically-measured kidney volumes and mean simulated renal artery flow rates. Percentages indicate the change from the preoperative to the postoperative conditions.

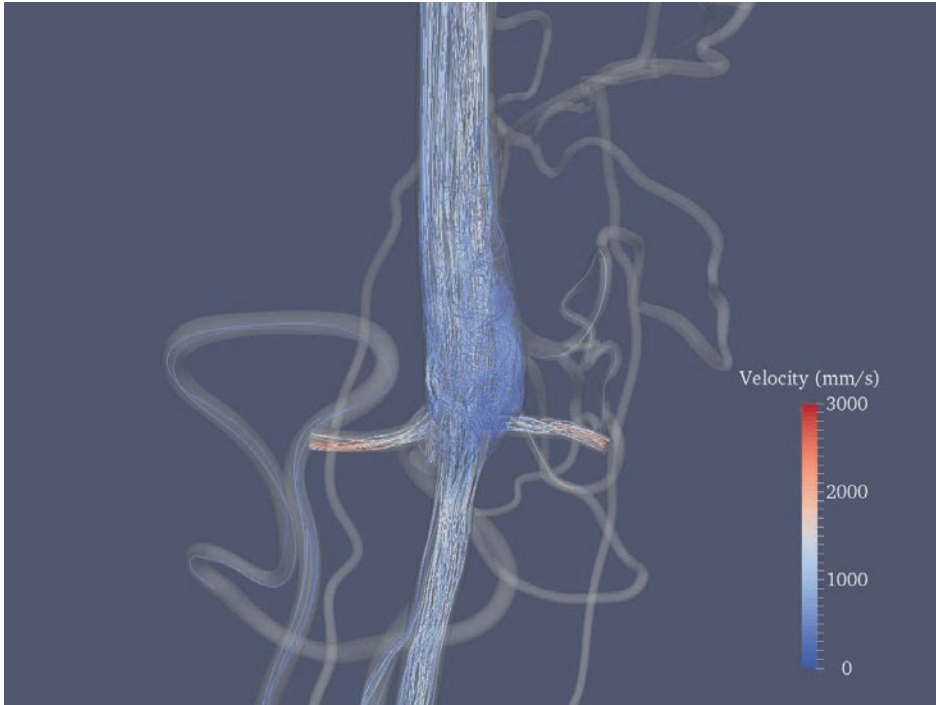


Figure 12. Velocity streamlines for the PA-50% model at mid-deceleration ($t=0.30$ s). Disturbed flow patterns are clearly evident in the region of the patch, propagating into the renal arteries.

Discussion

Abdominal aortic coarctation is a rare vascular disease recognized most frequently in pediatric-age patients. The aortic narrowings are commonly associated with ostial stenoses of the celiac, superior mesenteric, and renal arteries.¹³ This is clinically referred to as the middle aortic syndrome, which manifests in most patients with drug therapy resistant arterial hypertension.¹⁴

Classic canine experiments noted that the location of the abdominal coarctation plays a key role in the presence of hypertension.¹⁵ Hypertension is commonly observed in cases where the coarctation is suprarenal or involves the renal arteries. Conversely, hypertension is mostly absent when the coarctation is distal to the renal arteries. An investigation by Scott et al.¹⁶ of canine hypertension due surgically induced coarctation of the aorta that resulted in hypertension at 5 to 7 weeks, noted that transposition of a kidney to a level above the coarctation and contralateral nephrectomy resulted in disappearance of hypertension. These earlier experiments suggest that disturbed aortorenal blood flow contributes to hypertension in abdominal coarctation.

When treating middle aortic syndrome, conventional surgical reconstructive procedures and catheter-based interventions are favored over long-term drug therapy.^{1,7,17-20} Operative planning is usually derived solely from preoperative imaging.²¹ Surgical decisions are often based on technical issues at hand, rather than aiming to restore normal aortorenal blood flow. Unfortunately, endovascular balloon dilation with or without stenting of abdominal aortic narrowings has had limited use with mixed early results and few long-term successes. Open operations, such as TAB and PA, have been the most common form of treating abdominal aortic coarctations. These operations often lead to improved hypertension control, yet most cases still depend on antihypertensive therapy to maintain normal blood pressures for gender and age.

Many factors go into decision making for performing a PA versus a TAB. A PA is favored in most instances of a limited aortic coarctation distant from the CA, SMA and renal arteries. When assessing the long-term benefits of PA in younger patients, the patch is intentionally oversized to account for the child's expected growth. Nevertheless, the appropriate degree of patch oversizing has not been established. Likewise, the effects on renal artery blood flow accompanying a disproportionately enlarged aorta following a PA are unknown.

A TAB is the procedure of choice when treating more severe coarctations with abdominal aortic diameters of only a few millimeters. In this case, a PA would have near-overlapping sutures from the lateral walls of the patch. In the past, the authors have recommended a wide range of TAB diameters related to age, with the intent that the bypass diameter would at least be 60% to 70% of the predicted adult aorta.¹ These recommendations may be logical, but as noted with PA oversizing, the science behind such is meager.

Clinical Experience

Recently, the authors reviewed their experience with 155 children having renal artery stenotic disease and renovascular hypertension.⁶ Hypertension outcomes were better in children treated with renal artery reconstructions alone compared to those requiring additional aortic procedures. The hypertension cure, improved, and failure rates in patients without aortic pathology (n=98) were 50%, 34% and 16%, respectively. These outcome rates were 33%, 59% and 8% in patients additionally treated with PA (n=28); and 35%, 50% and 15% in patients additionally treated with TAB (n=29). Given the poorer outcomes in patients undergoing concomitant aortic procedures, one must question whether abnormal aortorenal flow remains after surgery, and if differences exist between surgical repair with TAB and PA.

Computational Modeling

Computational modeling is a widely used method in engineering fields that can be applied to study complex flow dynamics. Image-based computational tools have been developed for cardiovascular disease research,²² medical device evaluation²² and, more recently, virtual planning of surgical interventions.⁹ While in other engineering fields the 'virtual testing' paradigm has largely replaced the traditional 'build-and-test' (e.g. trial and error) paradigm, this is not yet the case in the medical field. As evident in the current investigation, the value of computational modeling is apparent in preoperative determination of the therapeutic impact of different sizes of TAB and PA in patients with the midaortic syndrome.

Computational modeling in this investigation provided data of much higher spatial (up to 0.05 mm) and temporal (0.025 ms) resolution than available in any contemporary imaging test. This high-resolution data revealed an unexpected and potentially relevant finding of high frequency disturbances in the renal arteries preoperatively that could explain an increased renin release in the kidneys, resulting in secondary hypertension. Persistent high frequency disturbances were also found in the postoperative models and might explain the continuing hypertension following both TAB and PA interventions in patients undergoing concomitant renal artery reconstructions.

Besides characterization of preoperative aortorenal blood flow, this study also analyzed the impact of different TAB diameters and degree of PA oversizing. In total, six different surgical treatment options were studied: three TAB diameters and three levels of PA oversizing. All surgical interventions resulted in reduced aortic pressures, and increased renal flows with restoration of systolic-dominated waveforms.

An unexpected finding of this investigation was that most surgical repairs resulted in a reduction in renal artery pressures (Figure 8). This acute response of the system, which does not account for any auto-regulatory processes following the surgery, is reflective of the large reductions in aortic pressures in all postoperative models (Figure 6).

Importantly, various degrees of high frequency disturbances persisted postoperatively, the exception being the treatment with a 0% PA which eliminated the high frequency disturbances completely. These results suggest that excessive PA oversizing and TAB lead to high frequency disturbances that may contribute to continued renin-mediated hypertension.

In the TAB operations, the high frequency disturbances could be explained by the turbulent mixing of antegrade flow through the remaining aortic stenosis and retrograde flow through the TAB. Changing the TAB graft diameter did not significantly impact the persistence of high frequency disturbances. Such flow abnormalities could explain why the patient in the present case report, who had undergone a TAB repair,

was still dependent on anti-hypertensive medication at 1-year follow-up. In an oversized PA, the dilated segment of the reconstruction induces flow disturbances. Flow clearly shows complex recirculation and vortices in the region of the patch (Figure 12), similar to what is observed in aneurysmal disease. The absence of dilation in the PA-0% case explains the lack of disturbances in this model. Furthermore, it may also explain the reduced hypertension cure rates of renal artery revascularizations in the authors' larger series of patients requiring concomitant aortic procedures.

Historically, renin-mediated hypertension has been linked to low perfusion pressure and low renal blood flow.²¹ The high frequency flow oscillations observed in the present work have not been described in the earlier literature. The most likely explanation for this is that contemporary clinical measurement devices lack the temporal resolution necessary to detect such high frequency flow oscillations. It has been recognized that Doppler ultrasonography, CTA and MRI can all be helpful in the evaluation of renovascular disease, but none have, at present, high enough sensitivity to rule out renovascular disease in a child with a suggestion of that diagnosis.²⁴

Limitations

The stiffness properties of the aortic wall could not be calculated with the available data in this study. Therefore, in the present investigation, the assigned stiffness parameters were derived from a previous study from our laboratory which characterized aortic stiffness in a cohort of pediatric patients with aortic coarctation.²⁵ In that study, the aortic stiffness was calculated using strain measurements from MRI and invasive pressure measurements from catheterization.

This investigation analyzed aortorenal blood flow in a single patient with a supra-renal abdominal aortic coarctation. While the results for this patient were clinically-validated, performing the same analysis in patients with different anatomical features might result in different outcomes, including the presence of high-frequency disturbances in the renal arteries. Additionally, the causality between the high frequency disturbances and excessive renin release should be further investigated. Furthermore, we tested six different surgical interventions with arbitrary TAB and PA sizes. Performing a parametric study of other patch and bypass sizes and configurations could result in different outcomes.

Furthermore, it is important to note that even though a specific intervention might theoretically render a better hemodynamic outcome, performance of the procedure itself may be inordinately challenging and risky, resulting in a technical failure and less successful outcome. Thus, acceptance of benefits defined by virtual testing must be tempered by clinical judgement and expertise.

Lastly, the results presented here do not take into account any of the vascular auto-regulations that undoubtedly occur after a vascular reconstruction. The magnitude

of the waveforms, specifically the pressure, might change as a result of systemic vasoreactivity, although the high frequency disturbances are likely to persist.

Conclusions

This study has revealed the presence of high frequency disturbances in renal blood flow and pressure following operative interventions for SAAC. These previously unrecognized disturbances may be a fundamental contributor to continued abnormal release of renin, and thus the basis of the often-seen persistent post-operative hypertension in this patient population.

Considerable value resides in computational modeling of vascular surgery procedures. Patient-specific modeling provides high-resolution hemodynamic information for differing interventions, and allows preoperative planning for complex procedures, such as those accompanying aortic reconstructions in young patients with SAAC. Collaborative efforts between biomedical engineers and clinicians will be essential to providing accurate modeling and simulation of feasible surgical procedures in this setting.

References

- 1 Stanley JC, Criado E, Eliason JL, et al. Abdominal aortic coarctation: Surgical treatment of 53 patients with a thoracoabdominal bypass, patch aortoplasty, or interposition aortoortic graft. *J Vasc Surg* 2008;48(5):1073–82. Doi: 10.1016/j.jvs.2008.05.078.
- 2 Fry WJ, Ernst CB, Stanley JC, et al. Renovascular hypertension in the pediatric patient. *Arch Surg* 1973;107(5):692–8.
- 3 Stanley JC, Fry WJ. Pediatric renal artery occlusive disease and renovascular hypertension. Etiology, diagnosis, and operative treatment. *Arch Surg* 1981;116(5):669–76.
- 4 Stanley JC, Zelenock GB, Messina LM, et al. Pediatric renovascular hypertension: a thirty-year experience of operative treatment. *J Vasc Surg* 1995;21(2):212–26; discussion 226–7.
- 5 Stanley JC, Criado E, Upchurch GR, et al. Pediatric renovascular hypertension: 132 primary and 30 secondary operations in 97 children. *J Vasc Surg* 2006;44(6):1219–28. Doi: 10.1016/j.jvs.2006.08.009.
- 6 Coleman DM, Eliason JL, Jackson T, et al. SS26 Surgical Management of Pediatric Renovascular Hypertension. *J Vasc Surg* 2017;65(6):138S. Doi: 10.1016/j.jvs.2017.03.258.
- 7 Rumman RK, Nickel C, Matsuda-Abenedini M, et al. Disease beyond the arch: A systematic review of middle aortic syndrome in childhood. *Am J Hypertens* 2015;28(7):833–46. Doi: 10.1093/ajh/hpu296.
- 8 Rocchini AP, Rosenthal A, Barger AC, et al. Pathogenesis of paradoxical hypertension after coarctation resection. *Circulation* 1976;54(3):382–7.

- 9 van Bakel TMJ, Lau KD, Hirsch-Romano J, et al. Patient-Specific Modeling of Hemodynamics: Supporting Surgical Planning in a Fontan Circulation Correction. *J Cardiovasc Transl Res* 2018;11(2):145–55. Doi: 10.1007/s12265-017-9781-x.
- 10 CRIMSON. The software for Cardiovascular Modelling and Simulation. www.crimson.software.
- 11 Lantz BMT, Foerster JM, Link DP, et al. Regional distribution of cardiac output: Normal values in man determined by video dilution technique. *Am J Roentgenol* 1981;137(5):903–7. Doi: 10.2214/ajr.137.5.903.
- 12 National High Blood Pressure Education Program Working Group on High Blood Pressure in Children and Adolescents. The fourth report on the diagnosis, evaluation, and treatment of high blood pressure in children and adolescents. *Pediatrics* 2004;114(2 Suppl 4th Report):555–76.
- 13 Cohen JR, Birnbaum E. Coarctation of the abdominal aorta. *J Vasc Surg* 1988;8(2):160–4. Doi: 10.1016/0741-5214(88)90404-1.
- 14 Panayiotopoulos YP, Tyrrell MR, Koffman G, et al. Mid-aortic syndrome presenting in childhood. *Br J Surg* 1996;83(2):235–40. Doi: 10.1002/bjs.1800830228.
- 15 Goldblatt H, Kahn JR, Hanzal RF. Studies on experimental hypertension: IX. The effect on blood pressure of constriction of the abdominal aorta above and below the site of origin of both main renal arteries. *J Exp Med* 1939;69(5):649–74.
- 16 Scott HW, Bahnson HT. Evidence for a renal factor in the hypertension of experimental coarctation of the aorta. *Surgery* 1951;30(1):206–17. Doi: 10.5555/URI:PII:0039606051900189.
- 17 Porras D, Stein DR, Ferguson MA, et al. Midaortic syndrome: 30 years of experience with medical, endovascular and surgical management. *Pediatr Nephrol* 2013;28(10):2023–33. Doi: 10.1007/s00467-013-2514-8.
- 18 Sandmann W, Dueppers P, Pourhassan S, et al. Early and Long-term Results after Reconstructive Surgery in 42 Children and Two Young Adults with Renovascular Hypertension due to Fibromuscular Dysplasia and Middle Aortic Syndrome. *Eur J Vasc Endovasc Surg* 2014;47(5):509–16. Doi: 10.1016/j.ejvs.2013.12.012.
- 19 Sethna CB, Kaplan BS, Cahill AM, et al. Idiopathic mid-aortic syndrome in children. *Pediatr Nephrol* 2008;23(7):1135–42. Doi: 10.1007/s00467-008-0767-4.
- 20 Tummo A, Marks SD, Stadermann M, et al. Mid-aortic syndrome: long-term outcome of 36 children. *Pediatr Nephrol* 2009;24(11):2225–32. Doi: 10.1007/s00467-009-1242-6.
- 21 Castelli PK, Dillman JR, Smith EA, et al. Imaging of Renin-Mediated Hypertension in Children. *Am J Roentgenol* 2013;200(6):W661–72. Doi: 10.2214/AJR.12.9427.
- 22 Taylor CA, Figueroa CA. Patient-specific modeling of cardiovascular mechanics. *Annu Rev Biomed Eng* 2009;11:109–34. Doi: 10.1146/annurev.bioeng.10.061807.160521.
- 23 van Bakel TM, Arthurs CJ, van Herwaarden JA, et al. A computational analysis of different endograft designs for Zone 0 aortic arch repair. *Eur J Cardio-Thoracic Surg* 2018;54(2):389–96. Doi: 10.1093/ejcts/ezy068.
- 24 Tullus K, Roebuck DJ, McLaren CA, et al. Imaging in the evaluation of renovascular disease. *Pediatr Nephrol* 2010;25(6):1049–56. Doi: 10.1007/s00467-009-1320-9.
- 25 Sotelo JA, Valverde I, Beerbaum PB, et al. Pressure gradient prediction in aortic coarctation using a computational-fluid-dynamics model: validation against invasive pressure catheterization at rest and pharmacological stress. *J Cardiovasc Magn Reson* 2015;17(Suppl 1):Q78. Doi: 10.1186/1532-429X-17-S1-Q78.

Chapter 11

Challenges of thoracic endovascular aortic repair for type B aortic dissection

Theodorus M.J. van Bakel^{1,3,4}, MD

C. Alberto Figueroa^{1,2}, PhD

Joost A. van Herwaarden³, MD, PhD

Santi Trimarchi^{4,5}, MD, PhD

1. Department of Surgery, University of Michigan, Ann Arbor, Michigan, USA.
2. Department of Biomedical Engineering, University of Michigan, Ann Arbor, Michigan, USA.
3. Department of Vascular Surgery, University Medical Center Utrecht, Utrecht, The Netherlands.
4. Thoracic Aortic Research Center, Policlinico San Donato IRCCS, San Donato Milanese, Italy.
5. Department of Biomedical Sciences for Health, University of Milan, Italy.

Journal of Endovascular Therapy. 2018;25:578-580

Feasibility of thoracic endovascular aortic repair (TEVAR) for type B aortic dissection (TBAD) continues to be a subject of debate. Current guidelines recommend optimal medical therapy (OMT) for acute TBAD with continued imaging surveillance,¹ TEVAR is reserved for patients who present with complications.¹ However, 50% of patients who are initially treated with OMT alone develop aneurysmal degeneration of the weakened aortic wall during follow-up.²

The study of Menichini et al.³ presents two patients with aneurysmal dilation of the thoracic false lumen following TBAD. Both patients were treated with TEVAR, Patient 1 in the chronic phase, Patient 2 in the sub-acute phase. Early follow-up results were satisfactory, but at 14-month follow-up a stent-graft-induced new entry tear (SINE) with aneurysmal dilation was observed at the distal end of the stent-graft in Patient 1. The dissected aorta in Patient 2 remained stable. With the caveat of the simplistic modeling approach of this paper, which considered the aorta as a linear elastic material and disregarded the pre-stress, computational analysis showed higher stress, torsional strain, and wall displacement in Patient 1 compared to Patient 2. The region of high stress and displacement corresponded well with the location of SINE. The authors conclude that tortuosity, curvature and thoracic aortic length have a strong influence on local stress distributions and risk of SINE. We agree that patient-specific anatomical features can impose challenges for successful endovascular repair of TBAD and would like to comment on planning TEVAR in such cases.

In TBAD, timing has important implications for the biomechanical properties of the intimal flap.⁴ In the acute phase (within 2 weeks from onset of dissection), the intimal flap is still thin and highly mobile. Covering the proximal entry tear with a stent-graft in this phase induces positive aortic remodeling by reducing perfusion of the false lumen, approximating the intima to its original position and opening the true lumen. This way, TEVAR in the acute phase has shown to improve survival compared to OMT alone.^{5,6} Following the acute phase, the intimal flap becomes thicker and less mobile (Figure 1).⁴ After 8-12 weeks, TBAD is classified as chronic. TEVAR in the chronic phase is more challenging as the thickened intimal flap does not approximate to the aortic wall as it would in the acute phase.⁷ Furthermore, complete thrombosis of the false lumen is less likely to occur due to formation of persistent distal intimal tears that accommodate perfusion of the false lumen after TEVAR.⁷ Consequently, aortic remodeling is limited.⁸

Another challenging factor when performing TEVAR for TBAD is the tortuosity of the dissected aorta. Tortuosity increases wall stresses due to the spring-back forces in the stent-graft,³ reduces stability in the landing zones,⁹ and increases hemodynamic displacement forces that can cause stent-graft migration.^{10,11} To secure stability, the stent-graft needs to be sized correctly. The proximal and distal landing zone length

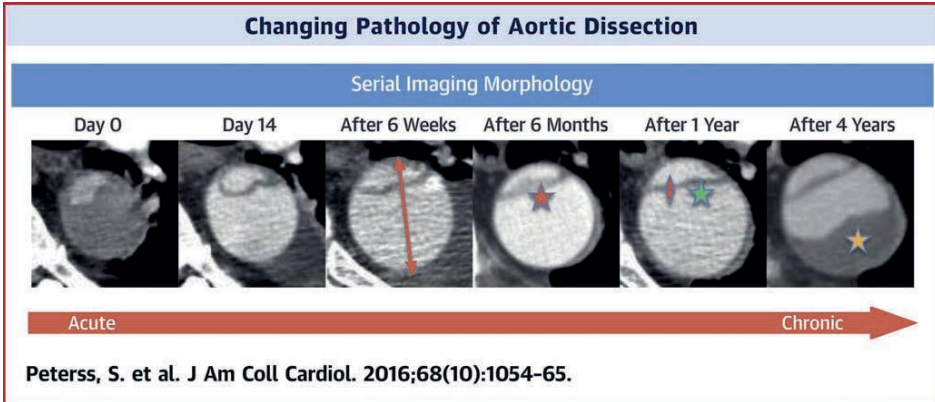


Figure 1. Changing morphology of a type B dissection over time by computed tomography in a single illustrative patient with multiple good quality images at the same aortic level.

Please note: 1) marked early increase in aortic diameter (orange arrow); 2) intimal thickening over time (orange star); 3) decreased flap motion over time (orange triangles); 4) flap straightening over time (green star); and 5) increased false lumen thrombosis over time (yellow star). Reprinted with permission from Peterss, et al.⁴

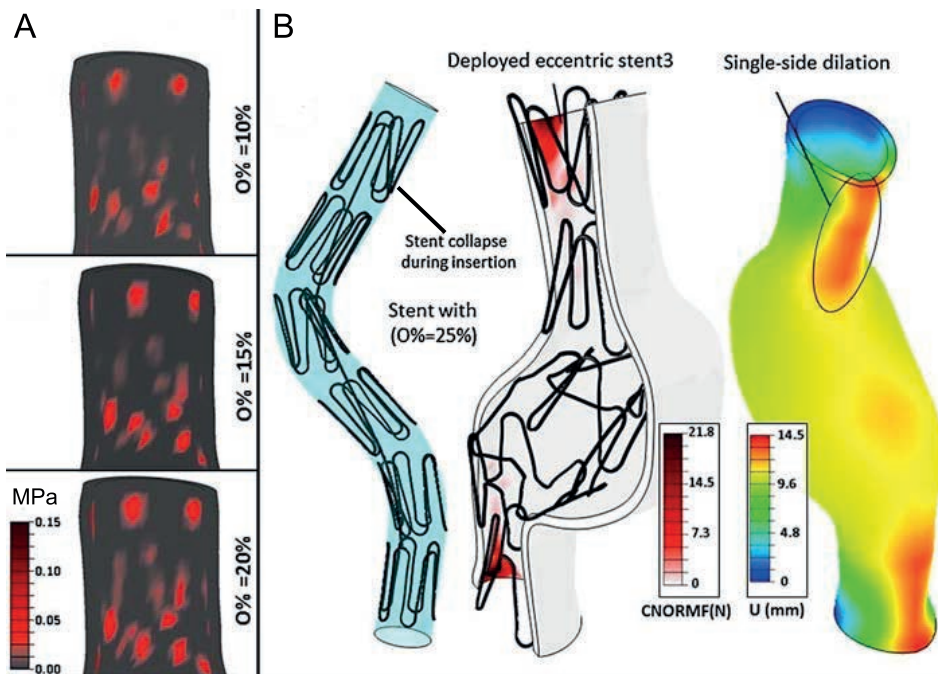


Figure 2. A: Contact stresses in the proximal landing zone for different percentages of oversizing (O%). B: Excessive oversizing (O%=25%) with stent-graft collapse and increased dilation (U) in the landing zones. Reprinted with permission from Altnji, et al.⁹

should be at least 2 cm to accommodate safe deployment. If the landing zones are angulated, longer lengths should be considered to provide a larger area of healthy

aortic wall for secure fixation.^{9,12} Oversizing of the stent-graft diameter aids fixation in the landing zones, yet excessive oversizing (>20%) needs to be avoided as this is known to induce disadvantageous stress distributions (Figure 2),⁹ and is associated with SINE.¹³ When planning for TEVAR, stent graft diameter is often selected based on the total aortic diameter (true lumen + false lumen). This approach is correct if the true lumen opens completely after stent-graft deployment. In the chronic phase, however, the thick intimal flap and false lumen thrombosis (Figure 3) can restrict expansion of the true lumen. The radial force that resides in the partially unfolded stent-graft increases the risk of SINE. Therefore, it is suggested to avoid important oversizing when planning TEVAR for chronic TBAD.^{1,7-9}

Preferably, one would treat all patients that will develop post-dissection aneurysmal dilation in the acute phase. However, it would be harmful to put patients who may never develop aneurysmal dilation at risk of TEVAR-related complications such as retrograde dissection, stroke and spinal cord ischemia. The challenge therefore remains selecting those patients that will develop aneurysmal dilation from those who will not. At this point, no guidelines are available to aid early patient selection. Future research may fill this void, using 4D flow magnetic resonance imaging and patient-specific computational modeling to identify hemodynamic characteristics that can predict the risk of aneurysmal dilation following uncomplicated TBAD.



Figure 3. Thickened dissection flap with false lumen thrombosis in a patient with a chronic type B dissection. Reprinted with permission from Kasirajan, et al.⁷

References

- 1 Erbel R, Aboyans V, Boileau C, et al. 2014 ESC Guidelines on the diagnosis and treatment of aortic diseases: Document covering acute and chronic aortic diseases of the thoracic and abdominal aorta of the adult. The Task Force for the Diagnosis and Treatment of Aortic Diseases of the European . *Eur Heart J* 2014;35(41):2873–926. Doi: 10.1093/eurheartj/ehu281.

- 2 Fattori R, Montgomery D, Lovato L, et al. Survival after endovascular therapy in patients with type B aortic dissection: a report from the International Registry of Acute Aortic Dissection (IRAD). *JACC Cardiovasc Interv* 2013;6(8):876–82. Doi: 10.1016/j.jcin.2013.05.003.
- 3 Menichini C, Pirola S, Guo B, et al. High Wall Stress May Predict the Formation of Stent-Graft-Induced New Entries After Thoracic Endovascular Aortic Repair. *J Endovasc Ther* 2018;25(5):571–7. Doi: 10.1177/1526602818791827.
- 4 Peterss S, Mansour AM, Ross JA, et al. Changing Pathology of the Thoracic Aorta From Acute to Chronic Dissection: Literature Review and Insights. *J Am Coll Cardiol* 2016;68(10):1054–65. Doi: 10.1016/j.jacc.2016.05.091.
- 5 Brunkwall J, Kasprzak P, Verhoeven E, et al. Endovascular repair of acute uncomplicated aortic type B dissection promotes aortic remodelling: 1 year results of the ADSORB trial. *Eur J Vasc Endovasc Surg* 2014;48(3):285–91. Doi: 10.1016/j.ejvs.2014.05.012.
- 6 Qin Y-L, Wang F, Li T-X, et al. Endovascular Repair Compared With Medical Management of Patients With Uncomplicated Type B Acute Aortic Dissection. *J Am Coll Cardiol* 2016;67(24):2835–42. Doi: 10.1016/j.jacc.2016.03.578.
- 7 Kasirajan K, Milner R, Chaikof EL. Late complications of thoracic endografts. *J Vasc Surg* 2006;94A–99A. Doi: 10.1016/j.jvs.2005.10.064.
- 8 Rohlffs F, Tsilimparis N, Diener H, et al. Chronic type B aortic dissection: indications and strategies for treatment. *J Cardiovasc Surg (Torino)* 2015;56(2):231–8.
- 9 Altnji HE, Bou-Said B, Walter-Le Berre H. Morphological and stent design risk factors to prevent migration phenomena for a thoracic aneurysm: a numerical analysis. *Med Eng Phys* 2015;37(1):23–33. Doi: 10.1016/j.medengphy.2014.09.017.
- 10 Figueroa CA, Taylor CA, Chiou AJ, et al. Magnitude and direction of pulsatile displacement forces acting on thoracic aortic endografts. *J Endovasc Ther* 2009;16(3):350–8. Doi: 10.1583/09-2738.1.
- 11 Marrocco-Trischitta MM, van Bakel TM, Romarowski RM, et al. The Modified Arch Landing Areas Nomenclature (MALAN) Improves Prediction of Stent Graft Displacement Forces: Proof of Concept by Computational Fluid Dynamics Modelling. *Eur J Vasc Endovasc Surg* 2018;55(4):584–92. Doi: 10.1016/j.ejvs.2017.12.019.
- 12 Marrocco-Trischitta MM, de Beaufort HW, Secchi F, et al. A geometric reappraisal of proximal landing zones for thoracic endovascular aortic repair according to aortic arch types. *J Vasc Surg* 2017;65(6). Doi: 10.1016/j.jvs.2016.10.113.
- 13 Nauta FJ, Conti M, Kamman A V, et al. Biomechanical Changes After Thoracic Endovascular Aortic Repair in Type B Dissection: A Systematic Review. *J Endovasc Ther* 2015;22(6):918–33. Doi: 10.1177/1526602815608848.

Chapter 12

Dynamic malperfusion in aortic dissection

Theodorus M.J. van Bakel^{1,2,3}, MD

Viviana Grassi⁴, MD

Himanshu J. Patel⁵, MD

Santi Trimarchi^{4,6}, MD, PhD

1. Department of Surgery, University of Michigan, Ann Arbor, Michigan, USA.
2. Department of Vascular Surgery, University Medical Center Utrecht, Utrecht, The Netherlands.
3. Thoracic Aortic Research Center, IRCCS Policlinico San Donato, San Donato Milanese, Italy.
4. Fondazione IRCCS Ca' Granda Ospedale Maggiore Policlinico Milano, Milan, Italy.
5. Department of Cardiac Surgery, University of Michigan, Ann Arbor, Michigan, USA.
6. Department of Biomedical Sciences for Health, University of Milan, Italy.

Journal of Endovascular Therapy. 2019;26:88-89

Mesenteric malperfusion is a devastating complication of acute Type B aortic dissection (TBAD) that occurs in 7% of patients and is associated with an in-hospital mortality rate of 31%.¹ The three most common pathways via which aortic dissection results in branch vessel occlusion are: (1) static compression, (2) dynamic compression, and (3) a combination of static and dynamic compression of the branching arteries (Figure 1).² In static compression, the intimal flap extends into the ostium of the branching artery, resulting in occlusion of the lumen. In dynamic malperfusion, the pressure gradient between the false lumen (high pressure) and the true lumen (low pressure) results in true lumen collapse with obstruction of the ostium of the branching vessel. This latter form of malperfusion is dynamic, because lowering blood pressure can diminish the pressure gradient, resolving true lumen compression. In many cases, a combination of static and dynamic compression is present.

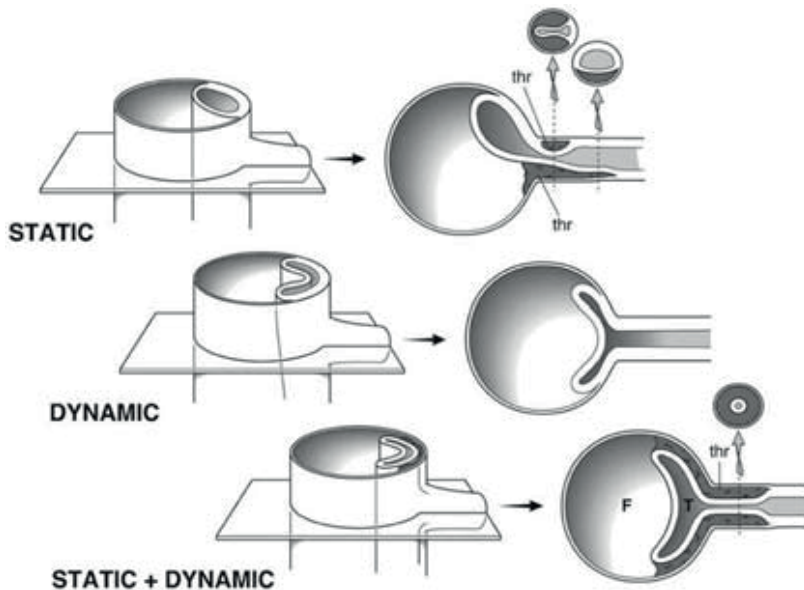


Figure 1. Diagram illustrating the different types of branch vessel obstruction: static, dynamic, and combination of static and dynamic. Reprinted with permission from Kamman, et al.²

To restore mesenteric perfusion, current guidelines recommend a combination of antihypertensive therapy and thoracic endovascular aortic repair (TEVAR).³ The purpose of TEVAR is to cover the proximal entry tear, reducing blood flow and pressure in the false lumen and increasing visceral perfusion via the true lumen. The radial force of the endograft in combination with reduced flow in the false lumen should expand the true lumen and ideally induce complete false lumen thrombosis.

The goal of antihypertensive therapy is to prevent dissection progression and reduce the pressure gradient between the false and true lumen.

The study by Guo, et al.⁴ presents the case of a 54-year-old male with chronic mesenteric malperfusion following TBAD. In the acute setting, the patient presented with intestinal ischemia due to TBAD with malperfusion of the superior mesenteric artery (SMA). He was treated with TEVAR, covering the proximal entry tear, yet the multichannel abdominal aortic dissection persisted. After four years, he presented with acute on chronic abdominal pain and hypertension. A large secondary entry tear, located at the end of the endograft, perfused two false lumens that compressed the true lumen, which caused mesenteric malperfusion. The symptoms of abdominal pain were relieved after fasting and blood pressure control. TEVAR was performed to cover the secondary entry tear. During the procedure, movement of the dissecting flaps was noted. The patient's abdominal pain resolved and he was discharged normotensive. At 12-month follow-up, the patient had gained weight and imaging showed improved perfusion of the SMA.

In this case, multichannel aortic dissection persisted despite covering the proximal entry tear with TEVAR and resulted in chronic mesenteric malperfusion. It is possible that the secondary tear was caused by deployment of the first endograft⁵ and accommodated perfusion of the false lumen after TEVAR, reducing the potential for false lumen thrombosis.⁶ Persistent false lumen patency alone, however, does not lead to mesenteric ischemia. We argue that this patient was probably suffering from chronic dynamic occlusion of the SMA. This is confirmed by the fact that the patient presented with hypertension and acute abdominal pain, which improved with blood pressure control. Moreover, clear movement of the intimal flap was seen among the two false lumens and the true lumen during the TEVAR procedure. The question remains whether the chronic mesenteric malperfusion syndrome could have been prevented. It could be that the patient presented in the study from Guo et al. was not compliant to antihypertensive therapy, the cornerstone therapy for aortic dissection, putting him at risk of complications such as chronic dynamic mesenteric obstruction. In some centers, patients presenting with acute TBAD and mesenteric malperfusion are not treated with TEVAR but with endovascular fenestration of the intimal flap.² During the fenestration procedure, the intimal flap is punctured and subsequently dilated to eliminate the pressure gradient between the false and true lumen, resolving dynamic obstruction of the branching vessels. If needed, self-expandable bare metal stents can be placed in the true lumen near the celiac artery and/or SMA to secure true lumen patency. Additional stents may be deployed in the branch vessels to relieve static obstructions. Patients who are successfully treated with a fenestration procedure have essentially been converted from complicated to uncomplicated TBAD. Now, the discussion starts whether patients with uncomplicated TBAD should be

treated with TEVAR.⁵ Further research with 4D flow magnetic resonance imaging⁷ and patient-specific computational modeling⁸ might help to identify hemodynamic characteristics that can predict chronic malperfusion syndromes and the risk of aneurysmal dilation following complicated and uncomplicated TBAD.

References

- 1 Jonker FHW, Patel HJ, Upchurch GR, et al. Acute type B aortic dissection complicated by visceral ischemia. *J Thorac Cardiovasc Surg* 2015. Doi: 10.1016/j.jtcvs.2014.11.012.
- 2 Kamman A V., Yang B, Kim KM, et al. Visceral Malperfusion in Aortic Dissection: The Michigan Experience. *Semin Thorac Cardiovasc Surg* 2017;29(2):173–8. Doi: 10.1053/J.SEMTCVS.2016.10.002.
- 3 Erbel R, Aboyans V, Boileau C, et al. 2014 ESC Guidelines on the diagnosis and treatment of aortic diseases: Document covering acute and chronic aortic diseases of the thoracic and abdominal aorta of the adult. The Task Force for the Diagnosis and Treatment of Aortic Diseases of the European . *Eur Heart J* 2014;35(41):2873–926. Doi: 10.1093/eurheartj/ehu281.
- 4 Guo B, Guo D, Shi Z, et al. Intravascular Ultrasound–Assisted Endovascular Treatment of Mesenteric Malperfusion in a Multichannel Aortic Dissection With Full True Lumen Collapse. *J Endovasc Ther* 2018.
- 5 van Bakel TMJ, Figueroa CA, van Herwaarden JA, et al. Challenges of Thoracic Endovascular Aortic Repair for Type B Aortic Dissection. *J Endovasc Ther* 2018;25(5):578–80. Doi: 10.1177/1526602818795153.
- 6 Kasirajan K, Milner R, Chaikof EL. Late complications of thoracic endografts. *J Vasc Surg* 2006;94A–99A. Doi: 10.1016/j.jvs.2005.10.064.
- 7 de Beaufort HW, Shah DJ, Patel AP, et al. Four-dimensional flow cardiovascular magnetic resonance in aortic dissection: Assessment in an ex vivo model and preliminary clinical experience. *J Thorac Cardiovasc Surg* 2018. Doi: 10.1016/j.jtcvs.2018.06.022.
- 8 van Bakel TMJ, Lau KD, Hirsch-Romano J, et al. Patient-Specific Modeling of Hemodynamics: Supporting Surgical Planning in a Fontan Circulation Correction. *J Cardiovasc Transl Res* 2018;11(2):145–55. Doi: 10.1007/s12265-017-9781-x.

Chapter 13

Summary and general discussion

The mechanical coupling of blood flow and vascular tissue is an essential part of the cardiovascular system. Various mechanisms have been identified that enable cardiovascular remodeling in response to hemodynamic stressors acting on global and local levels.¹ Furthermore, hemodynamic disturbances have been recognized as triggering factors in the pathogenesis of cardiovascular diseases.² To study these stressors and disturbances, highly detailed hemodynamic analyses are needed. Computational fluid dynamics (CFD) modeling techniques offer the unique potential to provide these highly detailed analyses, as they can be used to compute hemodynamics with a higher spatial and temporal resolution than any clinical imaging test. In this thesis, patient-specific CFD modeling techniques were used to study the pathogenesis of cardiovascular diseases and guide surgical planning and device optimization.

Patient-specific modeling of hemodynamics for surgical planning

The current paradigm in cardiovascular surgical planning relies on anatomical assessments, results from clinical studies and the experience of the surgeon performing the intervention. Patient-specific CFD modeling could enhance this paradigm, as computational models can be used to inform the surgeon on specific hemodynamic differences between surgical alternatives and identify an optimal solution. In **Chapter 2**, CFD modeling techniques were used to guide surgical planning in an 18-year-old female patient with a Fontan circulation suffering from pulmonary arteriovenous malformations (PAVMs) in her right lung. Patient-specific CFD simulations were performed to gain detailed information on local distribution of hepatic factors in the pulmonary circulation. It was found that her right lung was completely deprived from hepatic factors, causing PAVMs to form. Surgical revision was proposed to achieve a more balanced distribution of hepatic venous flow between both lungs. Two feasible surgical options were compared and the revision with most balanced distribution of hepatic factors was selected. The postoperative outcomes were consistent with the simulation results. This case is a good example of how CFD modeling can aid diagnosis and surgical planning of complex hemodynamic diseases.

Mechanical coupling of endograft and aorta

The second and third part of this thesis target optimization of devices for endovascular treatment of aortic aneurysms. Thoracic endovascular aortic repair (TEVAR) is the treatment of choice for descending thoracic aortic aneurysms.³ Due to its

superior early and mid-term outcomes over open surgery, the use of TEVAR is increasing rapidly.⁴ However, current endografts are made of materials much stiffer than the native thoracic aorta.^{5,6} The clinical consequences of this stiffness mismatch are largely unknown.

In **Chapter 3**, we assessed the impact of this stiffness mismatch on the heart in a cohort of patients with descending aortic aneurysms that were treated with TEVAR. In all patients, left ventricular stroke work was calculated using patient-specific CFD models before and after TEVAR. Cardiac remodeling was simultaneously assessed using morphologic measurements of the left ventricle. Our results showed that TEVAR increased left ventricular stroke work and induced left ventricular growth during follow-up. In **Chapter 4**, the impact of the stiffness mismatch on the unstented segments of the aorta was assessed in a patient with a stable ascending and rapidly growing proximal descending aneurysm who expired suddenly from ascending aortic rupture three months following branched zone 2 TEVAR. The results of our multi-parametric image-based computational analysis revealed that following TEVAR, wall stresses in the unstented segments of the aorta increased significantly and contributed to rupture of the ascending aortic aneurysm. Adverse left ventricular remodeling and increased aortic wall stresses are under-recognized consequences of TEVAR that should be considered in surgical planning, as they can lead to significant complications. Considering the emerging role of TEVAR, with endografts being deployed more proximally and in younger patients,⁷⁻⁹ medical device manufacturers should develop new endografts using materials that mimic the biomechanical properties of the native aorta more closely to overcome these disadvantageous effects of TEVAR.

Endovascular branch vessel preservation techniques

One of the anatomical contraindications for endovascular aortic repair is the presence of critical branch vessels in the area that will be covered by the endograft. In order to provide a minimally invasive alternative in patients unfit for open or hybrid repair, multiple options for endovascular vascularization of critical branch vessels have been proposed. **Chapter 5** presents an overview of the literature on currently investigated branched endografts for aortic arch deployment. Overall, the results of branched TEVAR are promising, yet high stroke rates were observed, especially when multibranch endografts were used.

In **Chapter 6**, CFD modeling techniques were used to test the postoperative hemodynamic performance of different single and double branched endograft designs for zone 0 TEVAR in a patient with an aortic arch aneurysm. Our computational results

showed that endograft design has significant impact on postoperative hemodynamic performance. Compared to preoperative, all endograft designs reduced blood flow and increased platelet activation potential (PLAP) in the cervical arteries. Endografts with two antegrade oriented inner branches showed better hemodynamic performance compared to single branched alternatives. The endograft design with a single retrograde oriented inner branch performed worst. In this design, all blood that flows to the supra-aortic arteries needs to make a U-turn in the aortic arch and pass through the single outlet, increasing blood shear rates and decreasing blood flow. One of the limitations of our simulation methods is that we do not simulate the deployment procedure itself. As reported in **Chapter 5**, most strokes following branched TEVAR occurred in the perioperative period and were attributed to guide-wire manipulation of atherosclerotic plaques in the aortic arch. Furthermore, it is reported that deployment of double branched endografts was associated with higher stroke rates compared to single branched alternatives. Following these results, I suggest that besides the endograft design, the deployment procedure should be further ameliorated to reduce stroke risks. Robotic catheter placement¹⁰ and carbon dioxide flushing of the endograft prior to insertion¹¹ could reduce the risk of air embolism during deployment. Additionally, the use of cerebral protection devices, which have proven to be effective at reducing embolization in transcatheter aortic valve replacement,¹² should also be investigated.

In the abdominal aorta, branched endografts are being used to vascularize the renal arteries in endovascular aortic repair (EVAR) of juxtarenal aortic aneurysms. One of the major complications of renal vascularization with EVAR is postoperative renal dysfunction due to stent-graft thrombosis and occlusion. Indeed, up to 25% of patients has postoperative renal failure,¹³⁻¹⁶ and up to 5% requires permanent dialysis.¹³⁻¹⁶ Interestingly, renal dysfunction seems to occur more frequently in patients whose renal arteries were vascularized using parallel stent-grafting procedures compared to branched alternatives.¹³ In **Chapter 7**, we tested the hemodynamic performance of different EVAR solutions with renal vascularization using similar CFD methods as in **Chapter 6**. The following EVAR solutions were tested: fenestrated endografts (F-EVAR); branched endografts (B-EVAR); parallel chimney stent-grafts (Ch-EVAR); and parallel periscope stent-grafts (P-EVAR). Our CFD simulation results revealed that Ch-EVAR and P-EVAR resulted in more renal flow disturbances than B-EVAR and F-EVAR. These results could explain why renal dysfunction occurs more frequently following parallel stent-grafting procedures compared to branched alternatives for renal vascularization.

Morphological studies for aortic repair

The complex hemodynamics that are observed in the human aorta partially originate in the unique aortic geometry, which includes non-planar curvatures and branches at the apex of the arch.¹⁷ Successful aortic repair necessitates consideration of this unique morphology and its hemodynamic consequences. TEVAR is the first line treatment for aortic disease affecting the descending thoracic aorta, because it provides low procedural morbidity and mortality, and satisfactory midterm results in selected patients.¹⁸ Endograft deployment in the aortic arch, however, is associated with higher rates of postoperative failure due to migration and endoleak.¹⁹ This is thought to be caused by angulation and tortuosity of the proximal landing zones, resulting in a hostile environment for endograft deployment.²⁰ Currently, the instructions for use of endografts do not specify different requirements for proximal landing zone length in more angulated aortic geometries. **Chapter 8** is a study that analyzed how increased angulation of the aortic arch changes the hemodynamic displacement forces in the proximal landing zones for TEVAR. The Modified Arch Landing Areas Nomenclature (MALAN) classification,²⁰ which merges Ishimaru's map²¹ with the Aortic Arch Classification,²² differentiates the proximal landing zones for TEVAR by type of arch. In this study, CFD models of healthy aortic arches (5 per type of arch) were constructed and pulsatile displacement forces were calculated in all landing zones. The results revealed significantly different displacement forces in the proximal landing zones between and within the types of arch. Specifically, the displacement forces in Type II and Type III arches were higher compared to the same zone in Type I arches. Furthermore, the displacement forces in zone 3 of Type II and Type III arches were higher compared to zone 2 in the same arch. Following these results, a longer proximal landing zone length that accommodates the higher angulation, tortuosity and displacement forces should be advised when planning TEVAR in zone 3 of a Type II or Type III arch. This could mean that, due to the anatomical restraint of the origin of left subclavian artery, a more proximal landing zone should be considered.

Increased hemodynamic displacement forces do not only act on the proximal landing zone, but on the entire surface of the endograft. Increased displacement forces have been associated with endograft migration and endoleak.²³ In **Chapter 9**, the displacement forces that act on endografts following deployment in Zone 2 were calculated in a cohort of four patients from the iCardioCloud database using patient-specific CFD simulations. The patient with the largest displacement force presented with Type Ib endoleak at 1-year follow-up. In this case, the displacement force vector was directed dorsocranial, perpendicular to the distal sealing zone, and its magnitude lied within the range of pull-out forces described by Rahmani et al.²⁴

Further investigation of the hemodynamic displacement force and the complex of compensatory radial and frictional forces, securing stability of the endograft in the sealing zones, is needed to reduce the risk of Type I endoleak. These mechanisms should be taken into account in preoperative planning and device development for TEVAR.

Studying the unique hemodynamic environment in the aorta can also help understand the pathophysiology of therapy resistant cardiovascular diseases. **Chapter 10** is a study of aortorenal hemodynamics in a pediatric patient with therapy resistant hypertension secondary to a suprarenal abdominal aortic coarctation (SAAC). SAAC is often associated with severe renin-mediated arterial hypertension.²⁵ Even after successful elimination of the pressure gradient across the coarctation with surgical repair, postoperative hypertension has been noted to persist.^{25,26} The pathophysiology of this persistent hypertension remains largely unknown. The patient in **Chapter 10** was surgically treated with a thoracoabdominal bypass (TAB), yet still depended on antihypertensive medication at 1-year follow-up. Patient-specific preoperative and postoperative models were created to investigate aortorenal hemodynamics in this case and test the outcomes of different TAB and patch aortoplasty (PA) surgeries. Our results revealed the unexpected finding of diastolic dominated renal flow waveforms with high frequency disturbances. These disturbances could explain increased renin release in the kidneys, resulting in secondary hypertension. Interestingly, all surgical repairs resulted in increased systolic dominated renal flow waveforms and decreased aortic pressure, yet various degrees of high frequency disturbances persisted. Only treatment with 0% PA oversizing eliminated the high frequency disturbances completely. This is unfortunate, as 0% oversizing is not feasible in pediatric patients because the surgical patch does not accommodate growth and will become a relative stenosis during follow-up. Collaborative efforts between biomedical engineers and clinicians will be essential to develop surgical devices and procedures that eliminate aortorenal disturbances and accommodate aortic growth during follow-up. Following the results of **Chapters 8-10**, we can conclude that the morphology of the aorta induces unique hemodynamic characteristics, which can make treatment challenging. Patient-specific CFD modeling offers the unique potential to study complex hemodynamics and aid surgical planning.

Endovascular repair of aortic dissection

Chapter 11 comments on endovascular treatment of type B aortic dissection (TBAD) from a biomechanical perspective. Standard treatment for acute TBAD is antihypertensive medical therapy, TEVAR is only performed additionally if complications are

present.²⁷ However, 50% of patients who are initially treated with OMT alone will develop aneurysmal degeneration of the weakened aortic wall during follow-up.²⁸ Some of these patients will require TEVAR, yet TEVAR is less successful in the chronic phase due to thickening and stiffening of the intimal flap. In this phase, the risk of endograft malposition and stent-graft induced new entry tears is increased.²⁹ From a biomechanical standpoint, one would treat all patients that are at risk for post-dissection aneurysmal dilation following uncomplicated TBAD in the acute phase. However, it would be harmful to put patients who may never develop aneurysmal dilation at risk of TEVAR-related complications such as retrograde dissection, stroke and spinal cord ischemia. The challenge remains to select those patients that will develop aneurysmal dilation from those who will not. At this point, no guidelines are available to aid early patient selection. Therefore, further research with 4D flow magnetic resonance imaging³⁰ and patient-specific computational modeling³¹ should be undertaken to identify hemodynamic characteristics that can predict the risk of aneurysmal dilation following complicated and uncomplicated TBAD.

Chapter 12 comments on a case of persistent mesenteric malperfusion following complicated TBAD treated with TEVAR.³² In this case, multichannel aortic dissection persisted despite covering the proximal entry tear, resulting in dynamic mesenteric malperfusion. We argue that endovascular fenestration of the intimal flap in the acute phase could have eliminated the pressure gradient and potentially prevented chronic mesenteric malperfusion. Again, further research with novel imaging-based techniques is needed to identify those patients that would benefit from endovascular fenestration of the intimal flap in the acute phase to prevent complications during follow-up.

Perspective

This thesis has shown that patient-specific CFD modelling is capable of providing non-invasive high-resolution hemodynamic analyses that help understanding of hemodynamics in complex anatomies. Furthermore, it enables highly controllable testing of different geometries, which can be used for surgical planning and device development. Nonetheless, there are multiple obstacles in the way of routine clinical application. Computations are time-consuming. In order to get meaningful results, it is critically important that the simulation workflow is set up in such a way that the computations reflect the actual anatomic and physiologic state of the patient. Constructing accurate geometric models is time-intensive and somewhat operator-dependent. Subsequently, the models need to be iteratively calibrated. The computations for each iteration typically require multiple days to run. At this point, despite

advances in high performance computing, real-time CFD analyses are not feasible yet. This limits the applicability for clinical decision making to elective cases. Automated workflows relying on data-driven simulations, machine and deep learning tools will help mitigate some of these issues in the future.

Multidisciplinary collaboration between clinicians and biomedical engineers is essential to utilize the capabilities of computational modelling for surgical planning and device development. The challenge for the future is to perform prospective studies in larger patient populations to verify the computational results with postoperative clinical outcomes.

References

- 1 Humphrey JD, Dufresne ER, Schwartz MA. Mechanotransduction and extracellular matrix homeostasis. *Nat Rev Mol Cell Biol* 2014;15(12):802–12. Doi: 10.1038/nrm3896.
- 2 Humphrey JD, Schwartz MA, Tellides G, et al. Role of mechanotransduction in vascular biology: Focus on thoracic aortic aneurysms and dissections. *Circ Res* 2015;1448–61. Doi: 10.1161/CIRCRESAHA.114.304936.
- 3 Hiratzka LF, Bakris GL, Beckman JA, et al. 2010 ACCF/AHA/AATS/ACR/ASA/SCA/SCAI/SIR/STS/SVM guidelines for the diagnosis and management of patients with Thoracic Aortic Disease: a report of the American College of Cardiology Foundation/American Heart Association Task Force on Practice Guidelines, A. *Circulation* 2010;121(13):e266-369. Doi: 10.1161/CIR.0b013e3181d4739e.
- 4 von Allmen RS, Anjum A, Powell JT. Incidence of descending aortic pathology and evaluation of the impact of thoracic endovascular aortic repair: a population-based study in England and Wales from 1999 to 2010. *Eur J Vasc Endovasc Surg Off J Eur Soc Vasc Surg* 2013;45(2):154–9. Doi: 10.1016/j.ejvs.2012.12.007.
- 5 Kleinstreuer C, Li Z, Basciano CA, et al. Computational mechanics of Nitinol stent grafts. *J Biomech* 2008;41(11):2370–8. Doi: 10.1016/j.jbiomech.2008.05.032.
- 6 Roccabianca S, Figueroa CA, Tellides G, et al. Quantification of regional differences in aortic stiffness in the aging human. *J Mech Behav Biomed Mater* 2014;29:618–34. Doi: 10.1016/j.jmbbm.2013.01.026.
- 7 Geisbüsch P, Kotelis D, Hyhlik-Dürr A, et al. Endografting in the Aortic Arch - Does the Proximal Landing Zone Influence Outcome? *Eur J Vasc Endovasc Surg* 2010;39(6):693–9. Doi: 10.1016/j.ejvs.2010.03.018.
- 8 van Bakel TM, Arthurs CJ, van Herwaarden JA, et al. A computational analysis of different endograft designs for Zone 0 aortic arch repair†. *Eur J Cardio-Thoracic Surg* 2018;54(2):389–96. Doi: 10.1093/ejcts/ezy068.
- 9 van Bakel TM, de Beaufort HW, Trimarchi S, et al. Status of branched endovascular aortic arch repair. *Ann Cardiothorac Surg* 2018;7(3):406–13. Doi: 10.21037/acs.2018.03.13.
- 10 Perera AH, Riga C V., Monzon L, et al. Robotic Arch Catheter Placement Reduces Cerebral Embolization During Thoracic Endovascular Aortic Repair (TEVAR). *Eur J Vasc Endovasc Surg* 2017;53(3):362–9. Doi: 10.1016/j.ejvs.2016.10.017.

- 11 Rohlfs F, Tsilimparis N, Saleptsis V, et al. Air Embolism During TEVAR: Carbon Dioxide Flushing Decreases the Amount of Gas Released from Thoracic Stent-Grafts During Deployment. *J Endovasc Ther* 2017;24(1):84–8. Doi: 10.1177/1526602816675621.
- 12 Giustino G, Sorrentino S, Mehran R, et al. Cerebral Embolic Protection During TAVR: A Clinical Event Meta-Analysis. *J Am Coll Cardiol* 2017;465–6. Doi: 10.1016/j.jacc.2016.12.002.
- 13 Li Y, Hu Z, Bai C, et al. Fenestrated and Chimney Technique for Juxtarenal Aortic Aneurysm: A Systematic Review and Pooled Data Analysis. *Sci Rep* 2016;6:20497. Doi: 10.1038/srep20497.
- 14 Martin-Gonzalez T, Pinçon C, Hertault A, et al. Renal outcomes analysis after endovascular and open aortic aneurysm repair. *J Vasc Surg* 2015;62(3):569–77. Doi: 10.1016/j.jvs.2015.03.075.
- 15 Reilly LM, Rapp JH, Grenon SM, et al. Efficacy and durability of endovascular thoracoabdominal aortic aneurysm repair using the caudally directed cuff technique. *J Vasc Surg* 2012;56(1):53–64. Doi: 10.1016/j.jvs.2012.01.006.
- 16 Tran K, Fajardo A, Ullery BW, et al. Renal function changes after fenestrated endovascular aneurysm repair. *J Vasc Surg* 2016;64(2):273–80. Doi: 10.1016/j.jvs.2016.01.041.
- 17 Morbiducci U, Ponzini R, Rizzo G, et al. Mechanistic insight into the physiological relevance of helical blood flow in the human aorta: an in vivo study. *Biomech Model Mechanobiol* 2011;10(3):339–55. Doi: 10.1007/s10237-010-0238-2.
- 18 Marrocco-Trischitta MM, Melissano G, Kahlberg A, et al. Chronic kidney disease classification stratifies mortality risk after elective stent graft repair of the thoracic aorta. *J Vasc Surg* 2009;49(2):296–301. Doi: 10.1016/J.JVS.2008.09.041.
- 19 Böckler D, Brunkwall J, Taylor PR, et al. Thoracic Endovascular Aortic Repair of Aortic Arch Pathologies with the Conformable Thoracic Aortic Graft: Early and 2 year Results from a European Multicentre Registry. *Eur J Vasc Endovasc Surg* 2016;51(6):791–800. Doi: 10.1016/J.EJVS.2016.02.006.
- 20 Marrocco-Trischitta MM, de Beaufort HW, Secchi F, et al. A geometric reappraisal of proximal landing zones for thoracic endovascular aortic repair according to aortic arch types. *J Vasc Surg* 2017. Doi: 10.1016/j.jvs.2016.10.113.
- 21 Ishimaru S. Endografting of the aortic arch. *J Endovasc Ther* 2004;11 Suppl 2:II62-71. Doi: 10.1583/04-1407.1.
- 22 Madhwal S, Rajagopal V, Bhatt DL, et al. Predictors of difficult carotid stenting as determined by aortic arch angiography. *J Invasive Cardiol* 2008;20(5):200–4.
- 23 Figueroa CA, Taylor CA, Chiou AJ, et al. Magnitude and direction of pulsatile displacement forces acting on thoracic aortic endografts. *J Endovasc Ther* 2009;16(3):350–8. Doi: 10.1583/09-2738.1.
- 24 Rahmani S, Grewal IS, Nabovati A, et al. Increasing angulation decreases measured aortic stent graft pullout forces. *J Vasc Surg* 2016;63(2):493–9.
- 25 Stanley JC, Criado E, Eliason JL, et al. Abdominal aortic coarctation: Surgical treatment of 53 patients with a thoracoabdominal bypass, patch aortoplasty, or interposition aorto-aortic graft. *J Vasc Surg* 2008;48(5):1073–82. Doi: 10.1016/j.jvs.2008.05.078.
- 26 Rumman RK, Nickel C, Matsuda-Abedini M, et al. Disease beyond the arch: A systematic review of middle aortic syndrome in childhood. *Am J Hypertens* 2015;28(7):833–46. Doi: 10.1093/ajh/hpu296.
- 27 Grabenwoger M, Alfonso F, Bachet J, et al. Thoracic Endovascular Aortic Repair (TEVAR) for the treatment of aortic diseases: a position statement from the European Association for Cardio-Thoracic Surgery (EACTS) and the European Society of Cardiology (ESC), in collaboration with the European Assoc. *Eur J Cardio-Thoracic Surg* 2012;42(1):17–24. Doi: 10.1093/ejcts/ezs107.

- 28 Fattori R, Montgomery D, Lovato L, et al. Survival after endovascular therapy in patients with type B aortic dissection: a report from the International Registry of Acute Aortic Dissection (IRAD). *JACC Cardiovasc Interv* 2013;6(8):876–82. Doi: 10.1016/j.jcin.2013.05.003.
- 29 Dong Z, Fu W, Wang Y, et al. Stent graft-induced new entry after endovascular repair for Stanford type B aortic dissection. *J Vasc Surg* 2010;52(6):1450–7. Doi: 10.1016/j.jvs.2010.05.121.
- 30 de Beaufort HW, Shah DJ, Patel AP, et al. Four-dimensional flow cardiovascular magnetic resonance in aortic dissection: Assessment in an ex vivo model and preliminary clinical experience. *J Thorac Cardiovasc Surg* 2018. Doi: 10.1016/j.jtcvs.2018.06.022.
- 31 Ben Ahmed S, Dillon-Murphy D, Figueroa CA. Computational Study of Anatomical Risk Factors in Idealized Models of Type B Aortic Dissection. *Eur J Vasc Endovasc Surg* 2016;52(6):736–45. Doi: 10.1016/j.ejvs.2016.07.025.
- 32 Guo B, Guo D, Shi Z, et al. Intravascular Ultrasound–Assisted Endovascular Treatment of Mesenteric Malperfusion in a Multichannel Aortic Dissection With Full True Lumen Collapse. *J Endovasc Ther* 2018.

Chapter 14

Samenvatting en discussie in het Nederlands

De mechanische koppeling van de bloedstroom en bloedvaten is een essentieel onderdeel van het cardiovasculaire systeem. Verscheidene mechanismen zijn geïdentificeerd die het mogelijk maken om het cardiovasculaire systeem te vervormen in respons op lokale en globale hemodynamische stressoren.¹ Daarbij is het bekend dat hemodynamische verstoringen cardiovasculaire ziekten kunnen uitlokken.² Zeer gedetailleerde analyses zijn nodig om deze stressoren en verstoringen te bestuderen. Computational fluid dynamics (CFD) modelleer technieken bieden de unieke mogelijkheid om zulke zeer gedetailleerde analyses te verschaffen, gezien zij gebruikt kunnen worden om hemodynamica te berekenen met een hogere resolutie dan elke beeldvormende klinische test. In dit proefschrift worden patiënt specifieke CFD modelleer technieken gebruikt om de pathogenese van cardiovasculaire ziekten te bestuderen en chirurgische planning en hulpmiddel ontwikkeling te ondersteunen.

Patiënt specifiek modelleren van hemodynamica voor chirurgische planning

De huidige methode voor het plannen van chirurgie voor cardiovasculaire aandoeningen bestaat uit anatomische beoordelingen, resultaten van klinische studies en de ervaring van de chirurg die de operatie uitvoert. Patiënt specifieke CFD-simulaties kunnen een bijdrage leveren aan deze methode door de operateur te informeren over hemodynamische verschillen tussen alternatieve interventies. In **Hoofdstuk 2** worden CFD modelleer technieken gebruikt bij het selecteren van een chirurgische interventie in een 18-jarige vrouwelijke patiënt met een Fontan circulatie die lijdt aan pulmonaire arterioveneuze vasculaire malformaties (PAVMs) in haar rechterlong. Patiënt specifieke CFD-simulaties werden gebruikt om gedetailleerd inzicht te krijgen in de lokale verdeling van metabolieten uit de lever in de longcirculatie. Er werd geconstateerd de rechterlong volledig verstoken was veneus bloed uit de lever. Het gebrek aan metabolieten uit de lever veroorzaakte het ontstaan en de progressie van PAVMs in de rechterlong. Chirurgische revisie van de Fontan circulatie werd voorgesteld om een meer gebalanceerde verdeling van veneus bloed uit de lever over de longen te bereiken. Twee chirurgische opties werden vergeleken en de optie die resulteerde in de meest gebalanceerde verdeling van metabolieten uit de lever over beide longen bewerkstelligde werd geselecteerd. De postoperatieve uitkomsten waren consistent met de resultaten van de simulaties. Deze casus is een goed voorbeeld van hoe CFD-simulaties kunnen bijdragen aan het plannen van chirurgische interventies voor complexe hemodynamica-gerelateerde ziekten.

Mechanische interactie tussen endograft en aorta

Het tweede en derde deel van dit proefschrift gaat over optimalisatie van hulpmiddelen (endografts) voor endovasculaire behandeling van aneurysmata van de thoracale aorta. Voor de meeste aandoeningen van de thoracale aorta is het endovasculair plaatsen van een endograft (TEVAR) tegenwoordig de eerste keus behandeling.³ Dankzij de superieure uitkomsten op vroege en middellange termijn neemt het aantal behandelingen met TEVAR gestaag toe.⁴ De huidige endografts worden echter gemaakt van een materiaal dat stukken stijver is dan de aortawand.^{5,6} De consequenties van dit verschil in stijfheid zijn grotendeels onbekend.

In **Hoofdstuk 3** hebben we onderzocht hoe de mismatch in stijfheid tussen endograft en aortawand de belasting op het hart beïnvloedt in een cohort van acht patiënten dat werd behandeld met TEVAR voor aneurysmata van de aorta descendens. Door middel van CFD-modellen werd de hoeveelheid energie die het linkerventrikel nodig heeft per hartslag berekend voor en na TEVAR. Daarnaast werd de groei van de linkerventrikel gemeten voor en na TEVAR. De resultaten van dit onderzoek toonden aan dat TEVAR de belasting op de linkerventrikel vergroot en dat de grootte van het linkerventrikel als gevolg daarvan toeneemt. Dit is ongewenst. In **Hoofdstuk 4** werden de gevolgen van de mismatch in stijfheid tussen endograft en aortawand op de onbehandelde segmenten van de aorta geanalyseerd. Deze studie bestudeert de casus van een patiënt met een stabiel aneurysma van de aorta ascendens en een snelgroeiend aneurysma van de aorta descendens. De patiënt was drie maanden na TEVAR-behandeling van de aorta descendens plotseling overleden aan een ruptuur van het aneurysma in de aorta ascendens. De resultaten van onze simulaties en beeldanalyses toonden dat de wandspanning in de onbehandelde segmenten van de aorta toeneemt na TEVAR. Deze verhoogde wandspanning heeft waarschijnlijk bijgedragen aan het ontstaan van de ruptuur in de aorta ascendens die reeds verzwakt was door aneurysmatische verwijding. Vergroting van de linkerventrikel en verhoogde wandspanning in de aorta zijn nadelige gevolgen van TEVAR. Deze nadelige gevolgen zouden meegenomen moeten worden bij het plannen van een TEVAR-behandeling omdat zij kunnen leiden tot significante complicaties. Aangezien het aantal TEVAR-behandelingen toeneemt, met plaatsing van endografts in de meer proximale aorta en jongere patiënt populaties,⁷⁻⁹ worden meer patiënten blootgesteld aan deze negatieve gevolgen. Om dit te voorkomen dient de medische industrie nieuwe materialen te ontwikkelen die de biomechanische eigenschappen van de aortawand beter nabootsen.

Technieken voor het behoud van zijtakken tijdens endovasculaire behandeling van de aorta

Een van de anatomische contra-indicaties voor endovasculaire behandeling van de aorta is de aanwezigheid van essentiële zijtakken in het segment van de aorta dat bedekt zal worden door de endograft. Om toch een minimaal invasieve behandeloptie te bieden aan patiënten die niet fit genoeg zijn voor open of hybride behandeling van de aorta worden meerdere oplossingen onderzocht die endovasculaire vascularisatie van deze essentiële zijtakken mogelijk maken. **Hoofdstuk 5** geeft een overzicht van de huidige literatuur over het gebruik van zogenoemde branched endografts. De resultaten uit de literatuur zijn veelbelovend, echter blijft postoperatief herseninfarct een belangrijke en zorgwekkende complicatie van volledig endovasculaire behandeling van de aortaboog.

In **Hoofdstuk 6** worden CFD-simulaties gebruikt om de postoperatieve hemodynamische prestaties van endografts voor totaal endovasculaire behandeling van de aortaboog getest. De verschillende endografts hebben één of twee interne aftakkingen om de essentiële bloedvaten in de aortaboog van bloedstroom te voorzien. De resultaten van de computersimulaties toonden aan dat het design van de aftakkingen in de endografts de postoperatieve hemodynamica in de halsslagaders significant beïnvloedt. In de halsslagaders verlaagde de totale hoeveelheid bloedstroom en vergrootte de hoeveelheid hemodynamische verstoringen in vergelijking met preoperatief. Endografts met twee interne aftakkingen zorgden voor minder verstoringen in de bloedstroom dan endografts met één enkele interne aftakking. De endograft met één enkele retrograad georiënteerde aftakking zorgde voor de meeste verstoringen. In dit design moet alle bloedstroom naar het hoofd en de armen van de patiënt een U-bocht maken in de aortaboog en door één aftakking heen. Dit verlaagt de totale hoeveelheid bloed en verhoogt de hoeveelheid hemodynamische verstoringen. Een limitatie van onze simulatiemethoden is dat we alleen kijken naar de postoperatieve hemodynamica en er geen rekening wordt gehouden met het plaatsen van de endograft zelf. In **Hoofdstuk 5** wordt beschreven dat de meeste herseninfarcten na een TEVAR-behandeling voorkomen in de perioperatieve periode. Deze infarcten worden met name toegeschreven aan het manipuleren van atherosclerotische plaques in de aortaboog tijdens de TEVAR-procedure. Daarbij wordt een hogere incidentie van herseninfarcten gerapporteerd na TEVAR-behandeling met endografts die twee of meer interne aftakkingen hebben. Deze resultaten in acht nemend, moeten we concluderen dat niet alleen het endograft design, maar ook de TEVAR-procedure zelf verbeterd moet worden om het risico op herseninfarcten te verkleinen. Hiervoor dienen nieuwe methodes voor de TEVAR-procedure onderzocht te worden, zoals gerobotiseerde katheter plaatsing¹⁰ en het spoelen van de endograft met koolstofdi-

oxide,¹¹ om het risico op luchtembolieën te verkleinen. Daarbij zou ook het gebruik van hulpmiddelen voor cerebrale bescherming,¹² bewezen effectief in het verlagen van het risico op herseninfarcten bij transkatheter aortaklep vervanging, getest kunnen worden.

Endografts met interne aftakkingen worden tevens gebruikt om de nierslagader van bloed te voorzien bij endovasculaire behandeling van abdominale aneurysmata (EVAR). Een van de vaakst voorkomende complicaties hierbij zijn postoperatieve nierfunctiestoornissen, veroorzaakt door trombose of occlusie van de stent-grafts die de nierslagaders van bloed voorzien. Tot wel 25% van de patiënten die behandeld worden met EVAR en stent-grafts in de nierslagaders krijgt te maken met nierfalen,¹³⁻¹⁶ waarvan tot 5% permanent gedialyseerd dient te worden.¹³⁻¹⁶ Wat ons daarbij opviel was dat nierfunctiestoornissen vaker voorkomen bij patiënten waarvan de nierslagaders van bloed voorzien worden door parallel geplaatste stent-grafts vergeleken met patiënten waarvan de nierslagaders vanuit de endograft zelf doorbloed worden.¹³ In **Hoofdstuk 7** hebben we de hemodynamische prestaties van verschillende endovasculaire oplossingen voor het doorbloeden van de nierslagaders door middel van CFD-simulaties vergeleken. De volgende opties werden vergeleken: endografts met vensters waardoor stent-grafts in de nierslagaders geplaatst konden worden (F-EVAR); endografts met ingebouwde aftakkingen waardoor stent-grafts in de nierslagaders geplaatst konden worden (B-EVAR); parallel geplaatste stent-grafts die als schoorsteen boven de endograft uitsteken (Ch-EVAR); parallel geplaatste stent-grafts die als periscoop van de onderkant van de endograft in de nierslagaders steken (P-EVAR). De simulaties toonden aan dat Ch-EVAR en P-EVAR meer verstoorde bloedstroom veroorzaakten dan B-EVAR en F-EVAR. Deze resultaten kunnen verklaren waarom nierfunctiestoornissen vaker voorkomen bij patiënten waarvan de nierslagaders door parallel-geplaatste stent-grafts worden doorbloed, dan bij patiënten die behandeld worden met endografts die ingebouwde zijtakken naar de nierslagaders hebben.

Morfologische studies voor behandeling van de aorta

De complexe hemodynamica die in de aorta gezien worden vinden hun origine deels in de unieke morfologie van de aorta, die onder andere bestaat uit de aortaboog met aftakkingen in de top van de boog.¹⁷ Voor succesvolle behandeling van de aorta is het noodzakelijk om rekening te houden met de unieke vorm van de aorta en de bijbehorende complexe hemodynamica. TEVAR is de eerste keus voor behandeling van ziekten van de aorta descendens, omdat de morbiditeit en mortaliteit van de TEVAR-procedure laag is, en de resultaten op de middellange termijn in geselecteerde

patiënten goed zijn.¹⁸ Endovasculaire behandeling in de aortaboog is echter minder succesvol, gezien migratie en endoleak vaker voorkomen.¹⁹ De reden hiervoor is dat de angulatie en tortuositeit van de proximale landingszones groter is in de aortaboog, wat ongunstig is voor stabiele plaatsing van een endograaf.²⁰ Op dit moment zijn er geen gespecificeerde instructies voor het plaatsen van een endograaf in een aortaboog met verhoogde angulatie. **Hoofdstuk 8** is een studie waarin geanalyseerd wordt hoe toegenomen angulatie van de aortaboog de hemodynamische krachten in de proximale landingszones voor TEVAR beïnvloedt. De Modified Arch Landing Areas Nomenclature (MALAN) classificatie²⁰ voegt Ishimaru's map²¹ en de Aortic Arch Classification²² samen en differentieert hiermee de proximale landingszones voor TEVAR per type aortaboog. In deze studie werden CFD-modellen gemaakt van gezonde aortabogen (5 per type aortaboog). Vervolgens werden de hemodynamische verplaatsingskrachten in alle proximale landingszones berekend. De simulatieresultaten lieten zien dat de verplaatsingskrachten in de verschillende proximale landingszones significant anders zijn, zowel binnen dezelfde aortaboog als tussen verschillende typen aortabogen. De verplaatsingskrachten in de landingszones in Type II en Type III aortabogen waren hoger vergeleken met de krachten in Type I bogen. Daarnaast waren de verplaatsingskrachten in zone 3 van Type II en Type III aortabogen groter vergeleken met dezelfde landingszone in Type I bogen. Aan de hand van deze resultaten kun je beargumenteren dat een langere landingszone noodzakelijk is wanneer je TEVAR plant te doen in zone 3 van Type II of Type III aortabogen. Dit kan betekenen dat het noodzakelijk is om naar een meer proximale landingszone op te schuiven.

Hemodynamische verplaatsingskrachten werken op de totale lengte van de endograaf. Verhoogde verplaatsingskrachten zijn geassocieerd met migratie van de endograaf en endoleak.²³ In **Hoofdstuk 9** zijn de verplaatsingskrachten die werken op de oppervlakte van een endograaf berekend na een TEVAR-behandeling in landingszone 2. Voor deze studie werden vier patiënten uit de iCardioCloud database geselecteerd, waarvan patiënt-specifieke CFD-simulaties werden gemaakt. De patiënt waarin de grootste verplaatsingskracht werd berekend presenteerde met Type Ib endoleak bij de 1-jaar postoperatieve controle. De verplaatsingskrachtsvector in deze patiënt stond loodrecht op de distale landingszone, en de grootte van de kracht lag binnen de range van pull-out krachten eerder beschreven door Rahmani et al.²⁴ Nader onderzoek naar de hemodynamische verplaatsingskracht en het complex van compensatoire krachten dat de endograaf op zijn plek houdt is noodzakelijk om het risico op Type Ib endoleak te verkleinen. Deze mechanismen dienen in acht genomen te worden bij het plannen van een TEVAR-behandeling en het ontwikkelen van nieuwe endograafs.

Onderzoek naar de unieke hemodynamica in de aorta kan tevens helpen bij het begrijpen van de pathofysiologie van therapieresistente cardiovasculaire ziekten. **Hoofdstuk 10** is een studie waarin de aortorenale hemodynamica onderzocht worden in een kind met therapieresistente hypertensie als gevolg van een supra-renale coarctatie van de abdominale aorta (SAAC). Een SAAC gaat vaak gepaard met ernstige renine-gemedieerde hypertensie.²⁵ Zelfs na succesvolle chirurgische behandeling wordt persisterende hypertensie vaak gezien.^{25,26} De pathofysiologie van de therapieresistente hypertensie is grotendeels onbekend. De patiënt in **Hoofdstuk 10** werd chirurgisch behandeld met een thoracoabdominale bypass (TAB), maar was na een jaar na de operatie nog steeds afhankelijk van antihypertensiva. Patiënt-specifieke preoperatieve en postoperatieve modellen werden gemaakt om de aortorenale hemodynamica in deze patiënt nader te onderzoeken en de uitkomsten van verschillende chirurgische TAB en patch aortoplasty (PA) behandelingen te testen. De simulatieresultaten toonden dat de nierslagaders preoperatief met name in de diastole werden doorbloed en dat de renale bloedstroom hoogfrequente verstoringen bevatte. Deze hoogfrequente verstoringen kunnen een verhoogde productie van renine in de nieren veroorzaken, wat bijdraagt aan het ontstaan van hypertensie. Alle chirurgische behandelingen waren succesvol in het verhogen van de renale bloedstroom en het verlagen van de druk in de aorta. Echter, de hoogfrequente verstoringen in de renale bloedstroom verdwenen alleen bij behandeling met PA waarbij de patch niet groter dan de aorta werd gemaakt. Dit is helaas niet wenselijk gezien de aorta in deze kinderen nog moet groeien en het plaatsen van een precies passende patch uiteindelijk zal resulteren in een stenose van de aorta. Nieuwe hulpmiddelen en procedures dienen ontwikkeld te worden die de hoogfrequente verstoringen wegnemen en tevens groei van de aorta niet in de weg staan. Uit **Hoofdstukken 8-10** kunnen we concluderen dat de morfologie van de aorta unieke hemodynamica veroorzaakt die behandeling soms lastig maakt. Patiënt-specifieke CFD-simulaties bieden de unieke mogelijkheid om complexe hemodynamica te bestuderen en verschillende behandelingen uit te testen.

Endovasculaire behandeling van aortadissecties

Hoofdstuk 11 bespreekt endovasculaire behandeling van type B aorta dissectie (TBAD) vanuit een biomechanisch perspectief. De huidige standaardbehandeling voor TBAD is antihypertensiva.²⁷ TEVAR is in de acute fase alleen geïndiceerd indien complicaties aanwezig zijn. Desalniettemin treedt bij 50% van de patiënten met een TBAD die initieel alleen met antihypertensiva behandeld zijn degeneratieve verwijding van de verzwakte aortawand op.²⁸ Een deel van deze patiënten zal behandeld

moeten worden met TEVAR om complicaties te voorkomen. TEVAR in chronische TBAD is echter minder succesvol dan in de acute fase. Dit komt doordat de intimaflap verdikt en verstijft naar verloop van tijd, waardoor het risico op gecompliceerde plaatsing en het ontstaan van nieuwe scheuren in de intimaflap bij TEVAR in de chronische fase groter is.²⁹ Vanuit een mechanisch oogpunt zou je alle patiënten die risico lopen op aneurysmatische verwijding van de aorta na ongecompliceerde TBAD graag willen behandelen in de acute fase. Het zou echter schadelijk zijn om patiënten die nooit een aneurysma zullen ontwikkelen bloot te stellen aan de risico's van TEVAR, zoals retrograde dissectie, herseninfarct en ischemie van het ruggenmerg. Het is dus een uitdaging om vroeg patiënten te selecteren die uiteindelijk een aneurysma zullen ontwikkelen. Op dit moment zijn er geen richtlijnen die helpen bij het selecteren van deze patiënten. Onderzoek met 4D flow magnetic resonance imaging³⁰ en patiënt-specifieke CFD-simulaties³¹ zou kunnen helpen om hemodynamische parameters te identificeren die het risico op aneurysmatische verwijding van de aorta na acute TBAD voorspellen.

Hoofdstuk 12 bespreekt de casus van een patiënt met persisterende ischemie van het mesenteriale vaatbed na een gecompliceerde TBAD.³² De patiënt in kwestie had, ondanks behandeling met TEVAR, een persisterende aortadissectie die resulteerde in dynamische malperfusie van het mesenteriale vaatbed. We bespreken dat endovasculaire fenestratie, waarbij een scheur gemaakt wordt in de intimaflap om het drukverschil tussen het valse en ware lumen op te heffen, chronische ischemie van het mesenteriale vaatbed had kunnen voorkomen. Ook in dit geval is nader onderzoek met nieuwe beeldvormende technieken noodzakelijk om patiënten te selecteren die baat hebben bij endovasculaire fenestratie van de intimaflap in de acute fase om complicaties op de lange termijn te voorkomen.

Perspectief

Dit proefschrift heeft aangetoond dat patiënt-specifiek computerondersteund modelleren van hemodynamica waardevol is voor non-invasieve hemodynamische analyses die kunnen helpen bij het begrijpen van complexe hemodynamica. Daarnaast is het mogelijk om doormiddel van computermodellen verschillende interventies te testen. Dit kan helpen bij het plannen van chirurgische interventies en het ontwikkelen van hulpmiddelen. Er zijn echter meerdere obstakels die het gebruik van computersimulaties in de alledaagse kliniek in de weg staan. De simulaties zijn tijdrovend. Om relevante resultaten te krijgen is het noodzakelijk dat de modellen de anatomie en fysiologie van de patiënt accuraat nabootsen. Het construeren van de modellen en het kloppend maken van de simulaties is arbeidsintensief en vereist

enige ervaring. Op dit moment is het, ondanks de snelle ontwikkeling van computer-software en hardware, nog niet mogelijk om real-time CFD-analyses te produceren. Dit limiteert de toepasbaarheid voor klinische doeleinden tot electieve ingrepen. De ontwikkeling van geautomatiseerde systemen, gebaseerd op machine learning en deep learning-technieken, zullen deze limitaties in de toekomst wegnemen.

Multidisciplinaire samenwerking tussen biomedische ingenieurs en klinici is essentieel om computermodelleren voor het plannen van chirurgie en ontwikkelen van nieuwe hulpmiddelen verder te ontwikkelen. De volgende uitdaging is om prospectieve studies uit te voeren, met grotere patiëntenpopulaties, die gebruikt kunnen worden om de simulatieresultaten te verifiëren met klinische uitkomsten.

Referenties

- 1 Humphrey JD, Dufresne ER, Schwartz MA. Mechanotransduction and extracellular matrix homeostasis. *Nat Rev Mol Cell Biol* 2014;15(12):802–12. Doi: 10.1038/nrm3896.
- 2 Humphrey JD, Schwartz MA, Tellides G, et al. Role of mechanotransduction in vascular biology: Focus on thoracic aortic aneurysms and dissections. *Circ Res* 2015;1448–61. Doi: 10.1161/CIRCRESAHA.114.304936.
- 3 Hiratzka LF, Bakris GL, Beckman JA, et al. 2010 ACCF/AHA/AATS/ACR/ASA/SCA/SCAI/SIR/STS/SVM guidelines for the diagnosis and management of patients with Thoracic Aortic Disease: a report of the American College of Cardiology Foundation/American Heart Association Task Force on Practice Guidelines, A. *Circulation* 2010;121(13):e266-369. Doi: 10.1161/CIR.0b013e3181d4739e.
- 4 von Allmen RS, Anjum A, Powell JT. Incidence of descending aortic pathology and evaluation of the impact of thoracic endovascular aortic repair: a population-based study in England and Wales from 1999 to 2010. *Eur J Vasc Endovasc Surg Off J Eur Soc Vasc Surg* 2013;45(2):154–9. Doi: 10.1016/j.ejvs.2012.12.007.
- 5 Kleinstreuer C, Li Z, Basciano CA, et al. Computational mechanics of Nitinol stent grafts. *J Biomech* 2008;41(11):2370–8. Doi: 10.1016/j.jbiomech.2008.05.032.
- 6 Roccabianca S, Figueroa CA, Tellides G, et al. Quantification of regional differences in aortic stiffness in the aging human. *J Mech Behav Biomed Mater* 2014;29:618–34. Doi: 10.1016/j.jmbbm.2013.01.026.
- 7 Geisbüsch P, Kotelis D, Hyhlik-Dürr A, et al. Endografting in the Aortic Arch - Does the Proximal Landing Zone Influence Outcome? *Eur J Vasc Endovasc Surg* 2010;39(6):693–9. Doi: 10.1016/j.ejvs.2010.03.018.
- 8 van Bakel TM, Arthurs CJ, van Herwaarden JA, et al. A computational analysis of different endograft designs for Zone 0 aortic arch repair†. *Eur J Cardio-Thoracic Surg* 2018;54(2):389–96. Doi: 10.1093/ejcts/ezy068.
- 9 van Bakel TM, de Beaufort HW, Trimarchi S, et al. Status of branched endovascular aortic arch repair. *Ann Cardiothorac Surg* 2018;7(3):406–13. Doi: 10.21037/acs.2018.03.13.
- 10 Perera AH, Riga C V., Monzon L, et al. Robotic Arch Catheter Placement Reduces Cerebral Embolization During Thoracic Endovascular Aortic Repair (TEVAR). *Eur J Vasc Endovasc Surg* 2017;53(3):362–9. Doi: 10.1016/j.ejvs.2016.10.017.

- 11 Rohlffs F, Tsilimparis N, Saleptsis V, et al. Air Embolism During TEVAR: Carbon Dioxide Flushing Decreases the Amount of Gas Released from Thoracic Stent-Grafts During Deployment. *J Endovasc Ther* 2017;24(1):84–8. Doi: 10.1177/1526602816675621.
- 12 Giustino G, Sorrentino S, Mehran R, et al. Cerebral Embolic Protection During TAVR: A Clinical Event Meta-Analysis. *J Am Coll Cardiol* 2017;465–6. Doi: 10.1016/j.jacc.2016.12.002.
- 13 Li Y, Hu Z, Bai C, et al. Fenestrated and Chimney Technique for Juxtarenal Aortic Aneurysm: A Systematic Review and Pooled Data Analysis. *Sci Rep* 2016;6:20497. Doi: 10.1038/srep20497.
- 14 Martin-Gonzalez T, Pinçon C, Hertault A, et al. Renal outcomes analysis after endovascular and open aortic aneurysm repair. *J Vasc Surg* 2015;62(3):569–77. Doi: 10.1016/j.jvs.2015.03.075.
- 15 Reilly LM, Rapp JH, Grenon SM, et al. Efficacy and durability of endovascular thoracoabdominal aortic aneurysm repair using the caudally directed cuff technique. *J Vasc Surg* 2012;56(1):53–64. Doi: 10.1016/j.jvs.2012.01.006.
- 16 Tran K, Fajardo A, Ullery BW, et al. Renal function changes after fenestrated endovascular aneurysm repair. *J Vasc Surg* 2016;64(2):273–80. Doi: 10.1016/j.jvs.2016.01.041.
- 17 Morbiducci U, Ponzini R, Rizzo G, et al. Mechanistic insight into the physiological relevance of helical blood flow in the human aorta: an in vivo study. *Biomech Model Mechanobiol* 2011;10(3):339–55. Doi: 10.1007/s10237-010-0238-2.
- 18 Marrocco-Trischitta MM, Melissano G, Kahlberg A, et al. Chronic kidney disease classification stratifies mortality risk after elective stent graft repair of the thoracic aorta. *J Vasc Surg* 2009;49(2):296–301. Doi: 10.1016/J.JVS.2008.09.041.
- 19 Böckler D, Brunkwall J, Taylor PR, et al. Thoracic Endovascular Aortic Repair of Aortic Arch Pathologies with the Conformable Thoracic Aortic Graft: Early and 2 year Results from a European Multicentre Registry. *Eur J Vasc Endovasc Surg* 2016;51(6):791–800. Doi: 10.1016/J.EJVS.2016.02.006.
- 20 Marrocco-Trischitta MM, de Beaufort HW, Secchi F, et al. A geometric reappraisal of proximal landing zones for thoracic endovascular aortic repair according to aortic arch types. *J Vasc Surg* 2017. Doi: 10.1016/j.jvs.2016.10.113.
- 21 Ishimaru S. Endografting of the aortic arch. *J Endovasc Ther* 2004;11 Suppl 2:II62-71. Doi: 10.1583/04-1407.1.
- 22 Madhwal S, Rajagopal V, Bhatt DL, et al. Predictors of difficult carotid stenting as determined by aortic arch angiography. *J Invasive Cardiol* 2008;20(5):200–4.
- 23 Figueroa CA, Taylor CA, Chiou AJ, et al. Magnitude and direction of pulsatile displacement forces acting on thoracic aortic endografts. *J Endovasc Ther* 2009;16(3):350–8. Doi: 10.1583/09-2738.1.
- 24 Rahmani S, Grewal IS, Nabovati A, et al. Increasing angulation decreases measured aortic stent graft pullout forces. *J Vasc Surg* 2016;63(2):493–9.
- 25 Stanley JC, Criado E, Eliason JL, et al. Abdominal aortic coarctation: Surgical treatment of 53 patients with a thoracoabdominal bypass, patch aortoplasty, or interposition aorto-aortic graft. *J Vasc Surg* 2008;48(5):1073–82. Doi: 10.1016/j.jvs.2008.05.078.
- 26 Rumman RK, Nickel C, Matsuda-Abedini M, et al. Disease beyond the arch: A systematic review of middle aortic syndrome in childhood. *Am J Hypertens* 2015;28(7):833–46. Doi: 10.1093/ajh/hpu296.
- 27 Grabenwoger M, Alfonso F, Bachet J, et al. Thoracic Endovascular Aortic Repair (TEVAR) for the treatment of aortic diseases: a position statement from the European Association for Cardio-Thoracic Surgery (EACTS) and the European Society of Cardiology (ESC), in collabo-

- ration with the European Assoc. *Eur J Cardio-Thoracic Surg* 2012;42(1):17–24. Doi: 10.1093/ejcts/ezs107.
- 28 Fattori R, Montgomery D, Lovato L, et al. Survival after endovascular therapy in patients with type B aortic dissection: a report from the International Registry of Acute Aortic Dissection (IRAD). *JACC Cardiovasc Interv* 2013;6(8):876–82. Doi: 10.1016/j.jcin.2013.05.003.
- 29 Dong Z, Fu W, Wang Y, et al. Stent graft-induced new entry after endovascular repair for Stanford type B aortic dissection. *J Vasc Surg* 2010;52(6):1450–7. Doi: 10.1016/j.jvs.2010.05.121.
- 30 de Beaufort HW, Shah DJ, Patel AP, et al. Four-dimensional flow cardiovascular magnetic resonance in aortic dissection: Assessment in an ex vivo model and preliminary clinical experience. *J Thorac Cardiovasc Surg* 2018. Doi: 10.1016/j.jtcvs.2018.06.022.
- 31 Ben Ahmed S, Dillon-Murphy D, Figueroa CA. Computational Study of Anatomical Risk Factors in Idealized Models of Type B Aortic Dissection. *Eur J Vasc Endovasc Surg* 2016;52(6):736–45. Doi: 10.1016/j.ejvs.2016.07.025.

Chapter 15

Review Committee

Acknowledgements

List of publications

Curriculum vitae

Review Committee

Prof. dr. J. Hendrikse
Department of Radiology
University Medical Center Utrecht

Prof. dr. P.A.F.M. Doevendans
Department of Cardiology
University Medical Center Utrecht

Prof. dr. G.J. de Borst
Department of Vascular Surgery
University Medical Center Utrecht

Prof. dr. D.P.V. de Kleijn
Department of Vascular Surgery
University Medical Center Utrecht

Prof. dr. A.J.J.C. Bogers
Department of Cardiothoracic Surgery
Erasmus Medical Center Rotterdam

Acknowledgements – Dankwoord

Geachte prof. Moll, u heeft mij geleerd dat internationale wetenschap niet alleen uit onderzoek bestaat, maar vooral ook uit goede vriendschap. Die vriendschap heb ik ervaren. Uw visie en aanstekelijk enthousiasme hebben mij van begin af aan gestimuleerd en bij moeilijkheden stond u altijd voor me klaar. Bedankt voor uw begeleiding tijdens dit promotietraject en de kans die u mij heeft gegeven om deel uit te maken van deze unieke onderzoeksgroep.

Dear Santi, thank you for your mentorship. You taught me a lot about research and social life. I will never forget the great times we had in Como, Roma, Houston, London, Valencia, and of course Milan!

Dear Alberto, Andrea, Oliver and Clara thank you for making us feel at home in Ann Arbor. Alberto, you are a great mentor and supervisor, thank you for having me in your lab. I can honestly say that I never learned more about physics, academia, politics and cooking than during lunch with you. Also, barbecuing will never be the same. I hope we will continue to meet and collaborate in the future!

Dear prof Patel, your passion and enthusiasm for cardiac surgery and engineering is contagious. Your expertise, vision, and our Saturday morning meetings have greatly contributed to this thesis. I would also like to thank you and Heena for the great dinners we have had at your place. You made Margot and myself feel very welcome. Thank you for everything!

Dear prof Eagle, I want to thank you for supporting me in Ann Arbor. During our time at the University of Michigan, Margot and I have experienced the true Go Blue spirit! We would also like to thank you and Darlene for your hospitality, we very much enjoyed our stay.

Beste Joost, veel dank voor de halfjaarlijkse meetings in Utrecht en je adviezen op afstand. Jouw expertise in de endovasculaire behandeling van aortapathologie heeft erg geholpen bij het onderzoek.

Geachte leden van de beoordelingscommissie: prof. dr. J. Hendrikse, prof. dr. P.A.F.M. Doevendans, prof. dr. G.J. de Borst, prof. dr. D.P.V. de Kleijn en prof. dr. A.J.J.C. Bogers, hartelijk dank voor het beoordelen van mijn proefschrift. Het was mij een eer en een genoegen om aan dit promotieonderzoek te werken.

Beste dr. den Hoed, hartelijk dank voor uw mentorschap en de goede raad die u mij de afgelopen jaren gegeven heeft.

Graag wil ik de Stichting Prof. Michaël-van Vloten Fonds bedanken voor het subsidiëren van dit promotietraject.

Heeren van de oude garde: Frederik Jonker, Jip Tolenaar, Guido van Bogerijen, jullie hebben deze internationale onderzoeksgroep opgezet en uitgebouwd, zonder jullie geen promotietraject Utrecht-Milaan-Michigan!

Foeke Nauta, je was de eerste Dutch-guy in het lab van Alberto en hebt me geholpen om verder te gaan waar jij gebleven was. Bedankt voor de samenwerking en vriendschap!

Arnoud Kamman, bedankt dat je me zo top hebt opgevangen in Ann Arbor. Ik zal mijn eerste American Football wedstrijd met -10 en sneeuw in the Big House nooit vergeten!

Hector de Beaufort, je kwam me ophalen van Milano Linate en we zijn naast huisgenoten meteen goede vrienden geworden. Ik heb mede dankzij jou een top tijd gehad in Milaan en daarnaast in Rome, Chianti, Houston en Valencia. Op naar een volgende dag in de wondere wereld van de thoracale aorta!

Viony Belvroy, bedankt voor de gezellige tijden in Houston, Utrecht en Valencia!

Ignas Houben, we hebben veel tijd samen doorgebracht in het lab en CVC, waar jij met je kenmerkende enthousiasme en gevoel voor humor de sfeer er altijd goed in wist te houden. Bedankt voor de samenwerking, de mooie tijd en de vriendschap!

Domenico Spinelli, thank you for showing us how to live like a true Sicilian. Nero d'Avola will never be the same!

Dear Chris Arthurs, thank you for all your help and patience. Your modeling expertise and advice has really helped me a lot. I hope to continue our fruitful collaboration in the future!

Dear Cardiovascular Biomechanics Lab: Fede, Dan, Jonas, Sabrina, Chris, Kritika, Vasilina, Nitesh, thank you for the wonderful time inside and outside the lab. Please come visit us for movie night in Rotterdam!

Dear Bèta lab: Prof Auricchio, Max, Rodrigo, Margherita, Michele, thank you for the great collaboration. Iteriamo!

Beste Susan en Cobie, ik wil jullie graag hartelijk bedanken voor alle hulp die jullie mij tijdens dit promotieonderzoek geboden hebben. Jullie zorgen er altijd voor dat onze zaken goed geregeld zijn in Utrecht, ook al zijn wij ver weg. Heel veel dank!

Dear Eva, Elise, Dan, and all others at MCORRP. Thank you for being so nice and welcoming. You really represent the warm UofM feeling!

Ladies at the Michigan Cardiovascular Center: Nickole, Mary, Emily, thank you for your endless help with the IRB's, patient inclusion, appointments, finding a white coat, finding the OR, etc. We would be lost without you!

JC Frenck, bedankt voor de aanmoedigingen en selfie-Friday. Ondanks de fysieke afstand waren jullie nooit ver weg!

Lieve Thieu, Karien, Fons en Clare, de afgelopen drie jaar zijn een rollercoaster geweest. Ondanks dat het niet makkelijk was dat Margot en ik zo ver weg waren, hebben we ons altijd gesteund gevoeld. Ik wil jullie daar heel erg voor bedanken. Jullie support heeft zeker bijgedragen aan het succes van dit traject.

Lieve Sophia, Pieter, Paul en Lizanne, bedankt dat jullie ervoor hebben gezorgd dat de hechte gezinsband niet heeft geleden onder onze afwezigheid. We kijken er naar uit om weer bij jullie in Rotterdam te wonen!

Lieve Pap en Mam, jullie hebben ons laten zien dat je met hard werken alles kunt bereiken. Dat voorbeeld heeft me zeker geholpen tijdens dit promotietraject. We willen jullie bedanken voor de onvoorwaardelijke support die jullie Margot en mij hebben gegeven. Jullie staan altijd voor ons klaar, waren de eersten die mij kwamen opzoeken in Milaan en de eersten die ons bezochten in Ann Arbor. We kijken met veel plezier terug op deze periode, zonder jullie was het niet gelukt!

Lieve Margot, ik hou van je! Ik kan je niet genoeg bedanken dat je met me mee bent gegaan naar de VS. Je hebt voor mij veel betekend in dit promotietraject door over alles mee te denken en me te steunen. Ik ben er ook super trots op hoe jij een goede baan bij de University of Michigan hebt bemachtigd en daar meteen excelleerde. Onze onvergetelijke road trips door Amerika waren de kers op de taart van dit bijzondere avontuur!

List of Publications

In peer-reviewed journals

de Beaufort HWL, Coda M, Conti M, **van Bakel TMJ**, Nauta FJH, Lanzarone E, et al. Changes in Aortic Pulse Wave Velocity of Four Thoracic Aortic Stent Grafts in an Ex Vivo Porcine Model. *PLoS One* 2017;12:e0186080.

Marrocco-Trischitta MM, de Beaufort HWL, Secchi F, **van Bakel TMJ**, Ranucci M, van Herwaarden JA et al. A Geometric Reappraisal of Proximal Landing Zones for Thoracic Endovascular Aortic Repair According to Arch Types. *J Vasc Surg* 2017;65:1584-1590.

Marrocco-Trischitta MM, **van Bakel TMJ**, Romarowski RM, de Beaufort HWL, Conti M, van Herwaarden JA et al. The Modified Arch Landing Areas (MALAN) Improves Prediction of Stent-Graft Displacement Forces: Proof of Concept by Computational Fluid Dynamics Modeling. *EJVES* 2018;55:584-592.

van Bakel TMJ, Arthurs CJ, van Herwaarden JA, Moll FL, Eagle KA, Patel HJ et al. A Computational Analysis of Different Endograft Designs for Zone 0 Aortic Arch Repair. *EJCTS Editor's Choice* – 2018;54:389-396.

van Bakel TMJ, Lau KD, Hirsch-Romano J, Trimarchi S, Dorfman AL, Figueroa CA. Patient-Specific Modeling of Hemodynamics: Supporting Surgical Planning in a Fontan Circulation Correction. *JCTR* 2018;11:145-155.

van Bakel TMJ, de Beaufort HWL, Trimarchi S, Marrocco-Trischitta MM, Bismuth J, Moll FL, et al. Status of Branched Endovascular Aortic Arch Repair. *ACS* 2018;7:406:413.

van Bakel TMJ, Romarowski RM, Morganti S, van Herwaarden JA, Moll FL, de Beaufort HW et al. Blood Flow After Endovascular Repair in the Arch: A Computational Analysis. *Aorta in press*

van Bakel TMJ, Figueroa CA, van Herwaarden JA, Trimarchi S. Challenges of Thoracic Endovascular Aortic Repair for Type B Aortic Dissection. *J EVT* 2018;25:578-580.

van Bakel TMJ, Grassi V, Patel H, Trimarchi S. Dynamic Mesenteric Malperfusion in Aortic Dissection. *J EVT* 2019;26:88-89

van Bakel TMJ, Arthurs CJ, Nauta FJ, Eagle KA, van Herwaarden JA, Moll FL, et al. Cardiac Remodeling following Thoracic Endovascular Aortic Repair for Descending Aortic Aneurysms. *EJCTS* 2018; Doi: 10.1093/ejcts/ezy399

van Bakel TMJ, Burris NS, Patel H, Figueroa CA. Ascending Aortic Rupture After Zone 2 Endovascular Repair: A Multiparametric Computational Analysis. *EJCTS* 2018; Doi: 10.1093/ejcts/ezy458

Tossas C, **van Bakel TMJ**, Arthurs CJ, Coleman DM, Eliason JL, Figueroa CA, Stanley JC. Computational Analysis of Renal Artery Flow Characteristics by Modeling Aortoplasty and Aortic Bypass Interventions for Abdominal Aortic Coarctation. *Journal of Vascular Surgery*. In press

van Bakel TMJ, Patel HJ, van Bogerijen HW, Upchurch GR, Bismuth J, de Beaufort HWL, et al. TEVAR for acute type B aortic dissection: Results from the International Registry of Acute Aortic Dissection Interventional Cohort (IRAD-IVC). *Submitted*

Houben IB, **van Bakel TMJ**, Burris NS, Moll FL, van Herwaarden JA, Patel HJ. Optimal Use of the Third Dimension in CT Assessment of Type A Aortic Dissection: Implications for TAAD Secondary Interventions. *Submitted*

Book Chapters

van Bakel TMJ, Nauta FJ, Conti M, Romarowski RM, Morganti S, van Herwaarden J, et al. Novel Understanding of Thoracic Aortic Diseases from Bioengineering Concepts. In: Stanger OH, Pepper JR, Svensson LG. Surgical Management of Aortic Pathologies: Current Fundamentals for the Clinical Management of Aortic Disease, Springer, Vienna, 2018. ISBN: 978-3-7091-4872-3.

de Beaufort HWL, **van Bakel TMJ**, Conti M, Nauta FJH, Morganti S, Romarowski RM, et al. The Potential for Flow Dynamics to Inform Stent Sizing for Thoracic Aortic Disease. In: RM Greenhalgh. Vascular and Endovascular Consensus Update. BIBA Publishing, London, 2017. ISBN: 978-0-9570419-6-7.

van Bakel TMJ, de Beaufort HWL, Romarowski RM, Conti M, van Herwaarden JA, Moll FL, et al. Computational Analysis of Hemodynamic Displacement Forces in the Aorta. In: European Society of Vascular Biomechanics book 2017; GEPROVAS Strasbourg, ISBN: 978-2-9544771-2-1.

Trimarchi S, de Beaufort HWL, **van Bakel TMJ**. Presentation of Acute Aortic Syndromes. In: Sellke F. Aortic Dissection and Acute Aortic Syndromes. Springer, Vienna, 2018. *In press*

Curriculum Vitae

Theodorus Marinus Johannes van Bakel (Diederik) was born on November 17 1989 in Dordrecht, the Netherlands. After graduating from the Johan de Witt-Gymnasium in 2008, he obtained his medical degree from the Erasmus University Rotterdam in 2015. After his graduation he worked as a resident at the General Surgery Department of the Ikazia Ziekenhuis Rotterdam. In March 2016, he was invited by Prof. dr. F.L. Moll to do PhD research at the Department of Vascular Surgery of the University Medical Center Utrecht. The main focus of his research was to assess aortic hemodynamics and biomechanics using computational modelling methods, which is presented in this thesis. Diederik started his research in Italy, under the supervision of Prof. dr. S. Trimarchi at the Thoracic Aortic Research Center of IRCCS Policlinico San Donato. He worked in collaboration with biomedical engineers from the Biomechanics for Endovascular Treatment of the Aorta (BETA) laboratory at the University of Pavia on projects studying the effect of endografts on aortic hemodynamics using ex-vivo and computational modelling methods. In November 2016, Diederik moved to Ann Arbor, MI, USA, to join the Computational Vascular Biomechanics Lab of Prof. dr. C.A. Figueroa at the University of Michigan. Here, he worked in close collaboration with Prof. dr. H.J. Patel to study aortic hemodynamics for optimization of surgical planning and device development. Additionally, he worked with Prof. dr. K.A. Eagle on studies for the International Registry of Acute Aortic Dissection (IRAD). Diederik has presented his work at several prestigious meetings, including the American Heart Association, the International Society for Neurovascular Disease, the European Society for Vascular Surgery, the European Association for Cardio-Thoracic Surgery, Charing Cross, and the Houston Aortic Symposium. In May 2018, he received the Grienfield Research Award for his work on cardiac remodeling following thoracic endovascular aortic repair. After the defense of his PhD thesis, Diederik will start working at the Department of Cardiothoracic Surgery at Erasmus Medical Center in Rotterdam.

